In silico exploration of MoS2 nanosheets for the photocatalytic reduction of CO2

Rémi Favre

Numéro National de Thèse : 2022ENSL0008

THESE

en vue de l'obtention du grade de Docteur, délivré par

l'École Normale Supérieure de Lyon

École Doctorale n°206
École Doctorale de Chimie (Chimie, Procédés, Environnement)

Discipline : **Chimie**

Soutenue publiquement le 16/09/2022, par :
Rémi FAVRE

Exploration *in silico* de nano-feuillets de MoS_2 pour la réduction photocatalytique du CO_2

Devant le jury composé de :

Dominique COSTA	Directrice de recherche *Chimie Paristech*	Rapporteure
Stéphane JOBIC	Directeur de recherche *Université de Nantes*	Rapporteur
Jean-Sébastien FILHOL	Professeur des Universités *Université de Montpellier*	Examinateur
Tangui LE BAHERS	Maître de Conférences *Université de Lyon*	Directeur de thèse
Pascal RAYBAUD	Chercheur EPIC H.D.R *IFP Energies nouvelles*	Co-encadrant

Numéro National de Thèse : 2022ENSL0008

THESE DE DOCTORAT DE L'UNIVERSITE DE LYON

opérée par

l'École Normale Supérieure de Lyon

École Doctorale n°206
École Doctorale de Chimie (Chimie, Procédés, Environnement)

Discipline : **Chimie**

Soutenue publiquement le 16/09/2022, par :
Rémi FAVRE

Exploration *in silico* de nano-feuillets de MoS_2 pour la réduction photocatalytique du CO_2

Devant le jury composé de :

Dominique COSTA	Directrice de recherche *Chimie Paristech*	Rapporteure
Stéphane JOBIC	Directeur de recherche *Université de Nantes*	Rapporteur
Jean-Sébastien FILHOL	Professeur des Universités *Université de Montpellier*	Examinateur
Tangui LE BAHERS	Maître de Conférences *Université de Lyon*	Directeur de thèse
Pascal RAYBAUD	Chercheur EPIC H.D.R *IFP Energies nouvelles*	Co-encadrant

Remerciements

En premier lieu, je souhaite bien évidemment remercier chaleureusement Tangui et Pascal pour m'avoir permis de participer à cette aventure de 3 ans. Le voyage a été tortueux, je me suis parfois perdu en chemin, mais ils ont toujours su me remettre sur la bonne route, même s'il a parfois fallu me pousser dans mes retranchements. J'ai énormément appris, tant sur le plan scientifique qu'humain, grâce à vous deux.

J'aimerais également remercier Dominique Costa et Stéphane Jobic pour avoir accepté d'être mes rapporteurs ainsi que Jean-Sébastien Filhol pour sa participation à mon jury.

Un grand merci également à tous les membres du laboratoire de chimie de l'ENS de Lyon que j'ai pu côtoyer au cours de ces 3 années. Mention particulière évidemment aux membres de l'équipe chimie théorique pour l'entraide mutuelle, tant sur des aspects scientifiques que personnels. Afin d'éviter de me lancer dans une liste où je vais oublier la moitié des noms, je vais me contenter de citer mes co-bureaux, Layla et Laleh, pour nos discussions qui m'ont souvent permis de me changer les idées. Je remercie également tout l'équipe administrative pour leur disponibilité et leur gentillesse à toute épreuve.

En ce qui concerne les gens du dehors (cf. The 100), un merci particulier à ma bande de lyonnais (Marie, Anaëlle, Karim, Enzo, Yannick, Enya) pour tous ces moments de détente entre deux journées intenses. Merci aussi aux membres de La Bande première du nom (Alizée, Thibault, Arthur, Céline, Gaëlle, Marine, Lou…) qui sont toujours dans ma vie même 8 ans après le lycée. Je me dois également de remercie Laurine et Léa, pour m'avoir accompagné pendant une partie de ce périple.

Même si l'athlétisme m'aura parfois pris beaucoup (trop) de temps, ces trois années n'auraient pas été les mêmes sans le soutien de mes coéquipiers de l'U.A.Maurienne puis de l'A.L.Echirolles. Là encore la liste est bien trop longue pour que je me risque à en entamer une mais sachez que je vous aime tous profondément. Mention particulière à mon coach Jérémie qui ne m'a jamais lâché durant ces années, même quand j'arrivai à peine à mettre

un pied devant l'autre. Je te promets qu'on reprendra bientôt notre conquête des sommets ensemble.

Là encore, cela a parfois représenté beaucoup de temps mais les jeux-vidéos m'ont grandement aidé à traverser les nombreux moments difficiles. Je remercie donc tous mes compagnons de jeux de ces trois années pour avoir su me redonner le sourire grâce à leur bonne humeur et leur humour inégalable. Merci notamment à ma team de vacanciers (Jean-Luc, Alexis, Mathieu, Bastien, PN et Benjamin), notre séjour dans le Sud s'annonce mémorable.

Merci bien évidemment à toute ma famille, qui m'a toujours soutenu et encouragé dans mes projets. Je ne le montre sûrement pas assez mais vous comptez tous énormément pour moi et si j'en suis là aujourd'hui c'est en grande partie grâce à vous.

Un merci tout particulier à Jean-Luc et Alexis, mes frères de cœur. Je vous ai déjà cité une fois mais cela ne suffisait pas à représenter à quel point vous comptez pour moi.

Table of Contents

List of Figures *1*

List of Tables *5*

Chapter I. Introduction *7*

References **10**

Chapter II. Bibliography *11*

II.1. The photocatalysis on semiconductors **11**

II.1.1. General principles 11

II.1.1.a. The photocatalysis mechanism 11

II.1.1.b. Efficiency measurement 12

II.1.2. The photon absorption 14

II.1.2.a. The challenges 14

II.1.2.b. Strategies to improve the step 16

II.1.2.c. Z-scheme principles 18

II.1.3. Charge separation and transport 20

II.1.3.a. Challenges 20

II.1.3.b. Strategies 21

II.1.4. Surface chemical reactions 22

II.1.4.a. Challenges 23

II.1.4.b. The strategies 23

II.1.5. Conclusions 23

II.2. The photocatalytic reduction of CO_2 ..... **24**

II.2.1. General principles 24

II.2.1.a. Interests 25

II.2.1.b. Approaches 25

II.2.1.c. Challenges 26

II.2.2. The mechanisms involved 27

II.2.2.a. Methods used in reactivity studies 28

II.2.2.b. Initialization steps 30

II.2.2.c. Reduction pathways on semiconductor surface 32

II.2.2.d. Control of the oxidation side 36

II.2.3. Efficiency obtained 36

II.2.3.a. On TiO_2 systems 37

II.2.3.b. On other metal oxides 38

II.2.3.c. On sulfides 39

II.2.3.d. On phosphides 41

II.2.4. Conclusion 41

II.3. Characteristics and application of MoS_2 as a semiconductor **42**

II.3.1. MoS_2 characteristics 42

II.3.1.a. Structural characteristic 42

II.3.1.b. Physical properties 43

II.3.2. MoS_2 utilization in photocatalysis 44

II.3.2.a. Possible applications 44

II.3.2.b. Ways to improve MoS_2 performances 45

II.3.2.c. MoS_2/SC heterostructures to obtain a Z-scheme mechanism 48

II.4. Conclusion **50**

II.5. References **52**

Table of Contents

Chapter III. Methodology 67

III.1. The density functional theory 67
III.1.1. Simplification of the Schrödinger equation 67
III.1.1.a. The Born Oppenheimer approximation 68
III.1.1.b. Hartree-Fock approximation 69
III.1.2. The formulation of the density functional theory 70
III.1.2.a. Hohenberg-Kohn theorems 71
III.1.2.b. The Kohn-Sham approach 72
III.1.3. Approximation of the exchange-correlation term 74
III.1.3.a. The Local Density Approximation (LDA) 74
III.1.3.b. The Generalized Gradient Approximation (GGA) 75
III.1.3.c. The hybrid functionals 75
III.1.3.d. Comparison of some functionals 76
III.1.3.e. The dispersion correction 78
III.1.4. The Self Consistent Field 78
III.1.5. DFT in Periodic Boundary Conditions 79
III.1.5.a. The Bloch theorem 79
III.1.5.b. The basis set 80
III.1.5.c. The pseudo potentials method 82
III.1.5.d. The implicit solvation model 83

III.2. The targeted properties 84
III.2.1. Bandgap and electronic structure 84
III.2.1.a. Bandgap definitions 84
III.2.1.b. Method used to determine the electronic structure 85
III.2.2. The charge transfer within the heterojunction systems 87
III.2.3. The photocatalysis mechanism: an electrocatalysis approach 88
III.2.3.a. The Computational Hydrogen method (CHE) 89
III.2.3.b. The surface charging approach 90
III.2.3.c. How to link charge, potential and energy? 91
III.2.3.d. Work at constant charge or at constant potential ? 92

III.3. References 94

Chapter IV. Evolution of the electronic structures of the MoS_2/TiO_2 (anatase) heterojunction 97

IV.1. Method 98
IV.1.1. Choice of the functional 98
IV.1.2. The TiO_2 structures 100
IV.1.2.a. The number of layers 100
IV.1.2.b. The hydration state 101
IV.1.2.c. The lattice parameters describing the TiO_2/MoS_2 interface 103
IV.1.3. The calculation parameters (vacuum, K-points, convergence criterion…) 104
IV.1.4. Summarize of the computational details 105

IV.2. Results 107
IV.2.1. MoS_2 2D-monolayer in physical interaction with TiO_2 anatase surfaces 107
IV.2.1.a. Bare and hydrated TiO_2 surfaces 107
IV.2.1.b. Sulfided and hydrated-sulfided TiO_2 surfaces 108
IV.2.2. MoS_2 nanoribbon in chemical interaction with TiO_2 anatase surfaces 110
IV.2.2.a. Bare and hydrated TiO_2 surfaces 110
IV.2.2.b. Chemical modification of the 1D-interface 114

IV.3. Discussion 115

IV.4. Conclusions 119

IV.5. References 120

Table of Contents

Chapter V. Reactivity study: CO_2 reduction mechanism on MoS_2 nanosheets 123

V.1. Calculation details 124

V.2. Results 126

V.2.1. Evolution of the edge sites under electrochemical conditions 126

V.2.1.a. Hydrogenation of the nanosheet 126

V.2.1.b. Hydroxylation of the nanosheet 127

V.2.1.c. Hydration of the nanosheet 129

V.2.2. Evolution of the hydrogen coverage as a function of the potential 130

V.2.2.a. On bare edges 130

V.2.2.b. On oxygenated edges 133

V.2.3. CO_2 adsorption 136

V.2.3.a. On bare and hydrogenated surfaces 136

V.2.3.b. On hydroxylated edges 138

V.2.4. Identifications of the CO_2 reduction mechanisms 139

V.2.4.a. On hydrogenated edges 139

V.2.4.b. On hydroxylated edges 144

V.3. Discussion 149

V.3.1. The activated species 149

V.3.2. The possible mechanisms 152

V.3.3. The overpotential applied 153

V.4. Conclusion 154

V.5. References 156

Chapter VI. Conclusions and perspectives 157

References 159

Appendix 161

A.1. Spatial localization of the most relevant interfacial states of MoS_2/TiO_2 heterostructures in chemical interaction 161

A.2. Extrapolation curves associated to all the intermediates considered in the mechanisms 167

List of Figures

FIGURE II-1 : THE FIVE MAINS STEPS INVOLVED IN THE PHOTOCATALYSIS MECHANISM. 12
FIGURE II-2 : CALCULATED SOLAR-TO-HYDROGEN CONVERSION EFFICIENCY AS FUNCTIONS OF PHOTON WAVELENGTH FOR PHOTOCATALYTIC ONE-STEP OVERALL WATER SPLITTING USING PHOTOCATALYSTS WITH VARIOUS QUANTUM EFFICIENCY. THE ASSOCIATED CALCULATIONS ASSUMED AM 1.5G SOLAR IRRADIATION [21]. 15
FIGURE II-3 : STRATEGIES FOR OBTAIN A VISIBLE LIGHT RESPONSE: (A) USE OF DOPING ELEMENT, (B) SOLID SOLUTION FORMATION, (C) DYE-SENSITIZATION (D) LOCALIZED SURFACE PLASMON RESONANCE, (E) QUANTUM CONFINEMENT AND (F) Z-SCHEME CONFIGURATION [53]. 18
FIGURE II-4 : THE TWO CHARGE CARRIER DYNAMICS THAT CAN HAPPEN IN TYPE II WITH (A) THE CLASSICAL TYPE II MECHANISM AND (B) THE Z-SCHEME MECHANISM. 19
FIGURE II-5: SURFACE HETEROJUNCTION ON A SINGLE TiO_2 PARTICLE DUE TO THE VARIATION OF ELECTRONIC STRUCTURE BETWEEN THE (101) AND (001) SURFACE ORIENTATIONS. 22
FIGURE II-6 : FREE-ENERGY DIAGRAM FOR THE REDUCTION OF CO_2 TO CH_4 ON THE MO EDGE OF $MoSe_2$, $\theta S = 0.5$, AT U 0 V AND U_L = - 0.38 V, THE LIMITED POTENTIAL WHERE ALL THE REACTION STEPS BECOMES EXERGONIC. 29
FIGURE II-7 : CONDUCTION BAND, VALENCE BAND POTENTIALS AND BANDGAP ENERGIES OF VARIOUS SEMI-CONDUCTORS PHOTOCATALYSTS RELATIVE TO THE REDOX POTENTIALS AT PH 7 OF COMPOUNDS INVOLVED IN CO_2 REDUCTION [165]. 30
FIGURE II-8 : STRUCTURES ASSOCIATED TO THE 2 ADSORPTION MODES ON TiO_2 ANATASE (101) WITH ONE OXYGEN VACANCY: A) MONODENTATE AND B) BIDENTATE. 31
FIGURE II-9 : THREE PROPOSED MECHANISM FOR THE REDUCTION OF CO_2 TO METHANE: A. THE FORMALDEHYDE PATHWAY B. THE CARBENE PATHWAY AND C. THE GLYOXAL PATHWAY [169]. 33
FIGURE II-10 : BAND EDGE POSITION WITH RESPECT TO THE VACUUM LEVEL AND THE NHE FOR SELECTED OXIDES AT PH (0). THE TOP SQUARES REPRESENT THE CONDUCTION BAND EDGES, THE BOTTOM SQUARES REPRESENT THE VALENCE BAND EDGES, THE TOP NUMBER IS THE CONDUCTION BAND LEVEL AND THE NUMBER BETWEEN THE SQUARES IS THE BANDGAP [214]. 39
FIGURE II-11 : BAND EDGE POSITION WITH RESPECT TO THE VACUUM LEVEL AND THE NHE FOR SELECTED CHALCOGENIDES AND SILICON AT PH = 0. THE TOP SQUARES REPRESENT THE CONDUCTION BAND EDGES, THE BOTTOM SQUARES REPRESENT THE VALENCE BAND EDGES, THE TOP NUMBER IS THE CONDUCTION BAND LEVEL AND THE NUMBER BETWEEN THE SQUARES IS THE BANDGAP [214] 40
FIGURE II-12 : DIFFERENT COORDINATION AND STACKING SEQUENCES OF THE THREE MAIN MoS_2 STRUCTURES: 1T, 2H AND 3R [230]. 43
FIGURE II-13 : FREE ENERGY DIAGRAM FOR THE REDUCTION OF CO_2 TO CH_4 ON THE NI-DOPED S EDGE OF MoS_2 AT 0V AND U_L= - 0.28 V, THE LIMITED POTENTIAL WHERE ALL THE REACTION STEPS BECOMES EXERGONIC [283]. 47
FIGURE II-14 : THE PROPOSED PHOTOCATALYTIC MECHANISM FOR $(BiO_2)CO_3/MoS_2$ HETEROJUNCTION [258]. 48
FIGURE II-15 : DIFFERENT CHARGE CARRIER MIGRATION PROPOSED FOR MoS_2/TiO_2 SYSTEMS: (A) MoS_2 ACTS AS A CO-CATALYST WHILE TiO_2 PLAY THE ROLE OF LIGHT HARVESTER [285] AND (B) MoS_2 AND TiO_2 ARE INVOLVED IN A TYPE II HETEROSTRUCTURE [297] 50
FIGURE III-1 : SUMMARY OF MEAN ABSOLUTE PERCENTAGE ERROR (MAPE) FOR THE INTERATOMIC DISTANCES, Δ; COHESIVE ENERGIES, ECOH; AND BULK MODULI, B0, OF THE 3D, 4D, AND 5D TRANSITION METALS SERIES EXCLUDING METALS WITH PARTICULAR CRYSTALLOGRAPHIC STRUCTURE: MN, LA, AND HG. MAPE IN Δ HAS BEEN MULTIPLIED BY A FACTOR OF 10 FOR A BETTER VISUALIZATION. 77
FIGURE III-2: PRINCIPLES OF THE SCF METHOD 79
FIGURE III-3 : ILLUSTRATION OF THE PSEUDISATION OF THE POTENTIAL AND OF THE WAVE FUNCTIONS OF THE VALENCE ELECTRONS .. 82
FIGURE III-4 : REPRESENTATION OF OPTICAL GAP E_{OPT}, THE MONOELECTRONIC BANDGAP E_{MONO}, THE FUNDAMENTAL GAP E_{FUND}, THE IONIZATION ENERGY IE, THE ELECTRONIC AFFINITY EA AND THE EXCITON BINDING ENERGY E_B. 84
FIGURE III-5 : TOTAL DOS OF TiO_2 ANATASE (101) WITH 8 LAYERS, EXPRESSED A FUNCTION OF THE ENERGY OF THE FERMI LEVEL. THE CALCULATIONS HAVE BEEN PERFORMED WITH THE HSE-06 FUNCTIONAL ON A 4×4×1 K-POINTS GRID AND D3-BJ DISPERSION CORRECTION. 85
FIGURE III-6 : DETERMINATION OF THE VACUUM POTENTIAL BY PLOTTING THE LOCAL POTENTIAL AS A FUNCTION OF THE Z COORDINATE. 86
FIGURE III-7 : TOTAL DOS OF TiO_2 ANATASE (101) WITH 8 LAYERS, EXPRESSED A FUNCTION OF THE VACUUM LEVEL. THE CALCULATIONS HAVE BEEN PERFORMED WITH THE HSE-06 FUNCTIONAL ON A 4×4×1 K-POINTS GRID AND D3-BJ DISPERSION CORRECTION. 86
FIGURE III-8 : DOS WITH ATOM DECOMPOSITION FOR TiO_2 ANATASE (101) WITH 8 LAYERS, EXPRESSED A FUNCTION OF THE VACUUM LEVEL. THE CALCULATIONS HAVE BEEN PERFORMED WITH THE HSE-06 FUNCTIONAL ON A 4×4×1 K-POINTS GRID AND D3-BJ DISPERSION CORRECTION. 87

List of Figures

Figure III-9 : Example of electrons transfer possible and Induce Electric Field associated (IEF) for a MoS_2 monolayer in physical interaction with TiO_2 anatase (101)..... 88

Figure III-10 : Spatial decomposition of the solid/electrolyte system into the solute, interface, and electrolyte regions for an fcc Pt(111) surface embedded in an electrolyte with a relative permittivity of ϵ_R = 78.4 and monovalent cations and anions with a concentration of 1M. The solute is described by density-functional theory, and the electrolyte is described by an implicit solvation model. The interface region is formed self-consistently as a functional of the electronic density of the solute. All properties are shown as a percentage of their maximum absolute value. The inset shows the relatively invisible peak in the Hartree potential at the interface [32]. 91

Figure III-11 : Example of the quadratic response between the potential and the energy. Each point corresponds to results obtained at different charges and the curves are interpolation curves. Example a) corresponds to the comparison of two configuration of a water molecule on a H_2O/Pd(111) system [33] while example (b) illustrates the evolution of surface energy of a CoOOH semiconductor as a function of the potential [38]. . 92

Figure III-12 : Example of G = f(U) interpolation curve for a MoS_2 nanosheet with 50%S on each edge. Calculations have been performed with PBE functional on a 3x3x1 K-Points grid with D3-BJ dispersion correction. 93

Figure IV-1: Example of epitaxial relationship between MoS_2 and TiO_2: a) High-Resolution Episcopic Microscopy (HREM) images of (002) MoS2 in epitaxial interaction with TiO_2 anatase (001) [5] and b) structure of a Mo6S14 in epitaxial interaction on TiO_2 anatase (101) obtained with DFT calculation [3]..... 97

Figure IV-2: Comparison of the classical type II mechanism and the Z-scheme mechanism of the type-II heterojunction. 98

Figure IV-3: Evolution of the surface energy as a function of the number of layers for a) TiO_2 anatase (101) and b) TiO_2 anatase (001)..... 100

Figure IV-4: Water adsorption structures on a) TiO_2 anatase (101) with θ=10.1 H_2O/nm^2 and b) TiO_2 anatase (001) with θ= 3.5 H_2O/nm^2. 101

Figure IV-5: Evolution of the band position of TiO_2 anatase (101) and (001) with implicit and/or explicit water solvation. Experimental values are taken from Grätzel study [17]..... 102

Figure IV-6: Slab supercell of a) TiO_2 anatase (101) and b) TiO_2 anatase (001) hydrated..... 103

Figure IV-7: Slab supercell before and after multiplication for a) TiO_2 anatase (101), b) MoS_2 monolayer, c) TiO_2 anatase (001) hydrated and d) MoS_2 monolayer..... 104

Figure IV-8: (a) structure of the TiO_2(101) and MoS_2 in epytaxic interaction. Ti, Mo, O and S atoms are in blue, grey, red and yellow respectively. (a) convergence of the electronic energy as a function of the k-points mesh in the x direction. (b) convergence of the electronic energy as a function of the k-points mesh in the y direction. (c) convergence of the electronic energy as a function of the vacuum thickness. (d) convergence of the electronic energy as a function of the SCF convergence criterion. 105

Figure IV-9: Molecular structure of MoS_2 monolayer physically adsorbed, DOS of these interfaces and evolution of the band position before and after junction for a) MoS_2/TiO_2 (101) and b) MoS_2/TiO_2 (001) hydrated. 107

Figure IV-10: DOS with element decomposition associated to MoS_2 in physical interaction on TiO_2 (101) on the left and TiO_2 (001) hydrated on the right..... 108

Figure IV-11: Molecular structure of MoS_2 monolayer physically adsorbed, DOS of the interfaces and evolution of the band position before and after junction for a) TiO_2 (101) with θ(S) = 1.3 S/nm^2 b) TiO_2 (001) with θ(S) = 1.7 S/nm^2 and $\theta(H_2O)$ = 3.5 H_2O/nm^2. 109

Figure IV-12: Evolution of the MoS_2 finite nanoribbon before (a)) and after restructuration induced by the transfer of half of S-atoms from the S-edge to M-edge (b))..... 111

Figure IV-13: Evolution of the band positions of MoS_2 when going from the monolayer to the nanoribbons and chemically modified nanoribbons. 111

Figure IV-14: Molecular structure of MoS_2 nanoribbon chemically adsorbed, DOS of the interfaces and evolution of the band position before and after junction for a) TiO_2 (101) b) TiO_2 (001) (interaction with M-edge) and c) TiO_2 (001) (interaction with S-edge). 112

Figure IV-15: Molecular structure of MoS_2 nanoribbon chemically adsorbed, DOS of the interfaces and evolution of the band position before and after junction for a) MoS_2 ribbon with 2 Mo rows b) MoS_2 ribbon with 4 rows sulfided and c) MoS_2 ribbon with 4 rows oxygenated..... 114

Figure IV-16: Comparison of the band position of the two materials after junction for all the cases in physical interaction on the left and chemical interaction on the right. 115

Figure IV-17: Comparison of the Z-scheme mechanism (a) and the type I mechanism (b) that could be implied when a heterojunction occurs between the MoS_2 sheet and the TiO_2 (101) surface in physical (a) or chemical (b) interaction. Due to the intrinsic semiconductors involved, the fermi levels are localized in the middle of the bandgap before interaction..... 116

List of Figures

Figure V-1 : Proposed mechanism associated to the use of TiO_2 as the light harvester and site for the oxidation reaction while MoS_2 will act as the reduction co-catalyst. 123
Figure V-2 : Structure of the MoS_2 50%S restructuration from two point of view: from the x direction on the left and from the y direction on the right. 125
Figure V-3 : Evolution of the hydrogen coverage on a MoS_2 Mo-edge. 126
Figure V-4 : Evolution of the hydrogen coverage on a MoS_2 S-edge. 127
Figure V-5 : Structures associated to the Mo-edge 50%OH+50%SH, the Mo-edge fully 100%OH and the S-edge 50%OH+50%S. 129
Figure V-6 : Optimized structure of the water adsorption on a MoS_2 S-edge 50%S. 129
Figure V-7 : Evolution of the hydrogen coverage as a function of the potential applied on Mo-edge 50%S. 131
Figure V-8 : Evolution of the hydrogen coverage as a function of the potential applied on S-edge 50%S. 132
Figure V-9 : Evolution of the hydrogen coverage as a function of the potential applied with the computational hydrogen electrode (CHE) method on a) Mo-edge 50%S and b) S-edge 50%S. 133
Figure V-10 : Evolution of the hydrogen coverage as a function of the potential applied on S-edge 50% hydroxylated. 134
Figure V-11 : Evolution of the hydrogen coverage the more favorable on a MoS_2 Mo-edge with 50%O/50%S as a function of the potential applied. 135
Figure V-12 : Evolution of the hydrogen coverage the more favorable on a MoS_2 Mo-edge 100%OH as a function of the potential applied. 135
Figure V-13 : CO_2 adsorption study as a function of the potential on a) the bare Mo-edge and b) the bare S-edge. . 136
Figure V-14 : CO_2 adsorption study as a function of the potential on a) the Mo-edge 50%H and b) the S-edge 50%H. 137
Figure V-15 : CO_2 adsorption study as a function of the potential on a) the Mo-edge 50%OH-50%SH and b) the S-edge 50%OH-50%S. 138
Figure V-16 : Reaction pathways on a Mo-edge 50%SH at - 1.30 V. The green pathway leads to HCOOH through COOH intermediate, the red pathway leads to HCOOH through OCHO intermediate and the blue pathway lead to CH_2O through OCHO intermediate. Black intermediate is not expected to be observed in the mechanism. . 140
Figure V-17 : Catalysis cycle of the mechanism favored on the Mo-edge hydrogenated for an overpotential of - 1.1 V. 142
Figure V-18 : Reaction pathway on a S-edge 50%SH at - 0.34 V. The green pathway leads to CO from chemically adsorbed CO_2, the red pathway leads to HCOOH through CO_2 adsorbed and OCHO intermediate and the blue pathway leads to CH_2O through CO_2 adsorbed and OCHO intermediate. Black intermediate is not expected to be observed in the mechanism. 142
Figure V-19: Catalysis cycle of the formation of CO on the S-edge hydrogenated for an overpotential of - 0.22 V. 144
Figure V-20 : Reaction pathway on a Mo-edge 50%OH-50%SH at - 0.41 V. The green pathway leads to HCOOH through COOH as intermediate, the red pathway leads to CO through CO_2 adsorbed as intermediate and the blue pathway lead to CO through COOH as intermediate. Black intermediates are not expected to be observed in the mechanism. 144
Figure V-21 : Reaction pathway on a Mo-edge 50%OH-50%SH at - 1.29 V. The green pathway leads to HCOOH through COOH as intermediate, the red pathway leads to CO through CO_2 adsorbed as intermediate and the blue pathway lead to CO through COOH as intermediate. Black intermediates are not expected to be observed in the mechanism. 145
Figure V-22 : Catalysis cycle of the mechanism favored on the Mo-edge 50%OH-50%SH for an overpotential of - 1.09 V. 146
Figure V-23: Reaction pathway on a Mo-edge 100%OH at - 1.28 V. Black intermediates are not expected to be observed in the mechanism. 147
Figure V-24 : Catalysis cycle of the mechanism favored on the Mo-edge 100% OH for an overpotential of - 1.07 V. 148
Figure V-25 : : Reaction pathway on a S-edge hydroxylated at - 1.30 V. 148
Figure V-26 : Electronic structure associated to a MoS_2 nanosheet and comparison with the standard potential of the targeted reactions and the overpotential required. 154
Figure A-1 : Localization of the most relevant states for MoS_2 in chemical interaction through the Mo-edge on TiO_2 anatase (101) 161
Figure A-2: Localization of the most relevant states for MoS_2 in chemical interaction through S-edge on TiO_2 anatase (001) 162

List of Figures

FIGURE A-3: LOCALIZATION OF THE MOST INDICATIVE STATES FOR MoS_2 IN CHEMICAL INTERACTION THROUGH MO-EDGE ON TiO_2 ANATASE (001)..... 163
FIGURE A-4 : LOCALIZATION OF THE MOST INDICATIVE STATES FOR MoS_2 WITH 2MO ROWS IN CHEMICAL INTERACTION THROUGH MO-EDGE ON TiO_2 ANATASE (101) 164
FIGURE A-5: LOCALIZATION OF THE MOST INDICATIVE STATES FOR MoS_2 SULFIDED IN CHEMICAL INTERACTION THROUGH MO-EDGE ON TiO_2 ANATASE (101). 165
FIGURE A-6: LOCALIZATION OF THE MOST INDICATIVE STATES FOR MoS_2 OXYGENATED IN CHEMICAL INTERACTION THROUGH MO-EDGE ON TiO_2 ANATASE (101). 166
FIGURE A-7 : EXTRAPOLATION CURVES ASSOCIATED TO ALL THE INTERMEDIATES CONSIDERED IN THE MECHANISTIC STUDY ON THE MO-EDGE 50%H..... 167
FIGURE A-8 : EXTRAPOLATION CURVES ASSOCIATED TO ALL THE INTERMEDIATES CONSIDERED IN THE MECHANISTIC STUDY ON THE S-EDGE 50%H..... 167
FIGURE A-9 : EXTRAPOLATION CURVES ASSOCIATED TO ALL THE INTERMEDIATES CONSIDERED IN THE MECHANISTIC STUDY ON THE MO-EDGE 50%OH-50%SH. 168
FIGURE A-10 : EXTRAPOLATION CURVES ASSOCIATED TO ALL THE INTERMEDIATES CONSIDERED IN THE MECHANISTIC STUDY ON THE MO-EDGE 100%H. 168
FIGURE A-11 : EXTRAPOLATION CURVES ASSOCIATED TO ALL THE INTERMEDIATES CONSIDERED IN THE MECHANISTIC STUDY ON THE S-EDGE HYDROXYLATED..... 169

List of Tables

TABLE IV-1: COMPARISON OF THE PERFORMANCE OF PBE AND HSE-06 FUNCTIONALS FOR THE GEOMETRY OPTIMIZATION OF MoS_2 AND TiO_2 BULK. *ESTIMATED FROM STS MEASUREMENT OF A 3-MONOLAYER BANDGAP OF MoS_2 [14, 15] AND DFT ESTIMATION OF THE BANDGAP REDUCTION FROM 3-MONOLAYER TO BULK MoS_2 [16]. SEE SECTION III.2.1.A FOR MORE INFORMATIONS. 99
TABLE IV-2: FRACTION OF ELECTRON TRANSFERRED FROM MoS_2 (I.E. A NEGATIVE VALUE INDICATES A LOSS OF ELECTRON) [30]. .. 117
TABLE V-1 : COMPARISON OF THE EXPERIMENTAL AND COMPUTATIONAL CALCULATION OF THE -TS TERM. THE COMPUTATIONAL TERM HAS BEEN DETERMINED WITH GAUSSIAN IN PBE0/6-311+G(D,P) IN GAS PHASE WITH THE HARMONIC APPROXIMATION.... 124
TABLE V-2 : ΔG ASSOCIATED TO THE DIFFERENT ACTIVATED SPECIES ON THE EDGES WHERE A REACTION CAN OCCUR. THE ENERGIES ARE CALCULATED AT THE POTENTIAL WHERE THE ACTIVATION BECOMES THERMODYNAMICALLY FAVORED. GREEN VALUES ARE FOR THE INTERMEDIATES THERMODYNAMICALLY FAVORED, YELLOW VALUES ARE FOR THE INTERMEDIATES CLOSE TO THE CO_2 VDW ENERGY AND RED VALUES ARE FOR THE INTERMEDIATES THERMODYNAMICALLY UNFAVORED. 150

Chapter I. Introduction

Even if it is well admitted by the scientific community, it is always important to recall that we are facing an unprecedent increase of the global energy consumption. From 15-17 TW in 2010 [1, 2], it is expected to reach 25-27 TW in 2050 [3]. In this context, the use of renewable energies is attracting more and more attention in order to proceed to an energy transition from fossil fuels. In 2011, 13% of the energy came from renewable sources, and this contribution is in expansion (19.1 % in France in 2020, + 84% in 30 years [4]). However, it has been estimated that only the insufficient value of 20 TW can be produced from wind, biomass, geothermal energy and tides [5]. On the other hand, the solar energy seems to represent an almost infinite energy source since the solar energy received on the Earth in one hour corresponds to the annual energy consumption [3]. However, due to the fact that the irradiation is not regular, the energy has to be stored under an alternative form. This requirement can be solved by transforming the solar energy in chemical energy, through the formation of chemical molecules that are storable and/or transportable [6, 7]. It is the basic principle of the photocatalysis on semiconductors, that start with the absorption of the light by the material, continue with the transfer of the photogenerated charge carriers to the active sites and finish with the use of these charges to do the chemical reactions.

Among various possible applications, the photocatalytic reduction of the CO_2 is attracting the attention of the scientific community for two main reasons. From an ecological point of view, reducing the atmosphere concentration in CO_2, a greenhouse gas, is one of the key factors to face the climate change [8, 9]. From an industrial point of view, transforming CO_2 into high energy compounds (methanol, methane, or higher alkanes…) that can be then combusted, could be a way of closing the carbon cycle of some industrial processes. However, due the numerous challenges raised by the CO_2 transformation, including the lack of understanding in the complete mechanism, the production rates rarely exceed tens of $\mu mol.g^{-1}.h^{-1}$ [10] that is not satisfying. In terms of energy conversion, we have difficulty to reach the value of the natural photosynthesis (between 0.25 and 1% in yearly average [11]), despite more favorable conditions (use of pure CO_2 especially).

To tackle these challenges, the present work proposes to use molybdenum disulfide (MoS_2) as a component of a photocatalyst to convert CO_2. This low-cost layer material, with interesting physical, chemical and electronic properties, including high charge carrier mobility and semiconducting bandgap, is attracting more and more attention to substitute actual materials for photocatalytic applications. In particular, its tunable nano-structure that can exhibit various 3D, 2D, 1D or 0D morphologies may help us to tune its chemical and physical properties, in order to fit with the requirements for efficient photocatalysis applications.

Moreover, since this material has lamellar structure, among the ways of improving its properties, it could be particularly interesting to build heterostructure with a second semiconductor, with the aim to overcome some limitations of MoS_2 alone such as its relatively small bandgap [12]. For instance, combining it with TiO_2 as the second semiconductor, we hope to be able to take advantage of its well-known efficiency in photocatalysis while trying to avoid some of its limitations (low visible absorption, high charge recombination).

The present work proposes the use of periodic density functional theory (DFT) calculations to provide a more rational knowledge regarding the applicability of MoS_2 based materials for CO_2 photoreduction. For that purpose, two main axes of research have been identified for the present theoretical study: the investigation of the electronic properties of MoS_2/TiO_2 heterostructures and the investigation of the CO_2 reduction mechanisms occurring on active sites located at the edges of MoS_2 nano-structures.

This manuscript is organized into six chapters (including this general introduction). The second chapter will provide a literature review on the general context of the thesis. It pinpoints the current knowledge and underlines the still open questions on the MoS_2/TiO_2 heterostructures and the CO_2 reduction mechanisms. The third chapter will present the Kohn-Sham DFT formalism used for our theoretical investigations and the relevant chosen computational parameters. The fourth chapter will focus on the MoS_2/TiO_2 heterostructures. The electronic structures obtained and the possible applications within the heterojunction formalism (type I, type II, Z-scheme) will be underlined. This chapter has been the subject of a recent publication in Phys. Chem. Chem. Phys. In chapter five, we will present investigations on the CO_2 reduction mechanisms occurring on various MoS_2 edges. We will give a particular

attention to the effect of the edge composition on the intermediates and products obtained. In the sixth chapter, we will propose some conclusions and perspectives to this work.

References

[1] M. Fontecave, *Angewandte Chemie International Editions,* vol. 50, pp. 6704-6705, 2011.

[2] C. Pasten and J. C. Santamarina, *Energy Policy,* vol. 49, pp. 468-476, 2012.

[3] N. S. Lewis and D. G. Nocera, *Proceedings of the National Academy of Sciences of the United States of America,* vol. 103, pp. 15729-15735, 2006.

[4] "Chiffres clés des énergies renouvelables 2021," 23 07 2021. [Online]. Available: https://www.statistiques.developpement-durable.gouv.fr/chiffres-cles-des-energies-renouvelables-edition-2021. [Accessed 05 2022].

[5] G. Centi and S. Perathoner, *ChemSusChem,* vol. 3, pp. 195-208, 2010.

[6] Y. Tachibana, L. Vayssieres and J. R. Durant, *National Photoniccs,* vol. 6, pp. 511-518, 2012.

[7] M. A. Green and S. P. Bremner, *National Materials,* vol. 16, pp. 23-34, 2017.

[8] E. J. Maginn, *The Journal of Physical Chemistry Lettters,* vol. 1, pp. 3478-3479, 2010.

[9] M. Mikkelsen, M. Jorgensen and F. C. Krebs, *Energy Environment Science,* vol. 3, pp. 43-81, 2010.

[10] S. N. Habisreutinger, L. Schmidt-Mende et J. K. Stolarczyk, *Angewandte Chemistry International Editions,* vol. 52, pp. 7372-7408, 2013.

[11] A. Fecant and H. Toulhoat, *Pour la Science,* vol. 459, pp. 56-63, 2016.

[12] P. Johari and V. B. Shenoy, *ACS Nano,* vol. 6, pp. 5449-5456, 2012.

Chapter II. Bibliography

II.1. The photocatalysis on semiconductors

With the aim to transform solar energy in chemical energy, the scientific community has developed artificial photocatalytic systems, inspired from natural photosynthesis [1, 2]. In particular, light-driven reaction can be realized on semiconductors, that manage to do both the light absorption and the catalysis of the chemical reaction.

II.1.1. General principles

In a semiconductor, the fundamental bandgap corresponds to the energy difference between the last occupied states, the valence band (VB) and the first unoccupied ones, the conduction band (CB). Contrary to the insulating materials, which have a too large bandgap to absorb the solar light, semiconductors can efficiently absorb the solar light due to their bandgap in the UV-Vis range [3]. As it will be deeply presented below, under a photon irradiation with an energy equal or higher than its gap, a semiconductor will be able to initialize the photocatalytic reactions.

II.1.1.a. The photocatalysis mechanism

The global photocatalysis mechanism is represented in Figure II-1. It is composed of 5 mains steps that occur successively during the process [4]:

- Light absorption: the semiconductor is able to absorb a photon with energy equal or higher than its gap. An electron of the VB is exciting to the CB. The empty state leaved behind is a quasiparticle named a hole and written h^+. The electron hole-pair is called the exciton;
- Exciton dissociation: separation of the electron and the hole;
- Charge diffusion: migration of the charge carriers in the material toward the surface;
- Charge transfer: transfer of the charge carriers on the surface-active sites. It corresponds to the sites where the reactants are adsorbed;

- Reactions: the charge carriers are available on the active site to react with adsorbed molecules. It may be reduction (for the electrons) or oxidation (for the holes) reaction.

In addition to its bandgap, some characteristics will define the materials and its photocatalytic activity: its dielectric constant, the charge carrier effective masses and the exciton binding energy.

The challenges and the strategies associated to this mechanism will be presented in detail in the following parts. In the first time, we will only discuss about the photon adsorption (step 1). In a second time we will treat the charge separation and transport (step 2, 3 and 4). Finally, the surface reaction (step 5) will be detailed.

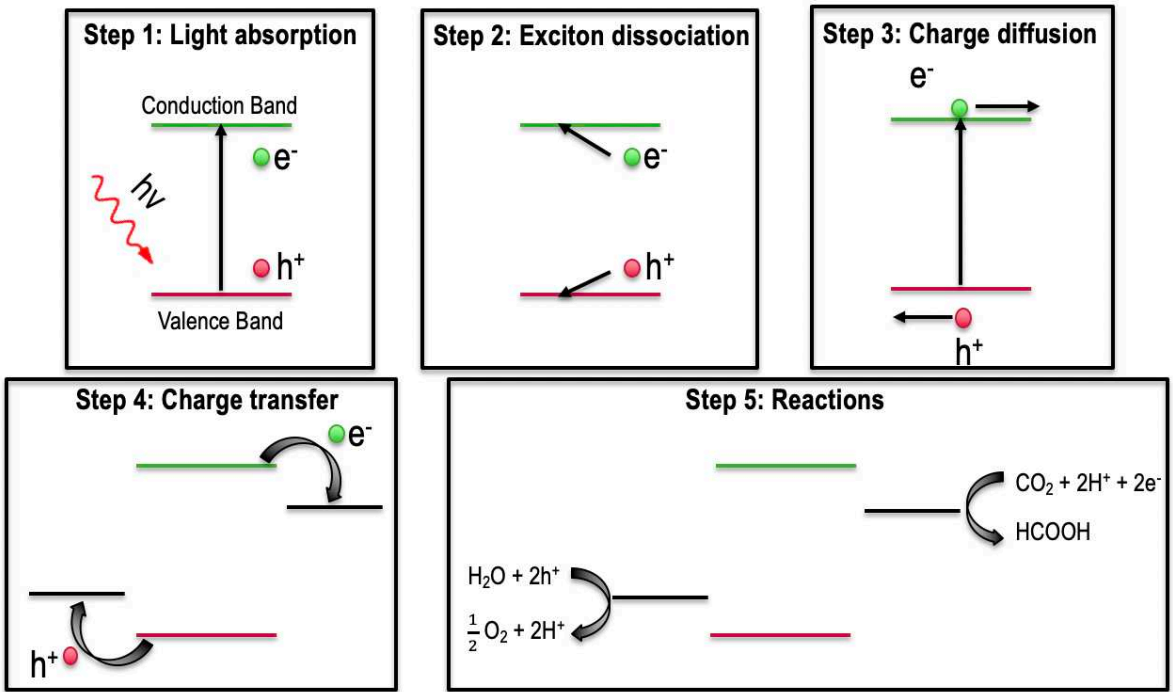

Figure II-1 : The five mains steps involved in the photocatalysis mechanism.

II.1.1.b. Efficiency measurement

In order to discuss about the viability of a process and to compare it between other processes, a value of efficiency is required. Nevertheless, there is no single way to measure the efficiency of a photocatalytic system. Depending on the background of the research team and the improvement they want to highlight, catalyst-based measurement or light-based measurement may be used.

In catalyst-based measurement, the catalytic performance is most of the time expressed in terms of rate of formation of a product. In general, it is written R and consider the amount of product obtained, the amount of catalyst and the reaction time:

$$R = \frac{[Product]}{Time[Catalyst]} \qquad (II.1)$$

Depending on the amount of product, it can be expressed in $mol.g^{-1}.h^{-1}$ or in $\mu mol.g^{-1}.h^{-1}$. The biggest limitation of this measurement comes from the non-consideration of the incident photon flux. Given that the efficiency of the process depends on the intensity and the wavelength of the incident light, a comparison between studies using different type of light is almost impossible.

In light-based measurement, the power conversion efficiency considers the energy stored in the chemical bond of the products and the energy of the incident light [5, 6]:

$$\eta = \frac{Output\ Energy\ as\ Chemical\ Bonds}{Input\ Energy\ of\ Incident\ Light} = \frac{\sum_i H_{c,i}^0 . r_i}{P} \qquad (II.2)$$

with $H_{c,i}^0$ the molar heat of combustion of the product i , r_i the rate of formation of the product i and P the power of the photon flux. The overall conversion efficiency can also be divided into three parts, that corresponds to the fundamental steps of the mechanism [7, 8]:

$$\eta_{tot} = \eta_{absorption} \times \eta_{separation} \times \eta_{reaction} \qquad (II.3)$$

with $\eta_{absorption}$ that represents the fraction of electron-hole pairs excited by the incident light (step 1 in Figure II-1), $\eta_{separation}$ that represents the fraction of photogenerated charge carriers that migrate successfully to the interface (step 2, 3 and 4 in Figure II-1), and $\eta_{reaction}$ represents the efficiency of the reactions at the interface (step 5 in Figure II-1). In actual photocatalysis studies, the target is a global conversion efficiency of 10% that is considered to be the efficiency making the process economically attractive. In the actual systems, efficiencies are most of the time lower than 1% [9, 10, 11, 12, 13] and reach the value of 2%

in the best cases [14, 15]. This is due to the complexity of the mechanism and the difficulty to optimize in the same time all the steps.

In both cases, focusing only on one aspect of the system (light intensity or amount of catalyst), it seems to be complicated to get a direct comparison of different photocatalytic systems, since the efficiency calculated is not directly related to the intrinsic properties of the material. As a consequence, a ranking of the materials has to be treated with precaution.

II.1.2. The photon absorption

As aforementioned, the first step consists in the excitation of an electron from the Valence Band of the semiconductor to its Conduction Band, if the energy of the incident light is equal or higher to the bandgap [16]. This bandgap could be direct (the electrons in the Valence Band and the Conduction Band have the same momentum, the same wave vector) or indirect (no equal momentum in the Conduction Band and the Valence Band). In that case, the electron has to interact with lattice vibration, called phonon, in order to obtain sufficient energy to increase or decrease its momentum, and do the transition to the Conduction Band [17, 18]. This indirect absorption is realized at a slower rate and a lower probability than the direct absorption.

The absorption can be quantified by the adsorption coefficient of the semiconductor [19]:

$$\alpha(h\nu) \propto \sum P_{12} g_V(E_1) g_c(E_2) \qquad (II.4)$$

with P_{12} the probability of the electronic transition from E_1 to E_2, $g_V(E_1)$ the electron density in the initial state and $g_c(E_2)$ the electron density in the final state.

If we aim a good global efficiency, this initialization step has to be realized in the best conditions in order to avoid a premature loss of energy. However, there are some challenges to overcome.

II.1.2.a. The challenges

The first challenge comes from the fact that the most intense solar radiation occurs in the visible range, that represents 43% of the light that reach the Earth. In the case of the

ultraviolet range, even with a quantum efficiency of 100% (meaning that all the photons are used to induce an electrochemical reaction without any loss), the global conversion efficiency will not reach values higher than 2% [20, 21]. On the other hand, in the case of light harvesting up to 650 nm, the targeted efficiency of 10% can be reached with a quantum efficiency of only 60%. It seems thus to be crucial to be able to harvest the visible light to obtain higher energy conversion (Figure II-2).

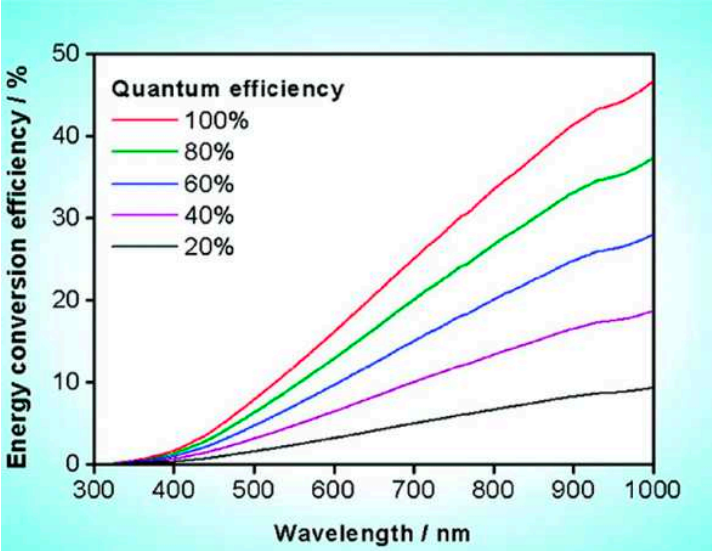

Figure II-2 : Calculated solar-to-hydrogen conversion efficiency as functions of photon wavelength for photocatalytic one-step overall water splitting using photocatalysts with various Quantum Efficiency. The associated calculations assumed AM 1.5G solar irradiation [21].

In addition, although we are focusing on the first step of the mechanism, the targeted reactions have already an impact on the construction of the system. As illustrated in Figure II-1 (step 5), the Valence Band has to be located at a lower energy than the oxidation potential and the Conduction Band has to be located at a higher energy than the reduction potential, in order to be able to transfer the electrons and the holes. Moreover, if we want to have a good driving force, an energy difference around 0.4 eV is required between the Valence band and the oxidation potential (same requirement on the reduction side).

Unfortunately, these two constraints require opposite band tuning. If we want to widely absorb visible light, we will focus on semiconductors with not too large bandgap. On the other hand, in order to be able to realize the reactions with good efficiency, a wide bandgap will be required. Consequently, many strategies have been considered to improve the quantum efficiency of the systems.

II.1.2.b. Strategies to improve the step

In order to improve the efficiency associated to the light absorption step, many techniques could be considered:

1) Introduction of a doping element in the semiconductor in order to modify its photophysical properties. Among the wide variety of modification that could be applied to improve the efficiency (charge mobility [22], particle size [23, 24, 25], surface structure [24]), our interest here is to favor the shift of the absorption toward the visible spectrum, the bathochromic shift. The introduction of doping element in the system leads to the creation of intrabandgap levels, creating acceptor level or donor level (as a function of the doping element) that shift the absorption toward the visible light (Figure II-3 a). The doping element could be a metal cation (Ni^{2+} [26], Cr^{3+} [27], Rh^{3+} [28](260)…) or a non-metal element (N, C, S or X^- [29, 30, 31, 32]). On the other hand, since dopants can also serve as recombination center, that decrease the photocatalytic activity [28], the doping has to be precisely controlled.

2) The use of solid solutions of isostructural semiconductors (Figure II-3 b). In these systems, the bandgaps and energy levels can be tuned by the variation of quantity of the wide bandgap semiconductor and the narrow bandgap semiconductor. Examples using oxides (GaN:ZnO [33, 34], $BiVO_4$ [35, 36]…) or sulfides ($(CuIn)_xZn_{2(1-x)}S_2$ [37], $(Cu_xAg_{1-x})_2ZnSnS_4$ [38]…) has been developed with success.

3) The development of dye-sensitized photocatalytic systems (Figure II-3 c). The global idea consists in the expansion of the usable wavelength through the excitation of a sensitizer [39, 40]. The dye molecule can absorb visible light, creating an electron-hole pair, and transfer the photogenerated electron into the Conduction Band of the semiconductor, that can then transfer it to the reactional site. The photogenerated hole is eliminated through the acceptance of an electron from and electron donor [39, 41]. The dye-sensitizer could be metal-complex ($Ru(bpy)_3^{2+}$ [42, 43, 44], $[Ru\text{-}(dcbpy)_2(dpq)]^{2+}$ [45]…) or organic compound (tetraphenylporphirine tetrasulfonic acid (TPPS), cyanocobalamin [46, 47]). To

be efficient, it is crucial to have a good stabilization of the dye-sensitizer on the surface of the semiconductor, in order to favor the transfer of the electron from the dye-sensitizer excited state, exhibiting a short life time [48].

4) Taking advantage of the localized surface plasmon resonance (LSPR) effect. This optical phenomenon can be described as the oscillation of the electron cloud of a metal nanoparticle in resonance with the electric field of the light. The visible light is harvested by the metal nanoparticles, with a frequency resonance that can be tuned by modification of the size and shape of the particle [49, 50]. The rest of the mechanism is similar to the one presented before (Figure II-3 d), only the light harvester is different. Concerning the metal used, it is most of the time Au or Ag.

5) The use of quantum dots, that are droplets or nanocrystals of a material [51]. They are very small compared to the wavelength of the visible light and can thus exhibit quantum confinement effects such as large absorption coefficients [52]. Once again, the global mechanism is similar than in the two previous cases (Figure II-3 e), with visible light absorption realized by Quantum Dots this time.

6) Building a Z-scheme system, composed of two semiconductors with narrow bandgaps, that may absorb visible light (Figure II-3 f). Given that our interest on semiconductors with narrow bandgap, this mechanism with two photons adsorbed will be more described in the next part.

As we can see, there are many possibilities to tune the light absorption in the targeted direction in order to obtain visible absorption while maintaining the good reduction and oxidation potential. This illustrate the possibility to use a wide variety of semiconductors for this step of photon absorption.

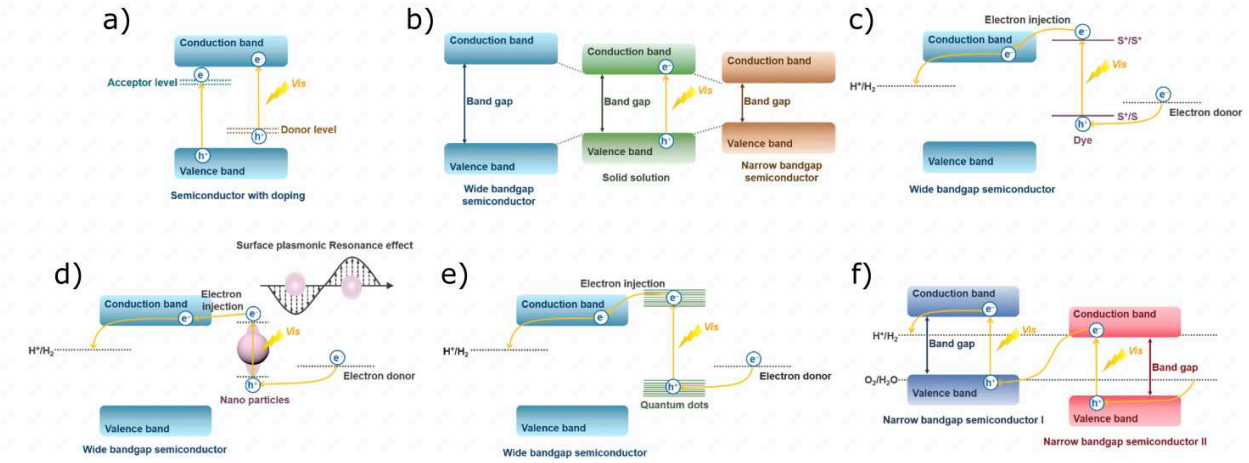

Figure II-3 : Strategies for obtain a visible light response: (a) use of doping element, (b) solid solution formation, (c) dye-sensitization (d) localized surface plasmon resonance, (e) quantum confinement and (f) Z-scheme configuration [53].

II.1.2.c. Z-scheme principles

Building artificial Z-scheme heterostructures has been inspired forty years ago by the natural photosynthesis process in order to obtain high photocatalytic performances [54]. As illustrated on Figure II-3 f, semiconductors able to form a type II heterojunction are required. In other words, we need semiconductors with bandgap overlapped. The global mechanism consists in the absorption of visible light by two semiconductors, followed by the recombination of the electrons photogenerated in the semiconductor II with the holes photogenerated in the semiconductor I. That results in the accumulation of photogenerated holes in the valence band of the semiconductor II, that exhibits a strong oxidation ability, and accumulation of the electrons in the conduction band of the semiconductor I, that exhibits a strong reduction ability. In other words, the Z-scheme mechanism manage to do spatial separation of the charge carriers, through visible absorption, while maintaining strong redox abilities.

However, in order to discuss the feasibility of a Z-scheme, it is important to have a look on the charge carrier dynamics that could happen after interaction and light absorption. To do that, the main parameter to consider is the position of the fermi levels of the two semiconductors, that may lead to the Z-scheme mechanism or the classical type II mechanism (Figure II-4). In the first case (Figure II-4 a), before interaction, the fermi level of the semiconductor 1 (SC_1) is lower than the fermi level of the semiconductor 2 (SC_2). When they are in contact, the interaction leads to the alignment of the fermi levels of the two semiconductors. The rise of

the fermi level of SC_1 creates a negative charge on its side at the interface while the fall of the fermi level of SC_2 creates a positive charge on its side at the interface. These charges create an induced electric field at the interface and a band edge bending occurs. As a consequence, the charge carrier migration favored after light absorption is the electron transfer from SC_1 to SC_2 and the hole transfer from SC_2 to SC_1: it is the classical type II mechanism.

On the other hand (Figure II-4 b), if before interaction the fermi level of the semiconductor 1 (SC_1) is higher than the fermi level of the semiconductor 2 (SC_2), it leads after interaction to the creation of the opposite charges at the interface and the creation of an induced electric field in the opposite direction. As a consequence, after light absorption, the recombination of the holes photogenerated in SC_1 with the electrons photogenerated in SC_2 is favored: it is the Z-scheme mechanism.

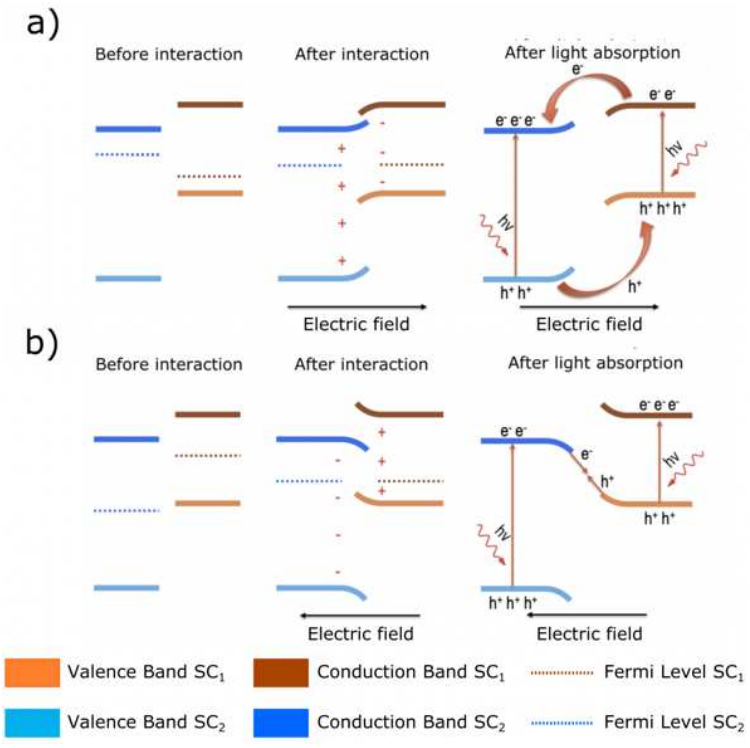

Figure II-4 : The two charge carrier dynamics that can happen in type II with (a) the classical type II mechanism and (b) the Z-scheme mechanism.

Although the classical type II mechanism offers also spatial charge separation, the electrons are not localized on the more reductive semiconductor (same thing for the holes on the oxidation side). As a consequence, the control of the fermi level is an important parameter in the build of direct Z-scheme photocatalyst. In addition to the relative position of the two fermi levels, it will be interesting to have high energy difference between the two fermi levels in order to increase the induced electric field and the charge transfer rate [55, 56].

Indeed, a high rate of charge exchange is required at the interface between the two semiconductors. To do so, a first strategy was to physically separate the two semiconductors and use a charge carrier mediator for the charge transfer between the two materials. In the case of the Z-scheme of 1st generation [57], also called traditional Z-scheme, they worked with liquid phase Z-schemes, with an electron mediator composed of a redox ion pair (Fe^{3+}/Fe^{2+} [58], IO^{3-}/I^{-} [59]…). After that, the Z-scheme of 2nd generation were all-solid-state Z-scheme [60], with a conductor at the interface that play the role of electron mediator and assure that charge carrier transfer between the two semiconductors. It is most of the time Au, Ag or Cu nanoparticles [61, 62]. With this new method, in addition to be exploited in liquid and gas phase, the charge transfer rate is higher and problems of pH sensitivity are avoided [63] Recently, the third Z-scheme generation is emerging, that is called direct Z-scheme photocatalyst [64]. In that case, the two semiconductors are in direct contact without external electron mediator added. Contrary to the previous systems, direct Z-scheme exhibit high charge transfer rate, shielding effect limited and good resistance to corrosion [63].

II.1.3. Charge separation and transport

In order to do the photocatalytic reactions, the photoexcited charge carriers have to reach the redox active sites. To do that with good efficiency, there are some challenges involved in these steps, with the aim to avoid side mechanisms.

II.1.3.a. Challenges

The first challenge to overcome comes from the natural recombination of the photogenerated electrons and holes. It could be a radiative recombination (a band-to-band recombination) or a non-radiative recombination through traps (impurity or defects) [53].

There is also the possibility to have electrons trapped in energy levels in the forbidden gap, that could have positive or negative impact on the system. In some cases, it could favor a spatial electron-hole separation, avoid the electron-hole recombination and increase the charge carrier lifetime [3, 65]. On the other hand, it also decreases the charge carrier's energy

and mobility, making them unable to reach the active sites. Among the tune of the characteristics of the semiconductor (dielectric constant, charge carrier effective masses, exciton binding energy) that influence this part of the mechanism, there are some strategies able to help the system to reach higher efficiency.

II.1.3.b. Strategies

The classical way to favor the migration of charge carriers to the active sites consists in the reduction of the migration distance. The simplest way to do that consists in the reduction of the particle size. It can be done by generating the charge carriers close to the surface, in a core-shell structure mainly [66]. The use of 1D or 2D materials seems to be really interesting from this point of view since they provide a large surface area with many reactive sites associated to a short charge carrier diffusion length [67, 68].

While they can have a positive impact on the system [69, 70, 71, 72], the defects act most of the time as recombination center and are reducing the photocatalytic performances [73, 74, 70, 75, 76, 77]. The reduction of the defect concentration is thus a main goal [78, 79] that can be obtained by controlling the defect concentration and type during the synthesis [80, 81, 82, 83, 84, 85, 86, 87]. The use of molten salt is the major technique used to obtain a homogeneous material [86, 88].

In order to avoid charge carrier recombination and increase the charge carrier lifetime, the spatial separation of the charge carriers can be realized through junctions between the light harvester semiconductor and another material such as the co-catalyst. [89, 90, 91, 92]. In other systems, a junction between two semiconductors with different bandgaps can be realized in order to separate the electrons and the holes. As we have seen in Figure II-4, depending on the fermi levels of the two materials, the charge carrier dynamics and the photocatalysis performances associated will change. This fermi level can be tuned by the use of doping elements in the semiconductor structure, that could be electron donor or electron acceptor. In case of increase of electron density, through the use of electron donor, the fermi level will rise close to the conduction band: it becomes a N-type semiconductor. On the other

hand, in case of doping though an electron acceptor, the hole density will increase and the fermi level will fall close to the valence band: it becomes a P-type semiconductor.

The photocatalytic performances can also be tuned by the surface orientations of the semiconductor, where the reaction will take place. By exposing different facets, some semiconductors are able to separate the charge carriers, with facets that favor reduction reaction and other facets that favor oxidation reaction [93, 94, 95]. As an example, it has been showed that the (101) and (001) TiO_2 anatase surface orientations exhibit different band structure and band edge positions [96]. As a consequence, the two facets are able to form a surface heterojunction on a single TiO_2 particle (Figure II-5). It will result in the transfer of the electrons and holes to the (101) and (001) facets respectively in order to separate the charge carriers and the half reactions.

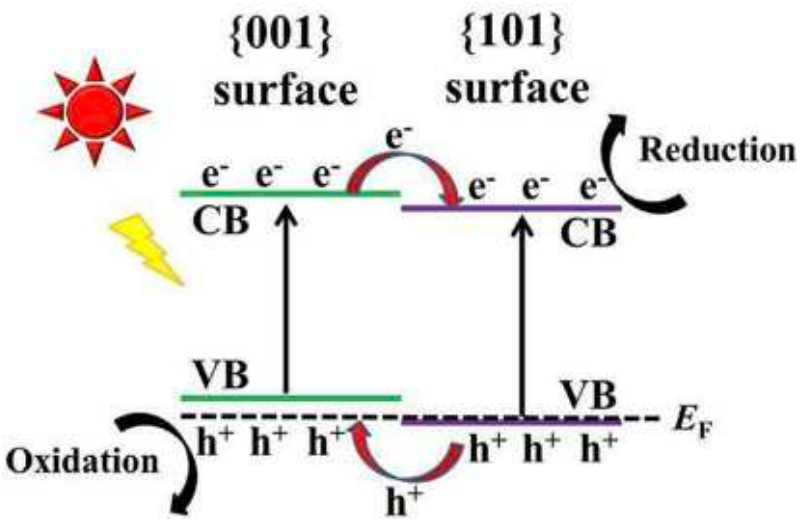

Figure II-5: Surface heterojunction on a single TiO_2 particle due to the variation of electronic structure between the (101) and (001) surface orientations.

In any case, the surface orientation will be crucial parameter in the photocatalytic performance since a good adsorption of the reactants will be required.

II.1.4. Surface chemical reactions

The photochemical mechanism ends with the oxidation and reduction reactions on the surface. In order to obtain a good efficiency, both kinetics and thermodynamics of the reaction involved will be important parameters. Globally, a good understanding in the mechanism will be required.

II.1.4.a. Challenges

In the chemical reactions involved, the biggest challenge consists in the control of the side reactions particularly for the CO_2 reduction process, targeted in the present work. In fact, if the previous steps have been done with good efficiency, a high quantity of electrons and holes are available with efficient reduction and oxidation potentials. Depending on the reactant available, several redox reactions can be realized. In particular, the risk of back reaction is most of the time present, that will lead to the oxidation of the reduction products and to the reduction of the oxidation products. In addition, side reactions could also be involved. These aspects have to be avoided.

II.1.4.b. The strategies

As discussed in II.1.3.b, the use of metal co-catalyst is a good way to reduce recombination and provide charge separation. Moreover, it can also provide active sites, catalyze the targeted reactions and decrease the activation energy required [97, 98, 99, 100]. The choice of the co-catalyst could be a crucial parameter to improve both the selectivity and the efficiency, with the aim to favor the targeted reaction while avoiding the side reactions. In addition, in order to avoid problems of back reaction, the use of hole scavengers or electron scavengers is recommended. For CO_2 reduction, we will describe this aspect in more details in the next chapter.

II.1.5. Conclusions

Composed of 5 successive steps, from the light absorption to the chemical reaction, the realization of a photocatalytic process is facing challenges at each step. Although these challenges can be overcome thanks to the strategies presented before, it may be difficult to optimize in the same time the 5 steps, that do not require the same properties. Indeed, the choice of the semiconductor is a crucial parameter since its characteristics play an important role in the mechanisms (bandgap, electronic structure, dielectric constant, exciton binding energy, charge carrier effective masses…). Given the progress realized for the water splitting

reaction ($H_2O \rightarrow H_2 + \frac{1}{2}O_2$), the scientific community is more and more attracted in extending these strategies to another reaction: the photocatalytic reduction of CO_2.

II.2. The photocatalytic reduction of CO_2

As exposed in the Introduction, the major part of our energy is produced by fossil fuels. In these processes, we are facing an important question related to the release of CO_2 greenhouse gas (37 Gt [101]) a number that is expected to double since 2035. In the nature, the cycle of emission and uptake of the CO_2 is involving 90 Gt [102] through the fixation by the plants and microorganisms, that are disturbed by the human emissions. As a consequence, the concentration of CO_2 in the atmosphere goes from 270 ppm in the preindustrial era [102] to 420 ppm in 2022 [103], far high in comparison to the natural variation (between 180 and 300 ppm [104]). As a consequence, the high rise in the CO_2 concentration is one of the key factors in the climate change [101, 105]. If we want to maintain a viable world, we have to invert this trend of the emissions of greenhouse gas. In that situation, reducing the emissions of CO_2, by capturing it and retransforming it, is studying intensively. Since a high input of energy could be required to realize these processes, the use of the solar energy as the driving force of the reaction could be the perfect choice.

II.2.1. General principles

Under solar radiation, the CO_2 can be reduced in many products (methanol, methane, carbon monoxide, formic acid…) that could lead to further products and many chemical applications. Due to the obvious interests in this field of search, many approaches have been proposed to realize these transformations. However, they are facing many challenges, most of which are not yet solved. These three aspects regarding interests, methods and challenges will be developed in the following parts.

II.2.1.a. Interests

In the actual context of climate crisis and energy transition, it seems to be crucial to use the abundant solar energy to chemically transform CO_2 into high energy compounds (methanol and methane mainly). These compounds, also named solar fuels [5, 106], can be then combusted or used in fuel cells. With these processes, other CO_2 molecules will be released and could be retransformed in solar fuels. In other words, the carbon cycles will be closed by the CO_2 reduction process, and the addition of CO_2 from fossil fuels will not be required anymore.

One of the other high interest in the conversion of the CO_2 comes from the storage of the solar energy in the chemical bonds (C-H bonds mainly) of the liquid or gaseous fuels produced. In other renewables sources, the energy supply is most of the time considered as undependable and irregular. On the other hand, solar fuels provide an attractive solution with a high-density storage through stable chemical bonds.

The use of CO_2 reduction products as fuels is not the only applications possible: most of them can be used as products in chemical synthesis. In that cases, CO_2 is no longer a waste that damage the environment but a precious resource for chemical applications. It could be characterized as a valuable, abundant and not expensive carbon feedstock that can replace fossil fuels [102, 107, 108].

II.2.1.b. Approaches

Many methods have been considered to successively harvest the solar energy and then use it to chemically transform the carbon dioxide:

- Photovoltaic cells can be used to harvest the light and convert it into electricity. This electricity is then used to do the electrochemical reduction of CO_2 on metal electrodes [109, 110]. The light harvesting and the reactions are separated.
- Solar energy can be also used in the water splitting reaction that produces H_2 in a photocatalytic process on semiconductors, as described in (II.1). This H_2 is then used to hydrogenate CO_2 in order to release our targeted chemical products [111]. If the two steps are done successfully, it avoids the problem of hydrogen storage [21].

- The CO_2 photoreduction can be directly realized on organometallic catalysis [110, 112, 113, 114] in a homogeneous process. The catalyst is most of the time a metal complex able to play the role of light antennas and catalyst. It is not so exploited because of the use of rare and expensive metal in the complex such as Ruthenium and Rhenium [115, 116].
- The use of photoelectrochemical cell has also been studied, in which the two functions (light harvesting and electroreduction) are combined into one device that required an external bias to proceed successfully [117, 118, 119].

Despite many investigations, the methods presented above did not offer complete satisfaction. However, an alternative process is possible: the direct photocatalytic reduction on semiconductors (described in I.1). With this process, that represents our field of interest, the idea is to take advantage on the progress done during the past decades on the water splitting reaction [21, 120] (in terms of mechanistic study, light harvesting, interface building…) and to extend it to the CO_2 photoreduction. However, contrary to the simple water splitting reaction ($2H_2O \rightarrow 2H_2 + O_2$), the CO_2 reduction is more challenging.

II.2.1.c. Challenges

The first challenge comes from the high oxidation state of the carbon atom in the CO_2 molecule (+IV) that can be reduced in many products with different oxidation states through the half reaction and the standard potential associated (at pH = 0) with few examples presented in equations $(II.5)$ - $(II.9)$:

$$CO_2 + 2H^+ + 2e^- \rightarrow HCOOH \qquad E^0 = -0.20\ V\ vs\ SHE \qquad (II.5)$$

$$CO_2 + 2H^+ + 2e^- \rightarrow CO + H_2O \qquad E^0 = -0.12\ V\ vs\ SHE \qquad (II.6)$$

$$CO_2 + 4H^+ + 4e^- \rightarrow HCHO + H_2O \qquad E^0 = -0.07\ V\ vs\ SHE \qquad (II.7)$$

$$CO_2 + 6H^+ + 6e^- \rightarrow CH_3OH + H_2O \qquad E^0 = +0.03\ V\ vs\ SHE \qquad (II.8)$$

$$CO_2 + 8H^+ + 8e^- \rightarrow CH_4 + 2H_2O \qquad E^0 = +0.17\ V\ vs\ SHE \qquad (II.9)$$

$$2H^+ + 2e^- \rightarrow H_2 \qquad E^0 = 0\ V\ vs\ SHE \qquad (II.10)$$

Depending on the reaction pathway taken and the electrochemical potential available, the final oxidation state of the carbon atom will be different and leads to the observation of many products in the experiments. The direct products presented above have thus been observed but also many derivate that come from subsequent chemical transformations (dimerization, reoxidation…). The lack of selectivity of the CO_2 reduction highlights its complex underlying mechanism. Moreover, these CO_2 reduction reactions are also in competition with the hydrogen evolution reaction (HER) represented in equation $(II.10)$. In order to improve both the photocatalytic performance and the selectivity, a good understanding is required. A review of the actual mechanisms proposed is presented in the following part.

Concerning the oxidation reaction, the ideal one would be the oxidation of water, that could be the solvent of the reaction, into oxygen or hydrogen peroxide. However, this aspect would create supplementary challenges due to the low solubility of CO_2 in water. An interesting solution could be the modification of the pH in order to transform CO_2 into bicarbonate HCO_3^- and carbonate CO_3^{2-} [130], soluble in water:

$$CO_2 + H_2O \rightleftarrows H^+ + HCO_3^- \qquad pK_a = 6.4 \qquad (II.11)$$

$$HCO_3^- \rightleftarrows H^+ + CO_3^{2-} \qquad pK_a = 10.3 \qquad (II.12)$$

In order to focus on one problem in the same time, the research investigates mainly the reduction side, that is more crucial to optimize. The counter oxidation is for now most of the time realized by a substitute reaction with sacrificial electron donors.

II.2.2. The mechanisms involved

After the transfer of an electron to the reactant, which initialize the mechanism, numerous chemical reactions can occur. Depending on the targeted product, the multistep reaction will involve the cleavage of C - O bonds and the formation of C - H bonds, associated to the transfer of up to eight protons and electrons (Equations $(II.5) - (II.9)$).

In this context, it is crucial to use all the available tools to bring precision to the complex CO_2 reduction mechanism as well as thermodynamic and kinetic barriers associated. By knowing that, optimization of both conversion rate and selectivity could be reached.

II.2.2.a. Methods used in reactivity studies

During the recent years, the CO_2 reduction mechanism has been intensively studied, involving a large variety of analytical technics. In addition to pure photocatalysis approaches, it appears to be interesting to extend the study to electrochemical and photoelectrochemical approaches. Although the way of creating the charge carriers is different depending on the type of system, the way of using these charges in the chemical mechanism is expected to be the same in all the systems. The next paragraphs will briefly describe these possible approaches.

In order to identify and quantify the reactional intermediates and the final products obtained, gas [122, 123] and ion-exchange [124] chromatography have been intensively used, in some cases, combined with mass spectrometry. The first one is useful to analyze volatile molecules whereas the second one is useful to identify ionic species (formate, oxalate…). In addition to the chromatographic methods, complementary insight are provided by spectroscopy methods such as EPR [125, 126, 127, 128], IR [129, 130, 131, 132], X-ray or Auger [133]. Considering that the identification and quantification of the intermediates is non-sufficient to the complete understanding of the mechanism, other characteristics can be brought by transient absorption measurements [127], surface-oriented studies [134, 135], kinetic analysis [136, 137] and tunneling microscopy [138]. Moreover, the behavior of the semiconductor used (excitation, charge-carrier mobility, lifetime, separation…) can be studied with photovoltaic methods [139, 140, 141]. Finally, studying the electrochemical reduction of CO_2 [110, 142, 143], can also help to provide important information on what happen after the charge separation induced by light absorption.

In addition to all these experimental methods, the use of computational chemistry could give further information. The main method consists in calculating the energies of the reactional intermediates with the computational hydrogen electrode (CHE) model [144], that consider the influence of the potential on the free energy of the different intermediates (Figure II-6). In particular, this approach is able to describe the potential required to obtain only exergonic steps.

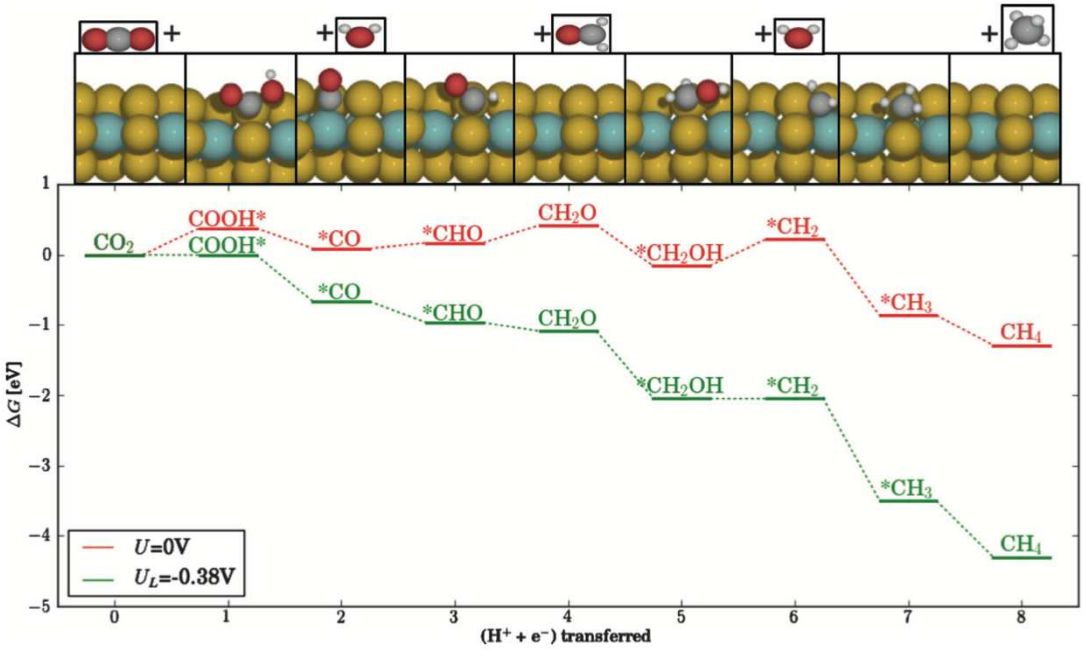

Figure II-6 : Free-energy diagram for the reduction of CO_2 to CH_4 on the Mo edge of $MoSe_2$, $\theta S = 0.5$, at U 0 V and U_L = -0.38 V, the limited potential where all the reaction steps becomes exergonic.

Although this method provides good results for other reactions [145, 146, 147, 148], it does not contain explicit consideration of the solvated protons or the solvent itself, that is challenging. Moreover, protons and electrons transfers are strictly coupled and the computed barriers of elementary reactions are not affected by the electrochemical potential. For the description of the complex CO_2 reduction mechanism, the use of advanced models may be required in order to avoid these drawbacks [149, 150, 151, 152, 153, 154, 155, 156, 157]. Among these strategies, this thesis will bring a particular attention on the surface charging approach [152], described in III.2.3.

By providing information on the energies of the adsorbates, reaction intermediates and transition states [109, 128, 138, 158, 159], computational chemistry seems to be crucial in the good understanding of the CO_2 reduction mechanism. Moreover, the calculated energies are helping to build the energetic profile of the reaction. In addition to the study of the chemical mechanism, the description of the complete photochemical mechanism (from the light absorption to the chemical reaction) can be realized computationally with TD-DFT approaches [160, 161, 162].

II.2.2.b. Initialization steps

Before talking about the successive reduction elementary steps that can occur in the mechanism, it seems to be important to focus on the activations step. Due to the combination of its closed-shell electronic configuration and its $D_{\infty h}$ symmetry [163, 164], the carbon dioxide is a stable and chemically inert compound. As a consequence, the addition of a single electrons causes a bending of the molecule, due to the electron repulsion between the new electron, localized on the carbon atom (electrophilic), and the free electron pairs of the oxygen atoms. As a consequence, the LUMO of CO_2 is high in energy with a weak electron affinity. The corresponding electrochemical potential is therefore very negative:

$$CO_2 + e^- \rightarrow CO_2^{\cdot -} \qquad E^0 = -1.49\ V\ vs\ SHE \qquad (II.13)$$

If we compare this very negative potential with the band positions of various semiconductors (Figure II-7), no semiconductors seem to have a sufficient potential to transfer a single electron to this free CO_2 molecule.

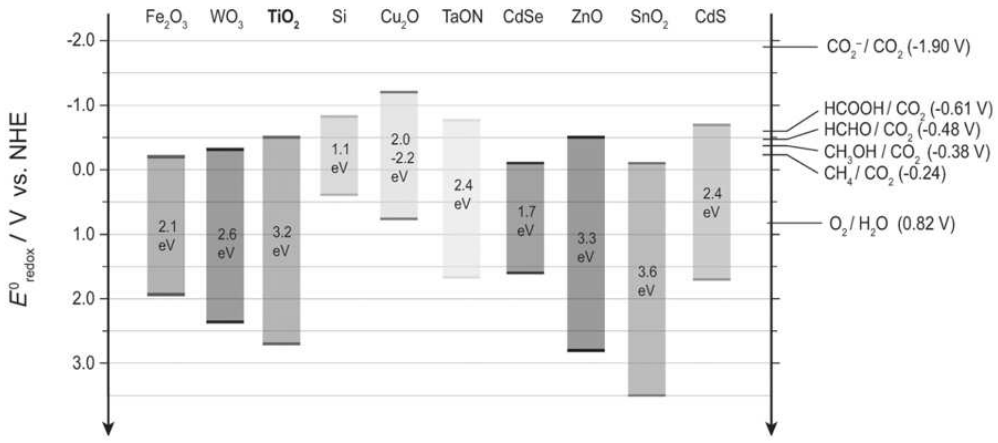

Figure II-7 : Conduction band, valence band potentials and bandgap energies of various semi-conductors photocatalysts relative to the redox potentials at pH 7 of compounds involved in CO_2 reduction [165].

On the other hand, if we have a look on the potential associated to the other reactions, it is less negative than the conduction band of some semiconductors and the reactions seems to be feasible. However, the reaction is expected to be realized with a series of one-electron steps and will face the problem of this very unfavorable first electron transfer. Given that this first electron transfer seems to be a strongly limiting step [138, 130], an activation through proton-assisted transfer could be an alternative.

To overcome this limitation, the adsorption of CO_2 on a semiconductor surface seems to be the clever way to prompt the activation of the inert molecule. This is related to the interaction with the surface atoms that leads to the formation of a $CO_2^{\delta-}$ that is partially charged [164]. This adsorbate, due to its nonlinear structure, has a lower barrier for the acceptance of an electrons, due to the LUMO that decreases with the bend of the molecule [163]. However, on some semiconductors, the adsorption interaction is not strong enough to reduce the barrier and the creation of defect is required to enable the electron transfer [159]. It is for example the case of TiO_2, that can activate CO_2 on oxygen vacancies with two adsorption modes (Figure II-8): a monodentate mode, with a CO_2 oxygen that fills the vacancy by bridging two Ti atoms, and a bidentate mode, with the two CO_2 oxygens in interaction with two Ti atoms. We will see in the following part that the adsorption mode is expected to influence the mechanism.

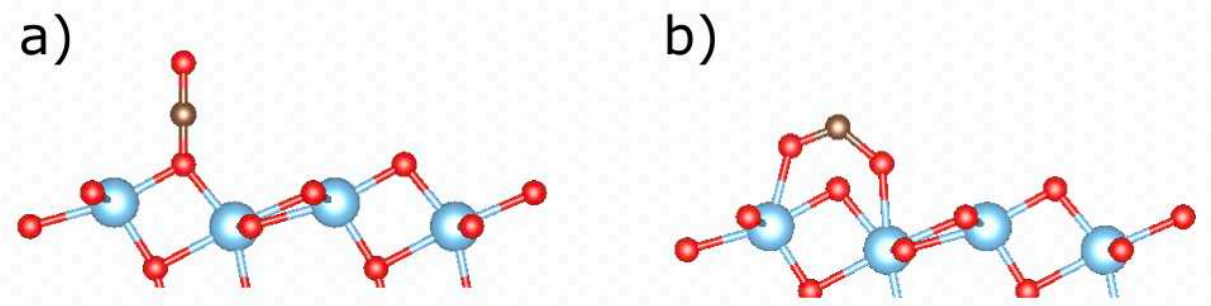

Figure II-8 : Structures associated to the 2 adsorption modes on TiO_2 anatase (101) with one oxygen vacancy: a) monodentate and b) bidentate.

In order to favor the activation of CO_2, the use of semiconductors decorated with co-catalysts seems to be interesting. In addition to favor the adsorption of bent CO_2, it favorizes the separation of the photo-induced charges at the metal-semiconductor, essential for the photochemical mechanism. Example of formation of bent anion radical $CO_2^{\cdot-}$ (compounds that appears after the first electron transfer) have been observed on Rh/TiO_2 particles and attributed to electron transfer from the d orbital of the Rh to the (C-O) π^* orbital [129]. Similar observations have been reported on Pt/TiO_2 [133, 166]. These systems seem to be able to provide active sites for the CO_2 reduction.

In addition, there is also the possibility to lower the activation barrier in aqueous solution thanks to the stabilization of the anion radical $CO_2^{\cdot-}$. This comes from the fact than bent $CO_2^{\cdot-}$, contrary to linear CO_2, has a dipole moment and is thus able to be stabilized by dipolar interaction with the water molecules [126]. However, the pH will be a crucial parameter in the behavior of the system [167, 168] since it is expected to modify the band positions of the

material, the electrochemical potentials, the solubility and the chemical form of CO_2 (Equations $(II.11)$-$(II.12)$)

II.2.2.c. Reduction pathways on semiconductor surface

Given that it has been identified as the more performant photocatalyst for the water splitting, TiO_2 has been strongly studied firstly for the CO_2 photoreduction. For this reason, the most detailed mechanistic studies have been done on TiO_2 systems but the results should be extended to other semiconductors. In many studies, in order to simplify the process, the investigations have been performed on the simplest system composed of TiO_2 nanoparticles dispersed in water solvent and illuminated with light (UV light due to the large bandgap of TiO_2). The main drawback in these studies came from the fact that both reduction an oxidation reaction are expected to be realized on the same sites or on neighboring sites [127]. That is expected to increase the risk of charge recombination and back reactions. Nevertheless, the use of a simple system, with the lowest number of species in the initial system (TiO_2, H_2O and CO_2), is an ideal subject for mechanistic studies.

After the activation step presented before, a series of elementary steps is expected to occur during the reduction process. It will be composed of transfer of particles (electrons, protons, hydrogen radical), the C-O bonds breaking and the creation of C-H bonds. Due to the nine oxidation number possibly observed for the C atom (from + IV in CO_2 to – IV in CH_4), eight reduction steps are expected to be observed during the complete mechanism. If we assume the existence of at least two intermediates by oxidation number, different pathways leading to different products are expected to be observed. Although all the mechanistic details are not yet fully elucidated, three details pathways have been proposed by Habisreutinger et al. [169](Figure II-9) to convert CO_2 into CH_4 on TiO_2. The intermediates described have been based on various experimental and theoretical approaches, described in II.2.2.a:

- The formaldehyde pathway (Figure II-9 A)
- The carbene pathway (Figure II-9 B)
- The glyoxal pathway (Figure II-9 C)

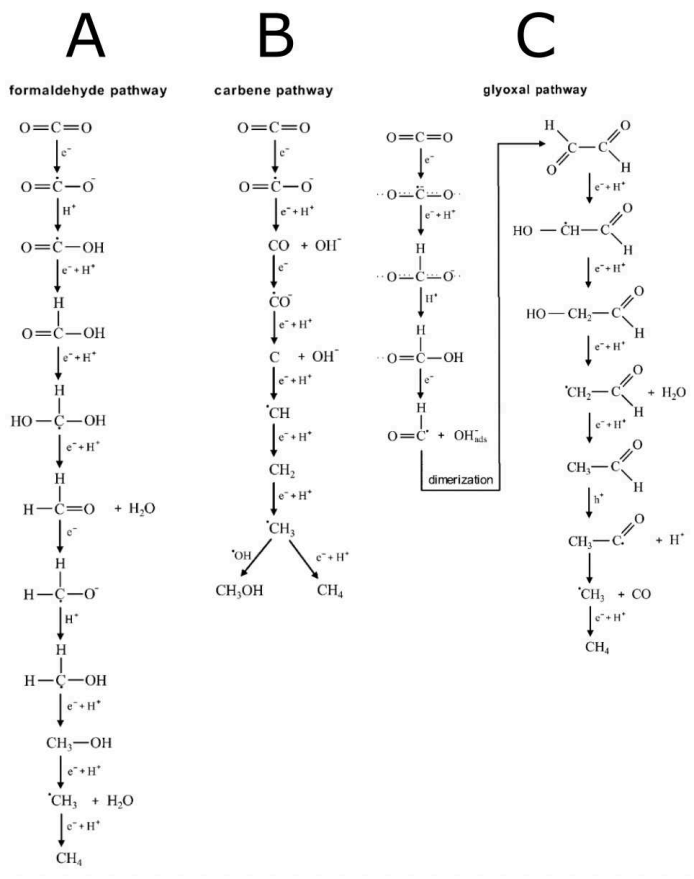

Figure II-9 : Three proposed mechanism for the reduction of CO_2 to methane: A. The formaldehyde pathway B. The carbene pathway and C. The glyoxal pathway [169].

The difference between the three mechanism originates from the activation step and the adsorption mode of the CO_2 molecule. Monodentate binding, through oxygen or carbon atoms, generally favors the formation of the carboxyl radical $\cdot COOH$ [130], intermediate in the formaldehyde pathway (Figure II-9 A). Instead of forming the carboxyl, there is also the possibility to cleave the C-O bond in order to form carbon monoxide CO, intermediate in the carbene pathway (Figure II-9 B). On the other hand, the bidentate binding of CO_2 molecule through its two oxygen on two metal sites will favor the formate anion $OCHO^-$, after attachment of a hydrogen on the free carbon atom [158]. It is the initialization step of the glyoxal pathway (Figure II-9 C).

The Formaldehyde pathway (Figure II-9 A)

After CO_2 adsorption and formation of the carboxyl radical $\cdot COOH$, it is expected to recombine with a hydrogen radical to form formic acid $HCOOH$ [170, 171]. After acceptance of another hydrogen radical, the dihydroxymethyl radical appears $\cdot CH(OH)_2$ which

immediately accepts another hydrogen radical to form formaldehyde CH_2O and liberates a water molecule. Finally, two more reduction steps lead to methanol CH_3OH and two others lead to methane CH_4.

In this pathway, it is interesting to note that the step where one C-O bond is cleaved appears very late, after four reduction steps. Nonetheless, this mechanism has not be observed experimentally despite the identification of methanol and formaldehyde species in some cases. The fact that the associated radicals have not been detected seems to indicate the non-feasibility of this mechanism. Moreover, by comparing the kinetic model associated to this pathway with experimental data [137], it is clear that the concentration profiles do not fit with the proposed mechanism.

Carbene Pathway (Figure II-9 B)

Contrary to the previous mechanism, the carbene pathway proposes an immediate cleavage of the C-O bond after attachment of a hydrogen radical leading to the formation of negatively charged hydroxyl species [125, 136, 137]. It seems to be favored when the radical $CO_2^{\cdot -}$ is adsorbed through the carbon atom. Afterthat, the adsorbed carbon monoxide CO can accept two additional electrons in order to leave a carbon atom on the surface (observed by ESR spectroscopy [136]). In the following steps, it could recombine with up to four hydrogen radicals in order to form successively a $\cdot CH$ radical, the carbene CH_2, the methyl radical $\cdot CH_3$ and finally the methane CH_4. The last step is in competition with the formation of methanol CH_3OH, in case of recombination with hydroxyl radical. The methanol is thus a side product of the mechanism, not an intermediate.

The combination of CO with methanol or methane, described in this mechanism, has been observed in many experiments [125, 172, 173]. Moreover, the competitive formation of methane and methanol has been observed, with various favored products depending on the hydrophilicity of the material and the quantity of water in the system [174, 175]. Additionally, the kinetic model associated to this pathway fits with experiment data [136, 137], making this pathway more plausible than the previous one.

Glyoxal pathway (Figure II-9 C)

In order to study the possibility of some intermediates to be oxidized instead of being reduced, some EPR studies has been performed [128, 176]. Due to the strong oxidation potential of the holes generated in TiO_2, and many other semiconductors, it is an aspect that cannot be completely ignored.

As described before, a bidentate $CO_2^{\cdot-}$ can be formed on the metallic surface. This radical anion, not observed in EPR studies, is suspected to immediately accept a hydrogen radical to form a bidentate formate $OCHO$, able to bind a proton to form formic acid $HCOOH$ chemically adsorbed in a monodentate mode [158].

It is the critical point of mechanism, due to the fact that formic acid has been identified to reform $CO_2^{\cdot-}$ in a monodentate mode very easily. The only way to go further imply a transfer of an electron from the CB to the acid coupled with the transfer of an oxygen to the metal. The energy gain associated to the bond O-Metal is expected to counterbalance the cost of the electron transfer [128]. The formyl radical $\cdot CHO$ formed, observable in EPR spectroscopy, is confirmed by other studies as a possible intermediate [177].

To go further in the reduction process, the proposed mechanism goes through C_2 intermediates, after dimerization of the radical $\cdot CHO$ in glyoxal $OCHCHO$. This intermediate, with an excellent electron affinity due to the π conjugation, can be then easily reduced into trans-ethane-1,2-semidione $\cdot HOCHCHO$ and glycolaldehyde $HOCH_2CHO$ successively. The vinoxyl radical $\cdot CH_2CHO$ can then be formed in order to give acetaldehyde CH_3CHO, observed as a product in some CO_2 reduction studies [178, 179]. At this point, an oxidation step is required to form the so unstable acetyl radical $\cdot CH_3CO$, that is decomposed into $\cdot CH_3$ and CO, a side product observed most of the time. As it was the case previously, the methyl radical $\cdot CH_3$ can finally give methane CH_4 or methanol CH_3OH, as a function of the second radical ($\cdot H$ or $\cdot OH$). With the proposed pathway, in addition to avoid intermediates that could be preferentially oxidized than reduced, there is also the possibility to recycle the side product CO in order to return to the beginning of the process.

II.2.2.d. Control of the oxidation side

Up to now, we were focusing on the reduction of CO_2 that involves the photogenerated electrons. However, the photogenerated holes cannot be completely neglected, since they are planned to migrate also in the direction of the surface, maybe faster than the electrons [180]. At the surface, they are expected to react with adsorbed water molecules or with hydroxide anions OH^-. Moreover, the valence band of the semiconductors are most of time located below the water oxidation potentials (Figure II-7):

$$2H_2O + 4h^+ \rightarrow O_2 + 4H^+ \qquad E^0 = 1.23\ V\ vs\ SHE \qquad (II.14)$$

In addition, it can also affect other adsorbed species (by-products, reaction intermediates…) and control the mechanisms presented before. In some cases, before reaching the six- or eight-electron reduction products, some intermediate could be oxidized instead of being reduced [176]. Since they can also create problems of surface recombination, the use of hole scavengers can be strongly recommended. They are most of the time organic or inorganic reducing agents that will give electrons to the system in order to trap the holes through the formation of inert side product (they can also be considered as sacrificial electron donors). The most commonly used are alcohols (propanol [181, 182, 183], ethanol [184, 185] or methanol [130, 186, 181]) or tertiary amines (triethanolamine TEOA [187, 188, 189] or triethylamine TEA [190]). Other hole scavengers can be found such as ascorbic acid [191], NaOH [192, 193], EDTA [187], NA_2SO_3 [194] or sometimes bicarbonate (or carbonate) anions when it occurs in solution [125, 126, 127, 128].

II.2.3. Efficiency obtained

The complete photocatalytic process involves many steps, from the physical mechanisms of photon absorption to the chemical reaction mechanisms (including desorption of products), that contributes to the global efficiency of the system. In this part, we will discuss the efficiency obtained for various systems composed of TiO_2 (the most studied and one of the most efficient for water spitting), other oxides, sulfides and phosphides semiconductors according to some reports published in the literature so far.

II.2.3.a. On TiO_2 systems

Made of abundant elements, TiO_2 represents the ideal candidate for photocatalysis applications since it can be considered as cheap, nontoxic and resistant to photo corrosion [195]. Very efficient in water splitting due to its dielectric constant and ideal band position [196, 197], it has also been strongly studied for CO_2 photoreduction since the earlier work of Inoue et al. [198]. However, in addition to the usual drawback of TiO_2 (no adsorption in the visible, high recombination), its band positions (Figure II-7) exhibit a strong oxidation potential and a weak reduction potential, that could limit its efficiency.

Despite these limitations, TiO_2 remains an attractive semiconductor, even in its simplest configuration composed of TiO_2 nanoparticles dispersed in a CO_2-saturated solution [199]. Starting from this simple system, many investigations have been done in order to improve the CO_2 reduction efficiency: modification of the CO_2 pressure [200], addition of hole scavengers to limit its strong oxidation potential [182], optimization of the particles size [201]…

One of the best efficiencies has been obtained with TiO_2 (P-25) nanoparticles in suspension in an aqueous solution composed of carbonate instead of gaseous CO_2 [202]. For low pH values, it has been showed to provide interesting formation of methane and methanol (3.4 $mg.L^{-1}.h^{-1}$).

Another improvement seems to be the use of sensitized TiO_2 particles in suspension. It consists in the use of TiO_2 nanoparticles loaded with metallic copper that acts as co-catalyst and hole scavenger in the same time, increasing the production of methanol mainly [203]. As an example, methanol production of 443 $\mu mol.g^{-1}.h^{-1}$ has been obtained with Cu/TiO_2 particles (3 wt% on P-25) [204]. Further improvement has been obtained by dispersing the particles on a mesoporous silicate (SBA-15) in order to form a Cu/TiO_2/SBA-15 system (2 wt%) with a good methanol production rate 627 $\mu mol.g^{-1}.h^{-1}$ [205]. The best copper co-catalyst seems to be CuO instead of pure Cu, that manage to produce 1602 $\mu mol.g^{-1}.h^{-1}$ of methyl formate (that comes from the reoxidation of the methanol) in a CuO/TiO_2 system (1 wt%) [186].

The preliminary benchmark on TiO_2 shows an interesting efficiency with further possibility to increase it (co-catalyst, silicate support…). However, systems made with other semiconductors could also been good candidates, with the aim to avoid the limitations of TiO_2:

- Raising the valence band in order to reduce the oxidation potential (no strong oxidation potential required) and get visible adsorption through a reduce bandgap.
- Raising the conduction band to increase the reduction potential
- Improving the efficiency of the exciton formation while decreasing the recombination

II.2.3.b. On other metal oxides

Although TiO_2 is known as the more efficient oxide in photocatalysis, other oxides are expected to show promising efficiency. They can be divided on two oxide types:

- The first one is composed of octahedrally coordinated d^0 metal (Ti^{4+}, as treated before, but also Zr^{4+}, Nb^{5+}, Ta^{5+}…). They are most of the times binary oxides but there are examples of more complicated compositions such as perovskites or perovskite-related structures [206, 207]: AMO_3 or AMO_4 with A a cation (alkali, alkaline earth, rare earth metal ion) [208, 209]
- The second group contains oxides with metal in a d^{10} configuration in a formula M_yO_z or $A_xM_yO_z$ with M = Ga, In, Sn, Sb or Ge and A is once again a cation.

As it is the case for TiO_2, their good performance in water splitting can make them good candidates for other reactions such as the CO_2 reduction. Their electronic structure is composed of a valence band that comes from 2p orbitals of oxygen and a CB that comes from an antibonding interaction between the t_{2g} orbitals of the metals and oxygen orbitals [195, 207]. Thus, the valence band is generally localized at a very oxidative potential (Figure II-10), and a very high bandgap is required to reach the reduction potential required, and an even higher bandgap is required to do the reaction to overpass the generally large overpotentials. The low efficiency expected has been observed in many cases [210, 211, 212, 213] but some improvements are still possible.

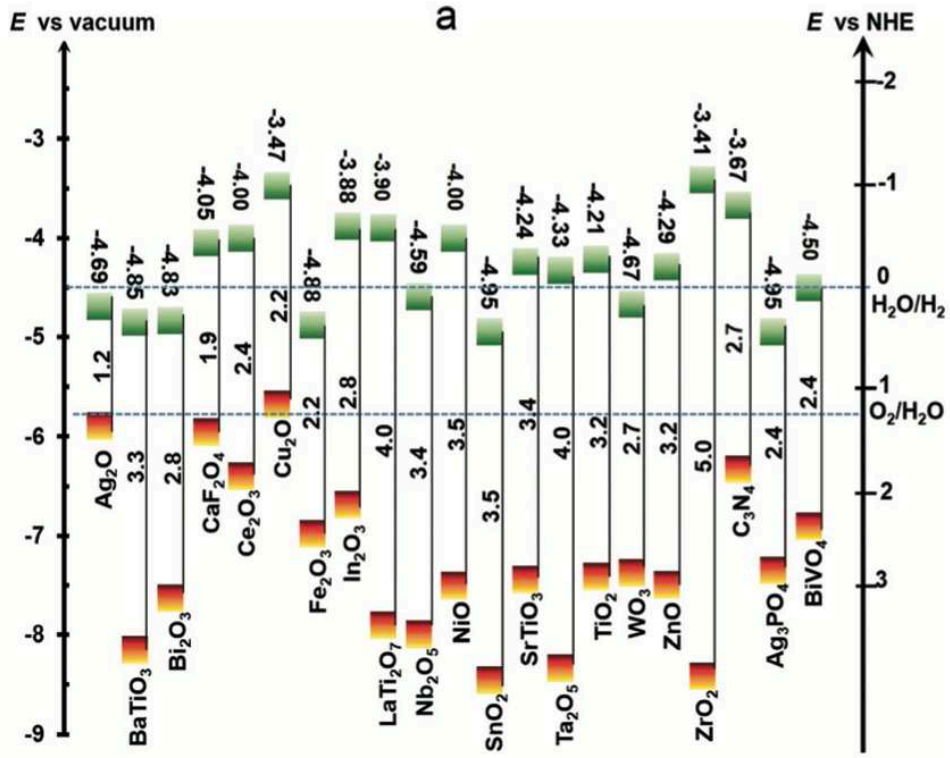

Figure II-10 : Band edge position with respect to the vacuum level and the NHE for selected oxides at pH (0). The top squares represent the conduction band edges, the bottom squares represent the valence band edges, the top number is the conduction band level and the number between the squares is the bandgap [214].

One of this improvement may be the use of oxides associated to Bi^{3+} cations, that induces a shift of the valence band due to the hybridization of Bi 6s and O 2p orbitals [215, 216]. As an example, $BiVO_4$ produce ethanol at 406.6 $\mu mol.h^{-1}$ while the reaction did not occur on vanadium oxide alone [217]. Another improvement may be the use of ferroelectric materials that leads to a strong band bending, an absorption facilitated and a good separation of the charge carriers [218, 219]. As an example, ferroelectric $LiNbO_3$ form formic acid at 7700 $\mu mol.h^{-1}$ with 2% of power conversion efficiency (11 times higher than TiO_2 P-25 particles) [220].

II.2.3.c. On sulfides

Due to the 3p orbitals of the sulfur atoms, sulfides compounds provide a valence band shifted upward (Figure II-11) in comparison with oxides (Figure II-10). Moreover, the CB may also be more reductive [208], making the sulfides good candidates with a narrowed bandgap that allows visible adsorption. However, in the case of some sulfides, the bandgap is very close (around 1 eV). In these conditions, in addition to a problem of absorbance in the infrared region, a small bandgap could make impossible the realization of the reactions.

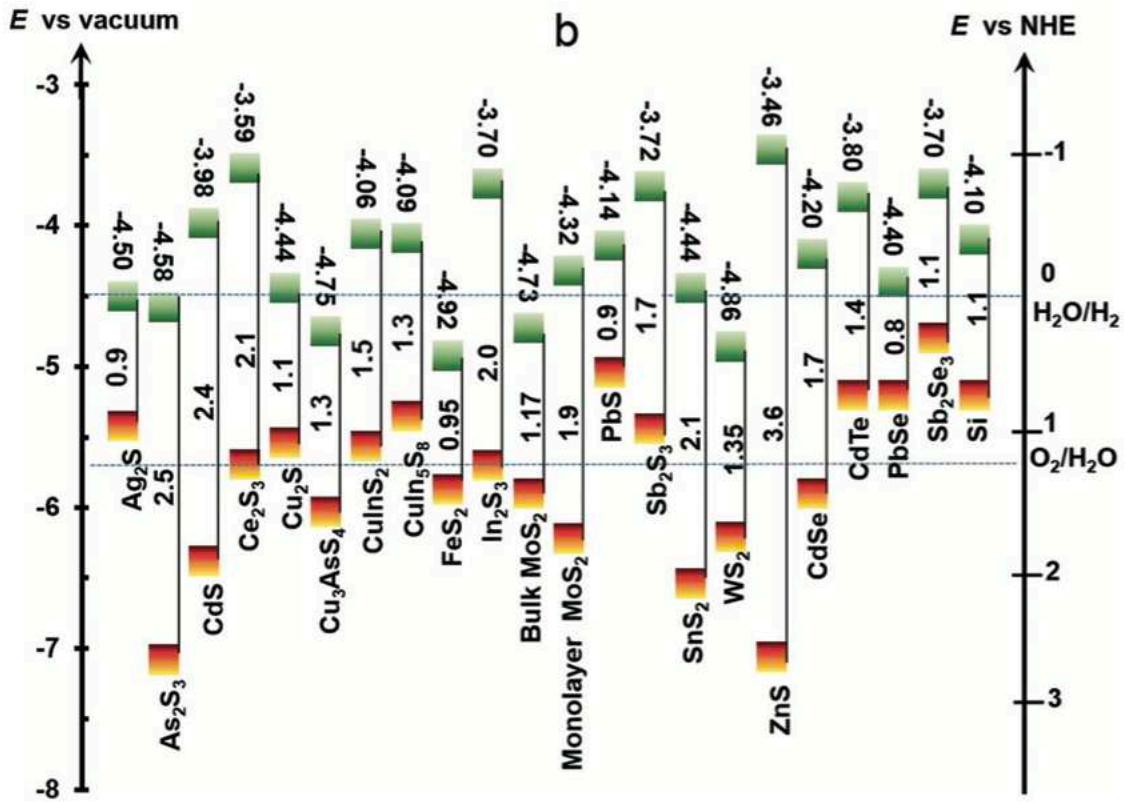

Figure II-11 : Band edge position with respect to the vacuum level and the NHE for selected chalcogenides and silicon at pH = 0. The top squares represent the conduction band edges, the bottom squares represent the valence band edges, the top number is the conduction band level and the number between the squares is the bandgap [214].

Another inconvenient comes from the sulfide instability under light irradiation due to the oxidation of the S^{2-} ions on the lattice into sulfur or sulfates [221] particularly when the reaction is undertaken in aqueous media. The use of hole scavenger is thus strongly recommended.

One of the most sulfide studied is CdS, a semiconductor with a bandgap able to absorb visible light (2.4 eV => 540 nm) and a conduction band with a higher reduction potential compared to TiO_2 (Figure II-7) [221]. In the case of CdS nanoparticles alone, the CO formation has been mainly observed (issued from CO_2 bidentate adsorption on Cd atoms) with a rate of 8.4 µmol.h^{-1} with a quantum yield of 9.8% (at 400nm) [222]. A higher rate is obtained with the use of a co-catalyst (TMA, that act also as hole-scavenger), with 58.3 µmol.h^{-1} of oxalate (comes from the dimerization of $CO_2^{\cdot-}$ radical) [213]. As it was the case with TiO_2, the use of silica support increases the formations rates (81.5 µmol.g^{-1}.h^{-1} of formic acid) but with side products produced in high quantity (formaldehyde and oxalate mainly) [223]. Another improvement has been found by creating a heterojunction with another sulfide, Bi_2S_3. A methanol formation rate of 88 µmol.g^{-1}.h^{-1} has been obtained with 15 wt % Bi_2S_3 [224], three times higher than the rates obtained with the semiconductors alone.

The other mostly studied sulfide is ZnS, that has the advantage to have a very strong reduction potential with a conduction band 1 eV more reductive than the one of CdS [225]. On the other hand, its large bandgap (3.66 eV) absorbs only in the UV. The main product obtained with ZnS is formic acid in many cases, with a high quantum yield. As an example, a formation rate of 75.1 µmol.h^{-1} has been obtained on ZnS nanoparticles with a quantum yield of 72% at 313 nm [226]. However, the competitive H_2 productions seems to be also mostly favored (86 µmol.h^{-1}). With ZnS, no positive influence of a co-catalyst has been observed, with a formic acid formation rate that decreased 15.4 µmol.h^{-1} [190]. On the other hand, the use of nanoparticles on a silica support increased once again the production rate (7000 µmol.g^{-1}.h^{-1}) [227].

Considering that our study will focus on MoS_2, the case of this material will be treated in a dedicated section II.3.

II.2.3.d. On phosphides

In addition to oxides and sulfides, further phosphides may reduce the CO_2 with good efficiency such as GaP or InP. The previous one has the advantage to have a visible bandgap (2.3 eV) with a conduction band with high reduction potential [198]. It is mainly used as photocathode in a photoelectrochemical cell to produce methanol with an external quantum yield of 2.6 % at 465 nm. [118]. Concerning InP, despite a conduction band located almost 1 eV lower, it successfully reduces CO_2 into formic acid with a rate of 140 µmol.h^{-1} under visible light radiation [119].

II.2.4. Conclusion

Despite the interest raised by the initial report of Inoue et al. [198], the CO_2 photoreduction remain a process with numerous unresolved questions on its physical and chemical mechanisms and on the effect of the photocatalyst (architecture, composition …). For these reasons, the rates of products are still lower than the natural photosynthesis and the H_2 production.

Due to the increase of CO_2 level in atmosphere and the needed in alternative energy resources, the photoreduction of CO_2 is attracted more and more attention with the aim to

bring answers to these unresolved questions. At this point, despite the good performance of TiO_2 in photocatalysis (specifically on water splitting), it does not seem to be the ideal candidate for the CO_2 reduction, even when combined with a co-catalyst. On the other hand, sulfides compounds presented promising result, with the advantage to be less favorable for the oxidation reaction, thanks to the energy of the S orbitals. Starting from that, other promising candidates could emerge in this new field of search, such as the Transition Metal Dichalcogenides (TMDs), like MoS_2.

II.3. Characteristics and application of MoS_2 as a semiconductor

Molybdenum disulfide (MoS_2) is an inorganic material of the dichalcogenides family. These chemical compounds are made of a transition metal (Mo in our case) associated to a chalcogen atom (group 16 in the periodic table, S in our case) [228]. This low-cost material and its physical, chemical and electronic properties are attracting more and more attention to substitute actual material for photocatalytic applications. In this part, the interest of this material will be demonstrated through a description of its characteristics and a description of its possible use in photocatalysis. Its limitations will also be highlighted and further way to improve its performance will be proposed, in particular in heterojunction systems.

II.3.1. MoS_2 characteristics

MoS_2 structures can be found under 3D, 2D, 1D or 0D structures, with characteristics and applications that may change depending on the dimension. In particular, the conduction character can vary. Since it can exist with a wide variety of size and shape, we will focus on a first time on the description of the various structural compounds of MoS_2. In a second time, we will describe the physical properties associated to semiconducting MoS_2.

II.3.1.a. Structural characteristic

In its bulk structure (3D), MoS_2 can be trigonal (T), hexagonal (H) or Rhombohedral (R). The three main structures are 1T, 2H and 3R phase, with 1T that coordinates in an octahedral structure while the two others coordinate in a trigonal prismatic structure [229, 230] (Figure

II-12). The nomenclature nX used indicates the number of layers (n) and the shape associated (X). As an example, the 2H phase is composed of 2 layers in hexagonal shape. The 1H MoS_2, composed of one Mo layer sandwiched by two S layers with a total thickness of 0.65 nm, can also be synthetized in order to obtain a very thin material [231]. When stacked, the MoS_2 layers are physically bounded with Van der Waals forces that stabilize the system [232].

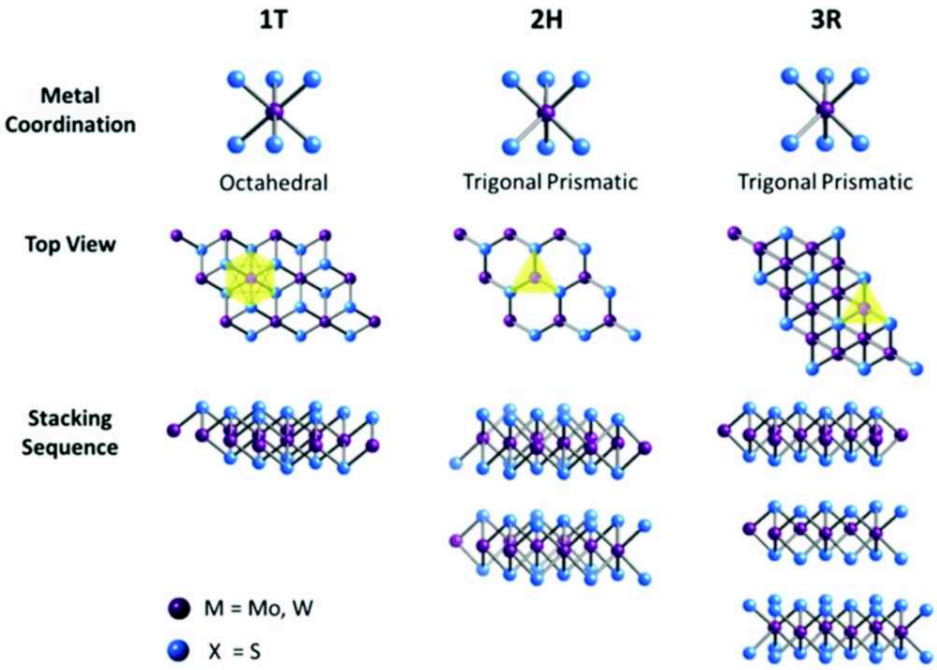

Figure II-12 : Different coordination and stacking sequences of the three main MoS_2 structures: 1T, 2H and 3R [230].

One of the interests on these materials comes from its structure that can be tuned easily through modification of the number of layers, modification of the size, addition of doping elements… As an example, it exists in 2D structures (nanosheet, nanoribbon…), 1D structures (nanowire, nanotube) or 0 D structure (quantum dots, nanoplatelets) [233]. This tunable nanostructure means that MoS_2 can be adapted in order to fit with the application targeted. In particular, by tuning its nano-structure, we are expected to be able to modifying its chemical and physical properties for photocatalytic applications as it has already been achieved for conventional catalytic processes [234].

II.3.1.b. Physical properties

The first tunable property comes directly from the MoS_2 phase. While 1T-MoS_2 is known to be metallic, 2H and 3R are semiconductors and by extension, 1H is also semiconducting.

However, due to non-linear properties, 3R phase is only used in nonlinear mass sensing [235] and will not interest us for photocatalytic applications.

Concerning H MoS_2, there is a strong interest that comes from its tunable number of layers, that have a strong impact on its optoelectronic properties. In particular, an indirect bandgap of 1.2 eV is observed in the bulk material while a direct bandgap of 1.8 eV in the monolayer [236], making the monolayer a promising material for photocatalytic applications.

In addition, its tunable structure makes MoS_2 easily doped. As a function of the requirement, it can be changed in a n-type semiconductor (when doped with Cr, Cu or Sc) or in a p-type semiconductor (when doped with Ni, Zn) [237]. In particular, doping MoS_2 with Ti may give either a n-type or a p-type as a function of the sites and level of doping [233].

Concerning the optical properties, MoS_2 provide a large absorption coefficient in the low visible (400-500 nm) but with a strong decrease above 500 nm [238]. Moreover, MoS_2 has a low photoluminescence quantum yield. In other words, the ratio of the number of photons absorbed to the number of photons emitted is between 0.01 and 6% [233]. However, due to the tunable structure of MoS_2, the quantum yield can be increased by chemical treatment [239]. In general, due to its tunable bandgap, MoS_2 have also tunable absorption properties (photoresponsivity, specific detectivity, response time [240]). Given that possibility, MoS_2 is able to provide a high charge carrier mobility and excellent absorption properties [241, 242, 243] that could be exploited through many applications, in particular in photocatalysis.

II.3.2. MoS_2 utilization in photocatalysis

Due to its attractive optoelectronic properties presented before, MoS_2 has been intensively studied for photocatalysis applications. In this part, MoS_2-based photocatalysts will be described. In a second time, the emerging problems and the possible ways to overcome them will be described.

II.3.2.a. Possible applications

First of all, MoS_2 has been used in the photocatalytic production of hydrogen via the hydrogen evolution reaction (HER). Given that MoS_2 is made of earth-abundant elements with promising physical and chemical properties [244, 245], it has been considered in replacement of noble

metal co-catalyst previously used (Pt mainly) [246]. In particular, MoS_2 monolayer has been identified to be more efficient than stacked systems for some reasons: more S atoms, active sites for the reaction, are exposed; better charge carrier separation occurs due to the stronger binding energy with the semiconductor; the conduction band is more reductive [247]. As an example, monolayer MoS_2/CdS produced H_2 with an efficiency 5 times higher than Pt/CdS (2.59 $mmol.h^{-1}$ vs 0.44 $mmol.h^{-1}$) [248].

From an environmental point of view, MoS_2 was also tested for the photocatalytic oxidation of pollutants. However, the valence band of MoS_2 is not enough oxidative to directly decompose pollutants [249] and it only serve most of the time as a co-catalyst that will avoid charge carrier recombination. MoS_2-based photocatalyst can be thus used in many processed like the degradation of toluene [250], the hydrodesulfurization of gasoline [251, 252, 234, 253], the treatment of heavy metals [254, 255, 256], the nitric oxygen removal [257, 258] or the photocatalytic disinfection of microbial pollutants [259, 260, 261].

Concerning the CO_2 photoreduction, there is still very few experimental studies in this field with MoS_2 based semiconductors. However, given that good performances of sulfides compounds for the CO_2 photoreduction (II.2.3.c), many applications involving MoS_2 are expected to emerge. In the actual researches, the idea is to take advantage to the tunable structure of MoS_2 with the use of metal doping. As an example, Au-MoS_2 and Ag-MoS_2 have been found to reduced CO_2 into CH_4 or CO with interesting selectivity (80% and 98%) [262]. In addition, DFT studies [263, 264] showed the favored activation of CO_2 on MoS_2 edges doped with N or Co. Given that it could be a strongly limited step, the activation of CO_2 on MoS_2 edges is already a promising clue to its photoreduction activity.

Despite promising properties, it appears to be difficult to take advantage of the excellent absorption properties of MoS_2. In particular, its small bandgap is limiting its efficiency on both reduction and oxidation side. Used most of the time only as co-catalyst, some strategies can help to improve its photocatalytic performances, either as an active semiconductor.

II.3.2.b. Ways to improve MoS_2 performances

As developed in II.1, the photocatalytic efficiency can be improved with many strategies. As an example, the modulation of energy band by doping [265, 266, 267] is one of the relevant strategies developed. Moreover, it is reported that it may also favor the adsorption of the

reactants [263, 264]. In order to promote visible light absorption, the used of photosensitizer [268] or surface plasmon resonance [269] can also be applied to MoS_2-based photocatalysts. In addition, given that the properties depend on the surface exposed, crystal face engineering would improve the properties of the materials [270].

In addition, new strategies can be employed due to the specific structure of MoS_2. In particular, the morphology is an important parameter to control in the MoS_2 synthesis. As presented before, the number of layers is expected to have a strong impact on the photocatalytic performances of the material, with a recombination rate that lowers with the decrease of the number of layers and a photocatalytic performance that increase [271, 272, 273].

Further improvements can be obtained with the use of amorphous MoS_x instead of crystalline MoS_2. It has been shown to improve the photocatalytic hydrogen production [242, 274] due to the hydrogen adsorption favored by the presence of many unsaturated sulfur atoms. Moreover, it seems to offer an excellent thermal stability (up to 350°C) [275].

Given that MoS_2 is mainly used as a co-catalyst, tuning the phase of MoS_2 could be an interesting strategy since the electrocatalytic activity of 1T-MoS_2 may be superior than that of 2H-MoS_2, due to the metallic aspect of the 1T phase and the good conductivity associated [276, 277, 278]. However, depending on the light harvester involved, the best co-catalyst could be 1T-MoS_2 (with TiO_2 for example [279]) or 2H-MoS_2 (with CdS for example [248]). Moreover, since the 1T-phase is metastable, it could be transformed in 2H-phase in case of long reaction time [280]. In case of higher performances with 1T-phase, an increase of its stability is required.

Another strategy that could be developed would be the use of MoS_2 in photo electrocatalysis systems, that have been identified as main candidate to unlock photocatalytic process [281]. In these systems, an external bias is applied in order to improve the efficiency of charge transfer and limit the charge carrier recombination [282]. Although not so studied yet, photo electrocatalysis could be a promising approach.

In addition to photo electrocatalysis approach, it is interesting to be inspired by the study of MoS_2 in electrocatalysis, in particular for the CO_2 reduction. With electrocatalysis approach,

that avoids problems of light harvesting with MoS_2, the intrinsic behavior of MoS_2 sites can be studied to mimic the reactive steps of the photocatalytic mechanism. In these systems, MoS_2 has begun to be identified as a good substitute to noble metal electrodes, with higher CO_2 reduction performances with higher current density and lower overpotential (CO_2/MoS_2 edges). Moreover, DFT mechanistic studies ran with the Computational Hydrogen Electrode approach [144] manage to propose an electroreduction mechanism from CO_2 to CH_4 on Ni-doped MoS_2 [283, 284](Figure II-13). However, although the proposed mechanism contains only exergonic steps (if a potential lower than – 0.28 V is applied), it could be limited by the first step that will require a proton-electron coupled transferred, the only type of transfer considered with this method. Further investigations on CO_2 electroreduction mechanism could help to avoid this problem.

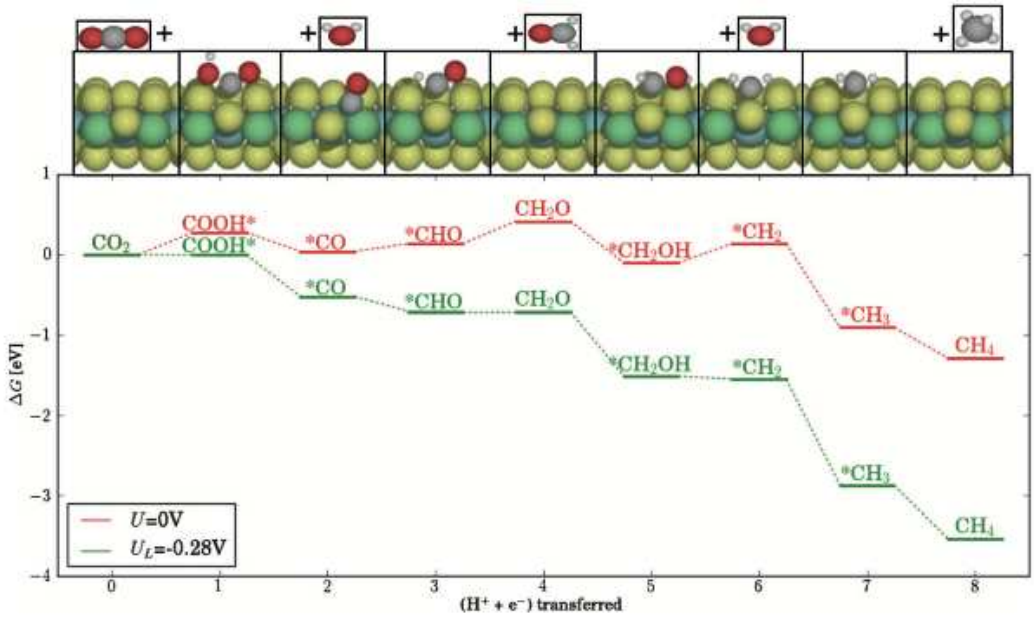

Figure II-13 : Free energy diagram for the reduction of CO_2 to CH_4 on the Ni-doped S edge of MoS_2 at 0V and U_L= - 0.28 V, the limited potential where all the reaction steps becomes exergonic [283].

To conclude, despite many strategies developed to increase MoS_2 performances, his use is mainly limited to a co-catalyst role, with charge carriers generated by another semiconductor and transfer to MoS_2, for reduction applications mainly. In that case, as with electrocatalysis approaches, MoS_2 seems to be very performant. Given these performances, it could be very interesting to be able to build systems with MoS_2 also as light harvester, in order to take advantage of its absorption properties. To do that, since MoS_2 seems to be limited by its small bandgap, band alignment through Z-scheme heterojunctions could be the ideal solution.

II.3.2.c. MoS_2/SC heterostructures to obtain a Z-scheme mechanism

Among all the strategies considered in actual works, the most interesting seems to be the formation of heterojunctions with other semiconductors, in particular in case of Z-scheme mechanism, that allow the use of semiconductors with small bandgaps such as MoS_2. An example has been obtained with $(BiO_2)CO_3/MoS_2$ systems [258], in which both semiconductors absorb one photon. Due to the fermi level alignment after contact, the electrons of $(BiO_2)CO_3$ are expected to recombine with holes of MoS_2 (Figure II-14), in order to provide charge separation and excellent reduction and oxidation properties.

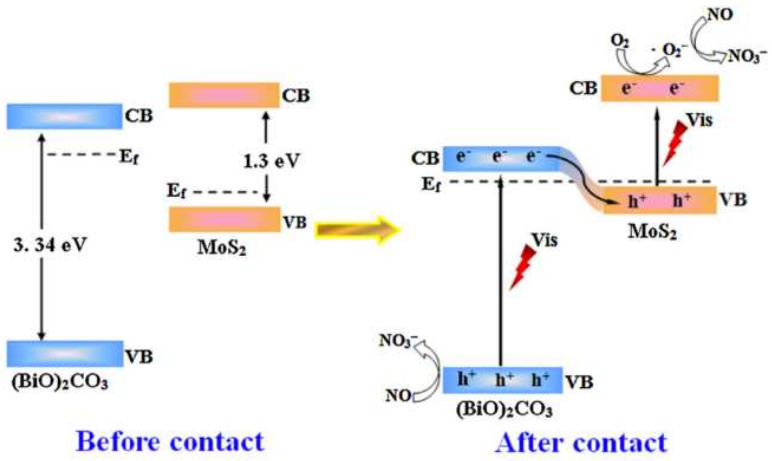

Figure II-14 : The proposed photocatalytic mechanism for $(BiO_2)CO_3/MoS_2$ heterojunction [258].

As a function of the amount of S doping in the MoO_3 structure, similar Z-scheme mechanism is expected with $MoO_{3-x}S_x/MoS_2$ heterojunctions [305]. Although it is difficult to determine precisely the amount of S-doping that will favor the Z-scheme mechanism and avoid the classical type II mechanism (Figure II-4), the particulate Z-scheme mechanism seems possible. This work could be extended to other semiconductors than $(BiO_2)CO_3$ and $MoO_{3-x}S_x$.

Due to their low cost, high stability and abundance, the combination of 2H-MoS_2 with TiO_2 in heterostructures systems has been intensively studied [285, 286]. The idea is to be able to combine the efficient photocatalytic activity of TiO_2 [287, 288] with the catalytic activity of MoS_2 for the activation, conversion and production of various compounds [289, 290].

In order to reach such heterostructures combining MoS_2 and TiO_2 within one material, efficient nano composites must be synthetized with MoS_2 nanosheets coated on TiO_2 in a core-shell structure, with various shapes of TiO_2 core (nanowire [291], nanobelt [271], nanotubes [292]…). In general, the junction is mainly localized on TiO_2 (101) surface, the most

stable and the most predominant surface [293, 294]. However, the few studies focusing on the (001) surface demonstrated excellent efficiency for the Hydrogen Evolution Reaction, 36.4 times higher than pure TiO_2 [295]. It illustrates the interest of MoS_2/TiO_2 systems for photocatalytic applications, either when the interaction occurs on the less stable surface. It could be extended to the CO_2 photoreduction, with rates of production 3 times higher than pure TiO_2, but still very low (10.6 μmol.g^{-1}.h^{-1}) [296]. In general, despite strategies considered to improve the semiconductor performance (see II.1), the photocatalytic activities obtained remain to be improved.

This can be explained by some challenges. First of all, the difficulty to produce a clean interfacial heterostructure. Small mismatch between MoS_2 and TiO_2 lattice generates a highly defective interface. As a consequence, only a small amount of MoS_2 is in intimate contact with TiO_2, that is limiting the charge transfer between the two materials. In addition, these MoS_2/TiO_2 systems will face the traditional poor visible light harvesting of TiO_2 and low electrical conductivity. Moreover, the impact of the structure (nature of the TiO_2 crystallographic facet, nature of the interaction, chemical composition of the interface…) on the optoelectronic is not well known.

Concerning the charge carrier mechanism proposed, it could be decomposed in two categories. In the first category, MoS_2 act as almost always only as a co-catalyst while TiO_2 harvest the light (Figure II-15 a). The loaded MoS_2 is here to provide active sites and avoid the recombination of the charge carriers photogenerated in TiO_2. In other studies, an alternative mechanism has been proposed with TiO_2 and MoS_2 that will absorb the light in a type II heterojunction with a classical type II mechanism (Figure II-15 b). It results in the accumulation of the electrons in TiO_2 and the accumulation of the holes in MoS_2, a good way to spatially separate the charge carriers (II.1.3.b). However, the low energy difference between the Conduction Band of TiO_2 and the Valence Band of MoS_2 will limit the photocatalysis applications (II.1.4.a). Nevertheless, the alternative Z-scheme mechanism, not considered in the actual studies, cannot be neglected and could provide a considerable increase in efficiency (II.1.2.c).

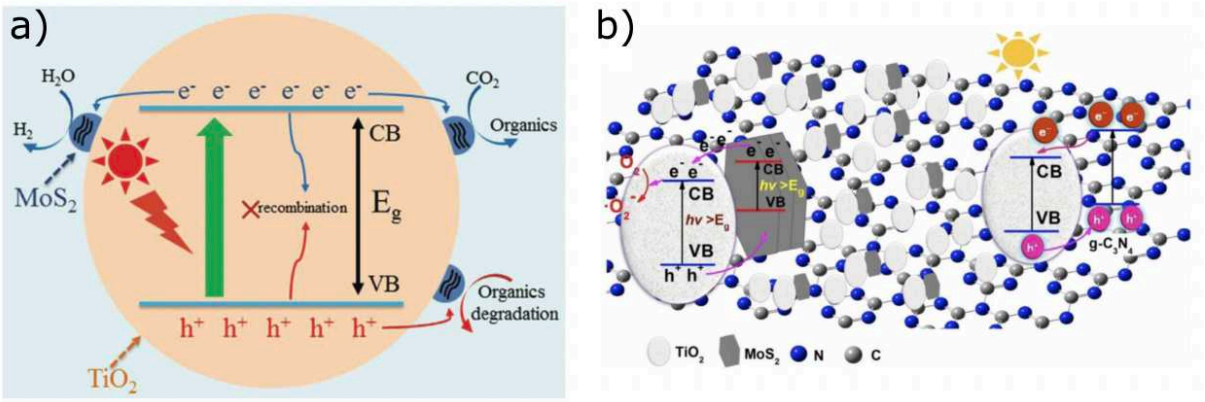

Figure II-15 : Different charge carrier migration proposed for MoS_2/TiO_2 systems: (a) MoS_2 acts as a co-catalyst while TiO_2 play the role of light harvester [285] and (b) MoS_2 and TiO_2 are involved in a type II heterostructure [297].

II.4. Conclusion

With the aim to realize an energy transition from fossil energies to renewable energies, the use of the abundant and powerful solar energy appears to be an interesting candidate. In particular, the use of solar energy to activate chemical molecules such as CO_2, H_2O… will permit to stock the solar energy under the form of chemical bonds. However, the mechanisms involved in such the photocatalytic reactions are complexed and each step requires investigations to optimize its efficiency. Despite many strategies to optimize these steps, the global energy conversion efficiencies are still not so satisfying.

Among the photocatalytic reactions possible, there is a growth of interest in the CO_2 photoreduction, that could be able to reduce the CO_2 concentration in the atmosphere while producing fuels. In other words, there is an ecological and an industrial interest in the realization of this reaction. However, due to the high number of possible products formed and the high number of electrons required, the actual work provides difficulties to obtain good conversion efficiency and selectivity.

In order to enhance the photocatalytic performances, in particular those of the CO_2 photoreduction process, transition metal dichalcogenides like MoS_2 are attracting the scientific attention for their interesting opto-electronic properties associated to a tunable 2D structure. The efficiency of MoS_2 has been illustrated by promising experiments when used as a co-catalyst or as a reduction electrode. However, due to its narrow bandgap, its use as photocatalyst seems to be limited but building an heterostructure with TiO_2 in order to reach a Z-scheme mechanism could overcome this limit.

With the aim to provide new insights into the nano-structuration of MoS_2/TiO_2 interfaces, the present work will first explore in Chapter IV by density functional theory (DFT) approach the evolution of the bandgap and Conduction Band/Valence Band positions for various 1D- or 2D-MoS_2/TiO_2-anatase heterojunctions. The two main surfaces orientations of TiO_2 will be considered (the (101) and the (001)) involving both physical van der Waals interaction and chemical epitaxy-like interaction with MoS_2 basal plane or edges [298, 299, 300]. In addition, the influence of key physico-chemical parameters at the interface will be studied: the surface states, the orientation of MoS_2 monolayer, the size of MoS_2 monolayers… The objective is to provide a description of the MoS_2/TiO_2 interface and a more general view on the evolution of the band position and the charge carrier pathway associated. In particular the feasibility of a Z-scheme mechanism will be discussed.

In a second time, given that the strong limitation of CO_2 photoreduction applications due to the lack in comprehension of the complete mechanism, we propose in Chapter V to study the CO_2 electro-reduction mechanism on MoS_2 nanosheets for various sites located at the edges of the MoS_2 nanosheets. In particular, the use of the Grand Canonical DFT approach (or surface charging approach) [152, 301, 302] instead of the mostly used Computational Hydrogen Electrode [144] will be bring a complementary view on the possible mechanisms, since it allows us to consider not only proton-electron coupled transfers. This approach will also provide us an approximate way to mimic the activation process once the charge transfer has been induced upon illumination. In addition, this method will help us to determine how the thermodynamic barriers up to formic acid depend on the electrochemical potential.

In Chapter III, we will start by presenting the fundamental aspects of the theoretical methodology used throughout this thesis.

II.5. References

[1] A. Kudo and Y. Miseki, *Chemical Society Reviews,* vol. 38, pp. 253-278, 2009.

[2] S. Zhu and D. Wang, *Advanced Energy Materials,* vol. 7, p. 1700841, 2017.

[3] M. R. Hoffmann, S. T. Martin, W. Choi and D. W. Bahnemann, *Chemical Reviews,* vol. 95, pp. 69-96, 1995.

[4] T. Le Bahers, M. Rérat and P. Sautet, *The Journal of Physical Chemistry C,* vol. 118, pp. 5997-6008, 2014.

[5] C. Roy, O. K. Varghese, M. Paulose and C. A. Grimes, *ACS Nano,* vol. 4, pp. 1259-1278, 2010.

[6] M. Halmann, V. Katzir, E. Borgarello and J. Kiwi, *Solar Energy Materials and Solar Cells,* vol. 10, pp. 85-91, 1984.

[7] Z. Chen, H. N. Dinh and E. Miller, in *Photoelectrochemical Water Splitting - Standards, Experimental Methods and Protocols*, Springer, 2013, pp. 7-16.

[8] R. Li and C. Li, "Chapter 1," in *Advances in Catalysis*, 2017, Elsevier.

[9] Z. Wang, Y. Inoue, T. Hisatomi, R. Ishikawa, Q. Wang, T. Takata, S. Chen, N. Shibata, Y. Ikuhara and K. Domen, *Nature Catalysis,* vol. 1, pp. 756-763, 2018.

[10] S. Mubeen, J. Lee, N. Singh, S. Krämer, G. D. Stucky and M. Moskovits, *Nature Nanotechnologies,* vol. 8, pp. 247-251, 2013.

[11] Y. Qi, Y. Zhao, Y. Gao, D. Li, Z. Li, F. Zhang and C. Li, *Joule,* vol. 2, pp. 2393-2402, 2018.

[12] Q. Wang, T. Hisatomi, Y. Suzuki, Z. Pan, J. Seo, M. Katayama, T. Minegishi, H. Nishiyama, T. Takata, K. Seki, T. Tamada, T. Yamada and K. Domen, *Journal of the American Chemical Society,* vol. 139, pp. 1675-1683, 2017.

[13] Q. Wang, T. Hisatomi, Q. Jia, H. Tokudome, M. Zhong, C. Wang, Z. Pan, T. Takata, M. Nakabayashi, N. Shibata, Y. Li, I. S. Shap, A. Kudo, T. Yamada and K. Domen, *Nature Materials,* vol. 15, pp. 611-615, 2016.

[14] X. Guan, F. A. Chowdurry, N. Pant, L. Guo, L. Bayssieres and Z. Mi, *The Journal of Physical Chemistry C,* vol. 122, pp. 13797-13802, 2018.

[15] X. Liu, Y. Liu, N. Liu, Y. Han, X. Zhang, H. Huang, Y. Lifshitz, S.-T. Lee, J. Zhong and Z. Kang, *Science,* vol. 347, pp. 970-974, 2015.

[16] K. Takanabe, *ACS Catalysis,* vol. 7, pp. 8006-8022, 2017.

[17] U. K. Mishra and Singh, in *Journal of Semiconductor Device Physics and Photonics*, Springer, 2008, pp. 46-50.

[18] S. O. Kasap and R. K. Sinha, "Chapter 3," in *Optoelectronics and Photonics: Principles and Practices*, Pearson Education, 2012.

[19] J. L. Gray, "Chapter 3," in *Handbok of Photovoltaic Science and Engineering*, Wiley, 2003.

[20] R. Abe, *Journal of Photochemistry and Photobioogy C,* vol. 11, pp. 179-209, 2010.

[21] K. Maeda and K. Domen, *The Journal of Physical Chemistry Letters,* vol. 1, pp. 2655-2661, 2010.

[22] Y. Yuan, J. Lv, X. Jiang, Z. Li, T. Yu, Z. Zou and J. Ye, *Applied Physical Letters,* vol. 91, no. 94107, 2007.

[23] Y. Qin, G. Wang and Y. Wang, *Catalysis Communications,* vol. 8, pp. 926-930, 2007.

[24] H. Kato, K. Asakura and A. Kudo, *Journal of the American Chemica Society,* vol. 125, pp. 3082-3089, 2003.

[25] A. Iwase, H. Kato and A. Kudo, *ChemSusChem,* vol. 2, pp. 873-877, 2009.

[26] R. Niishiro, H. Kato and A. Kudo, *Physical Chemistry Chemical Physics,* vol. 7, pp. 2241-2245, 2005.

[27] E. Borgarello, J. Kiwi, M. Gratzel, E. Pelizetti and M. Visca, *Journal of American Chemical Society,* vol. 104, pp. 2996-3002, 1982.

[28] W. Choi, A. Termin and M. R. Hoffmann, *The Journal of Physical Chemistry,* vol. 98, pp. 13669-13679, 1994.

[29] R. Asahi, T. Morikawa, T. Ohwaki, K. Aoki and Y. Taga, *Science,* vol. 293, pp. 269-271, 2001.

[30] J. Yuan, M. Chen, J. Shi and W. Shangguan, *Internation Journal of Hydrogen Energy,* vol. 31, pp. 1326-1331, 2006.

[31] K. Nishijima, T. Kamai, N. Murakani, T. Tsubota and T. Ohno, *International Journal of Photoenergy,* vol. 2008, p. 173943, 2008.

[32] H. Luo, T. Takata, Y. Lee, J. Zhao, K. Domen and Y. Yan, *Chemistry of Materials,* vol. 16, pp. 846-849, 2004.

[33] K. Maeda, K. Teramura, D. Lu, T. Takata, N. Saito , Y. Inoue and K. Domen, *Nature,* vol. 440, p. 295, 2006.

[34] K. Maeda, T. Takata, M. Hara, N. Saito, Y. Inoue, H. Kobayashi and K. Domen, *Journal of the American Chemical Society,* vol. 127, pp. 8286-8287, 2005.

[35] H. Liu, J. Yuan, Z. Jiang, W. Shangguan, H. Einaga and Y. Teraoka, *Journal of Solid State Chemistry,* vol. 21, pp. 16535-16543, 2011.

[36] H. Liu, J. Yuan, Z. Jiang, W. Shangguan, H. Einaga and Y. Teraoka, *Journal of Material Chemistry,* vol. 112, pp. 8521-8523, 2011.

[37] I. Tsuji, H. Kato, H. Kobayashi and A. Kudo , *The Journal of Physical Chemistry B,* vol. 109, pp. 7323-7329, 2005.

[38] S. Ikeada, T. Nakamura, T. Harada and M. Matsmura, *Physical Chemistry Chemica Physics,* vol. 12, pp. 13943-13949, 2010.

[39] W. J. Youngblood, S.-H. A. Lee, K. Maeda and T. E. Mallouk, *Accounts of Chemical Research,* vol. 42, pp. 1966-1973, 2009.

[40] M. Grätzel, *Nature,* vol. 414, pp. 338-344, 2001.

[41] J. Wilkomm, K. L. Orchard, A. Reynal, E. Pastor, J. R. Durrant and E. Reisner, *Chemical Sociey Reviews,* vol. 45, pp. 9-23, 2016.

[42] E. Borgarello, J. Kiwi, E. Pelizetti, M. Visca and M. Grätzel, *Journal of the American Chemical Society ,* vol. 103, pp. 6324-6329, 1981.

[43] E. Borgarello, J. Kiwi, E. Pelizetti, M. Visca and M. Grätzel, *Nature,* vol. 289, pp. 158-160, 1981.

[44] K. Gurunathan, P. Maruthamuthu and M. V. C. Sastri, *International Journal of Hydrogen Energy,* vol. 22, pp. 57-62, 1997.

[45] K. B. Dhanalakshimi, S. Latha, S. Anandan and P. Maruthamuthu, *International Journal of Hydrogen Energy,* vol. 26, pp. 669-674, 2001.

[46] H. Hagiwara, N. Ono, T. Inoue, H. Matsumoto and T. Ishihara, *Angewandte Chemie International Editions,* vol. 45, pp. 1420-1422, 2006.

[47] H. Hagiwara, M. Nagatomo, S. Ida and T. Ishihara, *Energy Procedia,* vol. 22, pp. 53-60, 2012.

[48] T. Oshima, M. Eguchi and K. Maeda, "Chapter 7," in *Semiconductors and Semimetals*, Elsevier, 2017.

[49] W. Hou and S. B. Cronin, *Advanced Functional Materials,* vol. 23, pp. 1612-1619, 2013.

[50] G. Dodekatos, S. Schünemann and H. Tüysüz, in *Solar Energy for Fuels*, Springer International Publishing, 2015, pp. 215-252.

[51] A. P. Alivisatos, *Science,* vol. 271, pp. 933-937, 1996.

[52] Y. Tachibana, "Chapter 9," in *On Solar Hydrogen & Nanotechnology*, John Wiley & Sons (Asia) Pte Ltd, 2005.

[53] Q. Wang and K. Domen, *Chemical Reviews,* vol. 120, pp. 919-985, 2020.

[54] A. J. Bard, *Journal of Photochemistry,* vol. 10, p. 59, 1979.

[55] S. Bai, J. Jiang, Q. Zhang and Y. Xiong, *Chemica Sociey Reviews,* vol. 44, pp. 2893-2939, 2015.

[56] J. Liu, B. Cheng and J. Yu, *Physical Chemistry Chemical Physics,* vol. 18, pp. 31175-31183, 2016.

[57] A. J. Bard, *Journal of Photochemistry,* vol. 10, pp. 59-75, 1979.

[58] K. Maeda, *ACS Catalysis,* vol. 3, pp. 1486-1503, 2013.

[59] R. B. Chandran, S. Breen, Y. Shao, S. Ardo and A. Z. Weber, *Energy Environmental Science,* vol. 11, pp. 115-135, 2018.

[60] H. Tada, T. Mitsui, T. Kiyonaga, T. Akita and K. Tanak, *Nature Materials,* vol. 5, pp. 782-786, 2006.

[61] P. Zhou, J. Yu and M. Jaroniec, *Advanced Materials,* vol. 26, pp. 4920-4935, 2014.

[62] H. Li, H. Yu, X. Quan, S. Chen and Y. Zhang, *ACS Applied Material Interfaces,* vol. 8, pp. 2111-2119, 2016.

[63] Q. Xu, L. Zhang, J. Yu, S. Wageh, A. A. Al-Ghamdi and M. Jaroniec, *Materials Today,* vol. 21, pp. 1042-1063, 2018.

[64] J. Yu, S. Wang, J. Low and W. Xiao, *Physical Chemistry Chemical Physics,* vol. 15, pp. 16883-16890, 2013.

[65] J. J. M. Vequizo, H. Matsunaga, T. Ishiku, S. Kamimura, T. Ohno and A. Yamakata, *ACS Catalysis,* vol. 7, pp. 2644-2651, 2017.

[66] S. Wang, T. Hisatomi, T. Takata, C. Pan, M. Katayama, J. Kubota and K. Domen, *Angewandte Chemie International Editions,* vol. 52, pp. 11252-11256, 2013.

[67] K. Maeda and T. E. Mallouk, *Bulletin of the Chemical Society of Japan,* vol. 92, pp. 38-54, 2019.

[68] M. Cargnello, T. Montini, S. Y. Smolin, J. B. Priebe, J. J. Delgado Jaen, V. V. T. Doan-Nguyen, I. S. McKay, J. A. Schwalbe, M.-M. Pohl, T. R. Gordon, Y. Lu, J. B. Baxter, A. Brückner, P. Fornasiero and C. B. Murray, *Proceedings of the National Academy o Sciences of the United States of America,* vol. 113, pp. 3966-3971, 2016.

[69] A. Yamakata, J. J. M. Vequizo and M. Kawaguchi, *The Journal of Physical Chemistry C,* vol. 119, pp. 1880-1885, 2015.

[70] J. Shi, J. Chen, Z. Feng, T. Chen, Y. Lian, X. Wang and C. Li, *The Journal of Physical Chemistry C,* vol. 111, pp. 693-699, 2007.

[71] X. An, T. Li, B. Wen, J. Tang, Z. Hu, L.-M. Liu, J. Qu, C. P. Huang and H. Liu, *Advanced Energy Materials,* vol. 6, p. 1502268, 2016.

[72] Z. Lai, A. Chaturvedi, Y. Wang, T. H. Tran , X. Liu, C. Tan, Z. Luo, B. Chen, Y. Huang, G.-H. Nam, Z. Zhang, Y. Chen, Z. Hu, B. Li, S. Xi, Q. Zhang, Y. Zong, L. Gu, C. Kloc, Y. Du and H. Zhang, *Journal of the American Chemical Society,* vol. 140, pp. 8563-8568, 2018.

[73] T. Takata and K. Domen, *The Journal of Physical Chemistry C,* vol. 113, pp. 19386-19388, 2009.

[74] M. de Respinis, M. Fravventura, F. F. Abdi, H. Schreuders, T. J. Savenije, W. A. Smith, B. Dam and R. van de Krol, *Chemistry of Materials,* vol. 27, pp. 7091-7099, 2015.

[75] G. Fu, S. Yan, T. Yu and Z. Zou, *Applied Physicals Letters,* vol. 107, p. 171902, 2015.

[76] P. Wu, J. Wang, J. Zhao, L. Guo and F. E. Osterloh, *Journal of Material Chemistry A,* vol. 2, pp. 20338-20344, 2014.

[77] K. Maeda, *Chemical Letters,* vol. 43, pp. 1287-1288, 2014.

[78] Y. Xu, A. Li, T. Yao, C. Ma, X. Zhang, J. H. Shah and H. Han, *ChemSusChem,* vol. 10, pp. 4277-4305, 2017.

[79] F. E. Osterloh, *Journal of Physical Chemistry Letters,* vol. 5, pp. 2510-2511, 2014.

[80] X. Wang, K. Maeda, Y. Lee and K. Domen, *Chemical Physics Letters,* vol. 457, pp. 134-136, 2008.

[81] J. S. Jang, S. H. Choi, N. Shin, C. Yu and J. S. Lee, *Jounal of Solid State Chemistry,* vol. 180, pp. 1110-1118, 2007.

[82] M. Muruganandham, Y. Kusumoto, C. Okamoto, A. Muruganandham, M. Abdulla-Al-Mamun and B. Ahmmad, *The Journal of Physical Chemistry C,* vol. 113, pp. 19506-19517, 2009.

[83] Y. Li, J. Du, S. Peng, D. Xie, G. Lu and S. Li, *International Journal of Hydrogen Energy,* vol. 33, pp. 2007-2013, 2008.

[84] K. Maeda, H. Terashima, K. Kase, M. Higashi, M. Tabata and K. Domen, *Bulletin of the Chemical Society of Japan,* vol. 81, pp. 927-937, 2008.

[85] K. Maeda, H. Terashima, K. Kase and K. Domen, *Applied Catalysis A,* vol. 357, pp. 206-212, 2009.

[86] G. Zhang, G. Li, T. Heil, S. Zafeiratos, F. Lai, A. Savateev, M. Antonietti and X. Wang, *Angewandte Chemie International Editions,* vol. 58, pp. 3433-3437, 2019.

[87] L. Lin, W. Ren, C. Wang, A. M. Asiri, J. Zhang and X. Wang, *Applied Catalysis B,* vol. 231, pp. 234-241, 2018.

[88] G. Zhang, G. Li, Z.-A. Lan, L. Lin, A. Savateev, T. Heil, S. Zafeiratos, X. Wang and M. Antonietti, *Angewandte Chemie,* vol. 129, pp. 13630-13634, 20117.

[89] M. Zhong, T. Hisatomi, Y. Kuang, J. Zhao, M. Liu, A. Iwase, Q. Jia, H. Nishiyama, T. Minegishi, M. Nakabayashi, N. Shibata, R. Niishiro, C. Katayama, H. Shibano, M. Katayama, A. Kudo, T. Yamada and K. Domen, *Journal of the American Chemical Society,* vol. 137, pp. 5053-5060, 2015.

[90] Y. Ham, T. Minegishi, T. Hisatomi and K. Domen, *Chemcial Communications,* vol. 52, pp. 5011-5014, 2016.

[91] T. Minegishi, N. Nishimura, J. Kubota and K. Domen, *Chemical Science,* vol. 4, pp. 1120-1124, 2013.

[92] K. Ueda, T. Minegishi, J. Clune, M. Nakabayashi, T. Hisatomi, K. Nishiyama, M. Katayama, N. Shibata, J. Kubota, T. Yamada and K. Domen, *Journal of the American Chemical Society,* vol. 137, pp. 2227-2230, 2015.

[93] T. Ohno, K. Sarukawa and M. Matsumara, *New Journal of Chemistry,* vol. 26, pp. 1167-1170, 2002.

[94] R. Li, F. Zhang, D. Wang, J. Yang, M. Li, J. Zhu, X. Zhou, H. Han and C. Li, *Nature Communications,* vol. 4, p. 1432, 2013.

[95] R. Li, H. Han, F. Zhang, S. Wang and C. Li, *Energy & Environmental Science,* vol. 7, pp. 1369-1376, 2017.

[96] J. Yu, J. Low, W. Xiao, P. Zhou and M. Jaroniec, *Journal of the American Chemical Society,* vol. 136, pp. 8839-8842, 2014.

[97] R. Godin, T. Hisatomi, K. Domen and J. R. Durrant, *Chemical Science,* vol. 9, pp. 7546-7555, 2018.

[98] E. Pastor, F. Le Formal, M. T. Mayer, S. D. Tilley, L. Francàs, C. A. Mesa, M. Grätzel and J. R. Durrant, *Nature Communications,* vol. 8, p. 14280, 2017.

[99] J. Zhu, S. Pang, T. Dittrich, Y. Gao, W. Nie, J. Cui, Chen R, H. An, Fan F and C. Li, *Nano Letters,* vol. 17, pp. 6735-6741, 2017.

[100] K. C. Christoforidis and P. Fornasiero, *ChemCatChem,* vol. 9, pp. 1523-1544, 2017.

[101] E. J. Maginn, *The Journal of Physical Chemistry Lettters,* vol. 1, pp. 3478-3479, 2010.

[102] M. Aresta and A. Dibenedetto, *Dalton Transactions,* pp. 2975-2992, 2007.

[103] "Atmospheric CO2 level for February 2022," [Online]. Available: http://www.co2now.org. [Accessed 2022].

[104] J. P. Smol, *Nature,* vol. 483, pp. S12-S15, 2012.

[105] M. Mikkelsen, M. Jorgensen and F. C. Krebs, *Energy Environment Science,* vol. 3, pp. 43-81, 2010.

[106] N. D. McDaniel and S. Bernhard, *Dalton Transactions,* vol. 39, pp. 10021-10030, 2010.

[107] M. Cokoja, C. Bruckmeier, B. Rieger, W. A. Herrmann and F. E. Kühn, *Angewandte Chemistry International Editions,* vol. 50, pp. 8510-8537, 2011.

[108] K. Huang, C.-L. Sun and Z.-J. Shi, *Chemical Society Reviews,* vol. 40, pp. 2435-2452, 2011.

[109] A. A. Peterson and J. K. Norskov, *The Journal of Physical Chemistry Letters,* vol. 3, pp. 251-258, 2012.

[110] E. E. Benson, C. P. Kubiak, A. J. Sathrum and J. M. Smieja, *Chemical Society Reviews,* vol. 38, pp. 89-99, 2009.

[111] W. Wang, S. Wang, X. Ma and J. Gong, *Chemical Society Reviews,* vol. 40, pp. 3707-3727, 2011.

[112] J. Schneider, H. Jia, J. T. Muckerman and E. Fujita, *Chemical Society Reviews,* vol. 41, pp. 2036-2051, 2012.

[113] J. Agarwal, E. Fujita, H. F. Schaefer and J. T. Muckerman, *Journal of American Chemical Society,* vol. 134, pp. 5180-5186, 2012.

[114] A. J. Morris, G. J. Meyer and E. Fujita, *Accounts of Chemical Research,* vol. 42, pp. 1983-1994, 2009.

[115] H. Takeda, K. Koike, H. Inoue and O. Ishitani, *Journal of American Chemical Society,* vol. 130, pp. 2023-2031, 2008.

[116] B. Gholamkhass, H. Mametsuka, K. Koike, T. Tanabe, M. Furue and O. Ishitani, *Inorganic Chemistry,* vol. 44, pp. 2326-2336, 2005.

[117] M. Halmann, *Nature,* vol. 275, pp. 115-116, 1978.

[118] E. E. Barton, D. M. Rampulla and A. B. Bocarsly, *Journal of American Chemical Society,* vol. 130, pp. 6342-6344, 2008.

[119] T. Arai, S. Sato, K. Uemura, T. Morikawa, T. Kajino and T. Motohiro, *Chemical Communication Journals,* vol. 46, pp. 6944-6946, 2010.

[120] K. J. Young, L. A. Martini, R. L. Milot, R. C. Snoeberger III, V. S. Batista, C. A. Schmuttenmaer, R. H. Crabtree and G. W. Brudvig, *Coordination Chemistry Reviews,* vol. 256, pp. 2503-2520, 2012.

[121] M. Gattrell, N. Gupta and A. Co, *Journal of Electroanalytical Chemistry,* vol. 594, pp. 1-19, 2006.

[122] K. J. P. Schouten, Y. Kwon, C. J. M. van der Ham, Z. Qin and M. T. M. Koper, *Chemical Science Journal,* vol. 2, pp. 1902-1909, 2011.

[123] T. Yui, A. Kan, C. Saitoh, K. Koike, T. Ibusuki and O. Ishitani, *ACS Applied Materials and Interfaces,* vol. 3, pp. 2594-2600, 2011.

[124] D. Connolly, A. Paul, M. Schulz, M. T. Pryce and J. G. Vos, *Inorganic Chemistry,* vol. 51, pp. 1977-1979, 2012.

[125] M. Anpo, H. Yamashita, Y. Ichihashi and S. Ehara, *Journal of Electroanalytical Chemistry,* vol. 396, pp. 21-26, 1995.

[126] N. M. Dimitrijevic, B. K. Vijayan, O. G. Poluektov, T. Rajh, K. A. Gray, H. Y. He and P. Zapol, *Journal of the American Chemical Society,* vol. 133, pp. 3964-3971, 2011.

[127] N. M. Dimitrijevic, I. A. Shkrob, D. J. Gosztola and T. Rajh, *The Journal of Physical Chemistry C,* vol. 116, pp. 878-885, 2012.

[128] I. A. Shkrob, N. M. Dimitrijevic, T. W. Marin, H. He and P. Zapol, *The Journal of Physical Chemistry C,* vol. 116, pp. 9461-9471, 2012.

[129] J. Rasko and F. Solymosi, *The Journal of Physical Chemistry,* vol. 98, pp. 7147-7152, 1994.

[130] N. Ulagappan and H. Frei, *The Journal of Physical Chemistry A,* vol. 104, pp. 7834-7839, 2000.

[131] W. Lin and H. Frei, *Journal of the American Chemical Society,* vol. 127, pp. 1610-1611, 2005.

[132] C. C. Yang, Y. H. Yu, B. van der Linden, J. C. S. Wu and G. Mul, *Journal of the American Chemical Society,* vol. 132, pp. 8398-8406, 2010.

[133] K. Tanaka, K. Miyahara and I. Toyoshima, *Yhe Journal of Physical Chemistry,* vol. 133, pp. 10066-10069, 1984.

[134] M. A. Henderson, *Surface Science Reports,* vol. 66, pp. 185-297, 2011.

[135] A. Fujishima, X. Zhang and D. A. Tryk, *Surface Science Reports,* vol. 99, pp. 461-468, 2010.

[136] S. S. Tan, L. Zou and E. Hu, *Catalysis Today,* vol. 131, pp. 125-129, 2008.

[137] K. Koci, L. Obalova and O. Solcova, *Chemical and Process Engineering,* vol. 31, pp. 395-407, 2010.

[138] J. Lee, D. C. Sorescu and X. Deng, *Journal of the American Chemical Society,* vol. 133, pp. 10066-10069, 2011.

[139] D. M. Adams, L. Brus, C. E. D. Chidsey, S. Creager, C. Creutz, C. R. Kagan, P. V. Kamat, M. Lieberman, S. Lindsay, R. A. Marcus, P. V. Metzger, M. E. Michel-Beyerle, J. R. Miller, M. D. Newton, D. R. Rolison, O. Sankey, K. S. Schanze, J. Yardley and X. Zhu, *The Journal of Physical Chemistry B,* vol. 107, pp. 6668-6697, 2003.

[140] A. Hagfeldt, G. Boschloo, L. Sun, L. Kloo and H. Pettersson, *Chemical Reviews,* vol. 110, pp. 6595-6663, 2010.

[141] D. W. Bahnemann, M. Higendorff and R. Memming, *The Journal of Physical Chemistry B,* vol. 101, pp. 4265-4275, 1997.

[142] D. T. Whipple and P. J. A. Kenis, *The Journal of Physical Chemistry Letter,* vol. 1, pp. 3451-3458, 2010.

[143] A. A. Peterson, F. Abild-Pedersen, F. Studt, J. Rossmeisl and J. K. Norskov, *Energy Environment Science,* vol. 3, pp. 1311-1315, 2010.

[144] J. K. Norskov, J. Rossmeisl, A. Logadottir, L. Lindqvist, J. R. Kitchin, T. Bligaard and H. Jonsson, *The Journal of Physical Chemistry B,* vol. 108, pp. 17886-17892, 2004.

[145] V. Stamenkovic, B. S. Mun, K. J. J. Mayrhofer, P. N. Ross, N. M. Markovic, J. Rossmeisl, J. Greeley and J. K. Norskov, *Angewandte Chemistry International Editions,* vol. 45, p. 2897, 2006.

[146] J. Greeley, I. E. L. Stephens, A. S. Bondarenko, T. P. Johansson, H. A. Hansen, T. F. Jaramilo, J. Rossmeisl, I. Chorkendorff and J. K. Norskov, *Nature Chemistry,* vol. 1, p. 552, 2009.

[147] J. A. Keith, G. Jerkiewicz and T. Jacob, *ChemPhysChem,* vol. 11, p. 2779, 2010.

[148] A. S. Bandarenka, A. S. Varela, M. Karamad, F. Calle-Valejo, L. Bech, F. J. Perez-Alonso, J. Rossmeisl, I. E. L. Stephens and I. Chorkendorff, *Angewandte Chemistry International Editions,* vol. 51, p. 11845, 2012.

[149] A. B. Anderson and T. V. Albu, *Journal of the American Chemical Society,* vol. 121, p. 11855, 1991.

[150] A. Y. Lozovoi and A. Alavi, *Physical Review B,* vol. 68, p. 245416, 2003.

[151] M. Otani and O. Sugino, *Physical Review B,* vol. 73, p. 115407, 2006.

[152] C. D. Taylor, S. A. Wasileski, J.-S. Filhol and M. Neurock, *Physical Review B,* vol. 73, p. 165402, 2006.

[153] E. Skulason, G. S. Karlberg, J. Rossmeisl, T. Bligaard, J. Greeley, H. Jonsson and J. K. Norskov, *Physical Chemistry Chemical Physics,* vol. 9, p. 3241, 2007.

[154] Y.-H. Fang and Z.-P. Liu, *The Journal of Physical Chemistry C,* vol. 113, p. 9765, 2009.

[155] S. Schnur and A. Gross, *Catalysis Today,* vol. 202, p. 87, 2013.

[156] J.-S. Filhol and M.-L. Doublet , *Catalysis Today,* vol. 202, p. 87, 2013.

[157] N. Bonnet, I. Dabo and N. Marzari, *Electrochimica Acta,* vol. 121, p. 210, 2014.

[158] H. He, P. Zapol and L. A. Curtiss, *Energy Environment Science,* vol. 5, pp. 6196-6205, 2012.

[159] V. P. Indrakanti, H. H. Schobert and J. D. Kubicki, *Energy Fuels,* vol. 23, pp. 5247-5256, 2009.

[160] M. Irikura, Y. Tamaki and O. Ishitani, *Chemical Science,* vol. 12, pp. 13888-13896, 2021.

[161] G. Dai and J. Liu, *Journal of Materials Science,* vol. 55, pp. 14301-14314, 2020.

[162] C. Ci, J. J. Carbo, R. Neumann, C. de Graaf and J. M. Poblet, *ACS Catalysis,* vol. 6, pp. 6422-6428, 2016.

[163] H. J. Freund and M. W. Roberts, *Surface Science Reports,* vol. 25, pp. 225-273, 1996.

[164] V. P. Indrakanti, J. D. Kubicki and H. H. Schobert, *Energy Environment Science,* vol. 2, pp. 745-758, 2009.

[165] P. D. Tran, L. H. Wong, J. Barber and J. S. C. Loo, *Energy Environment Science,* vol. 5, pp. 5902-5918, 2012.

[166] K. Tanaka and J. M. White, *The Journal of Physical Chemistry,* vol. 86, pp. 3977-3980, 1982.

[167] H. Kisch, *Angewandte Chemie,* vol. 125, pp. 842-879, 2013.

[168] H. Kisch, *Angewandte Chemie International Editions,* vol. 52, pp. 812-847, 2013.

[169] S. N. Habisreutinger, L. Schmidt-Mende and J. C. Stolarczyk, *Angewandte Chemie International Editions,* vol. 52, pp. 7372-7408, 2013.

[170] M. Subrahmanyam, S. Kaneco and N. Alonso-Vante, *Applied Catalysis B,* vol. 23, pp. 169-174, 1999.

[171] N. Sasirekha, S. J. S. Basha and K. Shanthi, *Applied Catalysis B,* vol. 62, pp. 169-180, 2006.

[172] O. K. Varghese, M. Paulose, T. J. LaTempa and C. A. Grimes, *Nano Letters,* vol. 9, pp. 731-737, 2009.

[173] K. Ikeue, S. Nozaki, M. Ogawa and M. Anpo, *Applied Catalysis B,* vol. 62, pp. 169-180, 2006.

[174] K. Ikeue, H. Yamashita, M. Anpo and T. Takewaki, *The Journal of Physical Chemistry B,* vol. 105, pp. 8350-8355, 2001.

[175] H. Yamashita, Y. Fujii, Y. Ichihashi, S. G. Zhang, K. Ikeue, D. R. Park, K. Koyano, T. Tatsumi and M. Anpo, *Catalysis Today,* vol. 45, pp. 221-227, 1998.

[176] I. A. Shkrob, T. W. Marin, H. He and P. Zapol, *The Journal of Physical Chemistry C,* vol. 116, pp. 9450-9460, 2012.

[177] E. B. Cole, P. S. Lakkaraju, D. M. Rampulla, A. J. Morris, E. Abelev and A. B. Bocarsly, *Journal of the American Chemical Society,* vol. 132, pp. 11539-11551, 2010.

[178] G. R. Dey, A. D. Belapurkar and K. Kishore, *Journal of Photochemistry and Photobiology A,* vol. 163, pp. 503-508, 2004.

[179] G. R. Dey and K. Pushpa, *Research on Chemical Intermediates,* vol. 33, pp. 631-644, 2007.

[180] B. Enright and D. Fitzmaurice, *The Journal of Physical Chemistry,* vol. 100, pp. 1027-1035, 1996.

[181] S. Kaneco, H. Kurimoto, Y. Shimizu, K. Ohta and T. Mizuno, *Energy,* vol. 24, pp. 21-30, 1999.

[182] S. Kaneco, Y. Shimizu, K. Ohta and T. Mizuno, *Journal of Photochemistry and Photobiology A,* vol. 115, pp. 223-226, 1998.

[183] B.-J. Liu, T. Torimoto and H. Yoneyama, *Journal of Photochemistry and Photobiology A,* vol. 113, pp. 93-97, 1998.

[184] D. W. Bahnemann, M. Hilgendroff and R. Memming, *The Journal of Physical Chemistry B,* vol. 101, pp. 4265-4275, 1997.

[185] J. J. Murcia, M. C. Hidalgo, J. A. Navio, V. Vaiano, P. Ciambelli and S. Sannino, *Catalysis Today,* vol. 196, pp. 101-109, 2012.

[186] S. Qin, F. Xin, Y. Liu, X. Yin and W. Ma, *Journal of Colloid and Interface Science,* vol. 356, pp. 257-261, 2011.

[187] G. Kim and W. Choi, *Applied Catalysis B,* vol. 100, pp. 77-83, 2010.

[188] S. Sato, T. Morikawa, S. Saeki, T. Kajino and T. Motohiro, *Angewandte Chemie,* vol. 122, pp. 5227-5231, 2010.

[189] S. Sato, T. Morikawa, S. Saeki, T. Kajino and T. Motohiro, *Angewandte Chemi Internationl Edition,* vol. 49, pp. 5101-5105, 2010.

[190] H. Fujiwara, H. Hosokawa, K. Murakoshi, Y. Wada, S. Yanagida, T. Okada and H. Kobayashi, *The Journal of Physical Chemistry B,* vol. 101, pp. 8270-8278, 1997.

[191] C. A. Craig, L. O. Spreer, J. W. Otvos and M. Calvin, *The Journal of Physical Chemistry,* vol. 94, pp. 7957-7960, 1990.

[192] I. H. Tseng, J. C. S. Wu and H.-Y. Chou, *Journal of Catalysis,* vol. 221, pp. 432-440, 2004.

[193] I. H. Tseng, W.-C. Chang and J. C. S. Wu, *Applied Catalysis B,* vol. 37, pp. 37-48, 2002.

[194] S. Liu, Z. Zhao and Z. Wang, *Photochemical and Photobiological Sciences,* vol. 6, pp. 695-700, 2007.

[195] X. Chen and S. S. Mao, *Chemical Reviews,* vol. 107, pp. 2891-2959, 2007.

[196] G. Rothenberger, D. Fitzmaurice and M. Gratzel, *The Journal of Physical Chemistry,* vol. 96, pp. 5983-5986, 1992.

[197] D. Dung, J. Ramsden and M. Grätzel, *Journal of the American Chemical Society,* vol. 104, pp. 2977-2985, 1982.

[198] T. Inoue, A. Fujishima, S. Konishi and K. Honda, *Nature,* vol. 277, pp. 637-638, 1979.

[199] S. Leytner and J. T. Hupp, *Chemical Physics Letters,* vol. 330, pp. 231-236, 2000.

[200] T. Mizuno, K. Adachi, K. Ohta and A. Saji, *Journal of Photochemistry and Photobiology A,* vol. 98, pp. 87-90, 1996.

[201] K. Koci, L. Obalova, L. Matejova, D. Placha, Z. Lacny, J. Jirkovsky and O. Solcova, *Applied Catalysis B,* vol. 89, pp. 494-502, 2009.

[202] Y. Ku, W.-H. Lee and W.-Y. Wang, *Journal of Molecular Catalysis A,* vol. 212, pp. 191-196, 2004.

[203] K. Hirano, K. Inoue and T. Yatsu, *Journal of Photochemistry and Photobiology A,* vol. 64, pp. 255-258, 1992.

[204] Slamet, H. W. Nasution, E. Purnama, S. Kosela and J. Gunlazuardi, *Catalysis Communications,* vol. 6, pp. 313-319, 2005.

[205] H.-C. Yang, H.-Y. Lin, Y.-S. Chien, J. Wu and H.-H. Wu, *Catalysis Letters,* vol. 131, pp. 381-387, 2009.

[206] A. Kubacka, M. Fernandez-Garcia and G. Colon, *Chemical Reviews,* vol. 112, pp. 1555-1614, 2012.

[207] H. W. Eng, P. W. Barnes, B. M. Auer and P. M. Woodward, *Journal of Solid State Chemistry,* vol. 175, pp. 94-109, 2003.

[208] K. Maeda and K. Domen, *The Journal of Physical Chemistry C,* vol. 111, pp. 7851-7861, 2007.

[209] Y. Inoue, *Energy Environment Science,* vol. 2, pp. 364-386, 2009.

[210] K. Sayama and H. Arakawa, *Journal of Physical Chemistry,* vol. 97, pp. 531-533, 1993.

[211] J. C. Hemminger, R. Carr and G. A. Somorjai, *Chemical Physics Letters,* vol. 57, pp. 100-104, 1978.

[212] M. Ulman, B. Aurian-Blajeni and M. Halmann, *Israel Journal of Chemistry,* vol. 22, pp. 177-179, 1982.

[213] B. R. Eggins, P. K. J. Robertson, E. P. Murphy, E. Woods and J. T. S. Irvine, *Journa of Photochemistry and Photobiology A,* vol. 118, pp. 31-40, 1998.

[214] J. Li and N. Wu, *Catalysis Science & Technology,* vol. 5, p. 1360, 2015.

[215] A. Kudo, K. Omori and H. Kato, *Journal of the American Chemical Society,* vol. 121, pp. 11459-11467, 1999.

[216] A. Walsh, Y. Yan, M. N. Huda, M. M. Al-Jassim and S. H. Wei, *Chemical Materials,* vol. 21, pp. 547-551, 2009.

[217] Y. Liu, B. Huang, Y. Dai, X. Zhang, W. Qin, M. Jiang and M.-H. Whangbo, *Catalysis Communications,* vol. 11, pp. 210-213, 2009.

[218] J. L. Giocondi and G. S. Rohrer, *The Journal of Physical Chemistry B,* vol. 105, pp. 8275-8277, 2001.

[219] P. M. Jones, D. E. Gallardo and S. Dunn, *Chemical Materials,* vol. 20, pp. 5901-5906, 2008.

[220] M. Stock and S. Dunn, *Ferroelectrics,* vol. 419, pp. 9-13, 2011.

[221] D. Meissner, R. Memming and B. Kastening, *The Journal of Physical Chemistry,* vol. 92, pp. 3476-3483, 1988.

[222] M. Kanemoto, K.-i. Ishihara, Y. Wada, T. Sakata, H. Mori and S. Yanagida, *Chemistry Letters,* vol. 21, pp. 835-836, 1992.

[223] H. Kisch and P. Lutz, *Photochemistry and Photobiology Sciences,* vol. 1, pp. 240-245, 2002.

[224] X. Li, J. Chen, H. Li, J. Li, Y. Xu, Y. Liu and J. Zhou, *Journal of Natural Gas Chemistry,* vol. 20, pp. 413-417, 2011.

[225] F. R. F. Fan, P. Leempoel and A. J. Bard, *Journal of Electrochemical Society,* vol. 130, pp. 1866-1875, 1983.

[226] M. Kanemoto, T. Shiragami, C. Pac and S. Yanagida, *The Journal of Physical Chemistry,* vol. 96, pp. 3521-3526, 1992.

[227] P. Johne and H. Kisch, *Journal of Photochemistry and Photobiology A,* vol. 111, pp. 223-228, 1997.

[228] Z. He and W. Que, *Applied Materials Today,* vol. 3, pp. 23-56, 2016.

[229] Y. Jiao, A. M. Hafez, D. Cao, A. Mukhopadhyay, Y. Ma and H. Zhu, *Small,* vol. 14, p. 1800640, 2018.

[230] R. J. Toh, Z. Sofer, J. Luxa, D. Sedmidubsky and M. Pumera, *Chemical Communications,* vol. 53, pp. 3054-3057, 2017.

[231] X. Li and H. Zhu, *Journal of Materials,* vol. 1, pp. 33-44, 2015.

[232] Z. Dai, W. Jin, M. Grady, J. T. Sadowski, J. J. Dadap, R. M. Osgood and K. Pohl, *Surface Science,* vol. 660, pp. 16-21, 2017.

[233] O. Samy, S. Zeng, M. D. Birowosuto and A. El Moutaouakil, *Crystals,* vol. 11, p. 355, 2021.

[234] H. Toulhoat and P. Raybaud, Catalysis by Transition Metal Sulfides. From molecular theory to industria applications, Paris: Technip Editions, 2013.

[235] S. Manzeli, D. Dumcenco, G. Migliato Marega and A. Kis, *Nature Communications,* vol. 10, p. 4831, 2019.

[236] P. Johari and V. B. Shenoy, *ACS Nano,* vol. 6, pp. 5449-5456, 2012.

[237] Y. C. Tsai and Y. Li, *IEEE Transactions on Electron Divices,* vol. 65, pp. 733-738, 2018.

[238] S. N. M. Halim, S. N. F. Zuikafly, M. F. M. Taib and F. Ahmad, in *Proceeding of the 2020 IEEE International Conference on Semiconductor Electronics (ICSE)*, Kuala Lumpur, 2020.

[239] M. Amani, D.-H. Lien, D. Kiriya, J. Xiao, A. Azcati, J. Noh, S. R. Madhvapathy, R. Addou, S. Kc, M. Dubey, K. Cho, R. M. Wallace, S.-C. Lee, J.-H. He, J. W. Ager III, X. Zhang, E. Yablonovitch and A. Javey, *Science,* vol. 35, pp. 1065-1068, 2015.

[240] H. S. Nalwa, *RSC Advanced,* vol. 10, pp. 30529-30602, 2020.

[241] Y. Wang, G. Li, P. Li, J. Hu and Q. Zhao, *Bandaoti Guangdian,* vol. 37, pp. 461-466, 2016.

[242] Y.-J. Yuan, H.-W. Lu, Z.-T. Yu and Z.-G. Zou, *ChemSusChem,* vol. 8, pp. 4113-4127, 2015.

[243] X. Jin, X. Fan, J. Tian, R. Cheng, M. Li and L. Zhang, *RSC Advanced,* vol. 6, pp. 52611-52619, 2016.

[244] Q. H. Wang, K. Kalantar-Zadeh, A. Kis, J. N. Coleman and J. N. Strano, *Nature Nanotechnology,* vol. 7, pp. 699-712, 2012.

[245] H. I. Karunadasa, E. Montalvo, Y. Sun, M. Majda, J. R. Long and C. J. Chang, *Science,* vol. 335, pp. 698-702, 2012.

[246] Q. Ding, B. Song, P. Xu and S. Jin, *Chem ,* vol. 1, pp. 699-726, 2016.

[247] Z. Li, X. Meng and Z. Zhang, *Journal of Photochemistry and Photobiology C,* vol. 35, pp. 39-55, 2018.

[248] K. Chang, M. Li, T. Wang, S. Ouyang, P. Li, L. Liu and J. Ye, *Advanced Energy Materials,* vol. 5, 2015.

[249] N. Singh, G. Jabbour and U. Schwingenschlögl, *The European Physical Journal B,* vol. 85, p. 392, 2012.

[250] M. Marchelek, B. Bajorowicz, P. Mazierski, A. Cybula, T. Klimczuk, M. Winiarski, N. Fijalkowska and A. Zaleska, *Catalysis Today,* vol. 252, pp. 47-53, 2015.

[251] X. Li, Z. Zhang, C. Yao, X. Lu, X. Zhao and C. Ni, *Applied Surface Science,* vol. 364, pp. 589-596, 2016.

[252] R. Prins, Handbook of Heterogeneous Catalysis, Weinheim: Wiley-VCH Verlagsgesellschaft, 1997.

[253] H. Topsoe, B. S. Clausen and F. E. Massoth, Hydrotreating Catalysis - Science and Technoogy, Berlin: Springer-Verlag, 1996.

[254] X. Wang, H. Hong, F. Zhang, Z. Zhuang and Y. Yu, *ACS Sustainable Chemistry & Engineering,* vol. 4, pp. 4055-4063, 2016.

[255] Y. Gao, C. Chen, X. Tan, H. Xu and K. Zhu, *Journal of Coilloid Interface Science,* vol. 476, pp. 62-70, 2016.

[256] W. Zhao, Y. Liu, Z. Wei, S. Yang, H. He and C. Sun, *Applied Catalysis B: Environmental,* vol. 185, pp. 242-252, 2016.

[257] M. Q. Wen, T. Xiong, Z. G. Zang, W. Wei, X. S. Tang and F. Dong, *Optics Express,* vol. 24, pp. 10205-10212, 2016.

[258] T. Xiong, M. Wen, F. Dong, J. Yu, L. Han, B. Lei, Y. Zhang, X. Tang and Z. Zang, *Appied Catalysis B: Environmental,* vol. 199, pp. 87-95, 2016.

[259] J. Gamage and Z. Zhang, *International Journal of Photoenergy,* 2010.

[260] S. Agnihotri, G. Bajaj, S. Mukherji and S. Mukherji, *Nanoscale,* vol. 7, pp. 7415-7429, 2015.

[261] M. J. Hajipour, K. M. Fromm, A. Akbar Ashkarran, D. Jimenez de Aberasturi, I. R. d. Larramendi, T. Rojo, V. Serpooshan, W. J. Parak and M. Mahmoudi, *Trends in Biotechnology,* vol. 30, pp. 499-511, 2012.

[262] S. Sun, Q. An, M. Watanabe, J. Cheng, H. H. Kim, T. Akbay, A. Takagi and T. Ishihara, *Applied Catalysis B: Environmental,* vol. 271, p. 118931, 2020.

[263] F. M. Enujekwu, Y. Zhang, C. I. Ezeh, H. Zhao, M. Xu, E. Besley, M. W. George, N. A. Besley, H. Do and T. Wu, *Applied Surface Science,* vol. 542, p. 148556, 2021.

[264] Z. Lu, Y. Cheng, S. Li, Z. Yang and R. Wu, *Applied Surface Science,* vol. 528, p. 147047, 2020.

[265] X. Liu, Z. Xing, Y. Zhang, Z. Li, X. Wu, S. Tan, X. Yu, Q. Zhu and W. Zhou, *Applied Catalysis B: Environmental,* vol. 201, pp. 119-127, 2017.

[266] X. Li, J. Yu, S. Wageh, A. A. Al-Ghamdi and J. Xie, *Small,* vol. 12, pp. 6640-6696, 2016.

[267] X. Ma, J. Li, C. An, J. Feng, Y. Chi, J. Liu, J. Zhang and Y. Sun, *Nano Research,* vol. 9, pp. 2284-2293, 2016.

[268] Q. Gu, H. Sun, H. Xie, Z. Gao and C. Xue, *Applied Surface Science,* vol. 396, pp. 1808-1815, 2017.

[269] W. Hou and S. B. Cronin, *Advanced Functional Materials,* vol. 23, pp. 1612-1619, 2013.

[270] B. Sheng, J. Liu, Z. Li, M. Wang, K. Zhu, J. Qiu and J. Wang, *Material Letters,* vol. 144, pp. 153-156, 2015.

[271] W. Zhou, Z. Yin, Y. Du, X. Huang, Z. Zeng, Z. Fan, H. Liu, J. Wang and H. Zhang, *Smal,* vol. 9, pp. 140-147, 2013.

[272] M. A. Lukowski, A. S. Daniel, F. Meng, A. Forticaux, L. Li and S. Jin, *Journal of the American Chemical Society,* vol. 135, pp. 10274-10277, 2013.

[273] Y. Yu, S.-Y. Huang, Y. Li, S. N. Steinmann, W. Yang and L. Cao, *Nano Letters,* vol. 14, pp. 553-558, 2014.

[274] L. Wei, Y. Chen, Y. Lin, H. Wu, R. Yuan and Z. Li, *Applied Catalysis B: Environmental,* vol. 144, pp. 521-527, 2014.

[275] F. Niefind, J. Djamil, W. Bensch, B. R. Srinivasan, I. Sinev, W. Grunert, M. Deng, L. Kienle, A. Lotnyk, M. B. Mesch, J. Senker, L. Dura and T. Beweries, *RSC Advances Journal,* vol. 5, pp. 67742-67751, 2015.

[276] J. Kibsgaard, J. V. Lauritsen, E. Laegsgaard, B. S. Clausen, H. Topsoe and F. Besenbacher, *Journal of the American Chemical Society,* vol. 87, p. 196803, 2006.

[277] M. Bollinger, J. Lauritsen, K. W. Jacobsen, J. K. Norskov, S. Helveg and F. Besenbacher, *Physical Review Letters,* vol. 87, p. 196803, 2001.

[278] S. Helveg, J. V. Lauritsen, E. Laegsgaard, I. Stensgaard, J. K. Norskov, B. Clausen, H. Topsoe and F. Basenbacher, *Physica Review Letters,* vol. 84, p. 951, 2000.

[279] K. Chang, X. Hai, H. Pang, H. Zhang, L. Shi, G. Liu, H. Liu, G. Zhao, M. Li and J. Ye, *Advanced Materials,* vol. 28, pp. 10033-10041, 2016.

[280] S. Bai, L. Wang, X. Chen, J. Du and Y. Xiong, *Nano Research,* vol. 8, pp. 175-183, 2015.

[281] X. Meng, Z. Zhang and X. Li, *Journal of Photochemistry & Photobiology C: Photochemistry Reviews,* vol. 24, pp. 83-101, 2015.

[282] Y. Qi, Q. Xu, Y. Wang, C. Chen, G. Jin and X.-Y. Guo, *ACS Nano,* vol. 10, pp. 2903-2909, 2016.

[283] K. Chan, C. Tsai, H. A. Hansen and J. K. Norskov.

[284] X. Hong, K. Chan, C. Tsai and J. K. Norskov, *ACS Catalysis,* vol. DOI: 10.1021/acscatal.6b00619, 2016.

[285] B. Chen, Y. Meng, J. Sha, C. Zhong, W. Hu and N. Zhao, *Nanoscale,* vol. 10, pp. 34-68, 2018.

[286] C. Maheu, E. Puzenat, C. Geantet, L. Cardenas and P. Afanasiev, *International Journal of Hydrogen Energy,* vol. 44, pp. 18038-18049, 2019.

[287] A. Fujishima, X. Zhang and D. A. Tryk, *Surface Science Report,* vol. 63, pp. 515-582, 2008.

[288] A. L. Linsebigler, G. Lu and J. T. Yates Jr, *Chemical Reviews,* vol. 1995, pp. 735-758, 95.

[289] C. G. Morales-Guio, L.-A. Stern and X. Hu, *Chemical Society Review,* vol. 43, pp. 6555-6569, 2014.

[290] B. Baubet, M. Girleanu, A.-S. Gay, A.-L. Taleb, M. Moreaud, F. Wahl, V. Delattre, E. Devers, A. Hugon, O. Ersen, P. Afanasiev and P. Raybaud, *ACS Catalysis,* vol. 6, pp. 1081-1092, 2016.

[291] M. Shen, Z. Yan, L. Yang, P. Du, J. Zhang and B. Xiang, *Chemical Communications,* vol. 50, pp. 15447-15449, 2014.

[292] X. Zhou, M. Licklederer and P. Schmuki, *Electrchemistry Communications,* vol. 73, pp. 33-37, 2016.

[293] M. Lazzeri, A. Vittadini and A. Selloni, *Physical Review B,* vol. 63, p. 155409, 2001.

[294] C. Arrouvel, M. Digne, M. Breysse, H. Toulhoat and P. Raybaud, *Journal of Catalysis,* vol. 222, pp. 152-166, 2004.

[295] Y.-J. Yuan, Z.-J. Ye, H. Lu, B. Hu, Y.-H. Li, D. Chen, J.-S. Zhong, Z.-T. Yu and Z. Zoou, *ACS Catalysis,* 2015.

[296] W. Tu, Y. Li, L. Kuai, Y. Zhou, Q. Xu, H. Li, X. Wang, M. Xiao and Z. Zou, *Nanoscale,* vol. 9, pp. 9065-9070, 2017.

[297] B. L. Abrams and J. P. Wilcoxon, *Critical Reviews in Solid State and Materials Sciences,* vol. 30, pp. 153-182, 2005.

[298] C. Arrouvel , M. Breysse, H. Touhoat and P. Raybaud, *Journal of Catalysis,* no. 232, pp. 161-178, 2005.

[299] D. Costa, C. Arrouvel, M. Breysse, H. Toulhoat and P. Raybaud, *Journal of Catalysis,* vol. 246, pp. 325-343, 2007.

[300] Y. Sakashita, Y. Araki, K. Honna and H. Shimada, *Applied Catalysis A,* vol. 197, pp. 247-253, 2000.

[301] M. Mamatkulov and J.-S. Filhol, *Physical Chemistry Chemical Physics,* vol. 13, p. 7675, 2011.

[302] S. N. Steinmann, C. Michel, R. Schwiedernoch and P. Sautet, *Physical Chemistry Chemical Physics,* vol. 17, pp. 13949-13963, 2015.

[303] M. Cokoja, C. Bruckmeier, B. Rieger, W. A. Herrmann and F. E. Kühn, *Angewandte Chemistry,* vol. 123, pp. 8662-8690, 2011.

[304] G. Rothenberger and D. Fitzmaurice, *The Journal of Physical Chemistry,* vol. 96, pp. 5983-5986, 1992.

[305] M. Shahrokhi, P. Raybaud and T. Le Bahers, *ACS Applied Materials Interfaces*, vol. 13, pp. 36465-36474, 2021.

Chapter III. Methodology

III.1. The density functional theory

The physical properties of a system, composed of light electrons moving around heavy nuclei, is directly related to the behavior of its electronic structure. To describe it precisely in the case of a system with N electrons, the calculation of the related wave function ($\Psi(r_1, r_2, r_3, \dots, r_N)$) is required. The time-independent Schrödinger equation ($H\Psi = E\Psi$) can directly give the wave function associated to a system but exact solution can be obtained only for one-electron based systems such as the hydrogenoid-like ions. For systems containing more than one electron, the electron-electron repulsion leads to a Schrödinger equation impossible to solve analytically. However, several strategies were proposed to bring a numerical solution to the Schrödinger equation based on different nature of approximations. The objective of this section is to show the different approximations that lead to the general formalism widely used in computational chemistry (including my own research work): the Density Functional Theory.

III.1.1.Simplification of the Schrödinger equation

As explained before, the Schrödinger equation is the fundamental equation used to describe a quantum system and to allow the determination of the energies and wave functions associated to this system. For a system composed of N_e electrons with coordinates $\vec{r_i}$, a mass m_e and a charge e, and N_N nuclei with coordinates $\overrightarrow{R_N}$, a mass m_N and an atomic number Z_N, the Schrödinger equation can be written as:

$$H\Psi = E\Psi \qquad \text{(III. 1)}$$

with H the Hamiltonian that can be decomposed in the following way [1]:

$$H = T_e + T_N + V_{ee} + V_{eN} + V_{NN} \qquad \text{(III. 2)}$$

With $T_e = -\frac{\hbar^2}{2m_e}\sum_{i=1}^{N_e} \nabla_i^2$, the kinetic energy of the electrons,

$T_N = -\frac{\hbar^2}{2}\sum_{N=1}^{N_N}\frac{\nabla_N^2}{m_N}$, the kinetic energy of the nuclei,

$V_{ee} = \sum_{i=1}^{N_e}\sum_{j<i}\frac{e^2}{|\vec{r_i}-\vec{r_j}|}$, the potential energy of the electron-electron interaction,

$V_{eN} = -\sum_{i=1}^{N_e}\sum_{N=1}^{N_N}\frac{Z_N e^2}{|\overrightarrow{R_N}-\vec{r_i}|}$, the potential energy of the electron-nucleus interaction,

$V_{NN} = \sum_{N=1}^{N_N}\sum_{N'<N}\frac{Z_N Z_{N'} e^2}{|\overrightarrow{R_N}-\overrightarrow{R_{N'}}|}$, the potential energy of the nucleus-nucleus interaction,

In order to know the energy and the wave function of a system, we need to solve this equation although this is quite impossible, even for a small number of particles, without approximations.

III.1.1.a. The Born Oppenheimer approximation

Due to the fact that the mass of a proton/neutron is 1836 times higher than the one of an electron, it is possible in first approximation to neglect the kinetic energy of the nuclei (composed of protons and neutrons). It is called the adiabatic approximation of Born Oppenheimer [2] in which the electrons instantaneously adapt to the small movements of the nuclei. The wave function can be thus written:

$$\Psi_n\left(\{\vec{r_i}\},\{\overrightarrow{R_N}\}\right) = \Phi_{\overrightarrow{R_N}}\left(\{\vec{r_i}\}, X\{\overrightarrow{R_N}\}\right) \qquad (III.3)$$

with $\Psi_n(\{\vec{r_i}\})$ and $X\{\overrightarrow{R_N}\}$ the electronic wave function and the wave function of the fixed atoms respectively.

The Schrödinger equation $(\mathrm{III}.1)$ can be expressed as it follows:

$$\left\{-\frac{\hbar^2}{2m_e}\left(\sum_{i=1}^{N_e}\nabla_i^2\right)+\sum_{i=1}^{N_e}\sum_{j<i}\frac{e^2}{|\vec{r_i}-\vec{r_j}|}+\sum_{i=1}^{N_e}\sum_{N=1}^{N_N}\frac{Z_N e^2}{|\overrightarrow{R_N}-\vec{r_i}|}+\sum_{N=1}^{N_N}\sum_{N'<N}\frac{Z_N Z_{N'} e^2}{|\overrightarrow{R_N}-\overrightarrow{R_{N'}}|}\right\}\Phi_{\overrightarrow{R_N}}(\{\vec{r_i}\})$$
$$= E_{el}\left(\overrightarrow{R_N}\right)\Phi_{\overrightarrow{R_N}}(\{\vec{r_i}\}) \qquad (III.4)$$

in which $\Phi_{\overrightarrow{R_N}}(\{\vec{r_i}\})$ is an eigenfunction of the Hamiltonian with the eigenvalue $E_{el}(\overrightarrow{R_N})$ for the atoms fixed at the coordinates $\overrightarrow{R_N}$. The equation $(III.4)$ is called the electronic Schrödinger equation.

Another equation describes the motion of the nuclei:

$$-\frac{\hbar^2}{2}\sum_{N=1}^{N_N}\frac{\nabla_N^2}{m_N}+E_{el}\left(\overrightarrow{R_N}\right)X\left(\left\{\overrightarrow{R_N}\right\}\right)=E_{nucl}X\left(\left\{\overrightarrow{R_N}\right\}\right) \qquad (III.5)$$

In which $E_{el}\left(\overrightarrow{R_N}\right)$ is the electronic energy obtained with the equation $(II.4)$ and E_{nucl} is the nuclei energy.

III.1.1.b. Hartree-Fock approximation

Thanks to Born-Oppenheimer approximations, it has been established that the electronic wave function should satisfy the static Schrödinger equation:

$$\left[-\frac{\hbar^2}{2m_e}\left(\sum_{i=1}^{N_e}\nabla_i^2\right)+\sum_{i=1}^{N_e}\sum_{j<i}\frac{e^2}{\left|\vec{r_i}-\vec{r_j}\right|}+\sum_{i=1}^{N_e}\sum_{N=1}^{N_N}\frac{Z_N e^2}{\left|\overrightarrow{R_N}-\vec{r_i}\right|}\right]\Psi_e=E_e\Psi_e \qquad (III.6)$$

that can be solved for systems without electron-electron interaction, in which the Slater determinant describes exactly the wave function:

$$\Psi_e(r_1,r_2,r_3,\dots,r_N)=\frac{1}{\sqrt{N!}}\begin{vmatrix}\Phi_1(r_1) & \Phi_2(r_1) & \dots & \Phi_N(r_1)\\ \Phi_1(r_2) & \Phi_2(r_2) & \dots & \Phi_N(r_2)\\ \vdots & \vdots & \ddots & \vdots\\ \Phi_1(r_N) & \Phi_2(r_N) & \dots & \Phi_N(r_N)\end{vmatrix} \qquad (III.7)$$

In case of electron-electron interaction, Hartree introduced the formulation of an external field in which each electron can move independently. In other words, each electron is considered to be under the influence of the mean-field created by all the other electrons. And the orbitals Φ_i are the solutions of the Hartree-Fock equations:

$$\hat{F}_i \Phi_i(r_i) = E_i \Phi_i(r_i) \qquad (III.8)$$

with $\hat{F}_i$ the Fock operator that take the following expression in the case of molecules:

$$\hat{F}_i = -\frac{\hbar^2}{2m_e}\nabla_i^2 + \hat{V}_{eN}(r_i) + \sum_j \hat{J}_j - \hat{K}_j \qquad (III.9)$$

with $\hat{V}_{eN}$ the electrostatic potential between the electron and the nuclei, $\hat{J}_j$ the coulomb operator that describes the mean potential created by the other electrons and $\hat{K}_j$ the exchange operator, a correction due to the antisymmetry of the wave-function.

$$\hat{J}_j \Phi_i(r_i) = \int \Phi_j^*(r) \frac{1}{|r - r_i|} \Phi_i(r_i) \Phi_j(r) dr \qquad (III.10)$$

$$\hat{K}_j \Phi_i(r_i) = \int \Phi_j^*(r) \frac{1}{|r - r_i|} \Phi_i(r_i) \Phi_j(r_i) dr \qquad (III.11)$$

With these approximations, the individual energy of each electron can be calculated and can be summed in order to obtain the total energy of a system.

III.1.2.The formulation of the density functional theory

The density functional theory aimed to reduce the N-body problem onto a problem with only one body in an effective field that describe all the interactions in the systems. The basic idea is that the properties of a system composed of electrons and nuclei are functional of the electron density. Instead of a wave function Ψ that depends on 3N coordinates of the N electrons, the electron density depends only of 3 coordinates. Electron density and wave function are related as follow:

$$\rho(r) = \int_{r_2} \dots \int_{r_N} \Psi(r_1, r_2, r_3, \dots, r_N) \Psi^*(r_1, r_2, r_3, \dots, r_N) dr_2 \dots dr_N \qquad (III.12)$$

III.1.2.a. Hohenberg-Kohn theorems

The use of electron density for quantic calculation has been described through two theorems, proposed by Hohenberg and Kohn [3]:

Existence theorem

Any observable parameter of a system in its fundamental state is a functional of the electron density. In particular, the electronic energy of a multi electron system in an external potential created by the nuclei can be written:

$$E[\rho(r)] = \int V_{ext}(r)\rho(r)dr + F[\,\rho(r)] \qquad (III.13)$$

with $\rho(r)$ the electronic density and $F[\rho(r)]$ a universal function of ρ that contains the kinetic contribution $T[\rho(r)]$ and the coulomb one $V_{ee}[\rho(r)]$ (independent from the external potential). $\int V_{ext}(r)\rho(r)dr$ represents the nuclei-electron interaction.

The variational principle

The electron density that minimizes the energy of the system is the exact density of the ground state. The electronic energy calculated from an approximated density cannot be lower:

$$E[\rho(r)] = \int V_{ext}(r)\rho(r)dr + F[\rho(r)] \geq E_{exact}[\rho_{exact}(r)] \qquad (III.14)$$

These two theorems show that the electron density of a system can define the Hamiltonian and observable values associated (the electronic energy for example). However, its determination is still impossible, due to the interelectronic interaction term contained in $F[\rho(r)]$.

III.1.2.b. The Kohn-Sham approach

In order to calculate the exact electron density of the ground state and the minimal energy associated, an exact expression of $F[\rho(r)]$ has to be obtained.

$$F[\rho(r)] = T[\rho(r)] + V_{ee}[\rho(r)] \qquad (III.15)$$

with T the kinetic energy of the electrons and V_{ee} interelectronic interaction term, both unknown for systems with electrons interaction. In the Kohn-Sham method [4], they used the following decomposition:

$$T[\rho(r)] = T_S[\rho(r)] + T[\rho(r)] - T_S[\rho(r)] \qquad (III.16)$$

with T_S the kinetic energy of a gas of electrons without interaction with the same electronic density as the system. In can be described with the monoelectronic molecular orbitals:

$$T_S[\rho(r)] = \sum_i f_i \int \Phi_i \left(\frac{1}{2}\nabla^2\right) \Phi_i(r) dr \qquad (III.17)$$

with f_i the occupation number of the orbital so $\rho(r) = \sum_i f_i \int |\Phi_i|^2$.

The second term, $V_{ee}[\rho(r)]$, can be decomposed as follow:

$$V_{ee}[\rho(r)] = E_H[\rho(r)] + V_{ee}[\rho(r)] - E_H[\rho(r)] \qquad (III.18)$$

with E_H the Hartree energy that represents coulomb interaction in the case of a classical charge distribution (that do not take to account the discrete distribution of the electrons):

$$E_H[\rho(r)] = \frac{1}{2} \int \frac{\rho(r)\rho(r')}{|r - r'|} dr \qquad (III.19)$$

Finally, $F[\rho(r)]$ can be written:

$$F[\rho(r)] = T_S[\rho(r)] + E_H[\rho(r)] + E_{xc}[\rho(r)] \qquad (III.20)$$

With

$$E_{xc}[\rho(r)] = V_{ee}[\rho(r)] - E_H[\rho(r)] + T[\rho(r)] - T_S[\rho(r)] \qquad (III.21)$$

By combining all the approximations presented before, Schrödinger equation depending on the position of the N electrons is replaced by a series of N-coupled equations based on the coordinate of single electron:

$$\left(-\frac{1}{2}\nabla^2 + V_{eff}(r)\right)\Phi_i(r) = \varepsilon_i\Phi_i(r) \qquad (III.22)$$

with $V_{eff}(r) = E_{ext}[\rho(r)] + V_H[\rho(r)] + V_{xc}[\rho(r)]$

$\rho(r) = \sum_i f_i \int|\Phi_i(r)|^2$

$V_H[\rho(r)] = \frac{1}{2}\int\frac{\rho(r')}{|r-r'|}dr'$ the Hartree potential

$V_{xc}[\rho(r)] = \frac{\partial E_{xc}[\rho(r)]}{\partial\rho(r)}$ the exchange-correlation potential

To conclude, by replacing the electron density of the system by the electron density of a system without interelectronic interaction, we obtain a method able to calculate the energy of the ground state. It is an exact formulation but the exchange-correlation terms are impossible to calculate due to the electron-electron correlation. Despite the fact that this term is small in comparison to the others (kinetic energy, hartree energy…), it cannot be neglected since it contains the major interactions of the systems.

Some approximations can be used to treat this exchange-correlation term, we will discuss it in the next paragraph.

III.1.3. Approximation of the exchange-correlation term

The E_{xc} functional are most of time expressed in terms of energy density ε_{xc} that depends on the electron density:

$$E_{xc}[\rho(r)] = \int \rho(r)\varepsilon_{xc}[\rho(r)]dr \qquad (III.23)$$

Frequently, this energy is decomposed in terms of exchange and correlation contributions:

$$E_{xc}[\rho(r)] = E_x[\rho(r)] + E_c[\rho(r)] \qquad (III.24)$$

It is the only term that required an approximation in DFT and will determine the precision of the calculation. As described further, the choice of the functional is a crucial parameter that has to be done carefully through preliminary investigations.

III.1.3.a. The Local Density Approximation (LDA)

Proposed for the first time by Kohn and Sham, it is based on the idea of the local substitution of the energy density ε_{xc} of a non-homogeneous system by the one of a gas of electrons with the same density. It consists in replacing the exchange-correlation energy of a non-homogeneous gas of electrons by the exact result obtained in the case of a homogeneous one. In other terms, the gas of electrons non-homogeneous is considered as locally homogeneous (the variations in the density are neglected) and the exchange-correlation terms depend only on local value.

$$E_{XC}^{LDA} = \int \varepsilon_{XC}[\rho(r)]\rho(r)dr \qquad (III.25)$$

with $\varepsilon_{XC}[\rho(r)]$ the exchange-correlation energy by particle for a homogeneous gas of electrons, that can be parametrized for different value of the global electronic density.

III.1.3.b. The Generalized Gradient Approximation (GGA)

In order to account for the spatial variation of the electron density, the GGA approximation proposed to describe the exchange-correlation term through the gradient of the density $\vec{\nabla}\rho(r)$:

$$E_{XC}^{GGA}[\rho(r)] = \int \varepsilon_{XC}\left[\rho(r), \vec{\nabla}\rho(r)\right] dr \qquad (III.26)$$

Different GGA functionals exist and differs from the functional chosen for $\varepsilon_{XC}[\rho(r), \vec{\nabla}\rho(r)]$. One of the GGA functional the most used is the PBE one [5]. This functional has been developed by combination of correct features of LDA with GGA formulation for the terms of high energetic contribution. In addition, some features implemented in PW91 [6], judged as correct but not mandatory, have been removed. Despite that, the PBE functional gives results close to those obtained with PW91 (7.9 % vs 8.0 % of precision in comparison with experimental results) on the structural description of small molecules. Moreover, the simpler form of PBE in comparison with PW91 made it easier to understand and improve onto hybrid functionals.

III.1.3.c. The hybrid functionals

In order to obtain an increased precision in the description of the exchange-correlation term, it has been proposed to mix the exchange correlation from GGA with a certain percentage of the exchange computed with the Hartree-Fock theory (from the wave function strategy). Those functionals could be the key of the success of DFT in molecular chemistry, in particular concerning the description of the electronic structure of the semiconductors. The percentage of the exact Hartree-Fock exchange depends on the functionals and can be fixed or variable.

An example of hybrid with fixed percentage is the PBE0 functional [7] that is composed of 25% of Hartree-Fock exact exchange:

$$E_{XC}^{PBE0} = \frac{3}{4}E_X^{PBE} + \frac{1}{4}E_X^{HF} + E_C^{PBE} \qquad (III.27)$$

On the other hand, some functionals are using a variable Hartree-Fock percentage as a function of the interelectronic distance: the range separated hybrid functionals. It is the case of HSE06 functional [8], that describe the exchange-correlation term as follow:

$$E_{XC}^{HSE} = \alpha E_X^{HF,SR}(\omega) + (1-\alpha)E_X^{\omega PBE,SR}(\omega) + E_X^{\omega PBE,LR}(\omega) + E_C^{PBE} \qquad (III.28)$$

With $E_X^{HF,SR}$ the short range Hartree-Fock exchange, $E_X^{\omega PBE,SR}$ and $E_X^{\omega PBE,LR}$ the short and long range PBE exchange functional, $\omega = 0.11\ a_0^{-1}$ the splitting parameter and $\alpha = {}^1/_4$ the HF mixing constant. The parameters have been fixed to reproduce the bandgap of TiO_2, a frequently investigated semi-conductor.

III.1.3.d. Comparison of some functionals

Since the choice of the functional is a crucial parameter of a study, it is important to have a look on their respective performances before making our choice. We based our choice on some benchmarks [9, 10, 11] from the literature. From Figure III-1, we can compare the performance of CA [12] and WVN [13] LDA functionals, PBE and PW91 GGA functionals, and RPBE [14] and PBEsol [15] functionals, that are functionals based on PBE with the aim to better describe the adsorption energies and the bulk solid lattice respectively. In this study, done on 30 transition metals, the interest of the use of PBE and PW91 GGA's functionals is illustrated with a precision almost three times higher in comparison with LDA's functionals. Concerning RPBE and PBEsol, that planned to improve PBE, they seem to be worse than the basic functionals, which illustrates once again the good compromise of PBE in the atomic description of metallic systems.

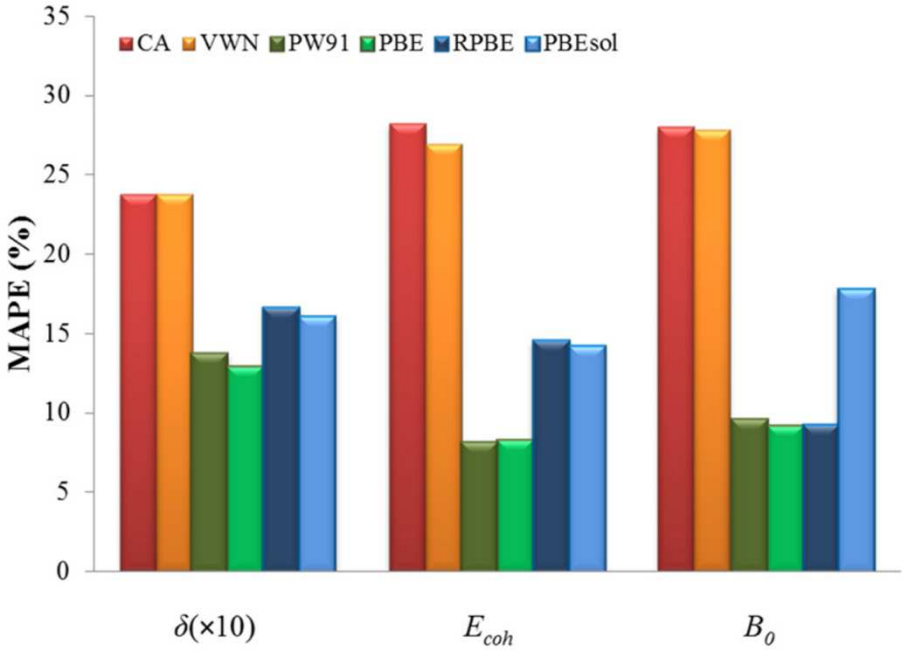

Figure III-1 : Summary of Mean Absolute Percentage Error (MAPE) for the interatomic distances, δ; cohesive energies, Ecoh; and bulk moduli, B0, of the 3d, 4d, and 5d transition metals series excluding metals with particular crystallographic structure: Mn, La, and Hg. MAPE in δ has been multiplied by a factor of 10 for a better visualization.

Since we plan to study semiconductors, it is important to describe precisely either the atomic structures or the electronic structures of the materials, requiring a higher accuracy and the use of hybrid functionals. Other benchmarks [10, 11] illustrates this by comparing PBE, PBE0, HSE03 [16] and HSE06 performances in the description of lattice parameters and bandgaps. It clearly shows the improvement of the semiconductor description by adding a fraction of exact Hartree Fock exchange. These results show a small improvement of the HSE's functional performances in comparison with PBE for the lattice parameter calculations (0.02 Å vs 0.06 Å of mean absolute error). On the other hand, for bandgap calculations, the improvement is not negligible (0.2 eV vs 1.1 eV for mean absolute error), showing that hybrid functional is required to describe precisely the electronic structure of semiconductors. In particular, the use of the range separated hybrid functional HSE06 appears to be the best compromise to describe precisely in the same time enthalpies, ionization potentials, electron affinities, bandgaps and lattice parameters.

Our choice to use PBE and HSE06 functional as a function of the targeted properties is illustrated on this benchmark and will be confirmed further with a benchmark on our own systems.

III.1.3.e. The dispersion correction

DFT provides a poor description of the dispersive-interactions (van der Waals type) because it requires a precise description of electronic correlation, not well described in usual DFT functionals. However, it is important for us to consider these interactions, if we want to study layered materials (such as MoS_2) in physical (van der Waals) interaction with an oxide support (TiO_2) or in case of physical adsorption of reactants on our systems. The correction of these dispersion forces can be added empirically to the total energy through terms in $\frac{1}{r^6}$ and $\frac{1}{r^8}$ with r the distance between the atoms.

In our case, we used the dispersion term as expressed in the DFT-D3-BJ method [17]:

$$E_{disp} = -\frac{1}{2}\sum_{i=1}^{N}\sum_{j=1}^{N} f_{d,6}(r_{ij})\frac{C_{6ij}}{r_{i,j}^{6}} + f_{d,8}(r_{ij})\frac{C_{8ij}}{r_{i,j}^{8}} \qquad (III.29)$$

with C_{6ij} and C_{8ij} the dispersion coefficients that are geometry-dependent and are adjusted on the basis of the local geometry (coordination number) around the atom i and j. It was not the case with previous DFT-D2 method [18].

The notation BJ comes from the use of Becke-Jonson damping , expressed as follow:

$$f_{d,n}(r_{ij}) = \frac{s_n r_{ij}^{n}}{r_{ij}^{n} + \left(a_1 R_{0ij} + a_2\right)^{n}} \qquad (III.30)$$

with $s_6 = 1$, $R_{0ij} = \sqrt{\frac{C_{8ij}}{C_{6ij}}}$ and a_1, a_2 and s_8 adjustable parameters.

III.1.4. The Self Consistent Field

As said in the second Hohenberg-Kohn theorem, the molecular orbitals of the ground state are obtained when the electron density from these orbitals minimize the total energy of the system. To obtain it, an iterative method called the Self Consistent Field (SCF) is used. The idea of this method is to start from an initial set of molecular orbitals ψ^{O} and to solve at each iteration n the Kohn-Sham equations in order to obtain the new molecular orbitals

$\psi^{n-1} \rightarrow \psi^{n}$. The SCF cycles stop when the system respects the convergence criterion fixed (Figure III-2).

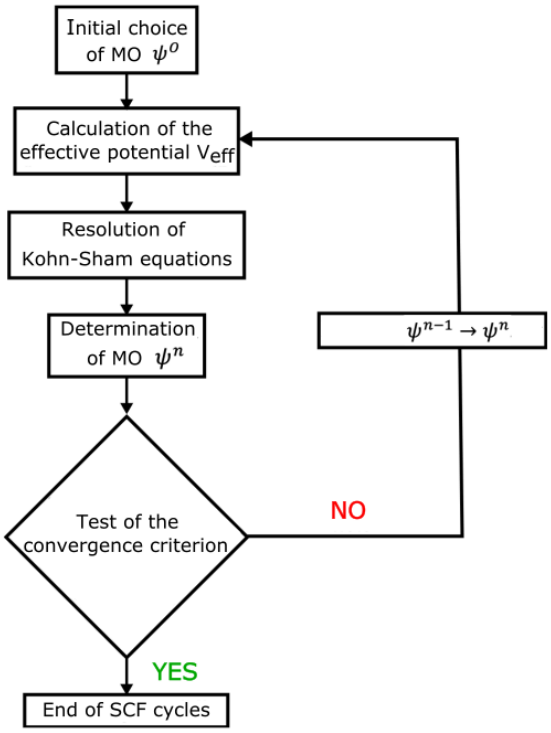

Figure III-2: Principles of the SCF method

III.1.5. DFT in Periodic Boundary Conditions

In order to apply DFT for "infinite" solids that can contains 10^{20} atoms in one cubic millimeter, further mathematical tricks have to be applied. The first one consists in using the symmetry properties and periodicity contained in a crystal and its surfaces. The systems can be represented as a cell, with (a, b, c) lattice parameters, that could be reproduced in the three directions at the infinite, in order to have exactly the same atom, with the same environment at the coordinate (x, y, z) and at the coordinate $(x + n_1 a, y + n_2 b, z + n_3 c)$ with $(n_1, n_2, n_3) \in \mathbb{Z}$. These periodic conditions imply reformulation of the wave function.

III.1.5.a. The Bloch theorem

The periodic conditions of the calculations imply specific solutions for the Schrödinger equation. The Bloch theorem [19] demonstrate that in a tridimensional periodic system the wave function has to be solution of Bloch equation and could be written as follow:

$$\Psi_{ik}(\vec{r}) = u_{ik}(\vec{r}) \qquad (III.31)$$

with $u_{ik}(\vec{r}) = u_{ik}(\vec{r} + \vec{T})$a periodic function, $e^{ik\vec{r}}$ the phase and k the wave vector in the reciprocal space with $k = (k_x, k_y, k_z) \rightarrow \begin{cases} k_x \epsilon \left[-\frac{\pi}{a}; \frac{\pi}{a}\right] \\ k_y \epsilon \left[-\frac{\pi}{b}; \frac{\pi}{b}\right] \\ k_z \epsilon \left[-\frac{\pi}{c}; \frac{\pi}{c}\right] \end{cases}$, that is called the first Brillouin zone.

Since k is a continuous variable, it can take an infinite number of values that will make the calculations impossible. The Brillouin zone has thus to be sampled in a finite number of k points, with an equal repartition along the three directions. The density of the k points mesh is a crucial parameter in the calculation and should be chosen in order to find a good compromise between precision (dense k point mesh) and calculation time (a smaller number of k points). As an example, a large unit cell (a, b, c) in the real space imply a small unit cell in the Brillouin zone $(a^* = \frac{2\pi}{a}, b^* = \frac{2\pi}{b}, c^* = \frac{2\pi}{c})$ and will not require a dense k point mesh in comparison with systems with small unit cell.

III.1.5.b. The basis set

If the wave function is a solution of a Bloch equation and can be expressed as presented in equation (II.29), the Fock operator will also depend on the wave factor:

$$\hat{F}_i \Phi_i(k; r_i) = E_i(k) \Phi_i(k; r_i) \qquad (III.32)$$

And each $\Phi_i(k; r_i)$ crystalline orbital can be expressed as:

$$\Phi_i(k; r_i) = \sum_j c_{j,n}(k) \Psi_j(k; r_i) \qquad (III.33)$$

With $\Psi_j(k; r_i)$ that are bloch functions that will represent our basis set able to describe the entire systems and can take different forms.

It could be a localized basis set, with Bloch functions that are Linear Combination of Atomic Orbitals (CLOA), like in the tight binding theory:

$$\Psi_j(k; r_i) = \frac{1}{\sqrt{N}} \sum_T e^{ikg} \varphi_j(r - r_j - T) \qquad (III.34)$$

That represents a summation of localized functions on all the cells starting from r_j, the coordinates in the 0-cell. The expression of the Atomic Orbitals can take different forms: Slater Type Orbitals (STO), Gaussian Type Orbitals (GTO) or Numerical basis set.

On the other hand, by using a Fourier transformation, the Bloch functions can be expressed as a linear combination of plane waves, that represents our Basis set:

$$\Psi_{ik}(\vec{r}) = u_{ik}(\vec{r}) e^{ik\vec{r}} = e^{ik\vec{r}} \sum_{G=-\infty}^{G=+\infty} C_G e^{iG\vec{r}} \qquad (III.35)$$

with $G = ia^* + jb^* + kc^*$ a vector of the reciprocal space. In order to be computed numerically, a truncation of the sum is required, in order to work with a finite size basis set.

$$\sum_{G=-\infty}^{G=+\infty} C_G e^{iG\vec{r}} \approx \sum_{G=-G_{max}}^{G=G_{max}} C_G e^{iG\vec{r}} \qquad (III.36)$$

Since the coefficients are higher for the plane wave of low energy, they manage to describe the system precisely if the limit energy is well parametrized. This limit energy, so called “cut-off energy”, will determine the size of the plane wave basis set and thus the precision of the energy calculation.

In this thesis, we mainly used plane waves basis set.

III.1.5.c. The pseudo potentials method

In case of plane wave basis set, in order to simplify the calculations, the pseudo-potential method consists in consider the explicit resolution of the valence electrons. The system studied is then composed of valence electrons in the pseudo-potential created by the nucleus and the other electrons. It is justified by the fact that the core orbitals have lower energies, are localized close to the nucleus and will not participate to the chemical bonds. On the other hand, valence orbitales, far from the nucleus, will do the chemical bonds and will contribute to the physical and chemical properties of the system. The core electrons can be then replaced by an external potential that will describe the screening effect of these electrons. It represents an important gain in terms of computational resources. In our calculation, we used augmented wave functions by projector operators thanks to the Projector Augmented Wave method (PAW) [20] . The wave functions of the valence electrons in the core region is replaced by pseudo wave functions, multiplied by a projected function that has to be dual to the pseudo wave function. As illustrated in, outside the core region, the pseudo potential $V^{PS}$and the pseudo wave functions Ψ^{PS} are equal to the real value $V^{PS}$and Ψ^{PS}, calculated by considering all the electrons.

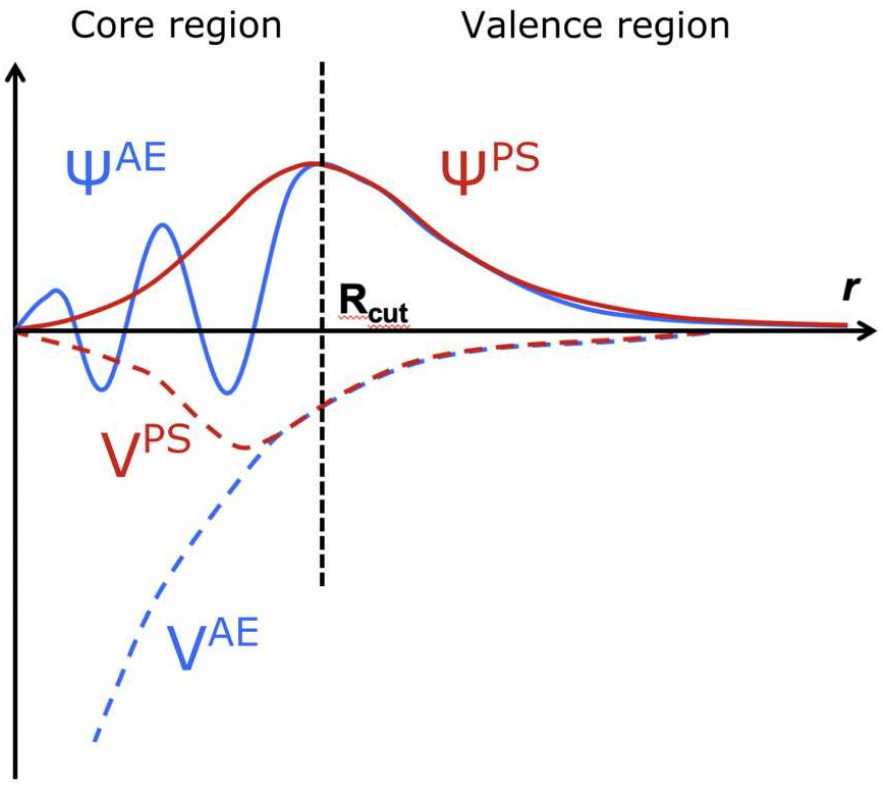

Figure III-3 : Illustration of the pseudisation of the potential and of the wave functions of the valence electrons

III.1.5.d. The implicit solvation model

It is well known that a system in vacuum and a system in a solvent will not have the same properties. If we want to describe precisely our systems, it will be important to consider the possible interactions with solvent. It could be treated as an explicit solvent, with solvent molecules added all around the solvated system which is very time consuming due to the optimization of the geometry and position of all the solvent molecules. Alternatively, it could be treated as implicit solvent in order to capture some effects of solvation through a continuum model. This idea proposed by Tomasi et al. [21] described the solvent as a dielectric medium continuous and polarizable.

Since calculations have been performed with the Vienna Ab-initio Simulation Package (VASP 5.4.1, [22, 23, 24, 25]) able to perform the targeted calculations in periodic boundary conditions, through plane wave basis set, the pure electrostatic interaction between the solvent and the surface can be include in the SCF method thanks to the VASPsol [26] tool that describes the dielectric constant ϵ as a continuous function that verify the Poisson-Boltzmann equation:

$$\nabla.\left[\epsilon\left(n_{solute}(\vec{r})\right)\nabla\Phi(\vec{r})\right] = -4\pi[N_{solute}(\vec{r}) - n_{solute}(\vec{r})] \qquad (III.37)$$

with $\Phi(\vec{r})$ the electrostatic potential, $N_{solute}(\vec{r})$ the effective core charges and $n_{solute}(\vec{r})$ the valence electronic charge density.

This equation is solved in each electronic step in order to obtain the electrostatic potential of the combine ionic and electronic charge density. It takes advantage of the use of plane wave basis set to express $N_{solute}(\vec{r})$ thanks to Gaussians after Fourier transformations:

$$N_{solute}(\vec{r}) = \sum_i \frac{Z_i}{(2\pi\sigma)^{3/2}} \exp\left(\frac{\left(\vec{r} - \overrightarrow{R_i}\right)^2}{2\sigma^2}\right) \qquad (III.38)$$

with σ the width of the Gaussian, R_i and Z_i the position and the charge of the nuclear specie I in the solute. If the width parameter is sufficiently small, the Gaussians do not interfere with solvent and the interaction energy will not depend on the Gaussian width.

III.2. The targeted properties

III.2.1. Bandgap and electronic structure

The bandgap is one of the main properties used to characterize a semiconductor because it directly impacts the first step of the photochemical mechanism: the light absorption. For this reason, we focused our study on the evolution of the bandgap for our systems.

III.2.1.a. Bandgap definitions

There are three different ways to define the bandgap (Figure III-4):

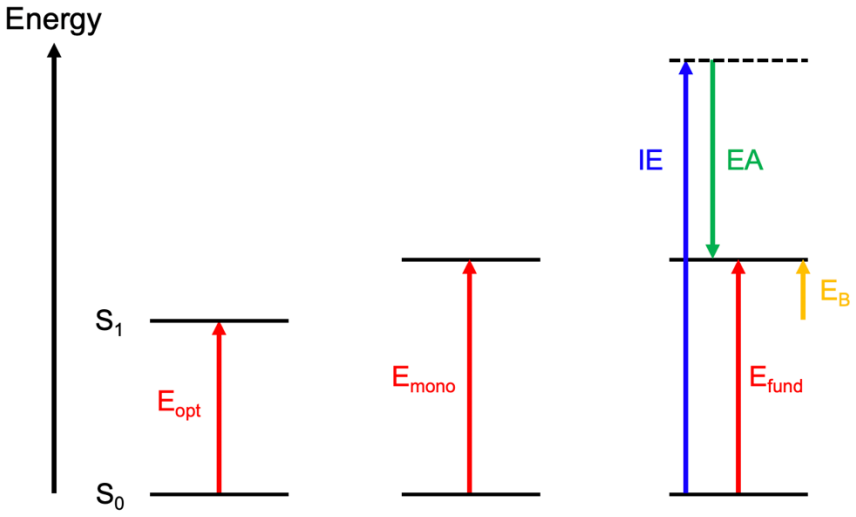

Figure III-4 : Representation of optical gap E_{opt}, the monoelectronic bandgap E_{mono}, the fundamental gap E_{fund}, the ionization energy IE, the electronic affinity EA and the exciton binding energy E_B.

- The monoelectronic bandgap: The energy difference between the HOMO (Highest Occupied Molecular Orbital) and the LUMO (Lowest Unoccupied Molecular Orbital). In the case of semiconductors, it corresponds to the energy difference between the bottom of the conduction band and the top of the valence band.
- The fundamental gap: the difference between the electronic affinity and the first ionization energy ($E_g = IE - EA$). However, the Koopmans theorem assumes that the first ionization potential is equal to the opposite of the HOMO energy ($IE = -\varepsilon_{HOMO}$). It can be also extended to the electronic affinity, that could be described as the opposite of the LUMO energy ($EA = -\varepsilon_{LUMO}$).

- The optical gap: the minimal energy required for an absorbed photon to do an electronic transition. The difference between the optical gap and the fundamental gap is the exciton binding energy E_B. In general, the exciton binding energy is below 100 meV. Thus, the difference between fundamental and optical bandgap can be considered, in general, negligible.

In general, the three definitions can be considered close to each other, if we consider the exciton binding energy negligible. However, in the case of MoS_2, a larger difference could be observed between optical gap and fundamental gap because of non-negligible exciton binding energies (≈ 400 meV). Unfortunately, the determination of the optical gap required the study of excited electronic states, is difficult to do in DFT in periodic boundary conditions. For this reason, we will describe the bandgap as the energy difference between the top of the valence band and the bottom of the conduction band ($E_g = E_{CB} - E_{VB}$), with an overestimation of the bandgap expected for MoS_2.

III.2.1.b. Method used to determine the electronic structure

In a VASP calculation, bands energies are given as a function of an internal reference, different for each calculation. As a consequence, for the drawing of the Density of States (DOS), the origin of the band energies is the Fermi energy (i.e the last occupied state), as represented in Figure III-5.

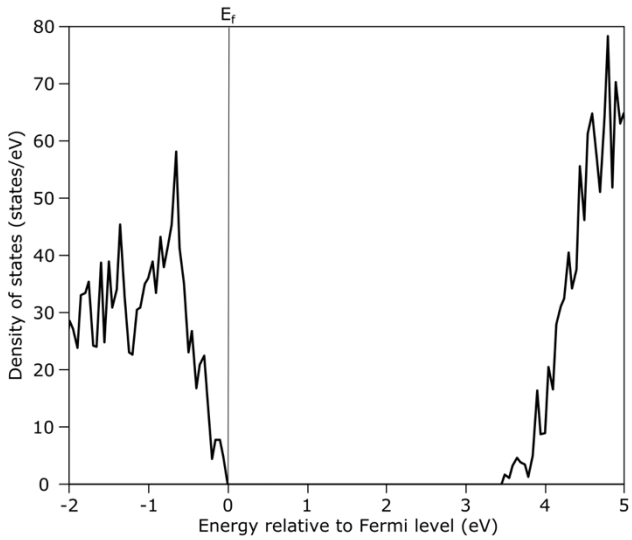

Figure III-5 : Total DOS of TiO_2 anatase (101) with 8 layers, expressed a function of the energy of the Fermi Level. The calculations have been performed with the HSE-06 functional on a 4×4×1 k-points grid and D3-BJ dispersion correction.

In order to be able to compare the results, together and with the literature, we need a common reference for each calculation. The reference chosen is the vacuum potential that could be obtained by plotting the Local potential as a function of Z coordinate (Figure III-6). Since we are working in periodic conditions, each slab is separated in the Z direction by a vacuum layer (15 Å in the presented case). Thus, the vacuum potential is the plateau value, reached for the Z coordinates that corresponds to this vacuum layer.

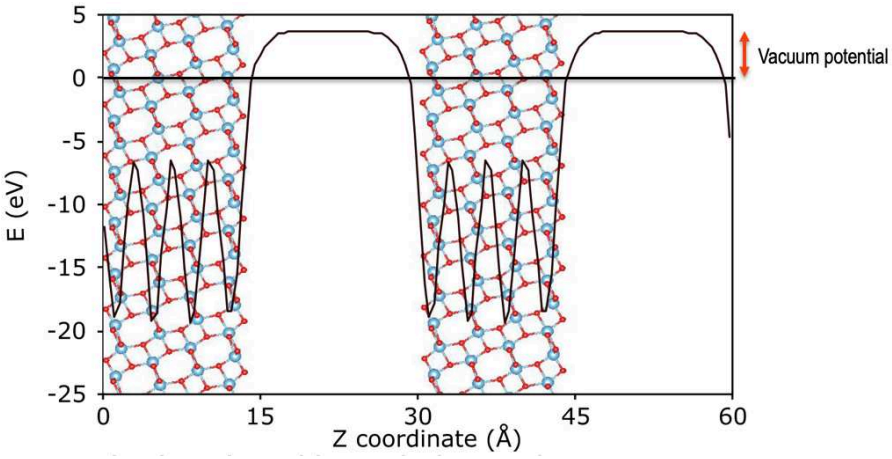

Figure III-6 : Determination of the vacuum potential by plotting the local potential as a function of the Z coordinate.

After obtaining the vacuum level associated to the calculation, all the energies can be then shifted, in order to be expressed as a function of the vacuum level. The DOS can be then replotted with an energy scale expressed as a function to the vacuum level (Figure III-7).

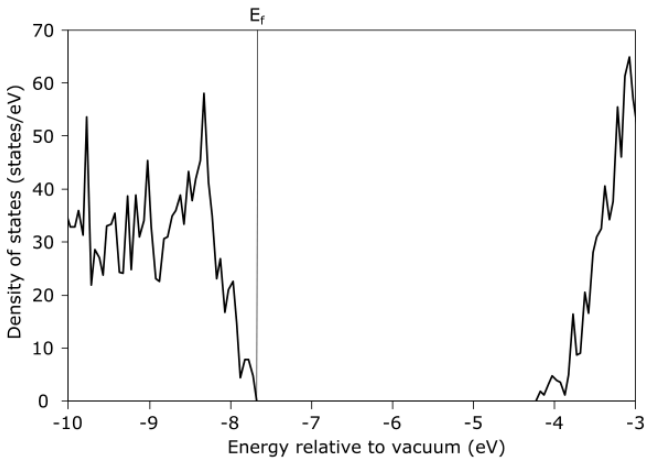

Figure III-7 : Total DOS of TiO_2 anatase (101) with 8 layers, expressed a function of the vacuum level. The calculations have been performed with the HSE-06 functional on a 4×4×1 k-points grid and D3-BJ dispersion correction.

The electronic structure of the plotted material can be obtained by analysis of the Figure III-7 above. The top of the valence band corresponds to the last occupied states (-7.7 eV vs

vacuum), the bottom of the conduction band corresponds to the first unoccupied states (-4.3 eV vs vacuum) and the bandgap is the energy difference between these two values ($E_g = 3.4\ eV$).

Moreover, since VASP is able to get the contribution of each atom to the total DOS of the system, we are able to plot the DOS projected on each type of atoms (Figure III-8), after summing all the contributions of each atoms' type.

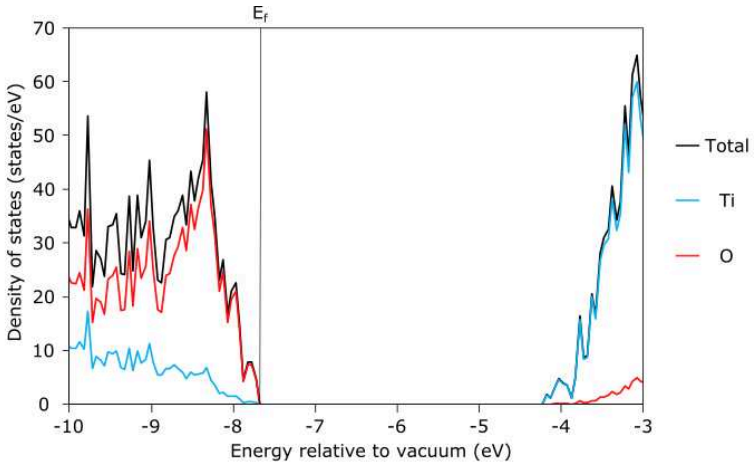

Figure III-8 : DOS with atom decomposition for TiO_2 anatase (101) with 8 layers, expressed a function of the vacuum level. The calculations have been performed with the HSE-06 functional on a 4×4×1 k-points grid and D3-BJ dispersion correction.

This feature gives us the atomic localization of both Conduction Band (mainly on Ti atoms) and Valence Band (mainly on O atoms). Moreover, in case of semiconductors in heterojunctions, as studied in this work, we are able to discuss the contribution and the relative band position of each semiconductor.

III.2.2. The charge transfer within the heterojunction systems

The creation of heterojunctions implies the creation of several chemical and physical interactions between the semiconductors involved. The interface electrons, involved in the interactions, can easily migrate from one semiconductor to the other as a function of the nature of the interaction. As explained in Figure II-4, this electron transfer is expected to create an induced electric field at the interface (Figure III-9), that will have a direct impact on the charge carrier migration after light absorption, and will influence in turn the photocatalytic mechanism.

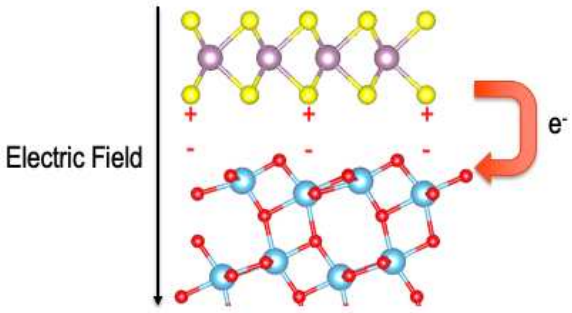

Figure III-9 : Example of electrons transfer possible and Induce Electric Field associated (IEF) for a MoS_2 monolayer in physical interaction with TiO_2 anatase (101).

To study the electron transfer between two semiconductors in interaction (physical or chemical), we proceeded to a Bader charge analysis [27]. It consists in dividing the charge density into volumes: the Bader volumes. Each volume contains a single charge density maximum and is separated from other volumes by surfaces where the charge density is a minimum. In general, there is one Bader volume for each atom with one charge density maximum at each atomic center. The dividing surfaces that are separating the volumes, called zero-flux surfaces, are localized in the bonding region between the atoms. The integration of the electron density in the Bader volume leads to the partial charge associated to the volume. It has been computed thanks a grid-based algorithm [28] that is been shown to be efficient, robust and able to scale linearly with the number of grid points.

This analysis gives us the charge before interaction (MoS_2 alone and TiO_2 alone) and after interaction (MoS_2/TiO_2) in order to be able to determine the direction of the charge transfer, the quantity involved and the direction of the induced electric field.

III.2.3. The photocatalysis mechanism: an electrocatalysis approach

Instead of studying directly the photocatalysis mechanism, that required the very time-consuming Time Dependent DFT method (TD-DFT), we propose to mimic it through an electrocatalytic mechanism. In that case, the first steps of the photochemical mechanism (light absorption, exciton dissociation, charge dissociation) are supposed to be already done, which allows us to work directly with electrons or holes added on the surface of our catalyst represented by the slab model. Given that approximation, our interest resides on the understanding of the CO_2 reduction chemical mechanism, simulating the elementary steps

once charges are already generated. The presence of these charge carriers on the surface impose the presence of an electrochemical potential, that could be treated with two approaches: the Computational Hydrogen Electrode approach [29], where the potential influence is treated with an external correction term, and the surface charging approach [30], where the potential influence is explicitly treated.

III.2.3.a. The Computational Hydrogen method (CHE)

This is the historical method used to describe the electrochemical kinetics of a catalyst. It has been initially developed by Norskov et al. [29] to study the oxygen evolution reaction (OER) on fuel cells. It can be resumed as follow:

- The electronic energy of a neutral slab is only calculated and give the energy at 0 V vs SHE. The calculated energies for the condensed phases can be assimilated to the Gibbs free energy assuming entropy variations during the reaction are negligible. Entropy corrections are considered only for desorbed molecules.
- Each electron transfer is coupled with a proton transfer: no charged intermediates are considered.
- The electrochemical potential applied affects only the electrochemical steps.
- The potential applied can be expressed as a linear term proportional to the number of electrons exchanged with respect to a reference slab:

$$G(U) - G_{ref}(U) = \Delta G(U) = -neU \qquad (III.39)$$

  with G(U) the energy of the system studied, $G_{ref}(U)$ the energy of the reference slab, n the number of electrons exchanged, e the elementary charge and U the potential.
- The proton hydration energy is supposed to be independent from the potential.

As a function of the potential applied, an endothermic step could become thermodynamically favored. It is thus possible to determine the potential at which all the electrochemical steps become favorable.

Since it is not a complicated method that requires only one DFT calculation for each intermediate, it has been mainly used and has obtained interesting results close to

experimental data. However, by treating explicitly the potential, improvement could be expected since it will consider the polarization of the surface due to the chemical reactions.

III.2.3.b. The surface charging approach

The surface charging approach (also called grand canonical DFT method) is aimed at tuning the electrochemical potential, not directly reachable in quantum chemistry, by the explicit modification of the total number of electrons in the system. To do that, we undertake calculation by modifying the number of electrons in the simulation cell (VASP offers this possibility), in order to create the wished charge. However, in periodic DFT calculations, the global system has to have a global neutral charge, in order to avoid problems of Coulomb potential divergence for an infinite charge system. If we want to model a charged surface, we need counterions, that could be explicit or implicit.

The explicit used of counterion, composed of counterions modeled around the system has been rejected because it is time-consuming: increase of the number of atoms, study of many configurations required… On the other hand, the implicit used of counterion consists in the use of a Poisson-Boltzmann charge distribution [31, 32], as implemented in VASPsol. This distribution is localized near to the surface and simulate an excess of counterion that comes from an electrolyte (Figure III-10). In these conditions, the implicit solvent acts as an electrolyte, that will play the role of the counterion. In all the calculations, the default dielectric constant has been used, that corresponds to a water solvent. The effective cavity surface tension has been fixed to zero and the Debye screening length has been fixed to 3Å, that correspond to a concentration of 1M.

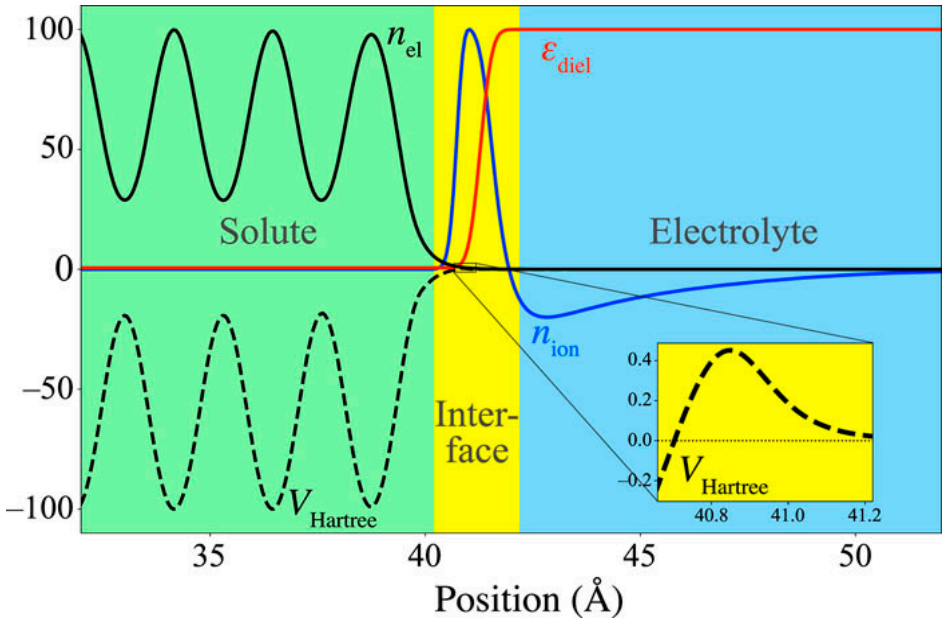

Figure III-10 : Spatial decomposition of the solid/electrolyte system into the solute, interface, and electrolyte regions for an fcc Pt(111) surface embedded in an electrolyte with a relative permittivity of ϵ_r = 78.4 and monovalent cations and anions with a concentration of 1M. The solute is described by density-functional theory, and the electrolyte is described by an implicit solvation model. The interface region is formed self-consistently as a functional of the electronic density of the solute. All properties are shown as a percentage of their maximum absolute value. The inset shows the relatively invisible peak in the Hartree potential at the interface [32].

III.2.3.c. How to link charge, potential and energy?

One of the simplest models to link the potential U of a surface to its charge Q is the capacitance model. In this model, they are linked by the linear relationship: $Q = C\ (U - U_0)$ with U_0, the potential of the neutral surface and C, the capacitance of the system. The capacitance C is not an external constant and is determined for each system. The Gibbs free energy of the surface can be then determined:

$$G(U) = E(U) - Q(U)FU \approx E(U_o) - \frac{1}{2}C(U - U_0)^2 \qquad (III.40)$$

with $E(U_0)$ the energy of the neutral surface [30]. This model and the quadratic response associated has been observed in many cases of metal/electrolyte interfaces [30, 33, 34, 35] (Figure III-11 a). In the example illustrated, the surface charging method manage to show a change in the configuration of a water molecule as a function of the potential on a H2O/Pd(111) system. This inversion cannot be shown with the CHE method in which the geometry does not change with the variation of the potential. In the case of a

semiconductor/electrolyte interface (Figure III-11 b) [36, 37, 38], the behavior is different with two quadratic responses, one on the oxidation side (the high potentials) and the other on the reduction side (the low potentials), separated by a plateau that corresponds to the bandgap of the semiconductor.

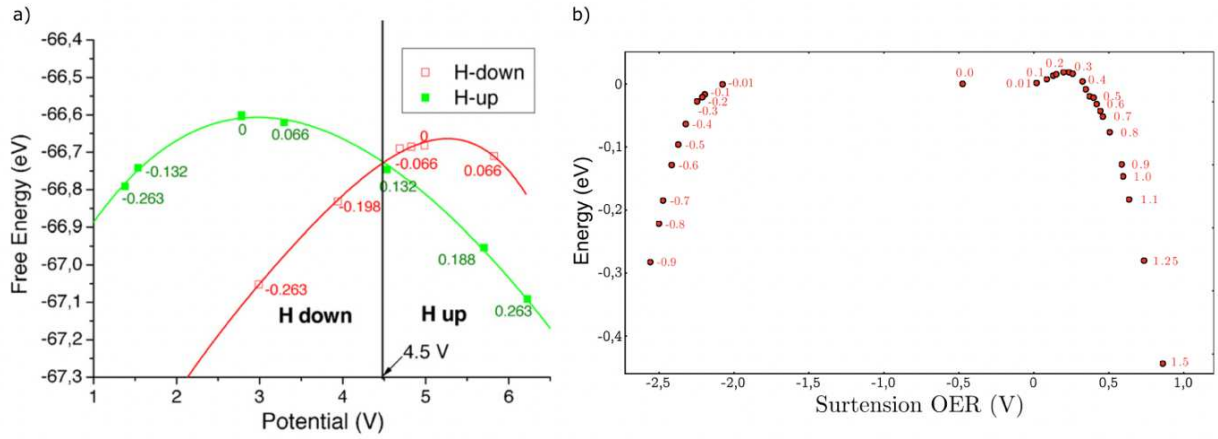

Figure III-11 : Example of the quadratic response between the potential and the energy. Each point corresponds to results obtained at different charges and the curves are interpolation curves. Example a) corresponds to the comparison of two configuration of a water molecule on a H_2O/Pd(111) system [33] while example (b) illustrates the evolution of surface energy of a CoOOH semiconductor as a function of the potential [38].

III.2.3.d. Work at constant charge or at constant potential ?

The surface charging approach allows us to study our systems with different charges (and as a consequence different electrochemical potential applied). It is thus possible to do two different comparisons of the systems:

- Constant charge approach: comparison of systems with the same global charge

- Constant potential approach: comparison of systems with the same potential, imposed for example by a potensiostat. The global charge will be different as a function of the systems.

In our case, we worked with a constant potential, that will be in real systems imposed by the photo-induced charge carriers. Since we cannot directly impose the electrochemical potential ourselves, an interpolation curved is created, based on the calculations done at different charges.

As illustrated in Figure III-12 for a MoS_2 slab, after 11 geometry optimizations for different charges varying from -1 *e* to +1 *e* by step of 0.2 e, an interpolation curved can be plotted in order to link the Gibbs free energy of our systems and the electrochemical potential applied on it. As expected, we have obtained interpolation curves that fit with the calculated points by considering a quadratic dependence between the potential and the Gibbs free energy. Although MoS_2 is a semiconductor, the curve obtained is similar to those obtained on metallic system (Figure III-11 a). This is due to the fact that we consider a finite monolayer, with only 5 Mo rows, that imply a high contribution of the edge states, expected to reduce the bandgap.

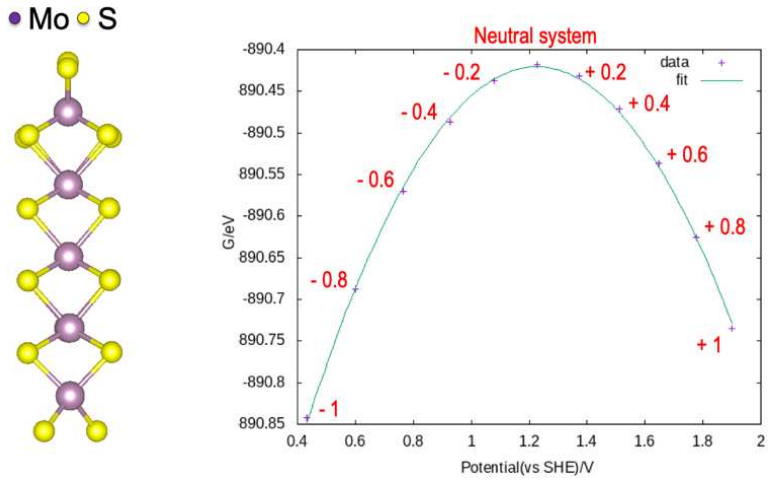

Figure III-12 : Example of G = f(U) interpolation curve for a MoS_2 nanosheet with 50%S on each edge. Calculations have been performed with PBE functional on a 3x3x1 K-Points grid with D3-BJ dispersion correction.

This method has been used on this thesis to study the mechanism of electroreduction of CO_2 on MoS_2 edges. By applying the same method on each reactional intermediate, we have been able to discuss the relative stability of each intermediate as a function of the potential and to determine possible reaction pathways as a function of the applied potential.

III.3. References

[1] P. M. W. Gill, «Density Functionall Theory (DFT), Hartree-Fock (HF) and the Self-consistent Field,» Cambridge, University of Cambridge, 1994, pp. 678-689.

[2] M. Born and R. Oppenheimer, *Annealen der Physik,* vol. 389, p. 457, 1927.

[3] P. Hohenberg and W. Kohn, *Physical Review,* vol. 136, p. 864, 1964.

[4] W. Kohn and L. J. Sham, *Physical Review,* vol. 140, p. 1133, 1965.

[5] J. P. Perdrew, K. Burke and M. Ernzerhof, *Physica Review Letters,* vol. 77, pp. 3865-3868, 1996.

[6] J. P. Perdrew, in *Electronic Structure of Solids '91*, Berlin, Akademie Verlag, 1991, p. 11.

[7] J. P. Perdrew, M. Ernzerhof and K. Burke, *Journal of Chemical Physics,* vol. 105, pp. 9982-9985, 1995.

[8] J. Heyd and G. E. Scuseria, *Journal of Chemical Physics,* vol. 121, pp. 1187-1192, 2004.

[9] P. Janthon, S. M. Kozlov, J. Vines, J. Limtrakul and F. Illas, *Journal of Chemical Theory and Computation,* vol. 9, pp. 1631-1640, 2013.

[10] A. V. Krukau, O. A. Vydrov, A. F. Izmaylov and G. E. Scuseria, *Journal of Chemical Physics,* vol. 125, p. 224106, 2006.

[11] J. Paier, M. Marsman, K. Hummer and G. Kresse, *The Journal of Chemical Physics,* vol. 124, p. 154709, 2006.

[12] D. M. Ceperley and B. J. Alder, *Physical Review Letters,* vol. 45, pp. 566-569, 1980.

[13] S. H. Vosko, L. Wilk and M. Nusair, *Canadian Journal of Physics,* vol. 58, pp. 1200-1211, 1980.

[14] B. Hamerm, L. B. Hansen and J. K. Norskov, *Journal of Physical Review B,* vol. 59, pp. 7413-7421, 1999.

[15] J. P. Perdrew, A. Ruzsinszky, G. I. Csonka, O. A. Vydrov, G. E. Scuseria, L. A. Constantin, X. Zhou and K. Burke, *Physical Review Letters,* vol. 10, p. 136406, 2008.

[16] J. Heyd, G. E. Scuseria and M. Ernzerhof, *Journal of Chemical Physics,* vol. 118, p. 8207, 2003.

[17] S. Grimme, S. Ehrlicg and L. Gorigk, *Journal of Computational Chemistry,* vol. 32, p. 1456, 2011.

[18] S. Grimme, S. Ehrlicg and L. Gorigk, *Journal of Computational Chemistry,* vol. 27, p. 1787, 2006.

[19] F. Bloch, *Zetschrift für Physik,* vol. 52, pp. 555-600, 1929.

[20] P. E. Blöchl, *Physical Review B,* vol. 50, p. 17953, 1994.

[21] J. Tomasi and M. Persico, *Chemical Review,* vol. 94, pp. 2027-2094, 1994.

[22] "Vasp," [Online]. Available: http://cms.mpi.univie.ac.at/vasp/vasp/vasp.html. [Accessed March 2022].

[23] G. Kresse and J. Hafner, *Physical Review B,* vol. 47, p. 558, 1993.

[24] G. Kresse and J. Furthmüller, *Computational Material Science,* vol. 66, pp. 15-50, 1996.

[25] G. Kresse and J. Furthmüller, *Physical Review B,* vol. 54, pp. 11169-11186, 1996.

[26] K. Mathew, R. Sundararaman, K. Letchworth-Weaver, T. A. Arias and R. G. Hennig, *Journal of Chemica Physics,* vol. 140, p. 084106, 2014.

[27] R. F. W. Bader, Atoms in Molecules: A Quantum Theory, Oxford: Oxford University Press, 1990.

[28] W. Tang, E. Sanville and G. Henkelman, *Journal of Physics Condensed Matter,* vol. 21, p. 084204, 2009.

[29] J. K. Norskov, J. Rossmeisl, A. Logadottir, L. Lindqvist, J. R. Kitchin, T. Bligaard and H. Jonsson, *Journal of Physical Chemistry B,* vol. 108, pp. 17886-17892, 2004.

[30] S. N. Steinmann, C. Michel, R. Schwiedernoch and P. Sautet, *Physical Chemistry Chemical Physics,* vol. 17, p. 13949, 2015.

[31] [Online]. Available: https://github.com/henniggroup/VASPsol.

[32] K. Mathew, V. S. C. Kolluru, S. Mula, S. N. Steinmann and R. G. Hennig, *Journal of Chemical Physics,* vol. 151, p. 234101, 2019.

[33] J.-S. Filhol and M. L. Doublet, *Catalysis Today,* vol. 202, pp. 87-97, 2013.

[34] C. D. Taylor, S. A. Wasileski, J. S. Filhol and M. Neurock, *Physical Review B,* vol. 73, pp. 1-16, 2006.

[35] N. Lespes and J.-S. Filhol, *Surface Science,* vol. 631, pp. 8-16, 2015.

[36] Y. Huang, R. J. Nielsen and W. A. Goddard, *Journal of the American Chemical Society,* vol. 140, pp. 16773-16782, 2018.

[37] E. Watanabe, H. Ushiyama and K. Yamashita, *ACS Applied Materials Interface,* vol. 9, pp. 9559-9566, 2017.

[38] A. Crutchet, P. Colinet, P. Michel, S. N. Steinmann and T. Le Bahers, *Physical Chemistry Chemical Physics,* vol. 22, pp. 7031-7038, 2020.

Chapter IV. Evolution of the electronic structures of the MoS_2/TiO_2 (anatase) heterojunction

As discussed in II.3.2.c, the use of the promising 2D MoS_2 material in combination with the efficient TiO_2 anatase may help to tackle the numerous challenges of the CO_2 photoreduction. With the aim to provide some rational guidelines towards the materials' nanostructuration of the TiO_2/MoS_2 interface, we propose in the present work to explore the evolution of the band gap and conduction band (CB)/valence band (VB) positions of various 1D- or 2D-MoS_2/TiO_2-anatase heterojunctions by using state of the art periodic density functional theory (DFT) calculations. We will focus on the two most abundant surface orientations of anatase particles ((101) and (001)). The contribution of the (001) surface orientation, neglected for its minor presence on anatase particles in vacuum conditions [1], could become more predominant under aqueous environment [2] encountered in reactions involving water as a reactant (such as water splitting). Hence, it will be also considered carefully in this work. In addition, beyond the physical van der Waals interaction, the chemical epitaxy-like interaction which has been reported in the literature [3, 4, 5] (Figure IV-1) will be also investigated. Moreover, the influence of key physico-chemical parameters of the interface on the CB/VB positions will be studied: sulfidation and hydration states, orientation of the MoS_2 monolayer, size of MoS_2 monolayers.

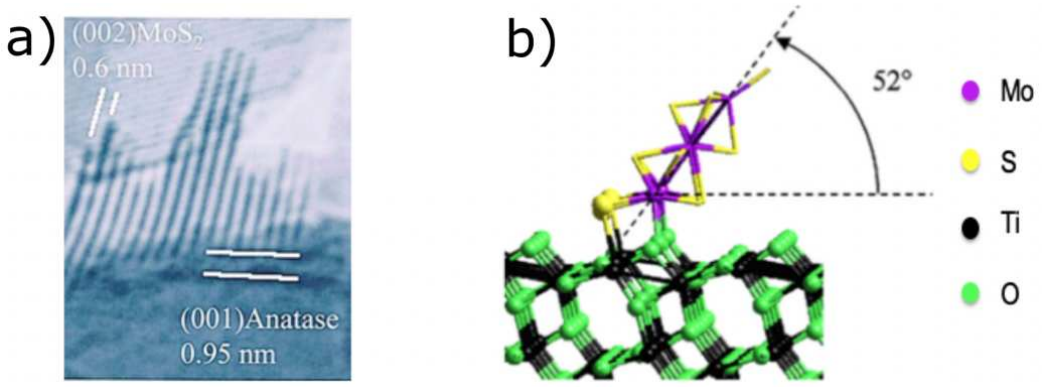

Figure IV-1: Example of epitaxial relationship between MoS_2 and TiO_2: a) High-Resolution Episcopic Microscopy (HREM) images of (002) MoS2 in epitaxial interaction with TiO_2 anatase (001) [5] and b) structure of a Mo6S14 in epitaxial interaction on TiO_2 anatase (101) obtained with DFT calculation [3].

The objective of this study is thus to provide a general view on the evolution of the band positions and the possible charge carrier pathway after the heterojunction as a function of

physico-chemical parameters accessible experimentally. The feasibility of a Z-scheme mechanism, different from the classical type II mechanism presented in the actual work on MoS_2/TiO_2, will also be discussed (Figure IV-2).

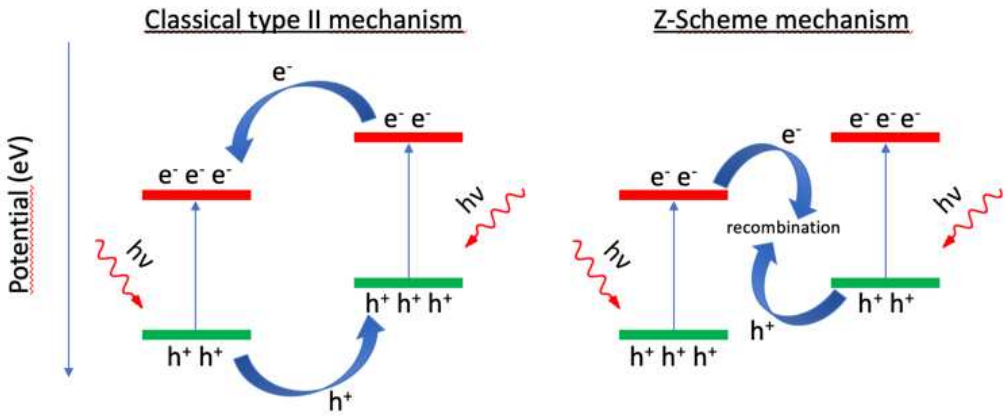

Figure IV-2: Comparison of the classical type II mechanism and the Z-scheme mechanism of the type-II heterojunction.

IV.1. Method

All the DFT calculations were periodic calculations performed using Vienna Ab Initio Simulation Package (VASP) code [6, 7]. In order to obtain a good precision for the study of the MoS_2/TiO_2 heterostructures, further preliminary investigations have been done. After exposing these preliminary results, all the computational details chosen for the heterojunction study will be summarized.

IV.1.1. Choice of the functional

The choice of the functional is a primordial preliminary step before starting a study. As explained in III.1.3.d, based on results obtained on benchmarks, two functionals have attracted our attention: PBE (a GGA functional, frequently used in solid-state chemistry and performing relatively fast calculations but that usually underestimate the bandgap [8]) and HSE-06 (a range separated hybrid functional, performing more time-consuming calculations but that usually gives more reliable bandgap [9]). The comparison has been done on the geometry optimization of the bulk material of our two main semiconductors, MoS_2 and TiO_2 anatase. Three properties have been considered to assess the functionals, the precision on the lattice parameter, the precision on the bandgap and the calculation time. The results obtained with and without D3-BJ dispersion correction [10] will also be compared and a

12x12x12 K-points mesh has been used for all calculations. The results obtained are summarized in Table IV-1.

MoS_2 Bulk						
Functional	**a = b (Å)**	**% error**	**c (Å)**	**% error**	**Bandgap (eV)**	**% error**
Experiments	3.16 [11]	/	12.30 [11]	/	~1.5*	/
PBE (no disp)	3.18	0.7	14.01	13.9	1.39	7.3
PBE (D3-BJ)	3.15	0.4	12.08	1.8	0.80	46.7
HSE-06 (no disp)	3.15	0.4	14.25	15.8	2.15	43.3
HSE-06 (D3-BJ)	3.12	1.4	12.04	2.1	1.39	7.3

TiO_2 anatase Bulk				
Functional	**a = b = c (Å)**	**% error**	**Bandgap (eV)**	**% error**
Experiments	5.46 [12]	/	3.20 [13]	/
PBE (no disp)	5.56	1.8	1.90	40.7
PBE (D3-BJ)	5.50	0.8	1.88	41.2
HSE-06 (no disp)	5.49	0.7	3.39	5.9
HSE-06 (D3-BJ)	5.45	0.2	3.38	5.7

*Table IV-1: Comparison of the performance of PBE and HSE-06 functionals for the geometry optimization of MoS_2 and TiO_2 bulk. *estimated from STS measurement of a 3-monolayer bandgap of MoS_2 [14, 15] and DFT estimation of the bandgap reduction from 3-monolayer to bulk MoS_2 [16]. See section III.2.1.a for more informations.*

The addition of the dispersion correction appears to be crucial to obtain a good description of MoS_2 for both structural parameters (in particular concerning the c coordinate) and the bandgap. This is due to the fact that MoS_2 is a 2D materials, with stacked layers along the c axis, with Van der Waals interactions between the layers. It is necessary to get a good description of the layer-layer interaction to obtain good precision on the bandgap. Since now, we will only discuss the results obtained with dispersion correction.

The lattice parameters calculated with the two functionals are almost equal: PBE being more precise on MoS_2 and HSE-06 on TiO_2, with a small percentage of error in all the cases (2.1% in the worst case but for the inter-layer direction that is acceptable). Concerning the bandgap, we observed the expected large underestimation of the PBE functional and the expected slight overestimation of the HSE-06 functional. However, the HSE-06 provides bandgap values closer to the experimental ones. Unfortunately, the calculation time increased considerably with the use of the HSE-06 functional (200-300 times higher than with PBE). To solve this problem, we used a strategy that consists in doing geometry optimization with PBE (D3-BJ) and then a single point calculation (only the PBE optimized geometry) with HSE-06 functional, that will describe better the electronic structures of the systems. Under these conditions, we managed to obtain precise results in the description of TiO_2 and MoS_2 bandgaps (1.38 eV with 12.2% error for

MoS_2 and 3.26 eV with 2% error for TiO_2), equivalent to those obtained with pure HSE-06 calculations.

IV.1.2. The TiO_2 structures

In order to describe with precision MoS_2/TiO_2 heterostructures, it appears to be crucial to be able to describe with precision the TiO_2 surfaces, that will be the support in the heterojunctions. The following parts will expose the choice of the different parameters in case of the two surfaces chosen, the (001) and the (101).

IV.1.2.a. The number of layers

When we build a surface from the bulk, after choosing the surface orientation targeted, we have the possibility to choose the number of layers modelled representing the surface thickness. As always, the idea is to find a good compromise between precision (large surface thickness) and calculation time (small surface thickness). The results obtained are summarized in Figure IV-3.

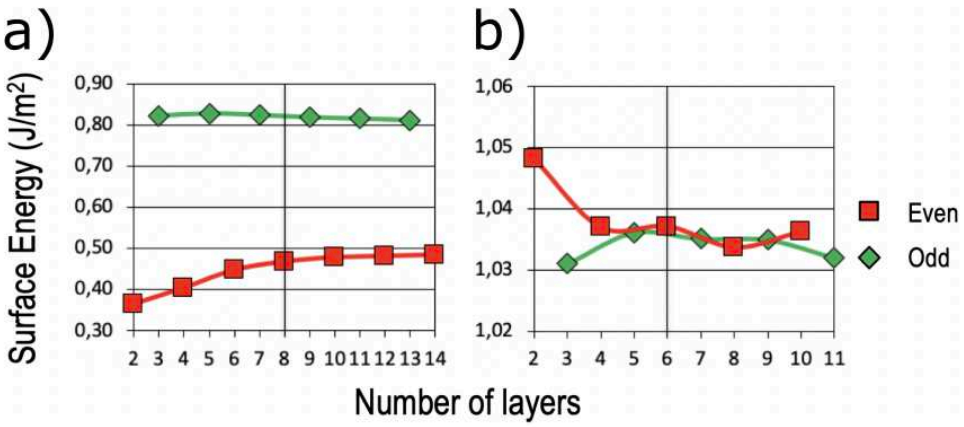

Figure IV-3: Evolution of the surface energy as a function of the number of layers for a) TiO_2 anatase (101) and b) TiO_2 anatase (001).

On each surface, we have separated the results obtained with an even and an odd number of layers. While this separation is not relevant on the (001) surface, it has a strong effect on the (101) surface orientation with a strong stabilization of the surfaces with an even number of TiO_2 layers. This is probably due to a broken symmetry of the system in case of an even number of layers associated giving rise to a dipole moment that strongly increase the surface energy. For the following calculations, we have chosen to work with 8 TiO_2 layers in case of the (101)

surface orientation and 6 TiO_2 layers for the (001) one. The number of layers chosen and the surface energies associated are in good agreement with other theoretical works [1].

IV.1.2.b. The hydration state

Given that the reactions targeted, the presence of water appears to be impossible to avoid since it can be a solvent, a reactant or a by-product in the same time. In order to study the influence of water on the electronic structure of our system, water has been considered under two hypotheses: First, water treated as implicit water solvent in the calculation; Then water treated both as an implicit solvent and explicitly by adding water molecules adsorbed on the surface. The hydrated surface structures have been modelled based on previous thermodynamical studies [2] and are presented on Figure IV-4.

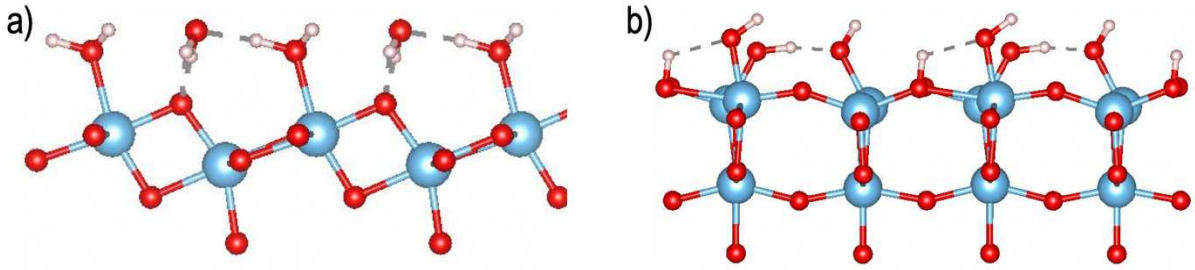

Figure IV-4: Water adsorption structures on a) TiO_2 anatase (101) with θ=10.1 H_2O/nm^2 and b) TiO_2 anatase (001) with θ= 3.5 H_2O/nm^2.

On the (101) surface orientation, a high coverage (θ = 10.1 H_2O/nm^2) is required to observed stable hydration of the surface with non-dissociative water molecules adsorbed in physical or chemical mode. Either in the case of chemisorption, the Ti-O distance (2.17 Å) seems to indicate a week adsorption. On the (001) surface orientation, a lower coverage is assumed (θ = 3.5 H_2O/nm^2) with dissociative adsorption only, that seems to stabilized the surface composed only of Ti atoms coordinated 5 times (Ti tend to be coordinated 6 times). The electronic structure associated to the two surfaces in the three conditions (bare surface, bare surface + implicit water solvent and hydrated surface + implicit water solvent) is presented in Figure IV-5.

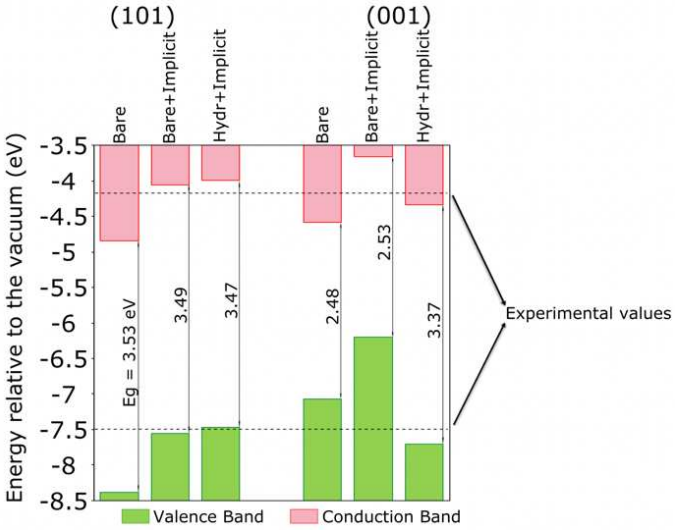

Figure IV-5: Evolution of the band position of TiO_2 anatase (101) and (001) with implicit and/or explicit water solvation. Experimental values are taken from Grätzel study [17].

On the (101) surface, adding implicit solvent in the calculation induces a shift in higher energy of both conduction and valence bands. While the band edges were far from the experimental values in the case of the bare surface, the implicit solvent brings them very close to the reference values. In case of the explicitly hydrated surface, due to the weak interactions between the water molecules and the surface, no significative changes are observed. On this surface, the use of implicit helps to have a good description of the opto-electronic properties of the materials while the weak water adsorption is not required.

On the (001) surface, a shift induced by the implicit solvent is also observed. In addition, the dissociative adsorption of water molecules on the surface leads to an increase of the bandgap by saturating the Ti ions. By combining both effects, we managed to obtain band edges close to the experimental values.

For the following results, implicit water solvent will be considered in all the calculations, with a bare surface for the (101) and a hydrated one for the (001) (Figure IV-6).

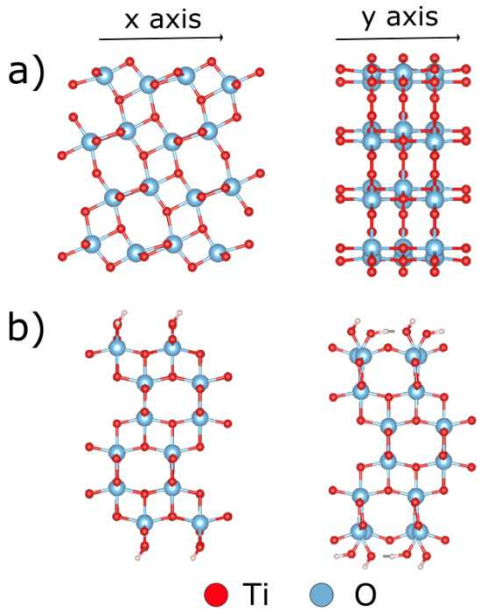

Figure IV-6: Slab supercell of a) TiO_2 anatase (101) and b) TiO_2 anatase (001) hydrated.

IV.1.2.c. The lattice parameters describing the TiO_2/MoS_2 interface

For building the TiO_2/MoS_2 interface, we will assume that TiO_2 is the support of the heterojunction. We thus decided to keep TiO_2 cell parameters and used a supercell approach to adapt MoS_2 and TiO_2 structures. In the case of the (101) surface, the best results have been obtained with a (4x1x1) TiO_2 anatase and a (5x2x1) 2D MoS_2. It represents a 2.12% dilatation on the x axis and 4.26% on the y axis for MoS_2. Concerning the (001) surface, the best results have been obtained with a (2x2x1) TiO_2 anatase and a (5x3x1) 2D MoS_2. It represents a 2.57% dilatation on the x axis and 6.60% on the y axis for MoS_2. The structures before and after expansion are represented in Figure IV-7.

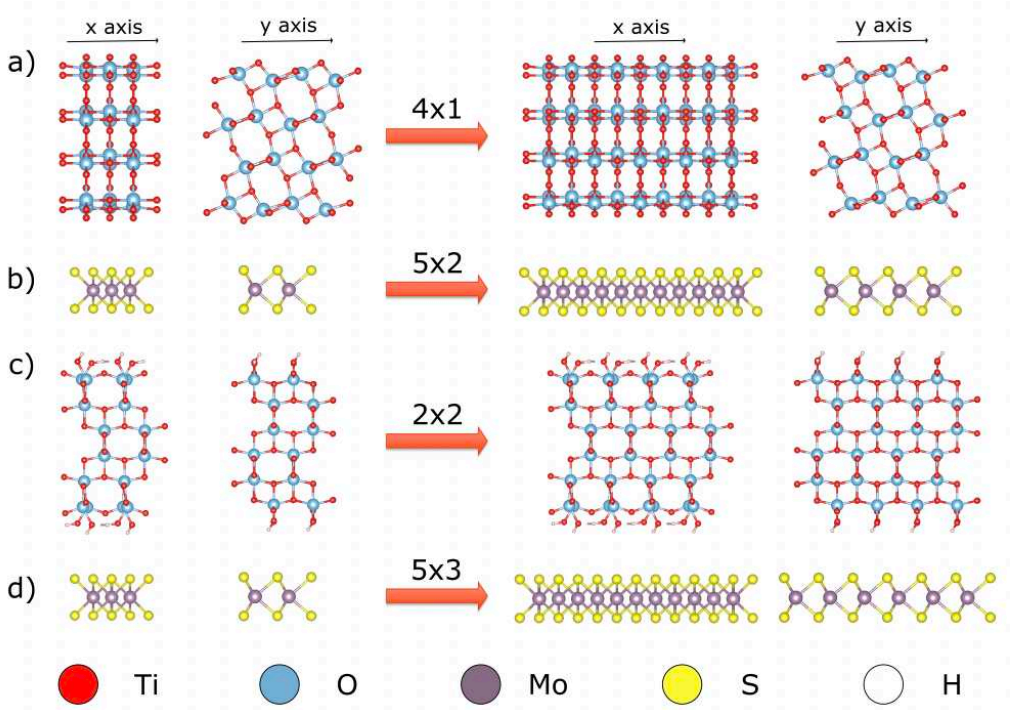

Figure IV-7: Slab supercell before and after multiplication for a) TiO_2 anatase (101), b) MoS_2 monolayer, c) TiO_2 anatase (001) hydrated and d) MoS_2 monolayer.

IV.1.3. The calculation parameters (vacuum, K-points, convergence criterion…)

In order to choose the calculations parameter for all our study, convergence tests have been done for three parameters (the vacuum layer, the convergence criterion and the K-point mesh). It has been performed on three systems: physical interaction on the (101) surface, physical interaction on the (001) surface and chemical interaction on the (101) surface. Three parameters have tested on this study: the K-points mesh, the vacuum layer between the slabs and the SCF energy convergence criterion. Given that the results obtained on the three systems are quite similar, we will present only the results obtained on one system: the chemical interaction on the (101) surface (Figure IV-8).

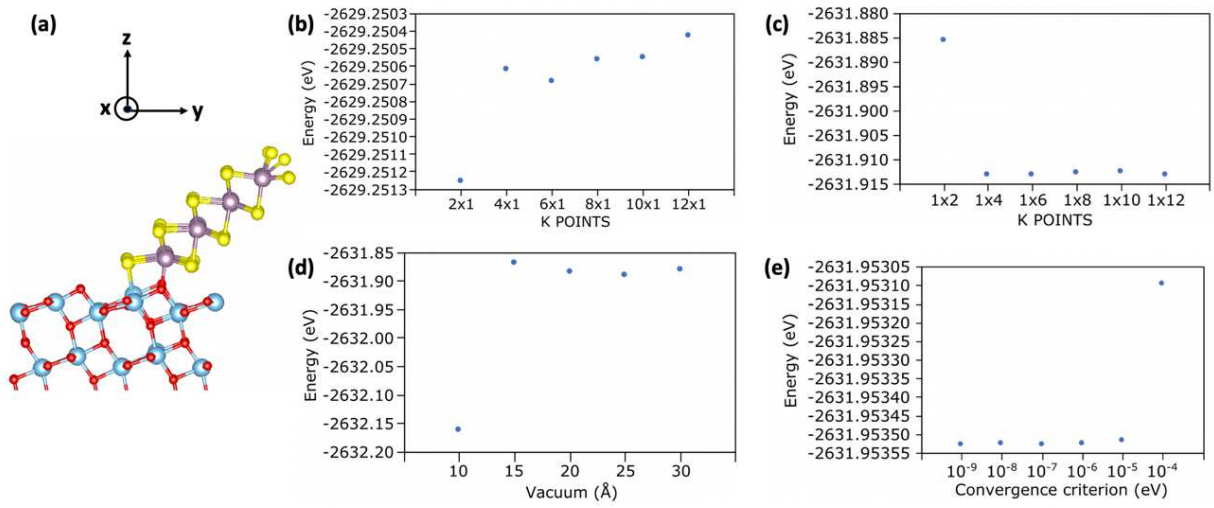

Figure IV-8: (a) structure of the TiO_2(101) and MoS_2 in epytaxic interaction. Ti, Mo, O and S atoms are in blue, grey, red and yellow respectively. (a) convergence of the electronic energy as a function of the k-points mesh in the x direction. (b) convergence of the electronic energy as a function of the k-points mesh in the y direction. (c) convergence of the electronic energy as a function of the vacuum thickness. (d) convergence of the electronic energy as a function of the SCF convergence criterion.

At the light of these results, we have chosen the following parameters for all the heterojunction studies. In all structures, a vacuum layer of 20 Å has been modelled between the slabs. Calculations were performed with a SCF energy convergence criterion of 10^{-6} eV on a 4x4x1 K-Points mesh. All the calculations parameters and the structural characteristics are summarized in the next part.

IV.1.4. Summarize of the computational details

DFT calculations were all performed using Vienna Ab Initio Simulation Package (VASP) code [6, 7]. Geometry optimizations were performed using the PBE functional [8], followed by a single point calculation using the range separated hybrid HSE-06 functional [9] along with a cut off-energy of 500 eV. In both cases, the van der Waals contributions were described using the Grimme D3 approach with Becke-Johnson damping (D3-BJ) [10]. The precision setting of VASP was set to “Normal” and a Gaussian smearing 0.05 eV was used. The convergence criterion for the SCF cycle was fixed at 10^{-6} eV per unit cell and the maximum forces were converged to below 0.02 eV/Å during the geometry optimization. To mimic aqueous conditions, in which water could be used either as a reactant or could be produced by the

redox reactions, implicit water solvent was added in interfacial systems and independent ones using the VASPsol code [18].

For the (001) surface of TiO_2, in addition to implicit water solvation (as described before), explicit hydration of the surface was used with a water coverage of 3.5 H_2O/nm^2. A 12x12x1 k-point mesh was used for the calculations on the separated materials (TiO_2 surfaces and MoS_2 monolayer) and a vacuum thickness of 20 Å was used.

For the physical interaction, one infinite 2D-MoS_2 nanosheet has been chosen which is known to exhibit larger bandgap than multilayers [19]. For the heterojunction, the MoS_2 nanosheet was optimized in parallel orientation with respect to the TiO_2 surfaces leading to a 2D-interface. For that, the unit cell of the two materials was multiplied in order to respect the commensurability of the respective lattice parameters.

In the case of MoS_2 on TiO_2 anatase (101), we used a 5x2x1 supercell for MoS_2 on a 4x1x1 supercell for TiO_2 and on the (001) surface, we used a 5x3x1 supercell for MoS_2 on a 4x4x1 supercell for TiO_2. In these cases, a reduced k-point mesh was used: 4x4x1 for the geometry optimizations at PBE-D3 level and 1x1x1 for the single point HSE06 calculations. Valence and conduction bands are determined from the last occupied state and the first unoccupied one. The Fermi level corresponds to the top of the valence band. These values are then adjusted with respect to the vacuum potential, different for each calculation, and determined by plotting the local electrostatic potential (Figure III-6)

For the chemical interaction, we chose one finite size MoS_2 nanoribbon exposing edges forming Mo-O-Ti or Mo-S-Ti chemical bonding along a 1D-interface with TiO_2. A tilting angle of the nanoribbon with respect to the TiO_2 surface is observed after geometry optimization. Various sizes of the nano-ribbon have been simulated. More details will be given in the results section.

In order to avoid artificial dipole moment in slab structures, symmetric slabs were modelled with one MoS_2 nanosheet added on each side of the TiO_2 slab leading to systems having between ~300 and ~500 atoms. We determined the electronic adhesion energies of each system without including vibrational and thermal contributions. This descriptor does not aim at providing the exact thermodynamic stability as a function of conditions, but rather at qualitatively apprehending the relative stability of the proposed systems. Complementary spin polarized calculations were performed when necessary.

IV.2. Results

IV.2.1. MoS_2 2D-monolayer in physical interaction with TiO_2 anatase surfaces

IV.2.1.a. Bare and hydrated TiO_2 surfaces

As a starting point for the investigation of the TiO_2/MoS_2 heterostructures, we focused on structures with MoS_2 physically adsorbed on TiO_2, i.e. interacting by van der Waals forces and eventually also by hydrogen bonding with TiO_2 (Figure IV-9).

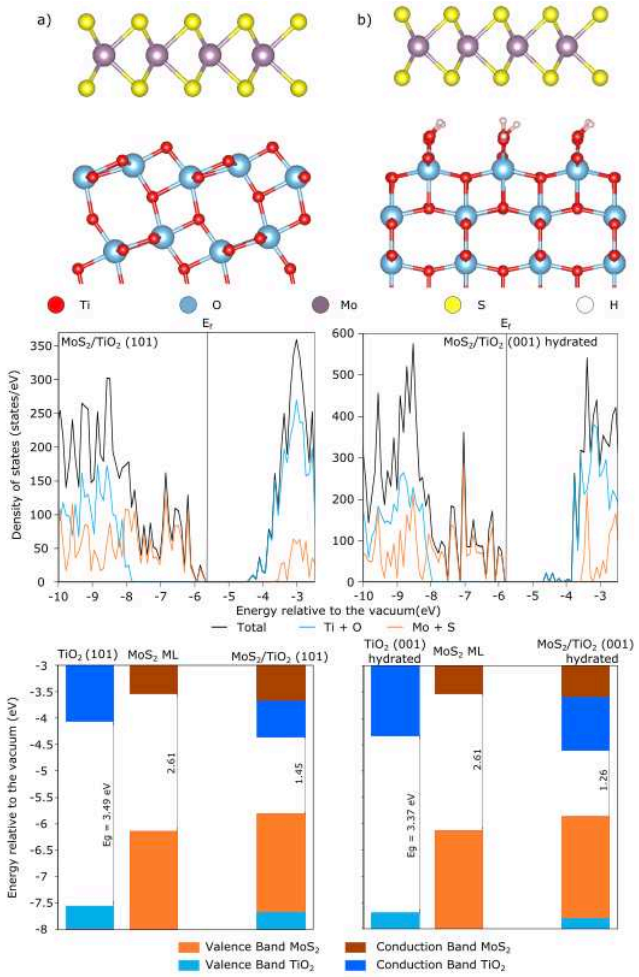

Figure IV-9: Molecular structure of MoS_2 monolayer physically adsorbed, DOS of these interfaces and evolution of the band position before and after junction for a) MoS_2/TiO_2 (101) and b) MoS_2/TiO_2 (001) hydrated.

For these architectures, the weak interaction energies (- 0.21 eV/MoS_2 for (101) and - 0.10 eV/MoS_2 for (001)) and the average distance between the O plane (on the surface for (101) and on the hydroxyls for (001)) and the S plane (2.87 Å for (101) and 3.02 Å for (001)) supports the idea of a van der Waals type of interaction as reported in the literature for similar systems [20, 21, 22].

As a consequence of this weak interaction between TiO_2 and MoS_2 in a van der Waals heterostructure, the electronic structures of the interface can be seen as the sum of the electronic structures of the two individual materials (Figure IV-9). The interface is a Type-II heterostructure (Figure IV-2) characterized by the existence of a bandgap (1.26 eV for (101) and 1.45 eV for (001)), with a valence band located on MoS_2 and a conduction band located on TiO_2.

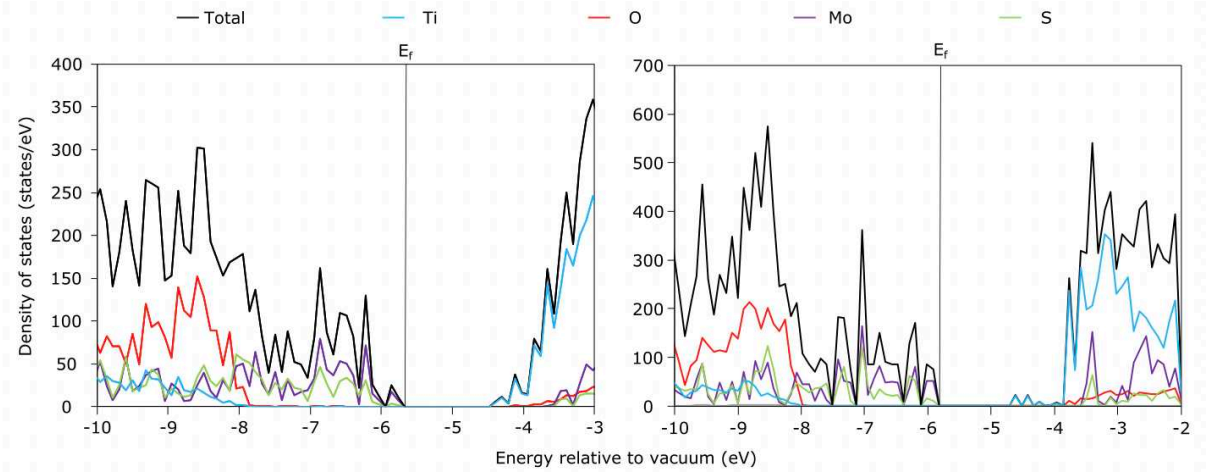

Figure IV-10: DOS with element decomposition associated to MoS_2 in physical interaction on TiO_2 (101) on the left and TiO_2 (001) hydrated on the right.

The density of states (DOS) with the projected states on each element (Figure IV-10), show that the valence band is mainly localized on the Mo atoms of MoS_2 while the conduction band is localized on the Ti atoms of TiO_2. Such type of heterostructure might eventually lead to a Z-type working principle photocatalysis with electrons photogenerated in MoS_2 recombining with holes photogenerated in TiO_2 (Figure IV-2). However, the rather large bandgaps of the heterostructures may question the feasibility of Z-type mechanism with respect to a standard Type II mechanism. To complete the electronic structure characterization of these interfaces, the charge transfer and charge density difference will be discussed later.

IV.2.1.b. Sulfided and hydrated-sulfided TiO_2 surfaces

Previous DFT [23] and experimental XPS [24] studies showed that the TiO_2 surface may be sulfided under sulfiding conditions (using H_2S as sulfiding agent for instance). Hence, the substitution of surface oxygen atoms by sulfur atoms on TiO_2 is thermodynamically stabilized under such conditions. Being inspired by these former studies, we considered two sulfided

TiO_2 surfaces (one for each orientation), as represented in Figure IV-11 with the MoS_2 monolayer physically adsorbed on.

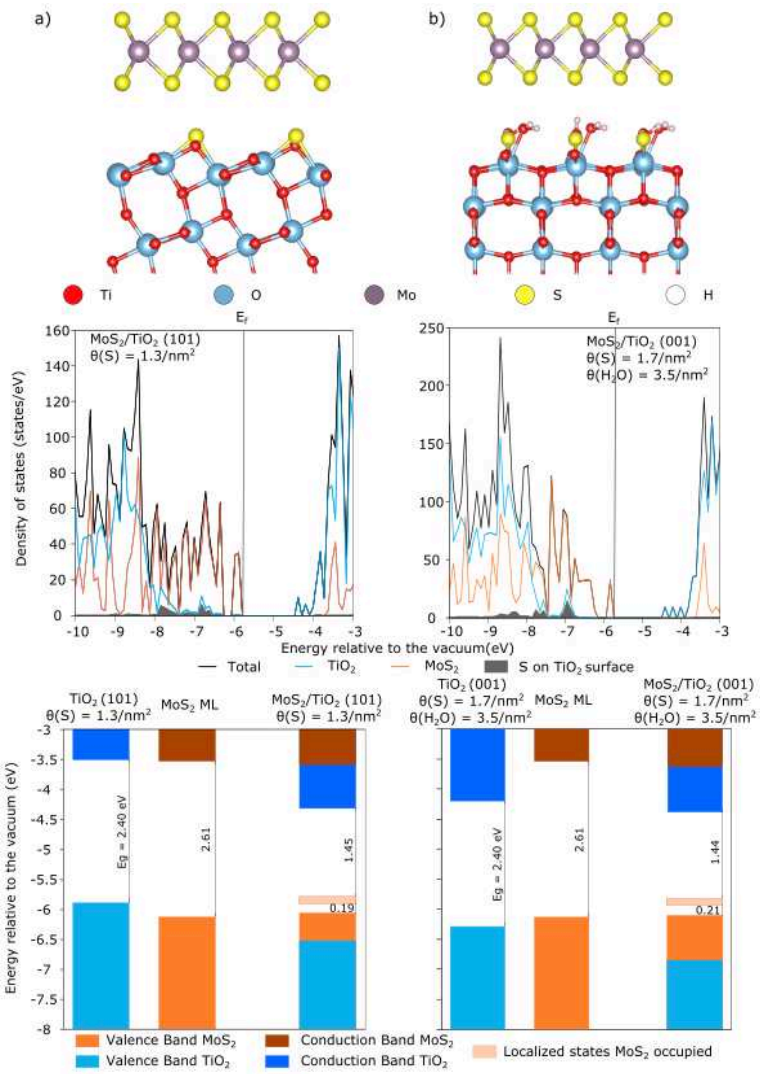

Figure IV-11: Molecular structure of MoS_2 monolayer physically adsorbed, DOS of the interfaces and evolution of the band position before and after junction for a) TiO_2 (101) with θ(S) = 1.3 S/nm² b) TiO_2 (001) with θ(S) = 1.7 S/nm² and θ(H_2O) = 3.5 H_2O/nm².

The first one (Figure IV-11 a) corresponds to a substitution of two oxygen atoms by unit cell on the (101) bare surface leading to a 1.3 S/nm² coverage on the surface. After optimizing the physical MoS_2/TiO_2-S heterostructure, the average distance between the two S planes (on the TiO_2 surface and on the MoS_2 nanosheet) is 2.73 Å and the average distance between the S plane of MoS_2 and the O plane of TiO_2 is 3.19 Å, thus larger than without sulfidation (2.87 Å), which explains the weaker adhesion energy of - 0.06 eV/MoS_2.

The second one (Figure IV-11 b) considers the same hydration state as for the non-sulfided (001) surface and the substitution of the four oxygen atoms by sulfur atoms per unit cell,

resulting in a coverage of 3.5 H_2O/nm^2 and 1.7 S/nm^2. After the junction with a MoS_2 the average distance between the two S planes (on the surface and on the nanosheet) is 3.42 Å (~0.7 Å greater than in the previous case) while the average distance between the S plane and the O plane is now 2.86 Å smaller than before sulfidation (3.02 Å). It is explained by the fact that after optimization, 8 OH groups remain while 8 OH groups are retransformed into 4 water molecules and 4 surface oxygen, closer to the nanosheet. So, the final hydroxylation state of surface is different from the non sulfided one. The average distance between the oxygen plane of the hydroxyls and the S plane of the nanosheet is 3.12 Å (3.02 Å before sulfidation). The adhesion energy remains small (- 0.10 eV/MoS_2) as in the non sulfided case, due to various compensation effects induced by van der Waals interactions and H-bonding.

The DOS with material decomposition associated to these structures (Figure IV-11) shows that the 3p states of the sulfur atoms located on both sulfided TiO_2 surfaces are mainly contributing to the top of valence band of TiO_2, whereas the 2p states of oxygen were contributing on the non-sulfided surfaces. Moreover, the 3p S states are higher in energy (~1 to 1.5 eV) with respect to the former 2p O states.

Concerning the evolution of the band positions after the junction, it is more important than for the previous non sulfided surfaces. On the sulfided (101) surface (Figure IV-11 a), we observe a decrease in energy of the conduction band of TiO_2 that could be driven by the sulfur-sulfur interaction across the interface. On the (001) sulfided and hydrated (Figure IV-11 b), this interaction is weakened due to the surface hydration. In both cases, we observe after interaction a decrease in energy of the valence band of TiO_2 (localized on the surface sulfur) and an increase of the valence band of MoS_2. The apparition of localized 4d Mo states at the top of the valence band could be induced by the shift of 3p S states of the TiO_2 surface at higher energy levels becoming closer to the top of the valence band of the MoS_2 nanosheet (than the 2p O states in the non-sulfided case).

IV.2.2. MoS_2 nanoribbon in chemical interaction with TiO_2 anatase surfaces

IV.2.2.a. Bare and hydrated TiO_2 surfaces

As discussed previously, the literature reports the possibility to grow MoS_2 nanosheet on top of anatase particles by epitaxy [3, 4, 5]. In that case, we consider a nanoribbon with infinite dimension only in the direction parallel to the TiO_2 surface forming a 1D chemical interface.

On the other direction, the finite size of the nanoribbon implies the creation of two different edges on MoS_2 usually called “Mo-edge” and “S-edge” [25] (Figure IV-12 a). The more favorable restructuration (Figure IV-12 b), corresponding to 50% sulfur atoms on each edge, has been chosen for building the epitaxial structure.

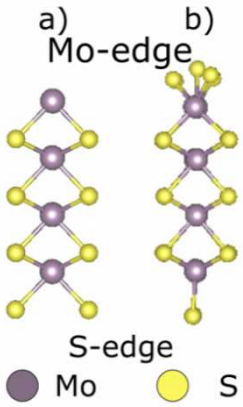

Figure IV-12: Evolution of the MoS_2 finite nanoribbon before (a)) and after restructuration induced by the transfer of half of S-atoms from the S-edge to M-edge (b)).

The formation of these edges has a strong impact on the electronic structure associated (Figure IV-13) with a decrease (~2 eV) of the bandgap with respect to the infinite nanosheet due to new electronic states localized on the edges. As already reported by previous DFT studies [26], these localized electronic states correspond to the top of the valence bands and the bottom of the conduction bands.

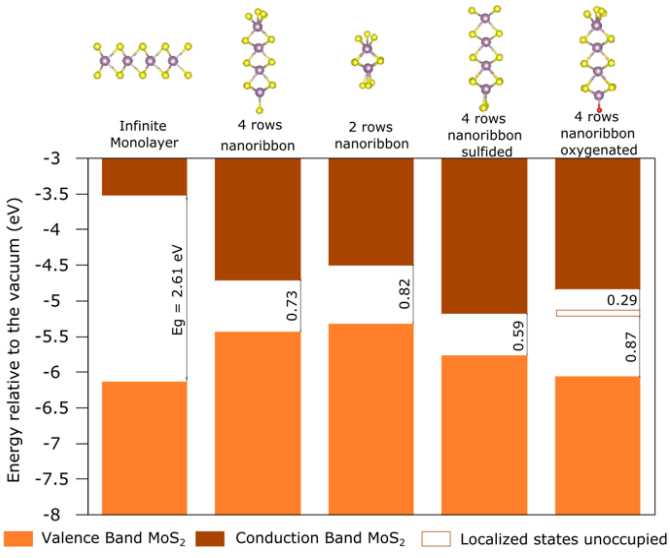

Figure IV-13: Evolution of the band positions of MoS_2 when going from the monolayer to the nanoribbons and chemically modified nanoribbons.

Depending on the way the interfacial structure is prepared, its chemical composition or the size of the MoS_2 nanoribbon may change. Particularly, if the genesis of the MoS_2 nanoribbon

is obtained through a sulfidation process of Mo-oxide precursor, some oxygen atoms may not be fully replaced by sulfur atoms at the interface and some Mo-O-Ti bridges may remain [3, 27]. Also, the size of the MoS_2 nanoribbon can be tuned by the experimental conditions such as sulfidation temperature. Changing such features have been invoked in the case of MoS_2 based catalysts [28]. These chemical modifications have been tested on the finite nanoribbon (Figure IV-13) but they have only a slight impact on the band positions, apart from oxygen doping which induces the apparition of a localized state and a down shift of the valence band induced by the 2p O state.

First, we focus on the ribbon without chemical modification and we explore to which extent a chemical interaction between MoS_2 and TiO_2 surface may influence the electronic structures of the heterojunctions compared to the van der Waals heterostructures presented before. For that purpose, we consider the TiO_2 (101) bare and the TiO_2 (001) hydrated surfaces.

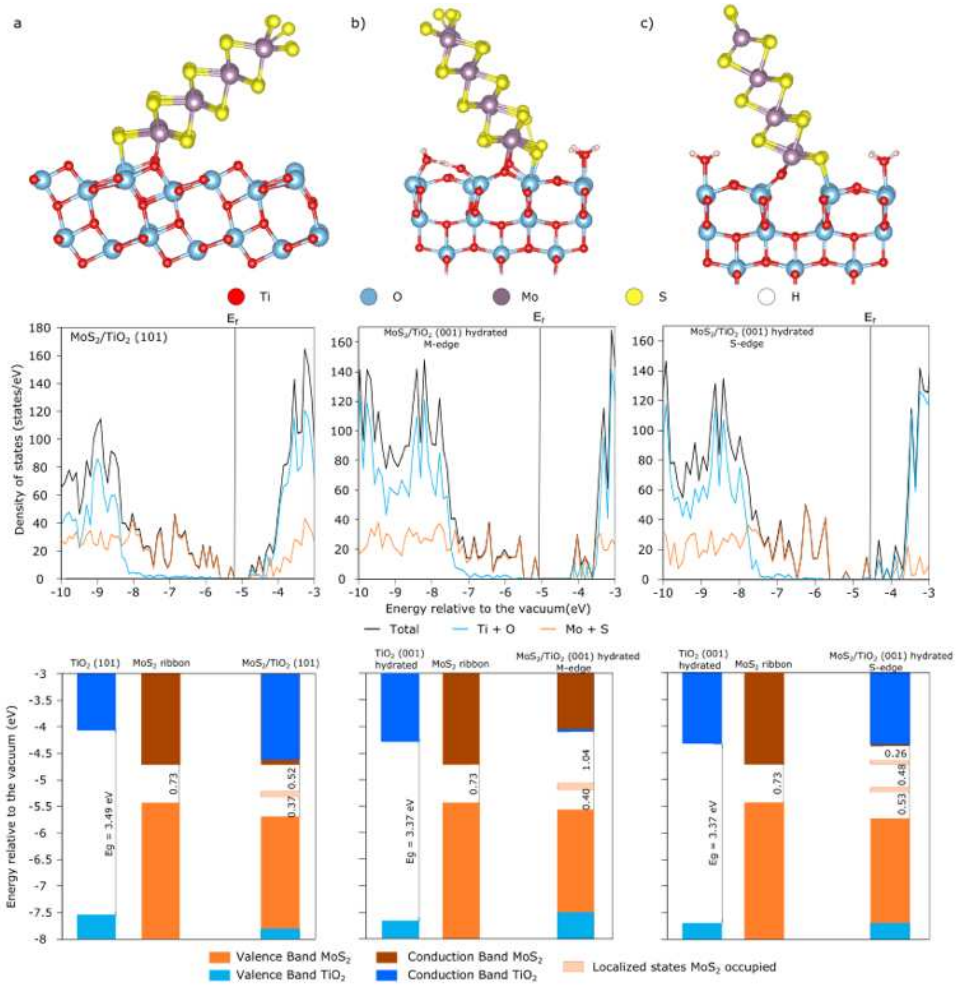

Figure IV-14: Molecular structure of MoS_2 nanoribbon chemically adsorbed, DOS of the interfaces and evolution of the band position before and after junction for a) TiO_2 (101) b) TiO_2 (001) (interaction with M-edge) and c) TiO_2 (001) (interaction with S-edge).

On the (101) surface, we optimized the interfacial system starting from a structure inspired by the one previously reported for Mo_6S_{12+x} clusters [3, 4]. After optimization, the MoS_2 nanoribbon is tilted with an angle of ~40° between the Mo plane and the (101) surface. The interaction with the TiO_2 surface occurs through the so-called "Mo-edge" of MoS_2 whereas the opposite "S-edge" is free (Figure IV-14 a). The stabilization at interface is ensured by 4 membered ring Mo-S-Ti-O. In the case of the hydrated (001) TiO_2 surface, we revisited the possible interactions of the two MoS_2 edges: the first one through the M-edge with an angle of ~58° (Figure IV-14 b) and the second one through the S-edge with ~68° (Figure IV-14 c). The interaction is ensured through Mo-O-Ti and Mo-S-Ti bridges in the first case and Mo-S-Ti-O rings in the second one. The adhesion energies calculated using the MoS_2 nanoribbon as a reference are - 0.24 eV / MoS_2 for the (101) surface, ~ 0 eV / MoS_2 for the (001) hydrated surface in interaction with the Mo-edge and - 0.21 eV for the (001) hydrated surface interacting with the S-edge.

The DOS associated to the systems in chemical interaction (Figure IV-14) illustrates the strong impact of the chemical interaction between the two semiconductors with large differences compared to the physical interaction. Although a bandgap is maintained, several localized and occupied states, localized on MoS_2, appears in the gap. If we compare the band positions before and after the junction (Figure IV-14), the impact of the chemical bonds on the band structure is clearly visible with a large variation of the band positions. The effect on TiO_2 is visible only with the (101) surface with a small fall of the conduction band after interaction. On MoS_2, the impact is the same in all the cases, with a bandgap increased after the interaction and the apparition of these localized states. Spatial charge analysis (A.1) has shown that the occupied and unoccupied states (including localized states) close to the Fermi level are located either at the interface or at the free MoS_2 nanoribbon edge. In the case of the (101) surface (Figure A-1) and (001) surface in interaction with the S-edge (Figure A-2), these localized states are at the interface whereas it is located at the free S-edge for the (001) surface in interaction with the Mo-edge (Figure A-3). Since the CB and VB of the materials are mainly localized at the interface (the only exception is with the (001) in interaction with the S-edge), the localized states at the interface could be a benefit, playing as catalytic center, or a drawback, playing a recombination center.

The electronic stricture of the interface is a type I heterojunction with the valence band edge and conduction band edge localized on MoS_2. Since the localized states could have unwished

and complicated behaviors, including the accumulation of the holes and the diminution of the global bandgap, we explored if chemical modifications of the interface or size effect of the MoS_2 nanoribbon could change the type of heterojunction and avoid the apparition of such localized states in the bandgap.

IV.2.2.b. Chemical modification of the 1D-interface

We have applied the same chemical modifications to the ribbon in chemical interaction with a TiO_2 surface as those applied on the nanoribbon alone (Figure IV-14): diminution of the number of Mo rows, increase of the sulfidation at the edge and oxygenation of the interface. Due to a significantly larger supercell of the (001) slab, these investigations have been undertaken on the (101) surface only.

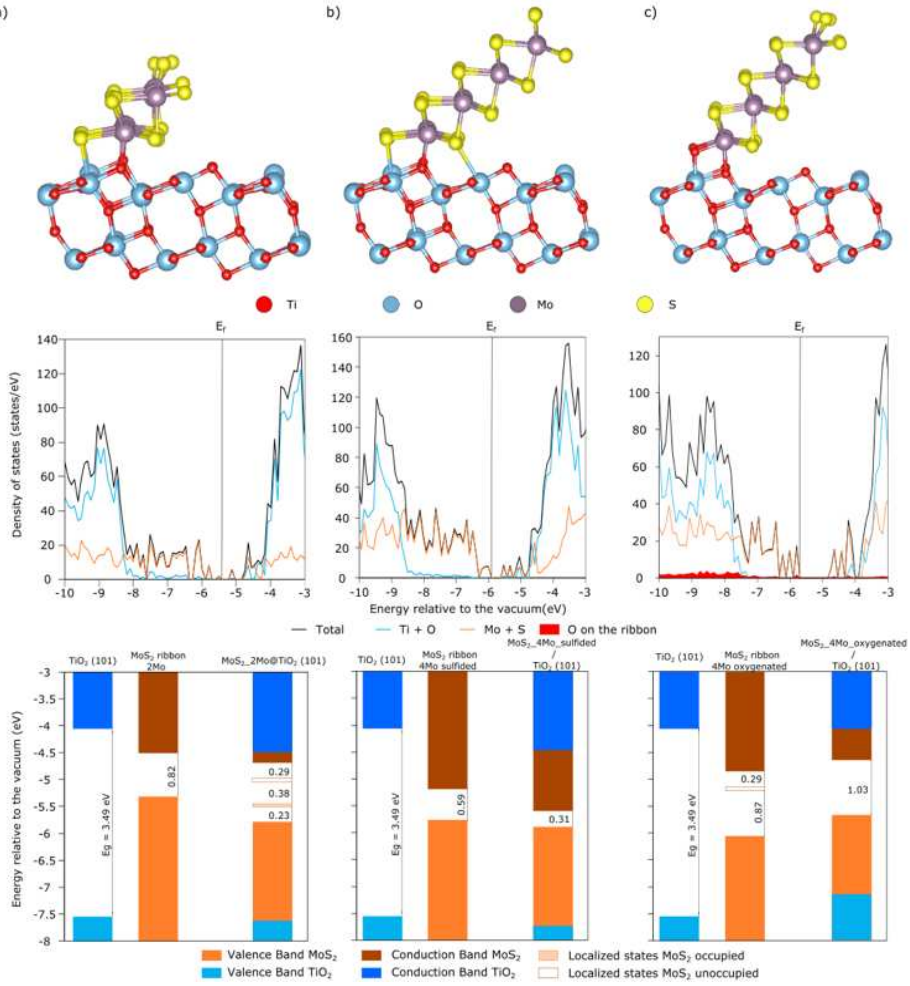

Figure IV-15: Molecular structure of MoS_2 nanoribbon chemically adsorbed, DOS of the interfaces and evolution of the band position before and after junction for a) MoS_2 ribbon with 2 Mo rows b) MoS_2 ribbon with 4 rows sulfided and c) MoS_2 ribbon with 4 rows oxygenated.

The DOS associated to these structures clearly reveal the effect of these 3 chemical modifications on the electronic properties. The diminution of the number of Mo rows (Figure IV-15 a) leads to a more complex electronic structure with a smaller bandgap and still localized states at the interface (Figure A-4) that could become recombination centers. In the cases of increased sulfidation at the free edge (Figure IV-15 b) or oxygenation at the interface (Figure IV-15 c), these localized states vanish. For the oxygenated interface, the bandgap is enlarged. In the sulfidation case, the CB located at the free edge and the VB which contains contribution on both edges (Figure A-5) could lead to a spatial separation of the electrons and the holes generated. The same possibility occurs for oxygenated interface, with a VB located at the interface and a CB with contribution on both edges (Figure A-6). In the three cases, a type I heterojunction is found with the conduction band and the valence band both localized on MoS_2.

IV.3. Discussion

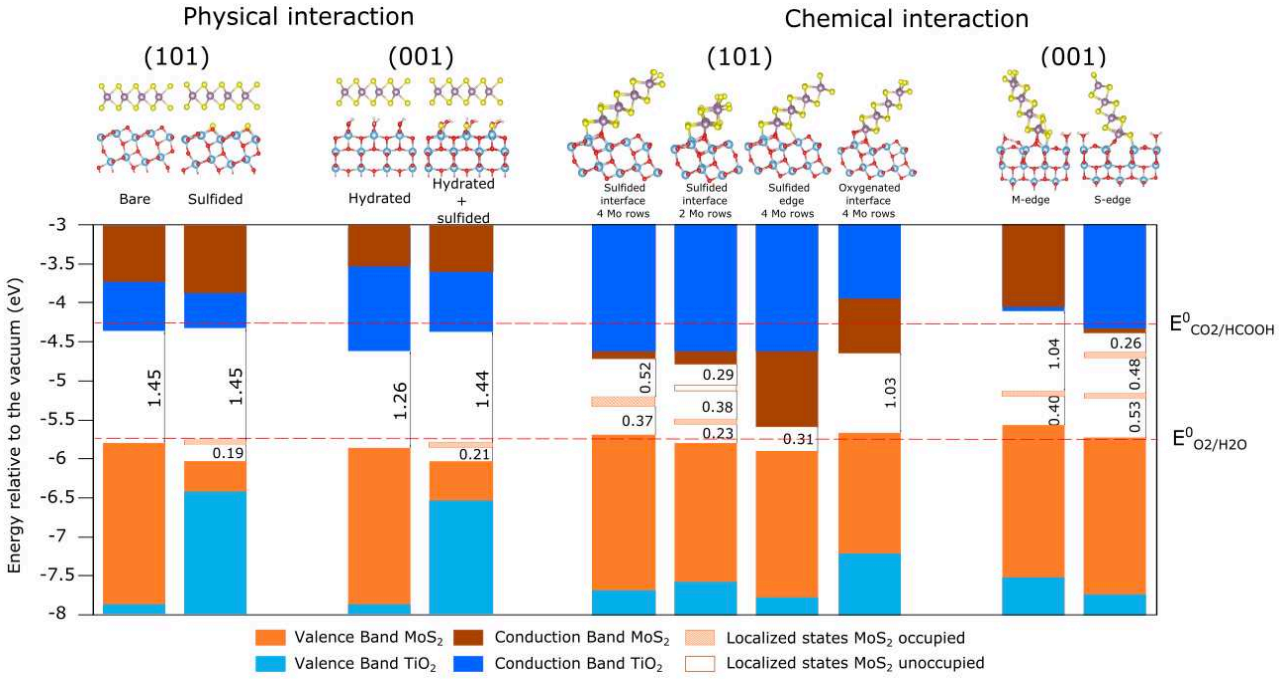

Figure IV-16: Comparison of the band position of the two materials after junction for all the cases in physical interaction on the left and chemical interaction on the right.

The comparison of the band positions of all the physical interaction structures (Figure IV-16) reveals that the strong modifications in the TiO_2 surface involves slight modifications in the band structures of MoS_2, because of the weak electronic interaction between the two

materials. On the other hand, modifications in the band structure of TiO_2 could modify its electronic properties. On the (001) surface, while the hydration of the surface leads to an increase of TiO_2 bandgap in comparison with the bare surface (Figure IV-5), the sulfidation of the surface involves a strong diminution of the band gap, with a significant upper shift of the valence band due to the 3p states of sulfur atoms at the top of the valence band. The same trend is observed with the sulfidation of the (101) surface. All cases correspond to a type II heterojunction, and two dynamics of charge carriers can be considered. On the one hand, the classical type II mechanism would imply the transfer of the holes in the VB of MoS_2, and the transfer of the electrons in the CB of TiO_2. In that case, the reduction and oxidation potential are limited by the energy difference between the VB of MoS_2 and the CB of TiO_2. Alternatively, a Z-scheme mechanism would imply the recombination of the holes generated in MoS_2 with the electrons generated in TiO_2 at the interface (Figure IV-17 a).

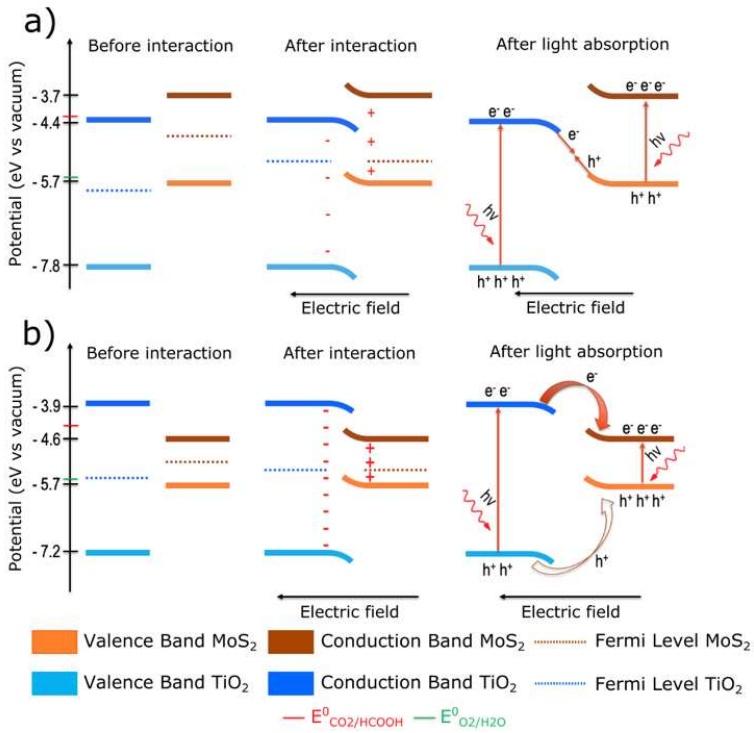

Figure IV-17: Comparison of the Z-scheme mechanism (a) and the type I mechanism (b) that could be implied when a heterojunction occurs between the MoS_2 sheet and the TiO_2 (101) surface in physical (a) or chemical (b) interaction. Due to the intrinsic semiconductors involved, the fermi levels are localized in the middle of the bandgap before interaction.

This induces an accumulation of electrons in MoS_2 and holes in TiO_2. In these conditions, the system will exhibit appropriate reduction and oxidation potentials, that could allow to achieve the targeted photoreduction of CO_2.

The strong effect of the sulfidation on the electronic structure (diminution of TiO_2 bandgap and apparition of a localized state), could favor one mechanism as a function of the behavior of these localized states. Depending on the mechanism, MoS_2 will act as the reducer or as the oxidizer (TiO_2 will do the opposite reaction in both cases). This could be an argument in the choice of the mechanism. To do that, tuning by sulfidation of the TiO_2 surface will be needed through the modification of the pressures in H_2S and H_2O.

Although a clear conclusion about the real mechanism is impossible without the knowledge of dynamics of charge carriers, the distribution of charges at the interface and the resulting orientation of the internal electric field before irradiation might be good driving force for the electron and hole transfer upon irradiation [29] as illustrated in Figure IV-17. Hence, the calculation of the Bader charge difference [30] between the sub-systems (MoS_2 nanosheet and TiO_2 surface) before and after junction has been performed (Table IV-2).

Interaction type	**Structure**	**Δe^- MoS_2 (per nanosheet)**	**Δe^- TiO_2**
2D Physical	(101) bare	- 0.02	+ 0.04
	(101) sulfided	+ 0.04	- 0.09
	(001) hydrated	- 0.18	+ 0.36
	(001) hydrated-sulfided	- 0.07	+ 0.15
1D Chemical	(101) 4 Mo rows	- 0.52	+ 1.04
	(101) 2 Mo rows	- 0.62	+ 1.25
	(101) sulfide edge	- 0.51	+ 1.02
	(101) oxygenated interface	- 0.19	+ 0.39
	(001) Mo-edge	- 0.22	+ 0.44
	(001) S-edge	+ 0.14	- 0.28

Table IV-2: Fraction of electron transferred from MoS_2 (i.e. a negative value indicates a loss of electron) [30].

In the case of physical interaction, a weak charge transfer occurs from one MoS_2 nanosheet to TiO_2, which is more significative with the (001) hydrated than with the (101) bare (+ 0.18 e^- vs + 0.02 e^- per MoS_2 sheet). Obviously, the presence of H-bonding enhances the transfer. Reversely, for both surfaces, the transfer is significantly attenuated by sulfidation of the (001) surface or even inverted for the (101) one (+ 0.07 e^- and - 0.04 e^-, respectively). As aforementioned, the presence of sulfur-atoms on TiO_2 surfaces induces an increase of the

distance between the MoS_2 sheet and the surface. The fact that the junction involving the TiO_2 (001) hydrated surface induces such a negative charge on TiO_2 and a positive one on MoS_2 could generate the proper internal field and enhance a Z-scheme mechanism: the holes generated on MoS_2 are attracted by the negatively charged TiO_2 and the electrons generated on TiO_2 attracted by the positively charged MoS_2, leading to the targeted electron-hole recombination at the interface (Figure IV-17 a). Moreover, the band gap of the MoS_2/(001) TiO_2 hydrated heterojunction is 0.2 eV smaller than the one of MoS_2/(101) TiO_2 which is also a parameter in favor of a Z-scheme mechanism. Hence, the stabilization of a heterojunction involving the hydrated (001) surface without sulfidation should be sought at the synthesis step. This result might explain in part the recent experimental studies on 2D-2D MoS_2/(001) TiO_2 nanojunctions [31] revealing a H_2 evolution rate 36.4 times higher than that of pure TiO_2. Our calculations show that the charge transfer thanks to a surface contact increases which could be explained by a Z-scheme mechanism enhancing a spatial separation of the charge carriers while maintaining a good reduction and oxidation power.

If we now summarize the band positions of all systems in chemical interaction (Figure IV-16), the various MoS_2 nanoribbons lead to modifications on the electronic structure of both materials. In fact, while the modification of the number of rows and the modification of the edge leads logically to slight modifications in the band positions, the sulfur/oxygen exchange at the interface implies the modification of the interaction with the TiO_2 surface and an increase of its conduction band and valence band. Concerning MoS_2, the modification of the number of rows and the sulfidation at the edge narrow the bandgap and eliminate the localized state in the gap. It is accompanied by a shift to the lowest energy in the second case. In the case of the oxygenated interface, the substitution of the sulfur at the interface has a low impact on MoS_2 electronic structure apart the vanishing of the localized states. Concerning the charge transfer analysis (Table IV-2), we observe once again an electron transfer from MoS_2 to TiO_2, except in the case with the ribbon in interaction with its S-edge. As expected, the charge transfer is stronger than with the physical interaction (higher than 0.5 electron by nanosheet in 3 cases). The strongest charge transfer occurs for the MoS_2 nanoribbon of smaller size (2 Mo rows) which may be explained by the strong delocalization of charge within the nanoribbon. Reversely, the charge transfer is limited by the presence of oxygen near the surface (+ 0.20 for the (101) with oxygenated interface and + 0.22 for the ribbon on the (001) hydrated) which is consistent with the large band gap observed for this

system. The impact of the electric field induced by this charge transfer on type I heterojunction can be discussed from Figure IV-17 b. Due to their respective band positions, these systems seem to lead to the accumulation of both electrons and holes in the conduction band and valence band of MoS_2. Nevertheless, due to the induced electric field, the hole transfer will face a barrier and could be limited in order to maintain a charge separation with a good oxidation potential. Except for these cases, these materials should have limited applications as heterojunctions for photocatalysis, particularly in the case of the CO_2 photoreduction. In these systems, MoS_2 should mainly be considered as acting as a co-catalyst.

IV.4. Conclusions

Thanks to state of the art DFT calculations involving the range-separated hybrid HSE06 functional, we showed how the various possible structural modifications of the MoS_2/TiO_2 heterojunction impact the resulting electronic properties: band gaps and CB/VB band positions. In particular, we distinguished the effects of a physical interaction and a chemical one between the MoS_2 and TiO_2 materials on the nature of the MoS_2/TiO_2 heterojunctions. A physical 2D-interface may lead to a type II or Z-scheme formalism. The analysis of the CBE/VBE band positions revealed that the physical interaction is compatible with a photocatalytic reduction process of CO_2. Moreover, a weak but non-negligible charge transfer occurs from the MoS_2 nanosheet to the hydroxylated (001) surface of TiO_2 which may induce of a Z-scheme mechanism more efficient for photon absorption processes in photocatalysis applications. The sulfidation of the TiO_2 surface does not improve the resulting electronic properties. By contrast, all chemical 1D-interfacial systems imply the formation of a type I heterojunction. The chemical interaction induces a stronger charge transfer at the interface than for the physical interaction but the type I mode will not obligatory enhance the photon absorption efficiency during photocatalysis.

To go further, the idea would be to evaluate the efficiency of these interfaces to perform the photocatalytic CO_2 reduction either by using the Computational Hydrogen Electrode [32, 33] or even using the Grand Canonical DFT (or surface charging approach) [34]. In order to begin to study this aspect, we proposed in the following chapter to investigate the CO_2 reduction mechanism on various MoS_2 edges with the surface charging approach.

IV.5. References

[1] M. Lazzeri, A. Vittadini and A. Selloni, *Physical Reviw B,* vol. 63, p. 155409, 2001.

[2] C. Arrouvel, M. Digne, M. Breysse, H. Toulhoat and P. Raybaud, *Journal of Catalysis,* vol. 22, pp. 152-166, 2004.

[3] C. Arrouvel, M. Breysse, H. Toulhoat and P. Raybaud, *Journal of Catalysis,* vol. 232, pp. 161-178, 2005.

[4] D. Costa, C. Arrouvel, M. Breysse, H. Toulhoat and P. Raybaud, *Journal of Catalysis,* vol. 246, pp. 325-343, 2007.

[5] Y. Sakashita, Y. Araki, K. Honna and H. Shimada, *Applied Catalysis A,* vol. 197, pp. 247-253, 2000.

[6] G. Kresse and J. Furthmüller, *Computationall Material Science,* vol. 6, pp. 15-50, 1996.

[7] G. Kresse and J. Furthmüller, *Physical Review B,* vol. 54, pp. 11169-11186, 1996.

[8] J. P. Perdrew, K. Burke and M. Ernzerhof, *Physical Review Letter,* vol. 77, pp. 3865-3868, 1996.

[9] J. Heyd and G. E. Scuseria, *Journal of Chemical Physics,* vol. 121, pp. 1187-1192, 2004.

[10] S. Grimme, S. Ehrlich and L. Goerigk, *Journal of Computational Chemistry,* vol. 32, pp. 1456-1465, 2011.

[11] K. K. Kam and B. A. Parkinson, *The Journal of Physical Chemistry,* vol. 86, p. 463, 1982.

[12] M. Horn, C. F. Schwerdtfeger and E. P. Meagher, *Zeitschrift für Kristallographie,* vol. 136, pp. 273-281, 1972.

[13] K. M. Reddy, S. V. Manorama and A. Ramachandra, *Materials Chemistry and Physics,* vol. 78, p. 239, 2002.

[14] D. J. Trainer, A. V. Putilov, C. Di Giorgio, T. Saari, B. Wang, M. Wolak, R. U. Chandrasena, C. Lane, T.-R. Chang, H.-T. Jeng, H. Lin, F. Kronast, A. X. Gray, X. Xi, J. Nieminen, A. Bansil and M. Iavarone, *Scientific Reports,* vol. 7, p. 40559, 2017.

[15] Y. L. Huang, Y. Chen, W. Zhang, S. Y. Quek, C.-H. Chen, L.-J. Li, W.-T. Hsu, W.-H. Chang, Y. J. Zheng, W. Chen and A. T. Wee, *Nature Communications,* vol. 6, p. 6298, 2015.

[16] M. Sharokhi, P. Raybaud and T. Le Bahers, *ACS Applieds Materials Interfaces,* vol. 13, pp. 36456-36474, 2021.

[17] M. Grätzel, *Nature,* vol. 414, p. 338, 2001.

[18] K. Matthew, R. Sundaraman, K. Letchworth-Weaver, T. A. Arias and R. G. Hennig, *Journal of Chemical Physics,* vol. 140, p. 084106, 2014.

[19] M. Shahrokhi, P. Raybaud and T. Le Bahers, *Journal of Material Chemistry C,* vol. 8, pp. 4920-4935, 2020.

[20] M. Shen, Z. Yan, L. Yang, P. Du, J. Zhang and B. Xiang, *Chemical Communications journal,* vol. 50, pp. 15447-15449, 2014.

[21] W. Zhou, Z. Yin, Y. Du, X. Huang, Z. Zeng, Z. Fan, H. Liu, J. Wang and H. Zhang, *Small,* vol. 9, pp. 140-147, 2013.

[22] H. Han, K. M. Kim, C.-W. Lee, C. S. Lee, R. C. Pawar, J. L. Jones, Y.-R. Hong, J. H. Ryu, T. Song, S. H. Kang, S. Choi and S. Mhin, *Physical Chemistry Chemical Physics,* vol. 19, pp. 28207-28215, 2017.

[23] C. Arrouvel, H. Toulhoat, M. Breysse and P. Raybaud, *Journal of Catalysis,* vol. 226, pp. 260-272, 2004.

[24] L. Coulier, J. van Veen and J. Niemantsverdriet, *Catalysis Letters,* vol. 79, pp. 149-155, 2002.

[25] H. Schweiger, P. Raybaud, G. Kresse and H. Toulhoat, *Journal of Catalysis,* vol. 207, pp. 76-87, 2002.

[26] P. Raybaud, J. Hafner, G. Kresse, S. Kasztelan and H. Toulhoat, *Journal of Catalysis,* vol. 189, pp. 129-146, 2000.

[27] R. G. Leliveld, A. J. van Dilen, J. W. Geus and D. C. Koningsberger, *Journal of Catalysis,* vol. 165, pp. 184-196, 1997.

[28] B. Baubet, A.-S. Gay, A.-L. Taleb, M. Moreaud, F. Wahl, V. Delattre, E. Devers, A. Hugon, O. Ersen, P. Afanasiev and P. Raybaud, *ACS Catalysis,* vol. 6, pp. 1081-1092, 2016.

[29] X. Li, C. Garlisi, Q. Guan, S. Anwer, K. Al-Ali, G. Palmisano and L. Zheng, *Materials Today,* vol. 47, pp. 75-107, 2021.

[30] R. F. W. Bader, Atoms in Molecules: A Quantum Theory, Oxford: Oxford University Press, 1990.

[31] Y.-J. Yuan, Z.-J. Ye, H. Lu, B. Hu, Y.-H. Li, D. Chen, J.-S. Zhong, Z.-T. Yu and Z. Zou, *ACS Catalysis,* 2015.

[32] M. Bajdich, M. Garcia-Mota, A. Vojvodic, J. K. Norskov and A. T. Bell, *Journal of the American Chemical Society,* vol. 135, pp. 13521-13530, 2013.

[33] L. Lv, Y. Shen, X. Gao, J. Liu, S. Wu, Y. Ma, X. Wang, D. Gong and Z. Zhou, *Applied Surface Science,* vol. 546, p. 149066, 2021.

[34] C. D. Taylor, S. A. Wasileski, J.-S. Filhol and M. Neurock, *Physical Review B,* vol. 73, p. 165402, 2006.

[35] R. Coehoorn, C. Haas, J. Dijkstra, C. J. F. Flipse and R. A. Degroot, *Physical Review B,* vol. 35, p. 6195, 1987.

Chapter V. Reactivity study: CO_2 reduction mechanism on MoS_2 nanosheets

In the previous results, we have investigated the various charge carrier migration pathways on MoS_2/TiO_2 heterostructures. In case of physical interaction between MoS_2 monolayer and TiO_2 surfaces, an induced electric field is expected to appear, in order to favor the Z-scheme mechanism. It would result in the accumulation of the electrons in MoS_2 and accumulation of the holes in TiO_2 with oxidation and reduction potentials, coherent with efficient CO_2 reduction on MoS_2.

However, in case of a type I heterojunction, as observed in the case of chemical interaction, the use of MoS_2 as a co-catalyst, as described in II.3.2.a, is also expected to provide active sites for the CO_2 reduction (Figure V-1).

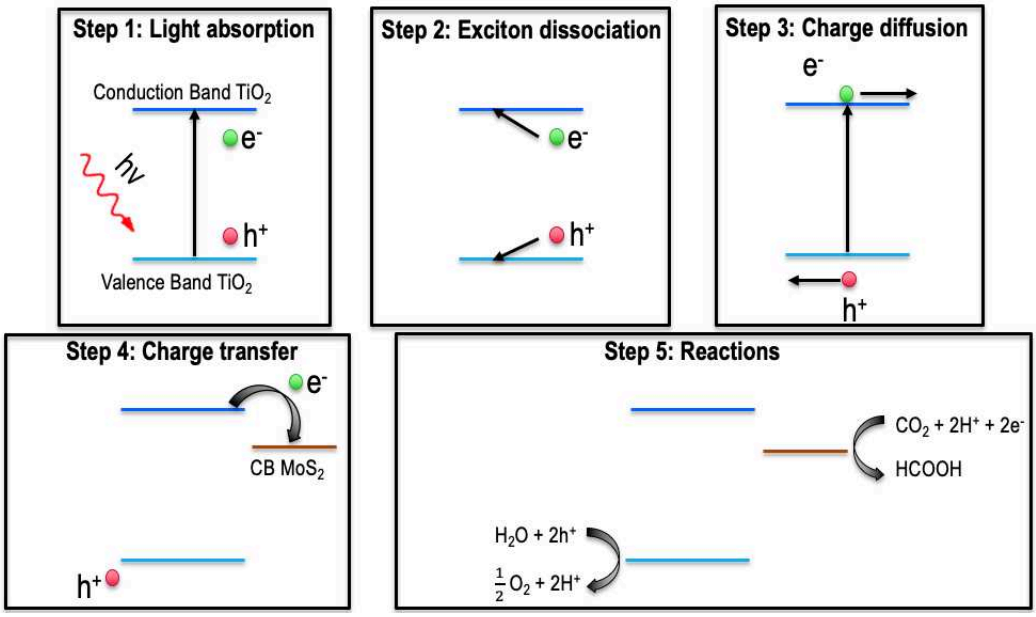

Figure V-1 : Proposed mechanism associated to the use of TiO_2 as the light harvester and site for the oxidation reaction while MoS_2 will act as the reduction co-catalyst.

Whatever the heterostructure type considered, identified as possible on our studies and/or proposed in other works, it appears to be crucial to have a more precise idea of the CO_2 reduction mechanisms possible on MoS_2 nanosheets. This is the topic of this section.

V.1. Calculation details

All the calculations were performed using DFT with periodic boundary conditions as implemented in the VASP software 5.4.1 [1, 2, 3, 4]. The GGA PBE functional [5] has been used with a description of the core electrons with the PAW pseudo-potential. A 3x3x1 k-points grid has been used for the slab calculations while a 12x12x12 grid has been used for bulk calculations. The energetic convergence criterion of the SCF cycles has been defined at 10^{-5} eV per supercell and a cut-off energy of 500 eV has been fixed. In order to describe long range interactions, D3-BJ dispersion correction has been added [6]. During the geometry optimizations, the relaxations were stopped when residual ionic forces are inferior to 0.025 eV.$Å^{-1}$.

The energy of free molecules was calculated by positioning them alone in a lattice, with the same calculation parameters than those used for the slabs. When required, entropy correction has been added with a term in -TS (at 298 K). Two methods have been considered to determine this term: a first one based on experimental entropy [7] and a second one based on quantum chemical calculations using the rigid rotator calculation (Gaussian16 code [8], 6-311+G(d,p)/PBE0 level of theory [9]). The two entropies are compared in Table V-1.

Molecule	-TS experimental (eV)	-TS computational (eV)
H_2	- 0.403	- 0.403
H_2O	- 0.583	- 0.583
O_2	- 0.633	- 0.633
CO	- 0.611	- 0.610
CO_2	- 0.660	- 0.660
HCOOH	- 0.769	- 0.766

Table V-1 : Comparison of the experimental and computational calculation of the -TS term. The computational term has been determined with Gaussian in PBE0/6-311+G(d,p) in gas phase with the harmonic approximation.

An energy difference of 0.003 eV is observed in the worst case. Since it does not represent a significative difference, we have chosen to work with the computed values, in order to avoid mixing computational and experimental data in the final ΔG calculations. In addition, it allows us to remove the vibrational contribution in order to be coherent with the surface calculation, where the vibrational contributions are not considered. However, the vibrational contribution

represents 10^{-5} eV in the more significative case (the formic acid HCOOH) so removing it does not really change the -TS value.

As explained in Chapter III, the electrochemical potential is explicitly treated by the surface charging approach based on the linear Poisson-Boltzmann equation, implement in VASPsol by Hennig group [10, 11]. The solvent effect and the distribution of the counter charge is integrated in VASPsol. This method describes thus the distribution of the electrolyte in the calculation, in order to play the role of counterion, in an implicit manner.

Concerning the MoS_2 nanosheet, the most stable stoichiometric structure [12] with 50% S on each edge has been considered (Figure V-2). It has been assumed that it remains the most stable one when we change the potential applied. MoS_2 has been modeled with 5 Mo layers in the z direction and 4 Mo rows in the x direction. In the y direction, two MoS_2 sheets have been modeled in order to obtain a symmetric system and avoid problem of dipole moment in the cell. In all the calculations, the symmetry has been maintained by applying the same modifications on the two nanosheets (same edge structure, same adsorption geometries…). Between each slab, approximately 40 Å of vacuum is added in the z direction.

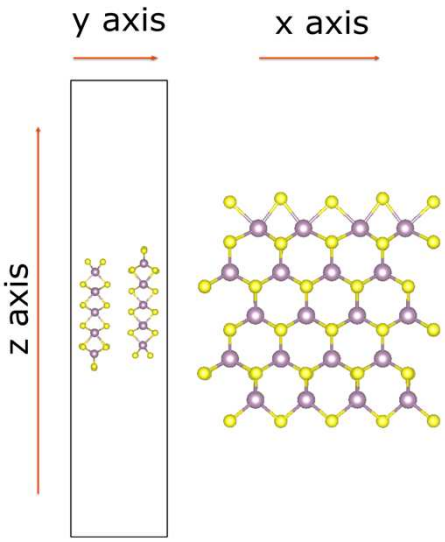

Figure V-2 : Structure of the MoS_2 50%S restructuration from two point of view: from the x direction on the left and from the y direction on the right.

This classical restructuration has been chosen to be the starting point of our mechanistic study. However, given that it is a tunable structure, our MoS_2 nanosheet is expected to face chemical modifications, depending on the experimental conditions, as explored by Nawras Abidi in our laboratory [13]. These chemical modifications on the edge structure, through hydrogenation, hydroxylation or hydration, are expected to strongly modify the catalytic

activity of the edge. All these chemical modifications will be presented in detail in the following part, in order to choose the most adapted edge structure for our mechanistic study.

V.2. Results

V.2.1. Evolution of the edge sites under electrochemical conditions

V.2.1.a. Hydrogenation of the nanosheet

First, we consider the hydrogenation of the MoS_2 nanosheet, with the aim of identifying the favorable adsorption sites for H atoms. Concerning the Mo-edge, it has been identified that the favored adsorption site is the sulfur site ($\Delta G = -0.48\ eV$) in order to form an SH (sulfhydryl) group (Figure V-3). Upon an increase of the H coverage, we observe an alternation in the orientation of the S-H bond, with half of the S-H oriented in one direction and the other part oriented in the opposite direction (see structure 100%H on Figure V-3). While the adsorption of the first H is thermodynamically favorable, the second one is isoenergetic whereas the following ones become thermodynamically unfavored ($\Delta G = +0.45\ eV$ for the third and fourth hydrogen atoms). After that, supplementary hydrogens may be adsorbed on Mo sites in order to form Mo-H bonds in a thermodynamically unfavored adsorption ($\Delta G = +0.45\ eV$ for the first three Mo-H and $= +0.97\ eV$ for the fourth one). However, these values calculated at 0 charge, do not include the effect of the potential applied, that will be considered later by applying the surface charging method (III.2.3.b) on the structures with different hydrogen coverages.

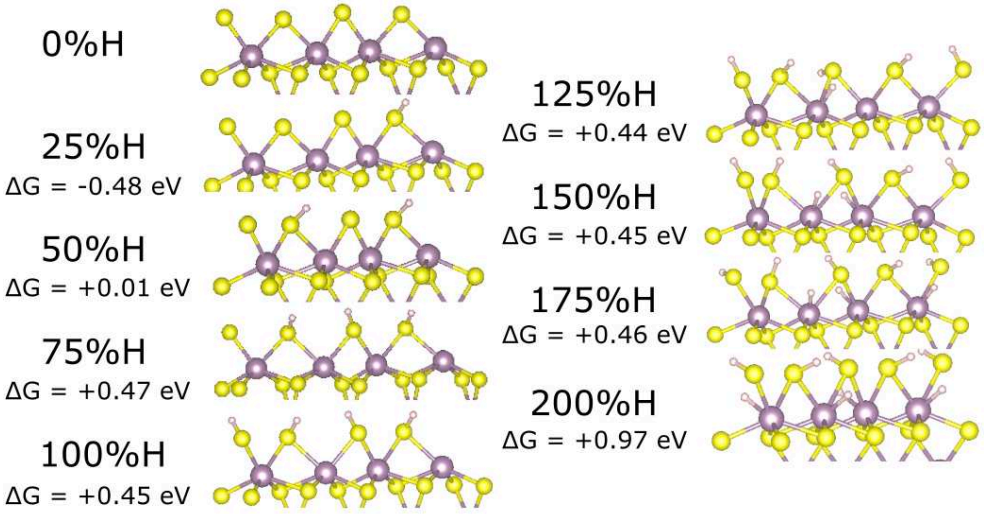

Figure V-3 : Evolution of the hydrogen coverage on a MoS_2 Mo-edge.

Concerning the opposite edge, the S-edge, the more favorable adsorption for H atoms are localized in bridging position between two Mo atoms with a slightly endothermic adsorption energies between - 0.18 and - 0.09 eV (Figure V-4). The adsorption on sulfur, through the formation of S-H bonds appears to be thermodynamically unfavored (between + 0.30 and + 0.36 eV as a function of the coverage). Once again, as explained above, the potential has to be considered to determine the stable structures in real conditions (once the system is charged).

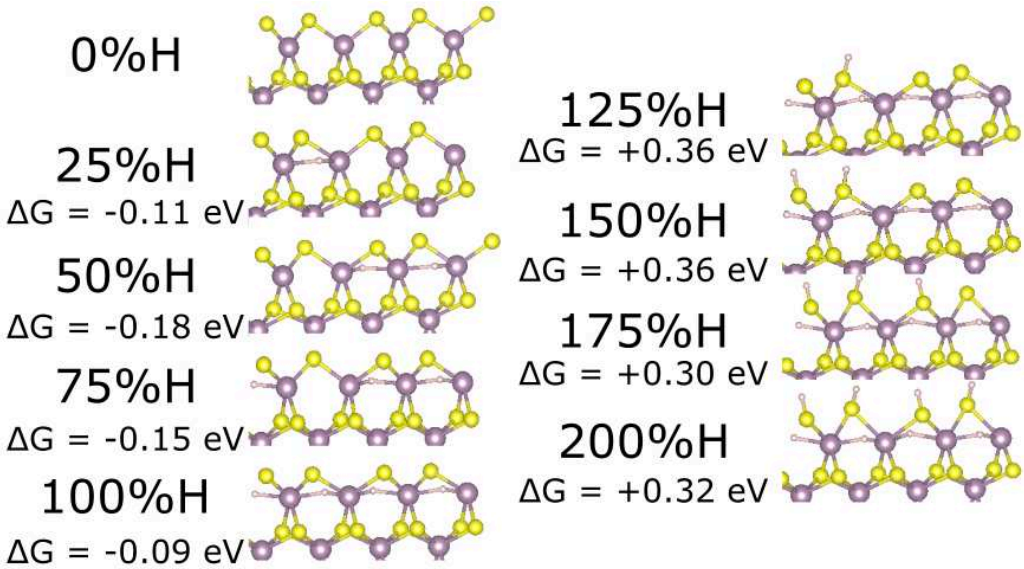

Figure V-4 : Evolution of the hydrogen coverage on a MoS_2 S-edge.

V.2.1.b. Hydroxylation of the nanosheet

Based on the preliminary work of N. Abidi [13], we know that hydroxyl groups can also be stabilized on MoS_2 edges under aqueous conditions. There are two different ways to consider the presence of hydroxyl groups on MoS_2 edges: the direct adsorption of hydroxyl groups on the edge and the substitution of surface sulfurs with oxygen atoms.

In the case of the direct adsorption of hydroxyl groups on the edges, the adsorption sites are the same as in the hydrogen adsorption case: on the sulfur atoms of the M-edge (through the formation of S-OH groups) and on molybdenum atoms of the S-edge (through the formation of a Mo-OH-Mo bridge). The OH adsorption is far more favorable on the S-edge, with adsorption energies of - 0.30 eV in average. In comparison, the adsorption is strongly unfavored on the Mo-edge (adsorption energies higher than + 1 eV). It can be easily explained by the steric repulsion, with Mo atoms that can strongly interact with the hydroxyl groups in the S-edge case while they are nearly inaccessible on the Mo-edge, leading to an unfavored adsorption on S sites. For these reasons, OH adsorption has been only considered on the S-

edge (Figure V-5 c). In order to confirm the stability of the OH groups and to study the possibility of removing hydrogen to help for the reduction reaction, the evolution of the hydrogen coverage as a function of the potential applied will be studied in the next part.

The second possibility to observe OH groups on MoS_2 edges is through an exchange H_2O/H_2S, starting from the hydrogenated structures presented before in case of presence of water, non-negligible in our case. The exchange can be considered by the following equation:

$$* - SH + H_2O \rightarrow * - OH + H_2S \qquad (V.1)$$

Where * symbolizes the Mo sites on the edge. The exchange energy has been found to be twice higher in the case of the S-edge than in the case of the Mo-edge (+ 0.8 vs + 0.4 eV), that seems to indicate that Mo-edge is less stable under aqueous conditions and H_2S desorption assisted by H_2O adsorption could more probably occur on this edge. In addition, the exchange energy seems to be independent from the coverage and is the same for all the SH, that may lead to the complete hydroxylation of the surface. On the S-edge, while the following exchanges appear to be more feasible (+ 0.4 eV), the first exchange (+ 0.8 eV) seems to strongly limit the hydroxylation of this surface. For these reasons, the exchange has been considered only in the case of the Mo-edge.

Two different OH coverages have been considered: the half exchange (100%SH gives 50%SH+50%OH as represented in Figure V-5 a) and the complete exchange (100%SH gives 100%OH as represented in Figure V-5 b). In both cases, the exchange is associated to a restructuration, with all OH and SH in top of the Mo atoms and linked with hydrogen bonds (in the previous 100%SH, SH were in bridge between two Mo).

In order to discuss the relative stability of the OH/SH groups and the possibility to use their H atoms for the reduction reaction, the evolution of the hydrogen and OH coverages as a function of the potential will be studied in the next part.

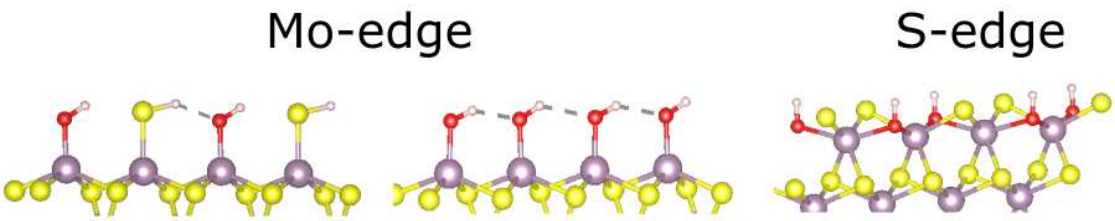

Figure V-5 : Structures associated to the Mo-edge 50%OH+50%SH, the Mo-edge fully 100%OH and the S-edge 50%OH+50%S.

V.2.1.c. Hydration of the nanosheet

In addition to the hydroxylation, it appears to be crucial to consider also the hydration of the edges, with the adsorption of non-dissociated water molecules. On the S-edge, the water molecules may interact with the Mo atoms of the edge, as it was the case for H and OH adsorption (Figure V-6). Chemical Mo-O bonds can be formed, longer than in the case of the hydroxylation (2.4 vs 2.1 Å), while one hydrogen atom points away from the surface and the other one points in the direction of the neighboring nanosheet. The adsorption energy is twice less exothermic than in case of the hydroxylation (- 0.15 vs - 0.30 eV).

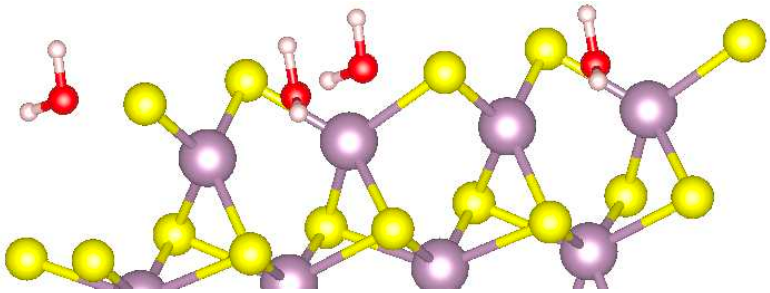

Figure V-6 : Optimized structure of the water adsorption on a MoS_2 S-edge 50%S.

On the Mo-edge, only physical adsorption has been observed with one hydrogen that is pointing toward a sulfur atom of the edge, with a neutral adsorption energy. For these reasons, only the S-edge has been considered to be possibly hydrated, while the Mo-edge do not adsorb molecules but interact with the water solvent, implicitly described in the calculations. However, the presence of water molecule on the edge seems to limit the approach of other molecules, such as our reactant, the CO_2. Despite many adsorption structures tested, we did not manage to identify stable CO_2 adsorbed on the edge without desorbing at least one water molecule. Given that the necessity to consider CO_2/H_2O exchange to possibly obtain activated species, reactivity studies have not been yet performed on hydrated edges.

V.2.2. Evolution of the hydrogen coverage as a function of the potential

Before studying the CO_2 reduction mechanism on these edges, it appears to be crucial to have a look on the effect of the potential on the hydrogen coverages, in order to choose the relevant edges' chemical state to study. To do that, we have used we surface charging approach to calculate the energetic variation of the edge as a function of the potential. The bare edge (surface with 0%H) serves as reference and corresponds directly to the interpolation curve calculated with the surface charging approach G(*) = f(U) where * stands for the edge without H adsorbed and U the potential applied.

In the case of the hydrogenated systems, the equation of the curve can be written as follows:

$$G(* + nH) = G(U) - n \times \left(G(H^+) + G(e^-)\right) \qquad (V.2)$$

where $G(U)$ is the interpolation curve calculated with the surface charging approach, n is the number of hydrogens added on the edge, $G(H^+)$ the energy of a proton and $G(e^-)$ is the energy of an electron. The term in parenthesis can be developed as follow:

$$G(H^+) + G(e^-) = \frac{1}{2}G(H_2) - U \qquad (V.3)$$

with U the potential applied and $G(H_2)$ the energy of a dihydrogen molecule.

V.2.2.a. On bare edges

First, we focus on the bare edges (Figure V-2) and the effect of hydrogenation on these edges (Figure V-3 and Figure V-4).

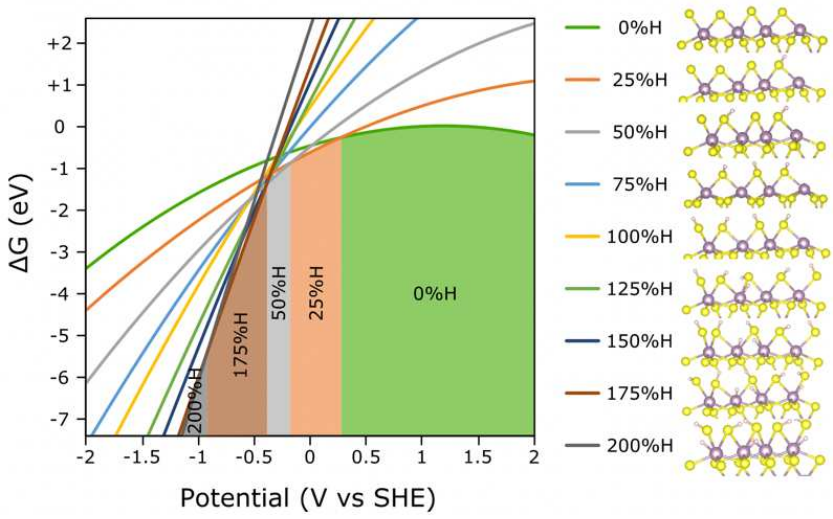

Figure V-7 : Evolution of the hydrogen coverage as a function of the potential applied on Mo-edge 50%S.

In case of the surface charging approach (Figure V-7), the results show the predominance of the bare surface on oxidation conditions (stable for all the potentials higher than 0.3 V). Concerning the adsorbed structures, four coverages can be observed to be stabilized successively with the diminution of the potential (25%H -> 50%H -> 175%H -> 200%H). In particular, despite unfavorable adsorptions without charge applied, the 200%H coverage appears to be the most stable when we reach potentials lower than – 0.9 V. Given that a negative potential is expected to be applied to do the reduction reaction, this result indicates a high stability of the high hydrogen coverages in this potential area. However, the curves are quite close in energy and the lower coverages cannot be completely ignored. The relatively good stability of the systems with lower coverages seems to indicate the lability of the hydrogen atoms, that could help to do the targeted reduction reactions.

However, although the study shows the stability of higher coverages (175% and 200%), we have limited the coverage to 50%H for the mechanistic study, in order to avoid problems of steric repulsion. With the aim to discuss the effect of the presence of hydrogen, the bare surface (0%H) will also be considered.

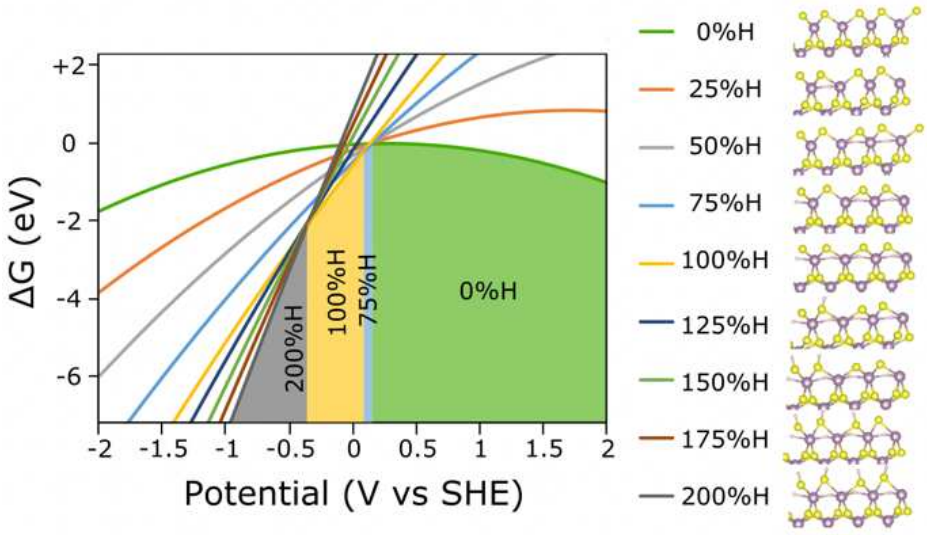

Figure V-8 : Evolution of the hydrogen coverage as a function of the potential applied on S-edge 50%S.

The same study has been performed on the S-edge, as represented in Figure V-8. It shows here again the predominance of the bare surface (0%H) for potentials higher than 0.2 V. In the lower potentials, we observe the successive predominance of the 75%H, the 100%H and the 200%H. Observed stable only in small potential range around 0.2 V, the 75%H seems not to be stable in reduction conditions. On the other hand, the 100%H is the most stable coverage between - 0.4 and 0.1 V while the 200%H is predominant for all the potentials under - 0.4 V. As it is the case on the Mo-edge, although the study shows the stability of higher coverages (100% and 200%), we have limited our mechanistic study to 50%H, not found stable but very close in energy. It allows us to compare the behavior of the two edges under the same coverage (50%H). For the same reason, the bare surface (0%H) will also be considered.

In addition to the two approaches presented above (H_2 as the hydrogen source and H_2O as the hydrogen source with the surface charging approach), the comparison with the CHE method [14] have also been performed for these two cases. In this method, the equations associated to the Gibbs energy of a system can be written as follow:

$$G(* + nH) = G(0) - n \times \left(G(H^+) + G(e^-)\right) = G(0) - n \times \left(\frac{1}{2}G(H_2) - U\right) \qquad (V.4)$$

with $G(0)$ the energy calculated without charging the surface and that does not depend on the potential. In other words, contrary to the surface charging approach that imply a quadratic

dependence in the potential, the CHE method implies a linear variation of the energy with the potential.

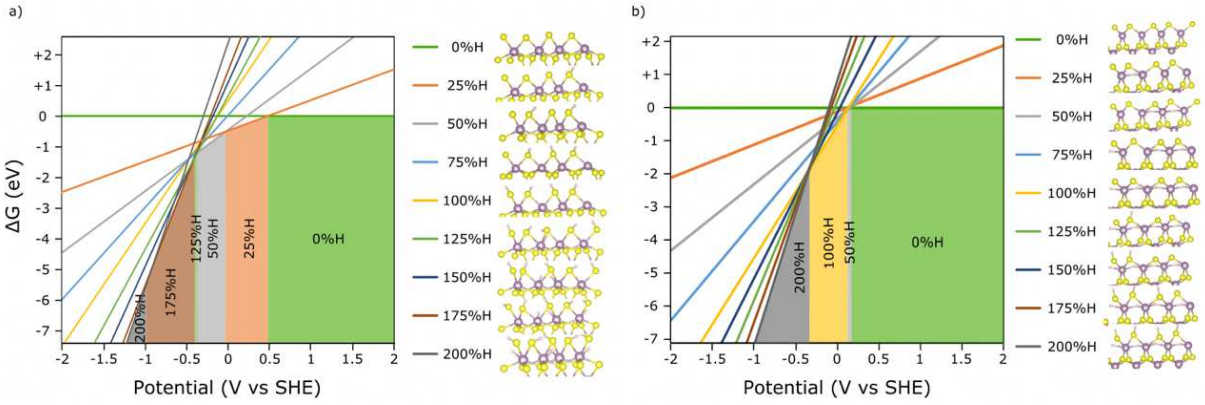

Figure V-9 : Evolution of the hydrogen coverage as a function of the potential applied with the computational hydrogen electrode (CHE) method on a) Mo-edge 50%S and b) S-edge 50%S.

When we use the CHE method instead of the surface charging one on the Mo-edge (Figure V-9 a), the global conclusion is the same with the bare surface stable at high potentials and the 200%H stable at low potentials. Nevertheless, some slight differences can be observed in the transition potentials (between 0.1 and 0.3 V of difference) and an additional intermediate coverage appears to be stabilized (125% H) in addition to those identified in the previous case. When the CHE method is applied on the S-edge (Figure V-9 b), the results are almost identical as those obtain with the surface charging method (Figure V-8) but with this time a short predominance range for the 50%H instead of the 75%H observed with the other method.

This comparison shows the small difference between the two methods for hydrogenation studies. However, given that the low energy difference between the coverages and the complexity of the CO_2 reduction mechanisms, the use of the most precise method could be decisive. In addition, working with the surface charging method allow the study of charged intermediates, like the radical $CO_2^{\cdot-}$ that can be involved after the first reduction step.

V.2.2.b. On oxygenated edges

After studying bare and hydrogenated surfaces, we can now study the effect on oxygenated surfaces. On the S-edge, the oxygenation is characterized by the presence of oxygens in bridge between the Mo atoms, observed to be stable for hydrogen (Figure V-4) and hydroxyl adsorption (Figure V-5 c). The bare edge is then composed of 50%O and 50%S. Given that the substitution of sulfur atoms by oxygens has been identified to be unfavored on this edge,

higher oxidation state has not been considered. The evolution of the H coverage as a function of the potential is represented on Figure V-10.

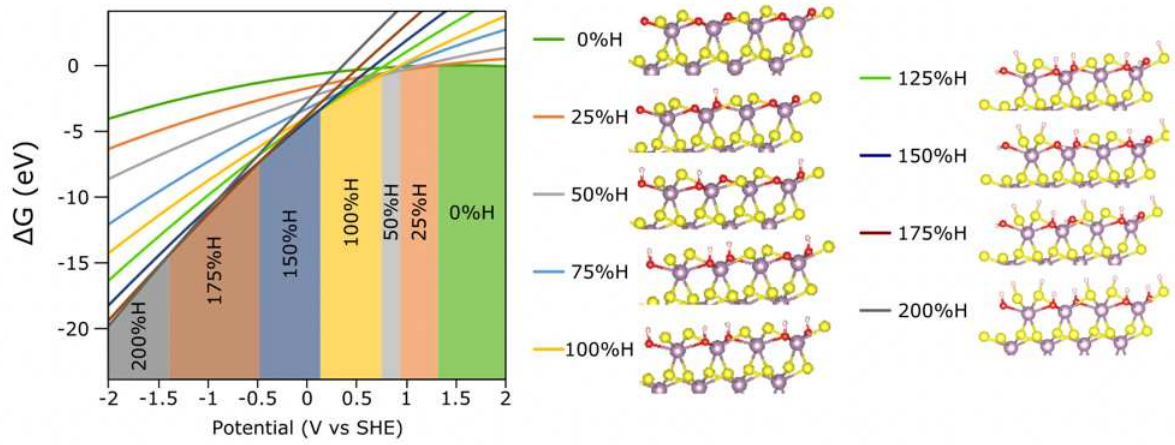

Figure V-10 : Evolution of the hydrogen coverage as a function of the potential applied on S-edge 50% hydroxylated.

When the H coverage is increased, we may form hydroxyls in a first time (the 100%H correspond to the hydroxylation structure Figure V-5 c) and sulfhydryl in a second time.

A wide variety of coverages seems to be possible to observe as a function of the potential. If we focus on the negative potentials, where the reduction reaction is expected to occur, all the coverages higher than 150%H can be obtained, with coexistence of hydroxyl and sulfhydryl groups. In the three cases, all the oxygens have been hydrogenated in order to form hydroxyls and the variation comes only from the number of sulfhydryl formed.

Although stable in a potential area that does not correspond to reductive potentials (between 0.1 and 0.7 V), the fully hydroxylated surface (100%H) has been chosen for the mechanistic study. Limiting the coverage at 100%H will help us to discuss only the effect of hydroxyls groups while the effect of the sulfhydryls is discussed on thee hydrogenated surfaces. The combined effect could be discussed later by increasing the coverage.

On the Mo-edge, it has been identified that H_2O/H_2S exchanges may happen, in order to oxidize the surface by the substitution of S atoms by O atoms.

$$* - S + H_2O \rightarrow * - O + H_2S \qquad (V.5)$$

Two different compositions have been considered and correspond to the half oxygenation of the surface (100%S -> 50%S + 50%O) or the complete oxidation of the surface (100%S -> 100%O).

The evolution of the H coverage as a function of the potential is represented on Figure V-11 for the half oxidation case (50%S + 50%O). As it was the case on the S-edge, it is more favorable to form hydroxyls in a first time and sulfhydryl in a second time (0.22 eV less favorable).

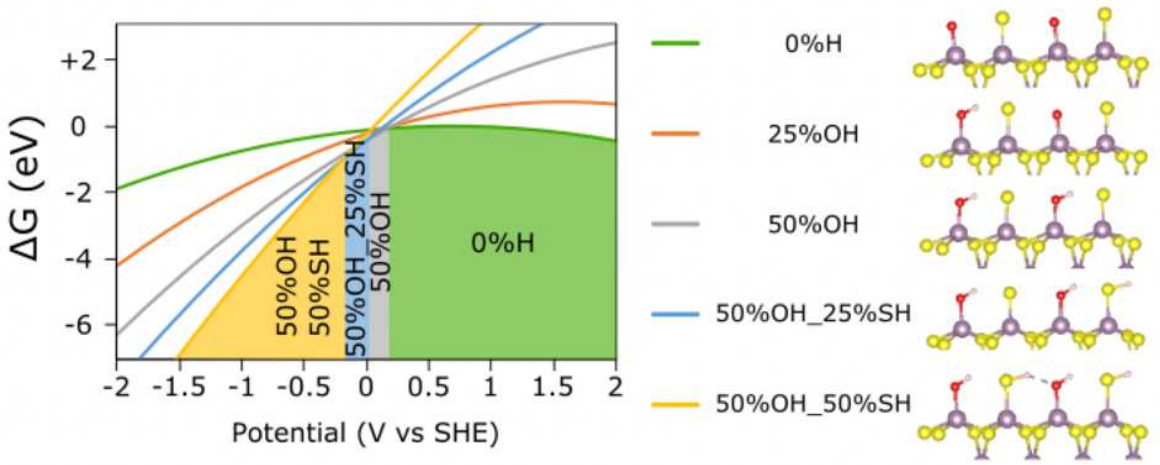

Figure V-11 : Evolution of the hydrogen coverage the more favorable on a MoS_2 Mo-edge with 50%O/50%S as a function of the potential applied.

Concerning the evolution of the H coverage (Figure V-11), the total hydrogenation (50%OH + 50%SH) appears to be the most stable for the potentials lower than - 0.2 V while the bare surface is the more stable for potentials higher than 0.2 V. Intermediate coverages (50%OH + 25%SH and 50%OH) may appear between - 0.2 and 0.2V.

For the mechanistic study, we decided to start with this fully hydrogenated surface, stable on very reductive potentials. The hydrogens from the sulfhydryls, less stables than the hydroxyls, could be used for the reduction step.

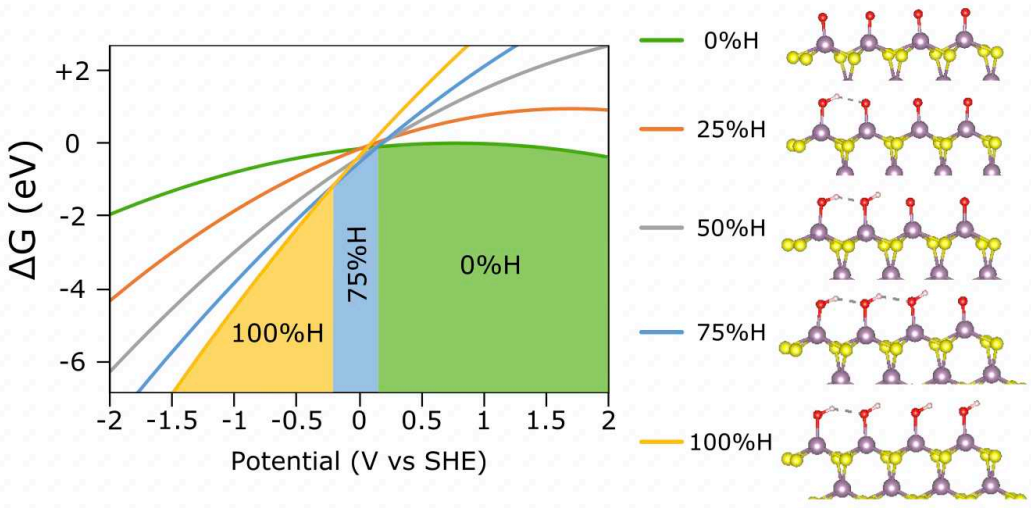

Figure V-12 : Evolution of the hydrogen coverage the more favorable on a MoS_2 Mo-edge 100%OH as a function of the potential applied.

In the case of the full oxidation of the surface (100%O), the conclusion is similar: the strong stability of the 100%H coverage (full OH) is reached for potentials lower than - 0.2 V (Figure V-12). We observe a predominance of 75%H coverage around the 0 potential and 0%H for all potentials higher than 0.2 V.

The results are very similar as those obtained with the half oxidation with the stabilization of the highest coverage. We have thus considered once again the 100%OH, stable on reductive potentials.

V.2.3. CO_2 adsorption

In this part, the objective is to compare the possibility to adsorb a CO_2 molecule on the edges considered. Thanks to the surface charging approach, we manage to discuss the variation of the energy as a function of the potential in order to determine the favorable adsorption state of CO_2 at a given potential.

V.2.3.a. On bare and hydrogenated surfaces

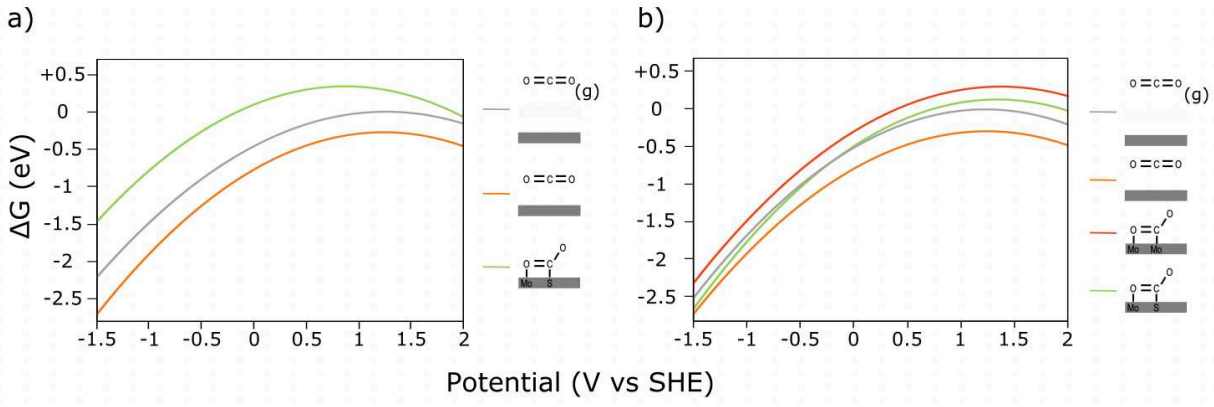

Figure V-13 : CO_2 adsorption study as a function of the potential on a) the bare Mo-edge and b) the bare S-edge.

First, we aim to study the possibility to activate the carbon dioxide molecule on edges without hydrogen, through the adsorption of a bended CO_2 (Figure V-13). On the Mo-edge (Figure V-13 a), the stable adsorption mode of CO_2 consists in the interaction through one O with a Mo site and through its C with a neighboring S site. The second O is pointing away the edge. However, the chemical adsorption remains less stable than CO_2 in gas phase and CO_2 in physical interaction, except for potentials higher than 3.7 V (strong oxidation conditions, not

interesting for our study). The only way to stabilize CO_2 seems to be through a physical adsorption associated to a $\Delta G = -0.31\ eV$.

On the S-edge, (Figure V-13 b) in addition to the adsorption mode presented above, a second one has been identified as less stable, with both O and C atoms in interaction with Mo sites of the edge. However, as for the Mo-edge, the physical adsorption is more stable than the chemical adsorption, with $\Delta G = -0.28\ eV$ comparing to the CO_2 in gas phase. To obtain chemical adsorption more stable than physical adsorption, a potential lower than - 1.9 V is required.

This study illustrates the difficulty of the direct CO_2 activation on both edges with most of the adsorption structures tested that lead to a desorption of the molecule. In the few chemical adsorption modes found stable, we obtain positive adsorption energies. Nevertheless, the chemical adsorption appears to be less unfavorable on the S-edge, with energies of the adsorbed structure close to the physical interaction, in particular when we reach the negative potential as low as - 1 V where the reduction reaction takes place. It should be noticed that none of the previous DFT studies [15, 16] on MoS_2 based system reported this adsorption step which reveals the difficulty to adsorb CO_2 in absence of an explicit potential applied. Even if it seems difficult, the surface charging approach seems to be able to capture the effects of potential on the stabilization of activated CO_2.

In order to study the effect of the pre-hydrogenation of the edge on the CO_2 stability, the same study has been performed with hydrogenated edges with 50%H on each edge (Figure V-14).

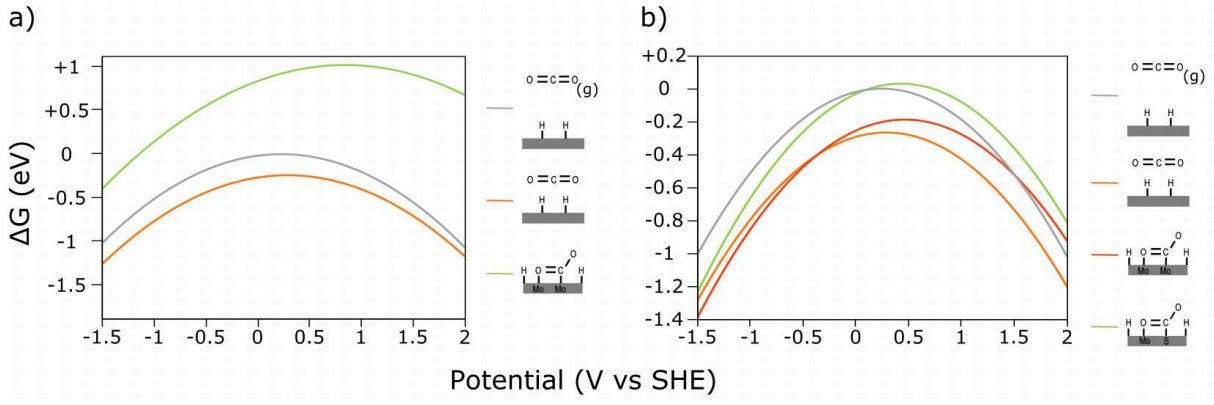

Figure V-14 : CO_2 adsorption study as a function of the potential on a) the Mo-edge 50%H and b) the S-edge 50%H.

On the Mo-edge, due to the hydrogenation of the sulfur atoms, the CO_2 adsorption occurs with both C and O atoms bonded on Mo atoms with a strongly positive adsorption energy.

Concerning the physical adsorption, the adsorption energy is similar with and without hydrogens on the surface ($\Delta G = -0.25\ eV\ vs\ \Delta G = -0.31\ eV$).

On the S-edge, the presence of hydrogens stabilizes the chemical adsorption of CO_2, observed as the more stable for potentials lower than - 0.34 V. Concerning the physical adsorption, the adsorption energy is once again similar with and without hydrogens on the surface ($\Delta G = -0.27\ eV\ vs\ \Delta G = -0.28\ eV$).

To conclude, while the hydrogenation of the Mo-edge increases the difficulty of the CO_2 adsorption, it strongly favors the adsorbed structure on the S-edge. This difference may come from the difference of adsorption sites, with the formation of Mo-H-Mo bridges on the S-edge that seems to stabilize the surface and favor the chemical adsorption.

In that latter case, the CO_2 adsorption could be the first step of the mechanism while in the former, a coupled mechanism involving simultaneous mono-hydrogenation will probably be required.

V.2.3.b. On hydroxylated edges

After illustrating the interest of the hydrogenation of the edges, it seems to be interesting to study if the hydroxylation of the edge can stabilize CO_2 adsorption structures (Figure V-15). One case has been considered on each edge: the Mo-edge 50%OH-50%SH (Figure V-15 a) and the S-edge 50%OH-50%S (Figure V-15 b).

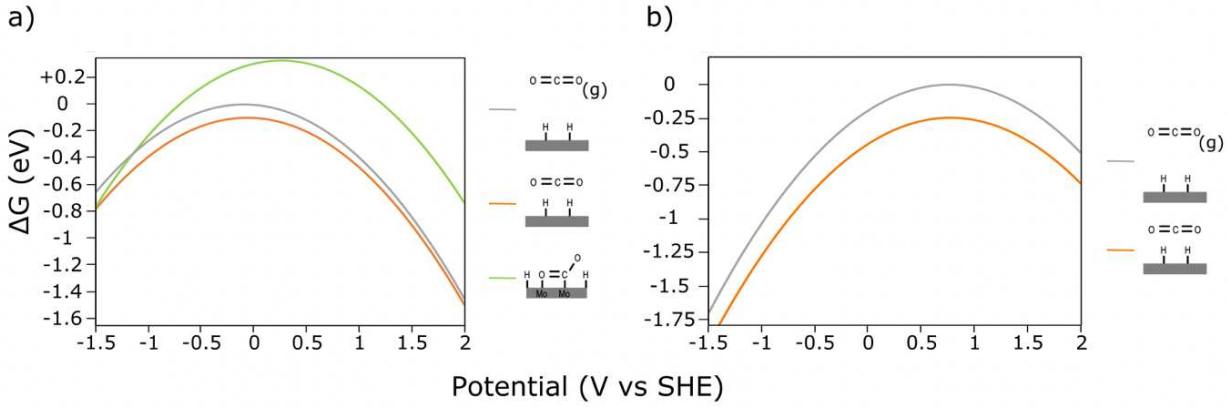

Figure V-15 : CO_2 adsorption study as a function of the potential on a) the Mo-edge 50%OH-50%SH and b) the S-edge 50%OH-50%S.

On the Mo-edge, while the activation through CO_2 adsorption has been shown to be unfavored on edges composed of S and SH, the presence of OH seems to favor the chemical

adsorption. Concerning the physical adsorption, we observed a diminution of the adsorption energy (0.11 vs 0.25 eV before oxidation of the edge). Although a potential lower than - 1.7 V is required to make the chemical adsorption more stable than the physical adsorption, the positive impact of the hydroxyls is clear if we compare with the results obtained on bare (Figure V-13) and hydrogenated surface (Figure V-14).

On the other hand, the presence of hydroxyls on the S-edge limits the possibility to adsorb CO_2 since the hydroxyls are occupying the sites usually used for CO_2 adsorption. For this reason, only physical adsorption has been observed with an adsorption energy (- 0.25 eV) close to those obtained on the bare edge (- 0.28 eV) and on the hydrogenated one (- 0.27 eV).

To conclude, the presence of OH instead of SH seems to stabilize the chemical adsorption and destabilize the physical one on the Mo-edge. The two hydroxylated edges (50%OH + 50%SH and 100%OH) may thus offer the possibility to observe mechanisms starting with the CO_2 adsorption instead of coupled steps. On the other hand, given that the impossibility to adsorb CO_2 on the S-edge 50%OH-50%S, the activation can only be done with a coupled step.

V.2.4. Identifications of the CO_2 reduction mechanisms

In this part, the objective is to compare the possibility to reduce a CO_2 molecule on the edges considered. Thanks to the surface charging approach, we will be able to discuss the variation of the energy of each intermediate as a function of the potential in order to determine the favorable mechanism of CO_2 reduction at a given potential. The interpolation curves associated to the intermediates considered are available in A.2.

V.2.4.a. On hydrogenated edges

In the present section, we studied directly the effect of the pre-hydrogenation of the surface, given that the bare surfaces have been identified to unable the CO_2 activation. We started with a coverage of 50%H and obtained the results presented in Figure V-16.

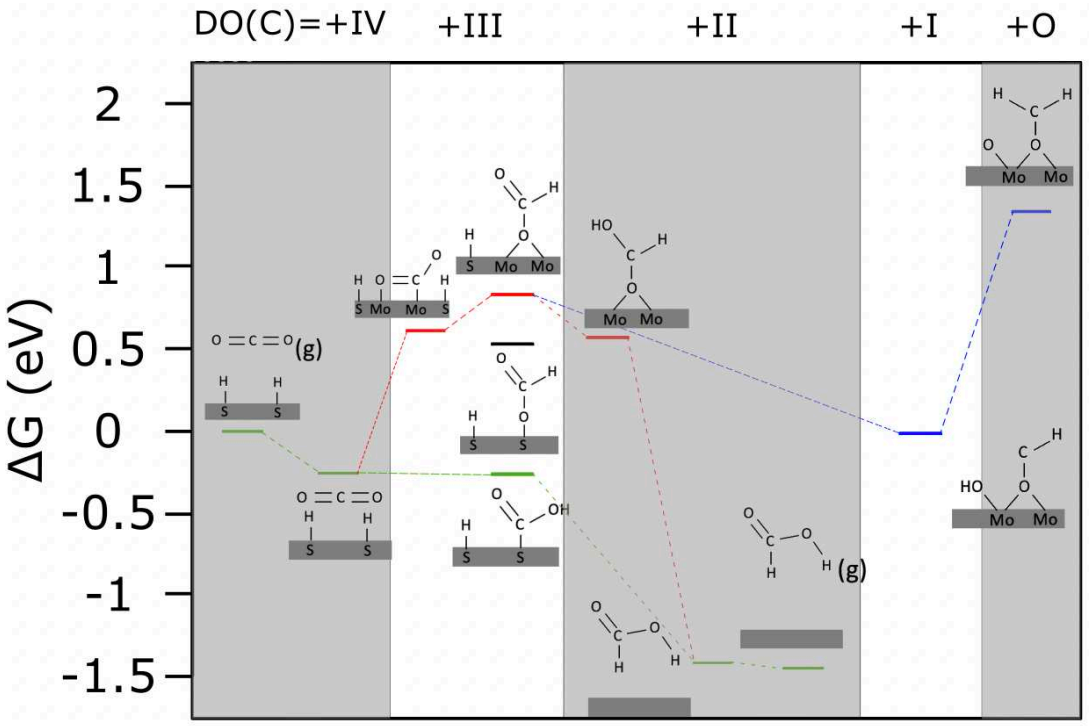

Figure V-16 : Reaction pathways on a Mo-edge 50%SH at - 1.30 V. The green pathway leads to HCOOH through COOH intermediate, the red pathway leads to HCOOH through OCHO intermediate and the blue pathway lead to CH_2O through OCHO intermediate. Black intermediate is not expected to be observed in the mechanism.

The energies presented have been calculated from the interpolation curves (Figure A-7) based on the surface charge calculations as described in the Method section. The potential chosen corresponds to the cross point of the CO_2 VdW curve and the COOH curve. In other words, under this value of - 1.30 V, the formation of the COOH intermediate is thermodynamically favored and all the subsequent ones.

The COOH intermediate has been identified to be formed on S atoms, through the formation of a C-S bond. Given the low stability of a CO_2 adsorbed on the surface ($\Delta G = +0.88\ eV$), we propose that a direct formation of the COOH occurs through a proton-electron coupled transfer. After the formation of this COOH, the following step appears to be the formation and the exothermic release of a HCOOH in VdW interaction ($\Delta G = -1.16\ eV$), given that the formation of a HCOOH adsorbed in a bridge mode between two Mo is strongly unfavored ($\Delta G = +0.82\ eV$). After its formation, the release of the product in gas phase can be done favorably ($\Delta G = -0.03\ eV$). Finally, the regeneration of the surface in order to restart a catalytic cycle, was not represented because strongly favored ($\Delta G = -1.69\ eV$). This pathway is represented in green on Figure V-16.

Concerning other possible intermediates, the formation of a OCHO has been identified to be stable through two modes (red and black paths): on top of a sulfur atom (however less favorable than COOH by $\Delta G = +\,0.78\ eV$) or in bridge position between two Mo atoms, inherited from the chemical adsorption mode of CO_2 ($\Delta G = +\,0.88\ eV$ for the adsorption and $\Delta G = +\,0.31\ eV$ for the OCHO formation). From this OCHO intermediate, two other intermediates can be considered: the formation of chemically adsorbed formic acid HCOOH ($\Delta G = -\,0.27\ eV$), probably followed by a physical adsorption ($\Delta G = -\,1.88\ eV$) or by a dissociation into HCO + O ($\Delta G = -\,0.85\ eV$), leading to an OH on the edge. In the case of release in physical adsorption, the final steps are the same than those presented for the green pathway.

In case of dissociation (blue pathway), the formation of the aldehyde CH_2O appeared to be strongly unfavorable ($\Delta G = +\,1.35\ eV$), probably due to the unstable top Mo-oxo species. At this stage, it can be suspected that the possible formation of aldehyde should preferentially occur from the transfer of an additional proton coming either from SH group or from the solvent and not from this OH. This step is beyond the scope of the present study.

To conclude on this Mo-edge, the formation of formic acid (HCOOH) has been identified to be thermodynamically favored from an applied potential of - 1.3 V, that corresponds to an overpotential of - 1.1 V versus the standard potential associated to the reduction of CO_2 to HCOOH. The mechanism proposed is a five-step mechanism (Figure V-17) that starts from CO_2 gas phase, adsorbed then in a physical mode ($\Delta G = -\,0.25\ eV$). The thermoneutral step is the formation of COOH intermediate that is followed by the formation and the physical adsorption of the formic acid ($\Delta G = -\,1.16\ eV$). After the release of the product in gas phase ($\Delta G = -\,0.03\ eV$), the regeneration of the surface ($\Delta G = -\,1.69\ eV$) is strongly favored. We obtain for the total reaction $\Delta G = -\,3.13\ eV$ at this potential. Half of this energy comes from the regeneration step, very exothermic due to high the stability of hydrogenated surfaces on the reductive potentials (Figure V-7). For this reason, the regeneration is not represented on the pathways (Figure V-16) and can be considered to be spontaneous. It will be the case for all the cases presented in this study.

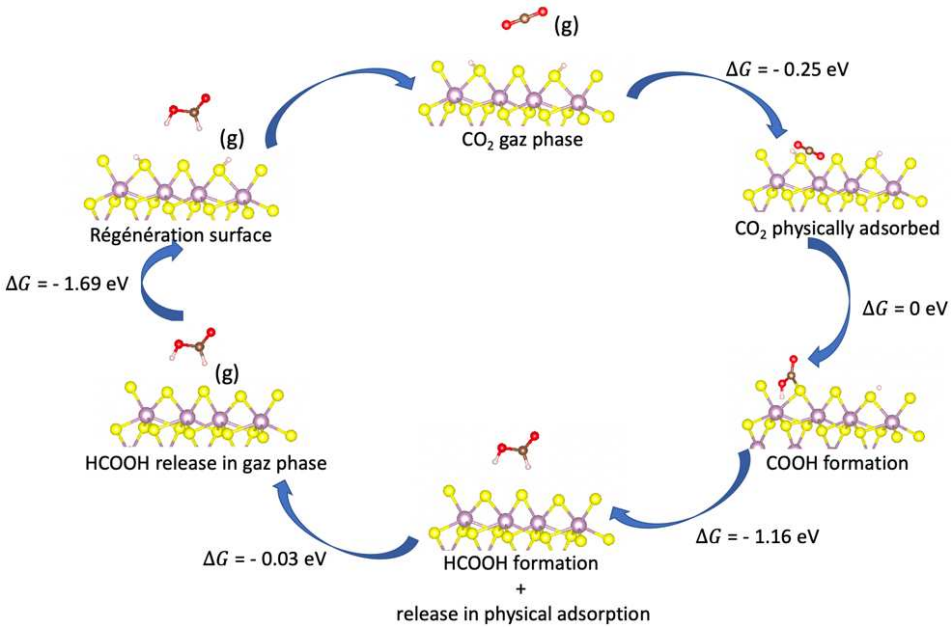

Figure V-17 : Catalysis cycle of the mechanism favored on the Mo-edge hydrogenated for an overpotential of - 1.1 V.

The same study has been performed on the S-edge, with an identical coverage of 50%H (Figure V-18).

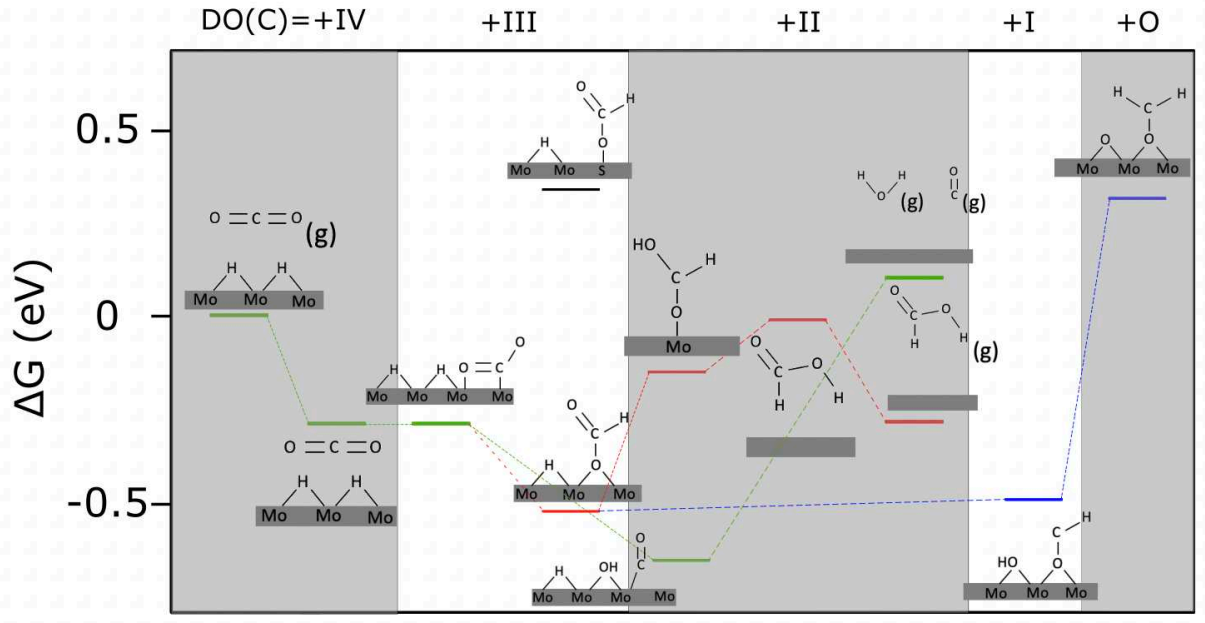

Figure V-18 : Reaction pathway on a S-edge 50%SH at - 0.34 V. The green pathway leads to CO from chemically adsorbed CO_2, the red pathway leads to HCOOH through CO_2 adsorbed and OCHO intermediate and the blue pathway leads to CH_2O through CO_2 adsorbed and OCHO intermediate. Black intermediate is not expected to be observed in the mechanism.

Again, the potential chosen corresponds to the crossing point of the CO_2 VdW curve and the CO_2 adsorbed curve: at a value of - 0.34 V, the formation of the CO_2 activated on the surface is thermodynamically favored which is a much lower value than on Mo-edge.

Following this activation, two intermediates can be formed: carbon monoxide, through the dissociation of the CO_2 molecule (green pathway) or OCHO, through the formation of a C-H bond with a neighboring H (red pathway). The formation of a COOH intermediate, which was favorable on the Mo-edge, is now unfavorable ($\Delta G = +\ 0.40\ eV$). Interestingly, the formation of the CO appears to be more favorable than the OCHO formation ($\Delta G = -\ 0.35\ vs\ -\ 0.23\ eV$) and could be the product favorably formed on this edge. After that, the release of CO and a water molecule seems to be a strongly endothermic ($\Delta G = +\ 0.73\ eV$) step. Nevertheless, the energy difference between the two intermediates is quite low so we cannot neglect the formation of OCHO on the edge. This intermediate can lead to the formation of a HCOOH ($\Delta G = +\ 0.38\ eV$), adsorb on the top of a Mo atom, or it can be dissociated in order to form an HCO ($\Delta G = +\ 0.03\ eV$) in bridge between two Mo atoms (blue pathway). Finally, the HCOOH can be unfavorably desorbed from the edge ($\Delta G = +\ 0.13\ eV$ for its release in physical interaction) but it is then favorably desorbed in gas phase ($\Delta G = -\ 0.35\ eV$). Concerning the HCO, it may lead to the formation of the formaldehyde CH_2O ($\Delta G = +\ 0.80\ eV$). For the same reason (Mo-oxo), this state is high in energy.

To conclude on this S-edge, the formation of carbon monoxide appears to be favored in comparison to the HCOOH formation that present steps strongly unfavored thermodynamically. In particular, the OCHO intermediate appears to be strongly stabilized, even if with change the potential. This make the step of formation of the formic acid (adsorbed or directly desorbed) endothermic for all the potentials.

Although the CO formation is favorable, the cost of its release could be problematic and it may preferentially face further reduction steps not studied here. One possible way would be to proceed through the further CO dissociation leading to 2 hydroxyls and one carbon as expected in the carbene pathway [17]. The applied potential of - 0.34 V corresponds to a rather small overpotential of - 0.22 V versus the standard reduction potential of CO_2 into CO. The mechanism proposed is a five-step mechanism (Figure V-19) that start from CO_2 gas phase, adsorbed then in a physical mode ($\Delta G = -\ 0.28\ eV$). The thermoneutral step is the adsorption of CO_2 intermediate that is followed by its dissociation ($\Delta G = -\ 0.35\ eV$). After that, the desorption of the products ($\Delta G = +\ 0.73\ eV$) is the strongly endothermic step while the regeneration of the surface is exothermic ($\Delta G = -\ 0.88\ eV$). For the global reaction, we obtain thus $\Delta G = -\ 0.78\ eV$.

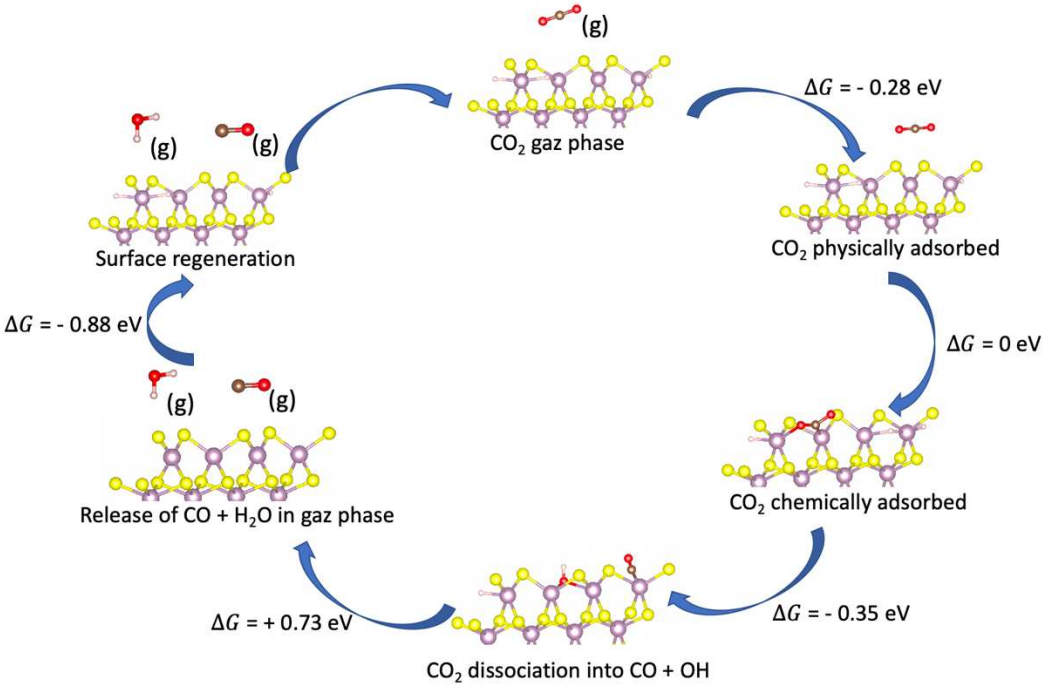

Figure V-19: Catalysis cycle of the formation of CO on the S-edge hydrogenated for an overpotential of - 0.22 V.

V.2.4.b. On hydroxylated edges

First, we focused on the possible mechanism on the structure with 50%OH and 50%SH of Mo-edge. The Gibbs free energy of the reaction intermediates are calculated at - 0.41 V (Figure V-20), that corresponds to the potential value where the activation of CO_2 through the formation of an adsorbed COOH becomes thermodynamically favored.

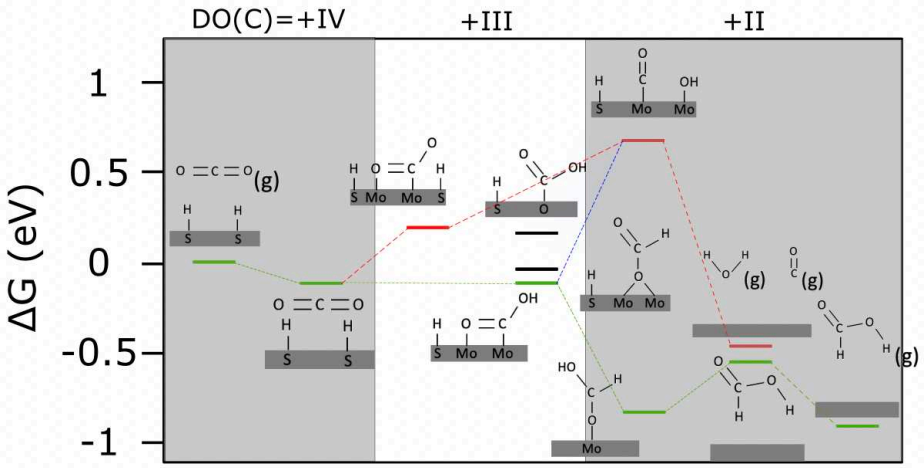

Figure V-20 : Reaction pathway on a Mo-edge 50%OH-50%SH at - 0.41 V. The green pathway leads to HCOOH through COOH as intermediate, the red pathway leads to CO through CO_2 adsorbed as intermediate and the blue pathway lead to CO through COOH as intermediate. Black intermediates are not expected to be observed in the mechanism.

This COOH is adsorbed on the edge through one Mo-O bond and one C-O bond. It can be formed directly via a proton—coupled electron transfer ($\Delta G = 0$), or eventually via pre-adsorbed CO_2 ($\Delta G = +0.31\ eV$), which captures a neighboring hydrogen with exergonic

energy ($\Delta G = -0.31\ eV$). CO adsorbed can be obtained from the dissociation of CO_2 ($\Delta G = +0.48\ eV$, represented in the red pathway) or from the dissociation of COOH ($\Delta G = +0.79\ eV$, represented in the blue pathway). If formed, the CO can be favorably released in gas phase with a water molecule ($\Delta G = -1.15\ eV$). The other intermediates that could be formed during the first electrochemical step (OCHO and OCOOH) appear to be less favorable than the COOH formation: $\Delta G = +0.27\ eV$ for OCOOH (COOH adsorbed on O site) and $\Delta G = +0.07\ eV$ for the OCHO. Given the small energy difference between the OCHO and the COOH (0.07 eV), both can be considered as precursors of the HCOOH formation ($\Delta G = -0.72\ eV$ or $\Delta G = -0.79\ eV$ respectively), following the green pathway. This HCOOH adsorbed on top of one Mo atom can thus be desorbed in physical interaction through a thermodynamically unfavored step ($\Delta G = +0.28\ eV$) that must be followed by its complete desorption in gas phase ($\Delta G = -0.36\ eV$).

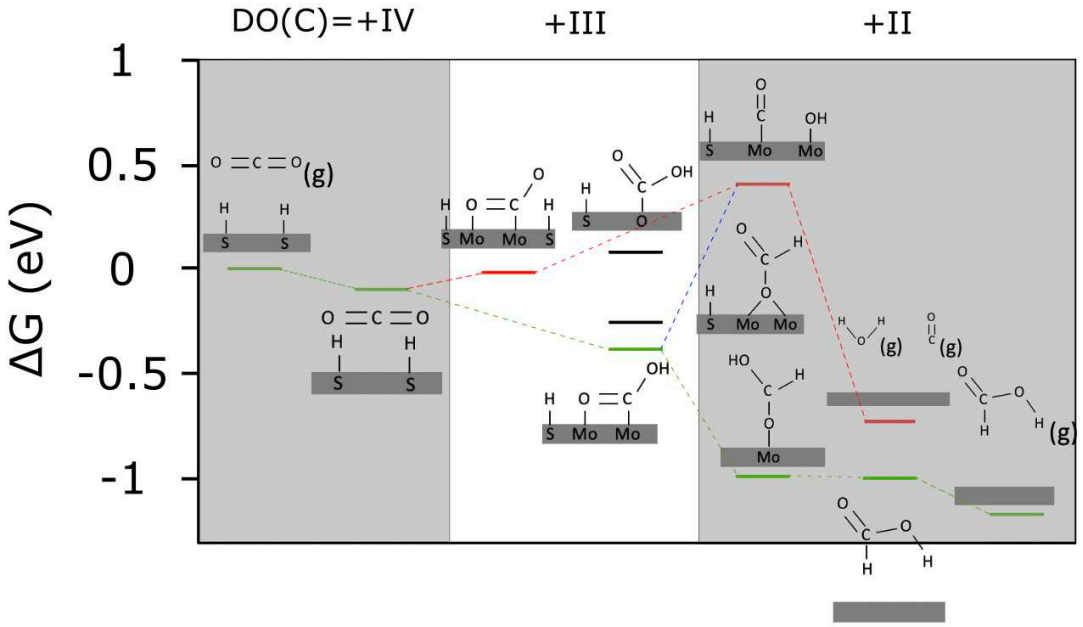

Figure V-21 : Reaction pathway on a Mo-edge 50%OH-50%SH at - 1.29 V. The green pathway leads to HCOOH through COOH as intermediate, the red pathway leads to CO through CO_2 adsorbed as intermediate and the blue pathway lead to CO through COOH as intermediate. Black intermediates are not expected to be observed in the mechanism.

In order to make more favorable the desorption steps, a second analysis has been done at -1.29 V (Figure V-21), that corresponds to the potential value where the HCOOH can thermodynamically go from chemical adsorption to physisorption. At this potential, the global conclusion on the mechanisms is unchanged: only an overall stabilization of all intermediates. If we focus on the HCOOH formation (represented in green), we obtain a six-step mechanism (Figure V-22) that starts with the physical adsorption of the CO_2 molecule ($\Delta G = -0.12\ eV$).

It can be followed by the formation of COOH with a proton-coupled electron transfer ($\Delta G = -0.27\ eV$) and the formation of our product, HCOOH, adsorbed on the edge ($\Delta G = -0.62\ eV$). Finally, after becoming in physical adsorption in the thermoneutral step, HCOOH is spontaneously desorbed ($\Delta G = -0.16\ eV$). The final regeneration step is strongly exothermic ($\Delta G = -1.93\ eV$).

To conclude on this edge composed of 50%OH and 50%SH, the formation of the formic acid (HCOOH) has been identified to be thermodynamically favored from an applied potential of -0.41 V, that corresponds to an overpotential of - 0.21 V versus the standard potential associated to the reduction of CO_2 in HCOOH. However, an applied potential of - 1.29 V is required to allow the desorption of the product. This corresponds this time to an overpotential of -1.09 V with a $\Delta G = -3.1\ eV$.

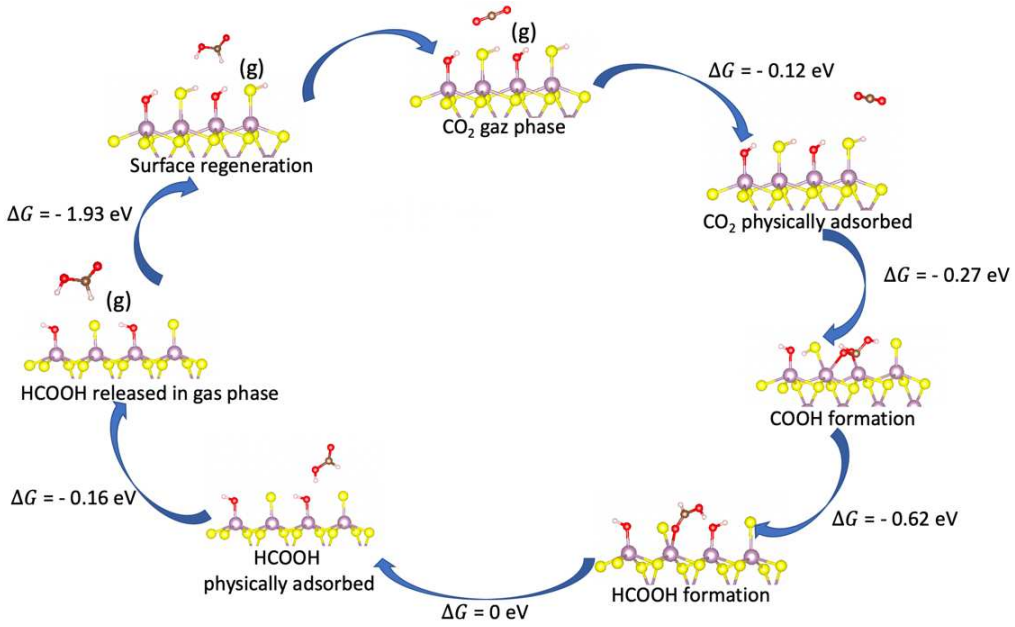

Figure V-22 : Catalysis cycle of the mechanism favored on the Mo-edge 50%OH-50%SH for an overpotential of - 1.09 V.

After the investigations on a mixed edge, composed of 50%OH and 50%SH, we studied the fully hydroxylated edge (100% OH). Given that this edge structure is similar to the mixed structure, with this time all SH replaced by OH, similar intermediates are expected to be

formed. For time reason, some intermediates have at this time only been studied on the mixed structure (50%OH + 50%SH), and are still missing in the study of the 100% OH (Figure V-23).

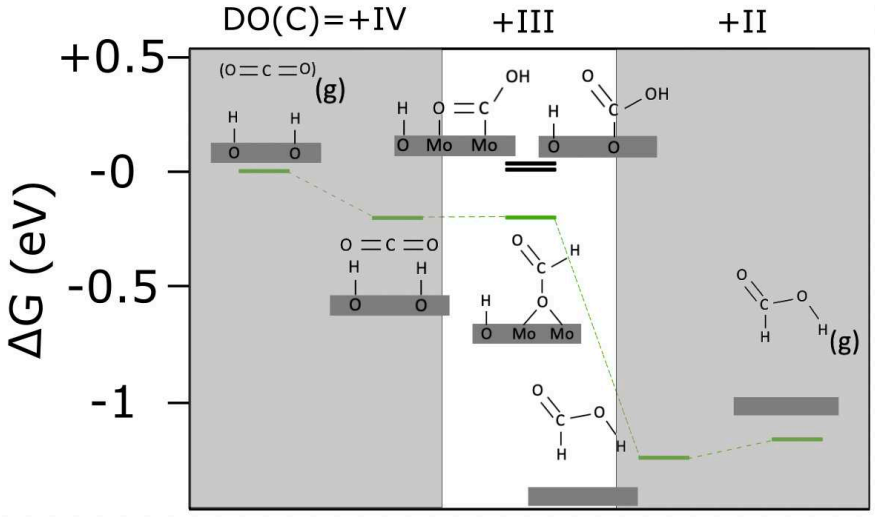

Figure V-23: Reaction pathway on a Mo-edge 100%OH at - 1.28 V. Black intermediates are not expected to be observed in the mechanism.

We have calculated the energy of the different intermediates at - 1.28 V, which corresponds to the potential value where the formation of the first intermediate and all subsequent ones, an OCHO adsorbed in bridge mode between two Mo atoms, becomes thermodynamically favored. At this potential, no CO_2 adsorption has been observed stable on this edge, the intermediate would be formed through a proton-coupled electron transfer. The other possible activated intermediates, COOH and OCOOH, are a little bit higher in energy ($\Delta G = +0.21\ eV$ and $\Delta G = +0.24\ eV$). After the activation through the OCHO intermediate, the formation of HCOOH is be strongly favored, given that the energy of a HCOOH in physical interaction with the edge ($\Delta G = -1.04\ eV$). No HCOOH adsorbed has been found stable, that could signify a spontaneous desorption of the product after its formation. Finally, the desorption the HCOOH product in gas phase can be done through a small endothermic step ($\Delta G = +0.08\ eV$).

To conclude on this edge, that correspond to a Mo-edge fully hydroxylated, the formation of the formic acid (HCOOH) has been identified to be thermodynamically favored from an applied potential of - 1.28 V, that corresponds to an overpotential of - 1.08 V below the standard potential associated to the reduction of CO_2 in HCOOH (- 0.2 V vs SHE). It can be done through a five-step mechanism (Figure V-24) with $\Delta G = -3.08\ eV$ for the total reaction.

However, the study on this edge is not complete. In particular, the identification of stable adsorption of CO_2 and HCOOH could be done inspired from those found on the 50%OH-50%SH edge.

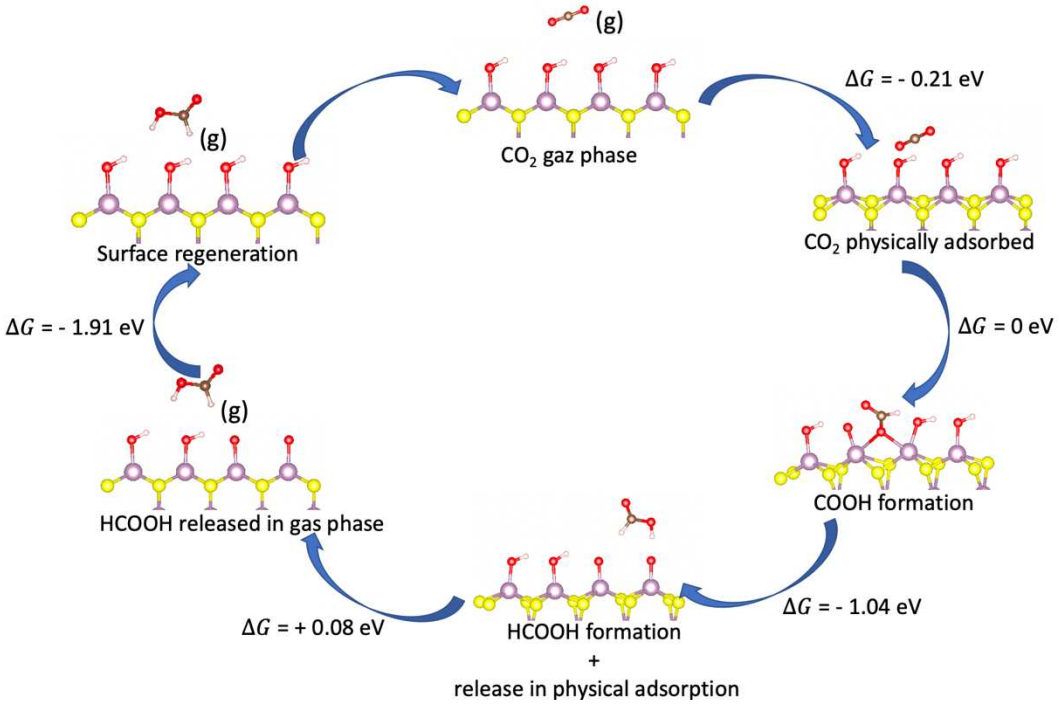

Figure V-24 : Catalysis cycle of the mechanism favored on the Mo-edge 100% OH for an overpotential of - 1.07 V.

To finish the investigation of the hydroxylated edges, we studied the mechanisms possible on the S-edge 50%S after hydroxyl adsorption (Figure V-25).

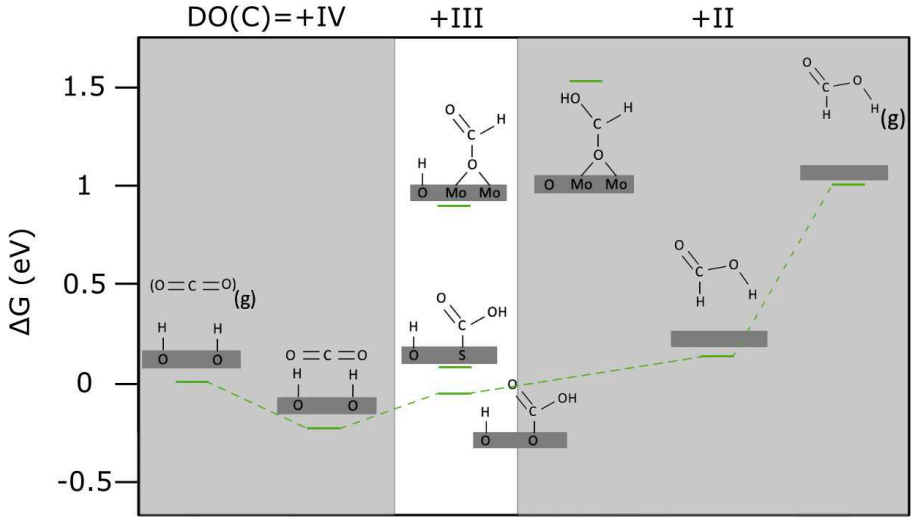

Figure V-25 : : Reaction pathway on a S-edge hydroxylated at - 1.30 V.

Given that no pathway has been identified to be stable, we have chosen to represent the energy of the different intermediates for a potential of - 1.30 V, a value that favored the HCOOH formation on the other edges.

As presented previously (Figure V-15 b), due to the presence of hydroxyls adsorbed, sites are not available for the direct adsorption of CO_2. Concerning the activation through a proton-coupled electron transfer, with the formation of COOH ($\Delta G = +0.31\ eV$), OCOOH ($\Delta G =$

$+ 0.17\ eV$) or OCHO ($\Delta G = + 1.12\ eV$), they are not stable enough to be thermodynamically favored without requiring unrealistic and too low potentials. In the case of the less unfavored activation step, the formation of a HCOOH adsorbed is strongly endothermic ($\Delta G = + 1.76\ eV$). The formation of a HCOOH directly desorbed in physical interaction is more realistic but still unfavored ($\Delta G = + 0.19\ eV$), such as its release in gas phase ($\Delta G = + 0.89\ eV$).

All these unfavored steps could be explained by the fact that the hydrogen used come from hydroxyl groups. As a consequence, the oxo group generated imply a destabilization of the edge, as observed on the study of the S-edge hydrogenated (Figure V-18).

Thus, further investigations could be done with other hydrogen sources. The first possibility could be to use hydrogens that comes directly from the solution, while the second possibility could be the increase of the hydrogen coverage, through the formation of S-H bonds, that could make easier the reduction step.

V.3. Discussion

After exposing the results obtained, the objective of this part is to compare our results to those presented in the literature. We will focus mainly on two aspects: the activation step (what is the activated species favorably formed) and the overpotential applied (what is the product favored and the overpotential associated).

V.3.1. The activated species

In our results, due to the consideration of different edge compositions and structures, we identified various activated species adsorbed on the edges: bent CO_2, formate OCHO or carboxylate COOH. In other words, it corresponds to the species stable after the first electrochemical step in order to obtain DO(C) = +III. The ΔG associated to this activated species, with CO_2 in physical interaction as the reference, are summarized in Table V-2. The edges without activated species thermodynamically favored are not presented.

	Potential applied (V)	ΔG_f(CO₂) (eV)	ΔG_f(OCHO) (eV)	ΔG_f(COOH) (eV)
Mo-edge 50%H	- 1.30	+ 0.88	+ 0.78	0
S-edge 50%H	- 0.34	0	- 0.23	+ 0.63
Mo-edge 50%OH-50%SH	- 1.29	+ 0.08	- 0.15	- 0.27
Mo-edge 100%OH	- 1.28	-	0	+ 0.21

Table V-2 : ΔG associated to the different activated species on the edges where a reaction can occur. The energies are calculated at the potential where the activation becomes thermodynamically favored. Green values are for the intermediates thermodynamically favored, yellow values are for the intermediates close to the CO_2 VdW energy and red values are for the intermediates thermodynamically unfavored.

This table illustrates the sensitivity of the different activated intermediates to different edge compositions which may lead to different products such as CO or HCOOH for instance. In many cases, there are some intermediates close in energy and that could be in competition. In some cases, like on the Mo-edge 50%OH-50%SH, the two intermediates favored (COOH and OCHO) are expected to both lead to the same product, HCOOH. They are just representing two different favorable ways to obtain formic acid and are both expected to be observed. In other cases, like on the S-edge 50%H, the two intermediates in competition (CO_2 adsorbed and OCHO) are expected to lead to CO and HCOOH formation respectively. At this point, due to the fact that the dissociation of CO_2 in CO is more favorable than the HCOOH formation, CO_2 is expected to be the main activated intermediate observed on this case, despite the fact that it is not the most stable one.

As shown in V.2.3, the activated species are directly dependent on the surface conditions. In case of bare surfaces, no activation of the reaction has been identified to be possible, with VdW interaction identified as the more stable. In case of hydrogenation of the surface, we identified the possibility to obtain a CO_2 adsorbed on the surface on the S-edge. On the Mo-edge, while the hydrogenation did not stabilize CO_2, the presence of OH instead of SH has been identified to stabilize it. In addition, the presence of hydrogen species (OH, SH and Mo-H-Mo) offers the possibility to activate the reaction through proton electron coupled transfer in order to obtain (COOH and/or OCHO). Due to the fact that the activated species are directly

dependent on the edge composition, it appears to be crucial to control it, by modification of the potential applied (V.2.2) or by modification of reactional conditions (increase of the pressure mainly). In addition to the control of the type of sites (S, O, SH, OH, Mo-H-Mo…), it may also help to control the number of active sites. As an example, the presence of a too high number of hydrogens on the edges may kill the activity by occupation of all the Mo and S of the edge. Although the presence of hydrogen helps the formation of intermediates, it should be limited.

If we compare our activated intermediates with those involved in the mechanisms proposed in the literature, we can find some similarities. In fact, we can associate the three intermediates observed (OCHO, COOH and CO_2) to the three pathways previously presented (II.2.2.c [17]).

As an example, the activation through the formation of a COOH adsorbed through its carbon, as observed on the M-edge 50%H, is the activation step proposed in the formaldehyde pathway. The adsorption of CO_2 followed by a dissociation in CO + OH, as observed on the S-edge 50%SH, is close to the activation process of the carbene pathway. Concerning the OCHO formation, observed on the Mo-edge 100% OH, is close to the activation process of the glyoxal pathway, despite an adsorption mode a little bit different (bridge mode between two metals instead of bidentate binding through the two oxygens).

Concerning the Mo-edge 50%OH-50%SH, the formation of a COOH seems to be close to the activation process of the formaldehyde pathway, an adsorption mode different (bidentate adsorption through both C and O atoms instead of monodentate adsorption with only one of them). These differences come mainly from the fact that the mechanistic study was mainly done on TiO_2 [17], that implies different adsorption modes.

If we compare our work with other published results, based on the Computational Hydrogen Electrode (CHE), the main difference comes from the fact than we have been able to identify the CO_2 adsorption while they only consider activation through the formation of COOH and OCHO [15, 16]. This difference in the activation step is expected to lead to differences in the mechanisms proposed.

V.3.2. The possible mechanisms

On our systems, we can identify three different mechanisms. The first one, favored under -1.3 V on the Mo-edge 50%H and on the Mo-edge 50%OH-50%SH, that tends to favorably form and desorb HCOOH after forming the COOH intermediate. These steps are common to the classical mechanism proposed for the formaldehyde pathway [17] but given that the low stability of the HCOOH adsorbed and the high stability of the desorbed structure, additional reduction steps to form formaldehyde, methanol or methane seems to be difficult to pursue.

The second mechanism, observed on the M-edge 100%OH, tends to favorably form HCOOH adsorbed through the OCHO intermediate, as expected in the glyoxal pathway. Between, -1.29 V and - 0.41 V, the low stability of the HCOOH desorbed might offer the possibility to go further in the glyoxal pathway, through the dissociation into CHO + OH and the dimerization HCOCHO. In case of potentials lower than - 1.29, the desorption will take the lead and avoid these aspects.

The third mechanism, observed on the S-edge 50%H, tends to favorably form a CO and a OH adsorbed on the hydrogenated edge by dissociation of the CO_2 adsorbed. It seems to be favorable for the initiation of the carbene pathway leading to CH_4. To do that, the CO must dissociate again in order to form a C and another OH adsorbed on the edge. In that case, the competitivity with the CO desorption has to be studied as well. Note that the release of CO may also be interesting, considering that CO is known to be converted into hydrocarbons by alternative chemical process such as Fischer-Tropsch synthesis.
Concerning the mechanisms found with the CHE method on S-edge doped with Ni [15, 16], the proposed mechanism starts is activated by the formation of a COOH, dissociated in the next step in CO + OH, an intermediate observed on the S-edge 50%H as described above. As it is the case in our work, the formation of carbon monoxide has been identified to be more favorable than the HCOOH formation. The next proposed steps (CO*->CHO*->CH_2O*) have been found thermodynamically unfavored to be realized in our case ($\Delta G = +\ 0.80\ eV$ for the reaction CHO* -> CH_2O*). That comes from the fact that we do not have enough hydrogens to stabilize the system and the CH_2O is formed by using a H from the OH group formed at the previous step. The oxo group formed is probably responsible of the destabilization. In case of

study at higher hydrogen coverage, we will have the possibility to use H from S-H groups. In that situation, the realization of further reduction steps through the formation of the CH_2O intermediate may be a competitive pathway.

V.3.3. The overpotential applied

In three cases (Mo-edge 50%H, Mo-edge 100%OH, Mo-edge 50%OH-50%SH), we managed to obtain a complete favorable mechanism from CO_2 activation (in OCHO or COOH) to HCOOH in physical interaction. In addition, it is very interesting to notice that these three similar mechanisms are expected to occur at the same potential (- 1.30, - 1.28 and - 1.29) and by extension are associated to the same overpotential (- 1.1 V). It seems to indicate that despite differences in the mechanism, the same reaction is expected on all the Mo-edge, no matter the composition of the edge (SH, OH or both). Given that the few reduction steps realized (only two), the overpotential is quite high in comparison to those observed experimentally (- 0.26 V on Pd-Sn alloy [18] and higher than - 0.8 V on copper [19]). For that reason, it could be interesting to investigate further the effect of doping MoS_2 with other metals which might lower this overpotential value.

If we assume that the side effects are limited, the electronic structure associated to our material is the same than an infinite MoS_2 monolayer (Figure V-26). We found the conduction band to start at – 3.53 V vs vacuum that corresponds to a potential of 3.53 – 4.45 = - 0.92 V vs SHE. In these conditions, the overpotential required will correspond to a Fermi level inside the conduction band (as targeted to do the reactions), with an energy difference of 0.4 eV between the potential applied and the edge of the conduction band.
If we want to reach this potential (i.e. this Fermi level), the charge carrier dynamics have to be in favor of the accumulation of electrons in the conduction band, in order to rise the Fermi level of the materials. In other words, an equilibrium has to be found between the events that accumulate electrons (light absorption, transfer from another semiconductor with higher conduction band edge…) and the events that consume these electrons (recombination with the holes, transfer to another semiconductor with a lower conduction band edge, reactions…). These phenomena could be simulated at a higher scale, for instance by using finite element

methods solving all the semiclassical equations of semiconductors leading to the density of charge carriers inside the materials and thus allowing to estimate the electron's Fermi level.

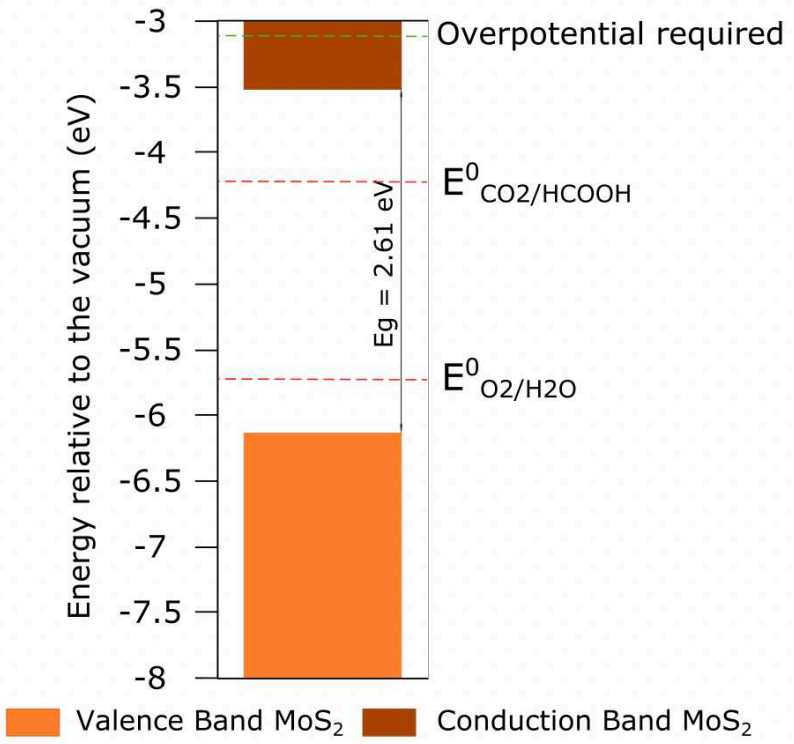

Figure V-26 : Electronic structure associated to a MoS_2 nanosheet and comparison with the standard potential of the targeted reactions and the overpotential required.

Concerning the S-edge, we have identified that the formation of CO appears to be favored at a significantly low potential of - 0.34 V that corresponds in that case to a very low overpotential (- 0.22 V). However, its unfavorable desorption may indicate that it is more favorable to form other products after further reduction steps. In that case, it will probably increase the overpotential in order to obtain value close to the experimental values and close to the expected conduction band of the material.

V.4. Conclusion

The mechanistic study on the Mo-edge has identified the favorable formation of formic acid (HCCOH) with an overpotential of - 1.1 V in all the edges composition. The presence of SH or OH seems to influence only the intermediate stabilized but not the product formed and the potential needed to be applied. To fully finalize the study on this edge, some investigations are still necessary on the fully hydroxylated edge (100% OH), where some intermediates have not been identified yet.

On the S-edge, the stabilization of CO has been identified but its desorption cost may be problematic. For this reason, investigations on further redaction steps are expected to be performed. In particular, it could be interesting to consider the carbene formation through the CO dissociation as described in the carbene pathway [17].

We have seen that the edges are expected to expose very high hydrogen coverages. It could be interesting to extend our study at these high coverages, that may help us to do further reduction steps. In particular, the highest presence of hydrogen will stabilize our CH_2O intermediates in a pathway that could lead at the end to the formation of CH_4.

Given that this strong stabilization of the high hydrogen coverages, the regeneration steps have been found to be strongly exothermic. For this reason, it could be interesting to consider it not only at the end of the mechanism, but also during the mechanism, between two reduction steps.

Due to the quite high overpotential required, the realization of the reaction need an accumulation of the electrons in the conduction band of the material. The complete conclusion on the feasibility of the reaction, that require to study the complete photochemical mechanism and all the charge dynamics involved, is beyond the scope of our work. However, the determination of the overpotential required, such as the electronic structures determined in Chapter IV, are already crucial parameters that will help to answer this question.

V.5. References

[1] G. Kresse and J. Hafner, *Journal of Physical Review B,* vol. 49, pp. 14251-14269, 1994.

[2] G. Kresse and J. Furthmüller, *Journal of Physical Review B,* vol. 54, pp. 11169-11186, 1996.

[3] H. Kresse and J. Furthmüller, *Journal of Computational Material Science,* vol. 6, pp. 15-50, 1996.

[4] G. Kresse and D. Joubert, *Physical Review B,* vol. 57, pp. 1505-1509, 1999.

[5] J. Perdrew, K. Burke and M. Ernzerhof, *Physical Review Letter,* vol. 77, pp. 3865-3868, 1996.

[6] S. Grimme, S. Ehrlich and L. Goerigk, *Journal of computational chemistry,* vol. 32, p. 1456, 2011.

[7] M. Bajdich, M. Garcia-Motta, A. Vojvodic, J. K. Norskov and A. T. Bell, *Journal of the American Chemical Society,* vol. 135, pp. 13521-13530, 2013.

[8] M. Frisch, G. Trucks, H. Schlegel, G. Scuseria, M. Robb, J. Cheeseman, G. Scalmani, V. Barone, G. Petersson and e. a. , *Revision A,* vol. 3, 2016.

[9] C. Adamo and V. Barone, *The Journal of Chemical Physics,* vol. 110, p. 6158, 1999.

[10] [Online]. Available: https ://github.com/henniggroup/VASPsol.

[11] K. Mattew and R. G. Hennig, *Condensed Matter - Materials Science,* pp. 1-6, 2016.

[12] P. Raybaud, J. Hafner, G. Kresse, S. Kasztelan and H. Toulhoat, *Journal of Catalysis,* vol. 189, pp. 129-146, 2000.

[13] N. Abidi, A. Bonduelle-Skrzypczak and S. N. Steinmann, *The Journal of Physical Chemistry C,* vol. 125, pp. 17058-17067, 2021.

[14] J. K. Norskov, L. Rossmeisl, A. Logadottir, L. Lindqvist, J. R. Kitchin, T. Bligaard and H. Jonsson, *The Journal of Physical Chemistry B,* vol. 108, pp. 17886-17892, 2004.

[15] K. Chan, C. Tsai, H. A. Hansen and J. K. Norskov, *ChemCatChem,* vol. 6, pp. 1899-1905, 2014.

[16] X. Hong, K. Chan, C. Tsai and J. K. Norskov, *ACS Catalysis,* p. DOI: 10.1021/acscatal.6b00619, 2016.

[17] S. N. Habisreutinger, L. Schmidt-Mende and J. K. Stolarczyk, "Angew. Chem. Int. Ed. 2013, 52, 7372 – 7408," *Angewandte Chemistry International Editions,* vol. 52, pp. 7372-7408, 2013.

[18] X. Bai, W. Chen, C. Zhao, S. Li, Y. Song, R. Ge, W. Wei and Y. Sun, *Angewandte Chemistry International Edition,* vol. 56, pp. 12219-12223, 2017.

[19] D. Ren, J. Fong and B. S. Yeo, *Nature Communications,* vol. 9, 2018.

Chapter VI. Conclusions and perspectives

The work presented in this manuscript aimed at providing a better understanding of the challenging carbon dioxide photoreduction using MoS_2 semiconductor by using quantum computational chemistry. In particular, we brought a strong attention in the use of MoS_2 as both a light harvester in combination with a larger bandgap semiconductor (TiO_2) and as a co-catalyst to perform the CO_2 reduction reactions.

After illustrating in Chapter II the challenges associated to the CO_2 photoreduction as well as the interests and limits in the use of MoS_2 in photocatalysis, we have presented in Chapter III the theoretical methods and tools used to describe the different steps of the photocatalysis mechanism.

With the aim to overcome the limit of the small bandgap of MoS_2, Chapter IV was dedicated to the study of MoS_2/TiO_2 heterostructures. The results obtained have shown two different types of heterostructures as a function of the nature of the interaction: a type II heterojunction in the case of physical interaction at the MoS_2/TiO_2 interface and a type I heterojunction in the case of chemical interaction. The latter type I heterojunction could be used in photocatalysis only if MoS_2 is considered as a co-catalyst of the system and TiO_2 will be the main semi-conductor harvesting photons. In the former type II heterojunction, the charge transfer seems to be in favor of a Z-scheme mechanism, although this would require further investigations on the kinetics of charge transfer mechanisms. For both heterojunctions, the presence of MoS_2 may help for the charge separation and the conduction bands of MoS_2 would collect electrons available for the further reduction of CO_2 as investigated in Chapter V.

This PhD manuscript has confirmed the interest of MoS_2 in photocatalysis, although a Z-scheme mechanism seems to be required to reach high reduction and oxidation potentials. In order to confirm the Z-scheme mechanisms identified on our MoS_2/TiO_2 systems, the use of experimental methods will be now required: self-confirmation by photocatalytic reactions [1], selective photodeposition of a noble metal [2], in situ X-ray photoelectron spectroscopy (XPS)

irradiated analysis [3], surface photovoltage technique (SPV) [4] or femtosecond TDR Spectroscopic analysis [5].

In Chapter V, a mechanistic study has been performed on MoS_2 edges with the surface charging approach, with the aim to increase the understanding in the CO_2 reduction mechanism. In particular, our approach brought precision on the first electrochemical step, with identification of CO_2 adsorbed on the edges, impossible to consider in previous approaches. Among this first step, our work shows that the mechanism and the product formed will clearly depend on the edge (Mo-edge or S-edge) and its composition (hydrogenation, hydroxylation and coverage associated). To complete the mechanistic study, complementary calculations are required. In particular, the study of the effect of the hydrogenation coverages would be mandatory to better quantify the overpotential required for the H transferred to the CO_2 molecule and the optimal source of this H (either on the surface or from the solvent). From now on, a strong collaboration with experimental works could increase the precisions of the mechanism. Given that the impact of the edge composition on the mechanism, it is crucial to work with realistic edge composition that fit with the experimental conditions (pH, pressure, temperature…). To do that, additional thermodynamic studies on the relative stability of the edges have to be performed.
Beyond that, we suggest to undertake a multi-scale study of the complete photochemical mechanism on these systems, from the light absorption to the desorption of the products. These aspects can be developed through TD-DFT calculations [6] or with the use of COMSOL Multiphysics [7]. A particular attention should be raised on the possibility for the material to reach the targeted overpotential determined. If the Z-scheme proposed in Chapter IV is confirmed, the mechanisms identified are expected to take place on the edges of MoS_2 monolayer in physical interaction with TiO_2 surfaces. These heterostructures will be thus intensively studied on this multi-scale approach.

References

[1] W. Yu, J. Chen, T. Shang, L. Chen, L. Gu and T. Peng, *Applied Catalysis B,* vol. 219, p. 693, 2017.

[2] Q. Xu, B. Zhu, C. Jiang, B. Cheng and J. Yu, *Solar RRL,* vol. 2, p. 1800006, 2018.

[3] J. Low, B. Dai, T. Tong, C. Jiang and J. Yu, *Advanced Materials,* vol. 31, p. 1802981, 2019.

[4] H. Li, Y. Gao, Y. Zhou, F. Fan, Q. Han, Q. Xu, X. Wang, M. Xiao, C. Li and Z. Zou, *Nano Letters,* vol. 16, p. 5547, 2016.

[5] M. Zhu, Z. Sun, M. Fujitsuka and T. Majima, *Journal of Materials Chemistry A,* vol. 2, p. 3381, 2014.

[6] M. Irikura, Y. Tamaki and O. Ishitani, *Chemical Science,* vol. 12, pp. 13888-13896, 2021.

[7] A. T. Garcia-Esparza and K. Takanabe, *Journal of Materials Chemistry A,* vol. 4, p. 2894, 2016.

Appendix

A.1. Spatial localization of the most relevant interfacial states of MoS_2/TiO_2 heterostructures in chemical interaction

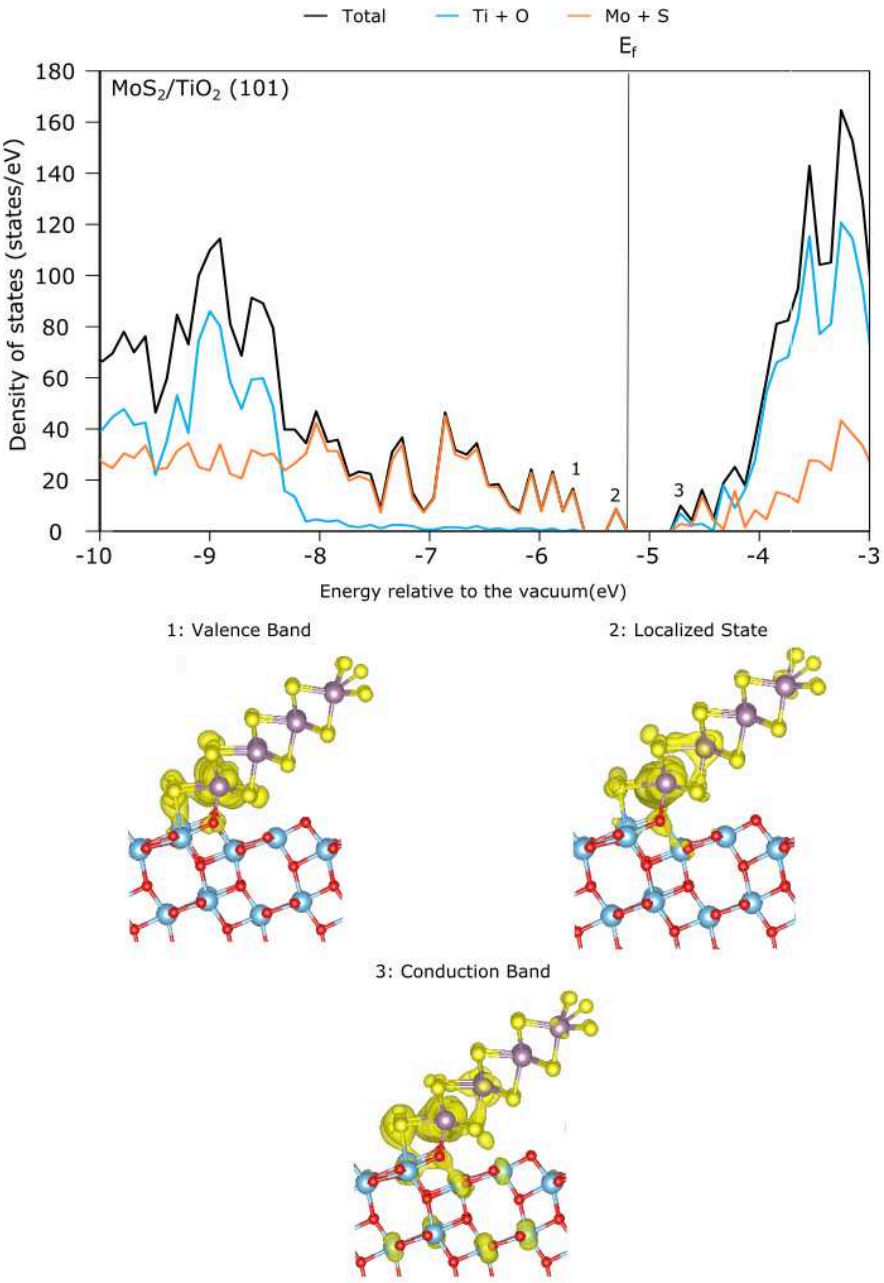

Figure A-1 : Localization of the most relevant states for MoS_2 in chemical interaction through the Mo-edge on TiO_2 anatase (101).

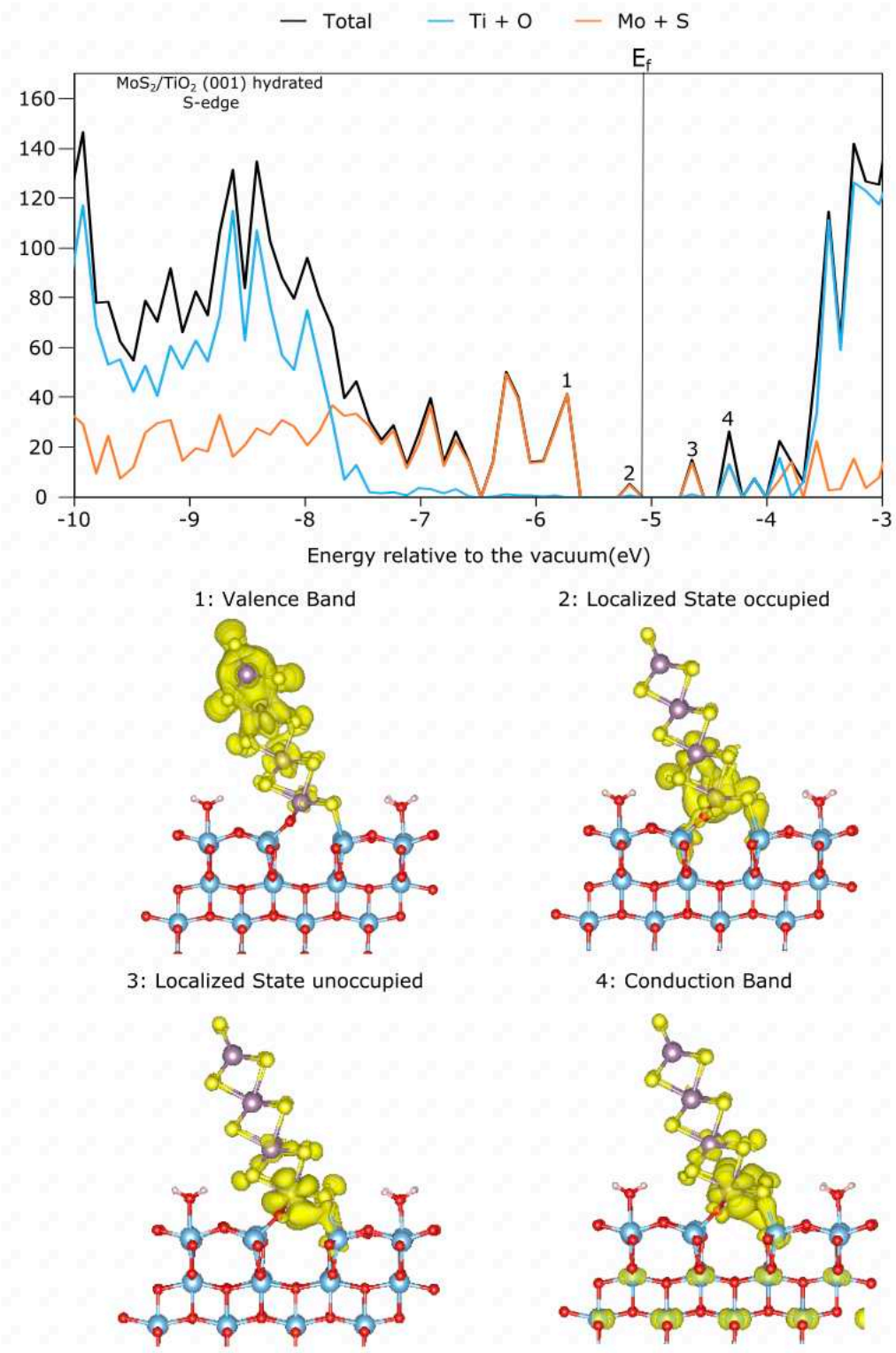

Figure A-2: Localization of the most relevant states for MoS_2 in chemical interaction through S-edge on TiO_2 anatase (001).

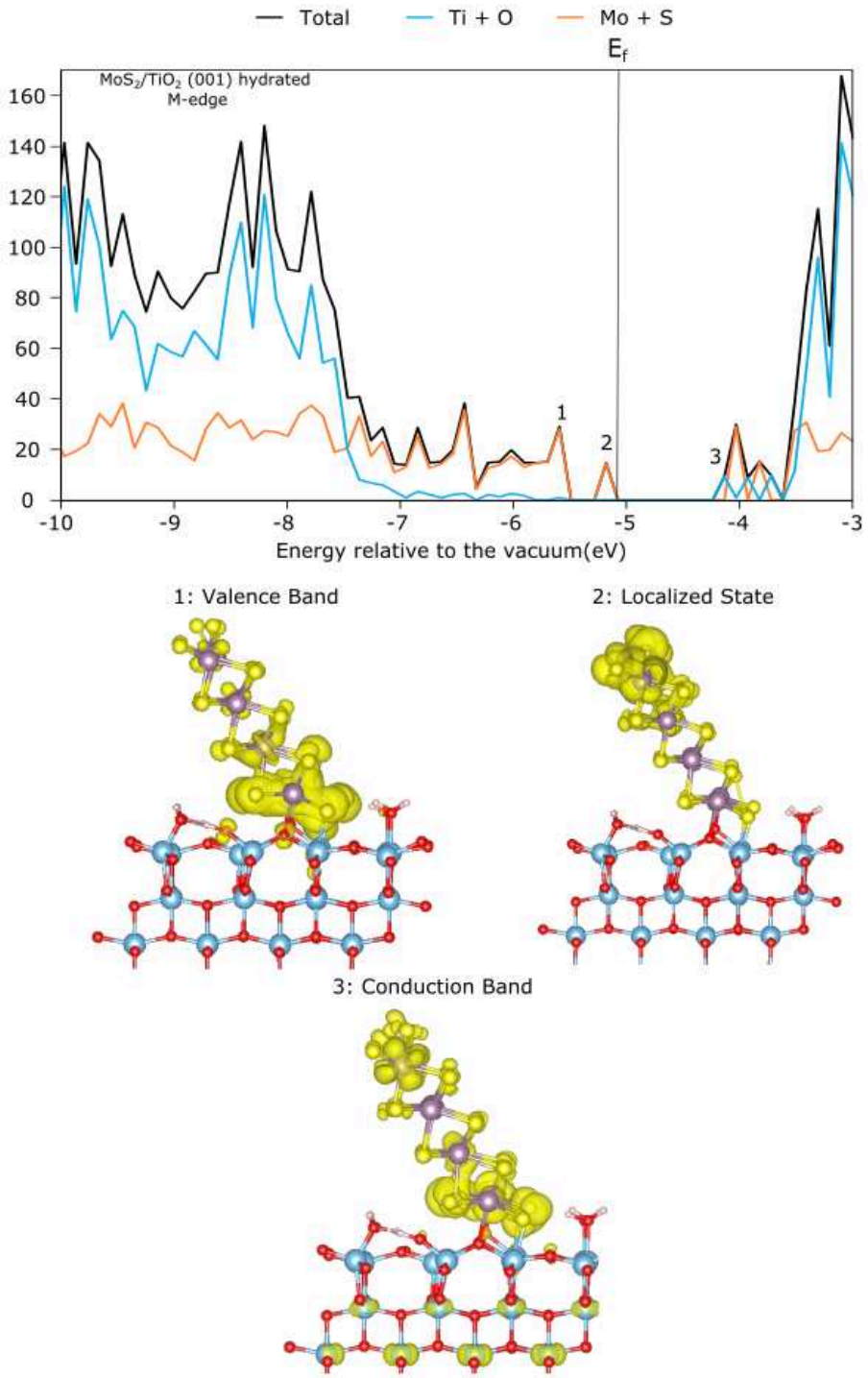

Figure A-3: Localization of the most indicative states for MoS_2 in chemical interaction through Mo-edge on TiO_2 anatase (001).

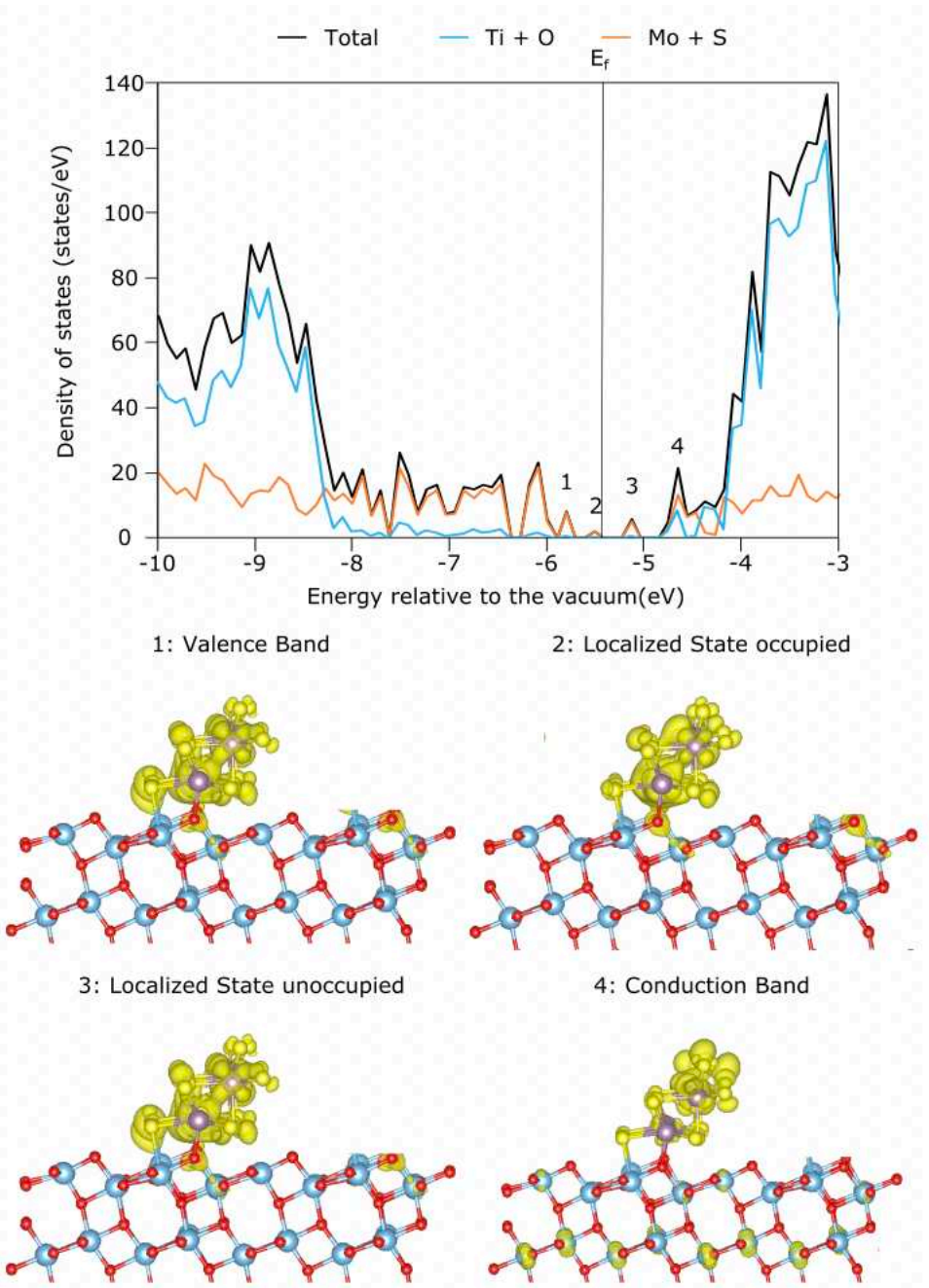

Figure A-4 : Localization of the most indicative states for MoS_2 with 2Mo rows in chemical interaction through Mo-edge on TiO_2 anatase (101)

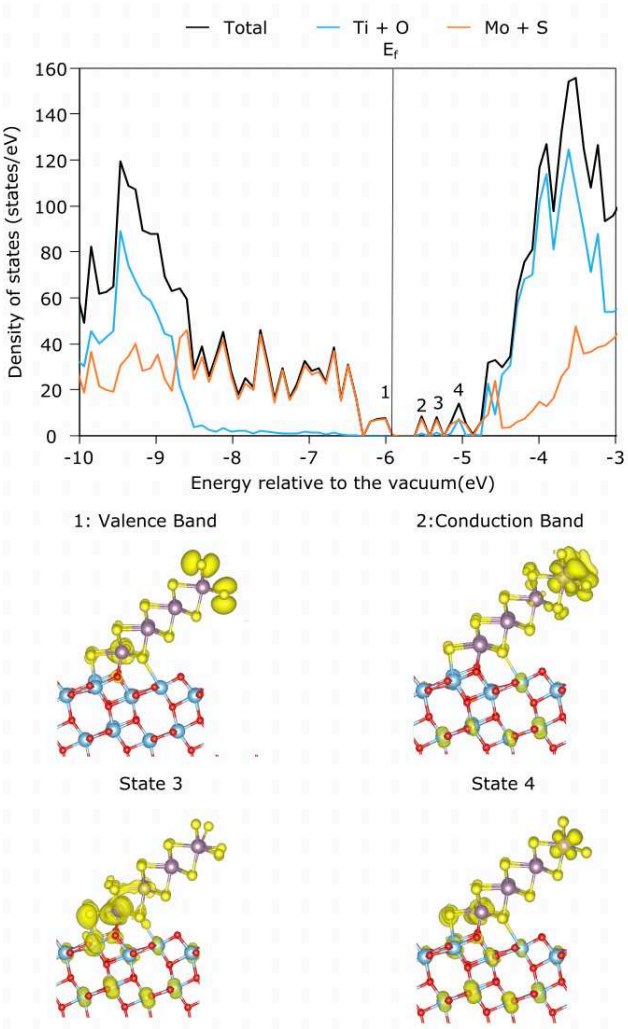

Figure A-5: Localization of the most indicative states for MoS_2 sulfided in chemical interaction through Mo-edge on TiO_2 anatase (101).

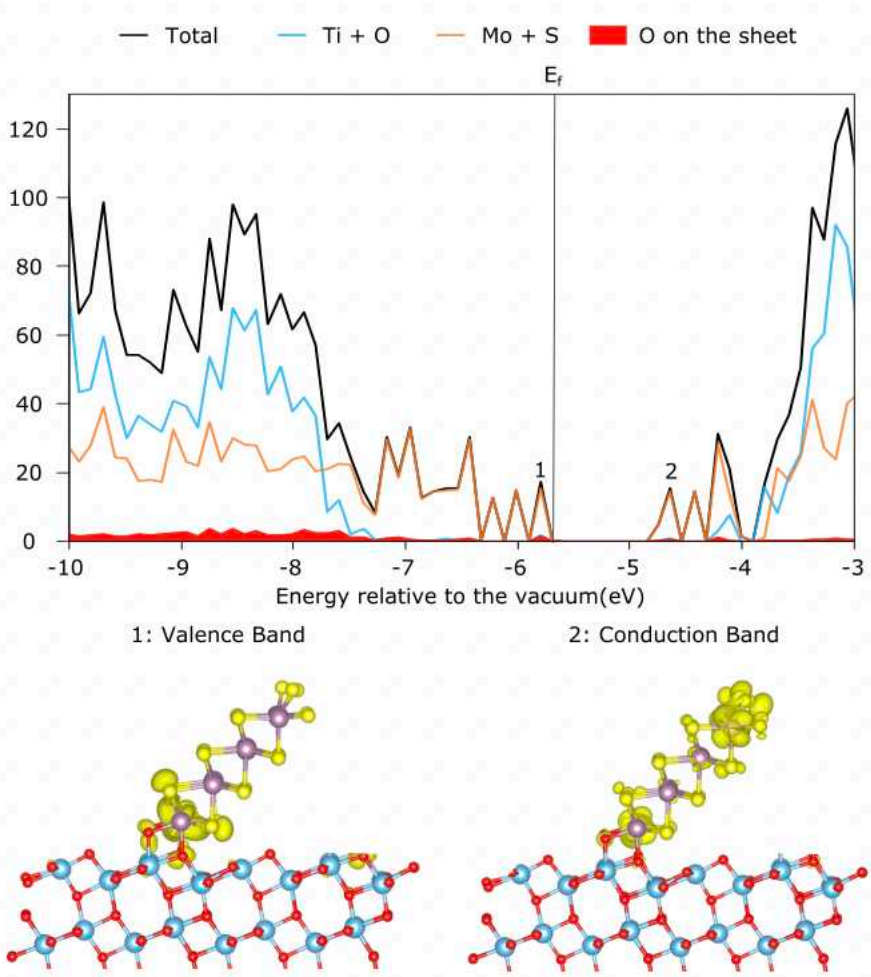

Figure A-6: Localization of the most indicative states for MoS_2 oxygenated in chemical interaction through Mo-edge on TiO_2 anatase (101).

A.2. Extrapolation curves associated to all the intermediates considered in the mechanisms

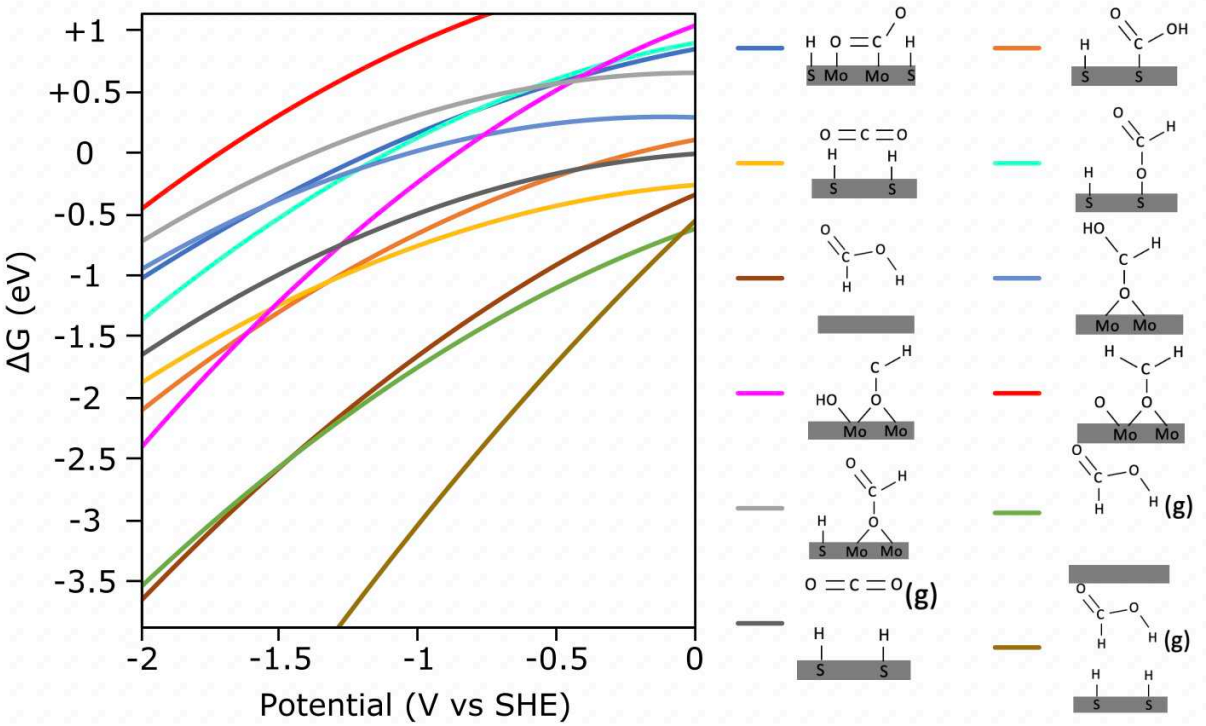

Figure A-7 : Extrapolation curves associated to all the intermediates considered in the mechanistic study on the Mo-edge 50%H.

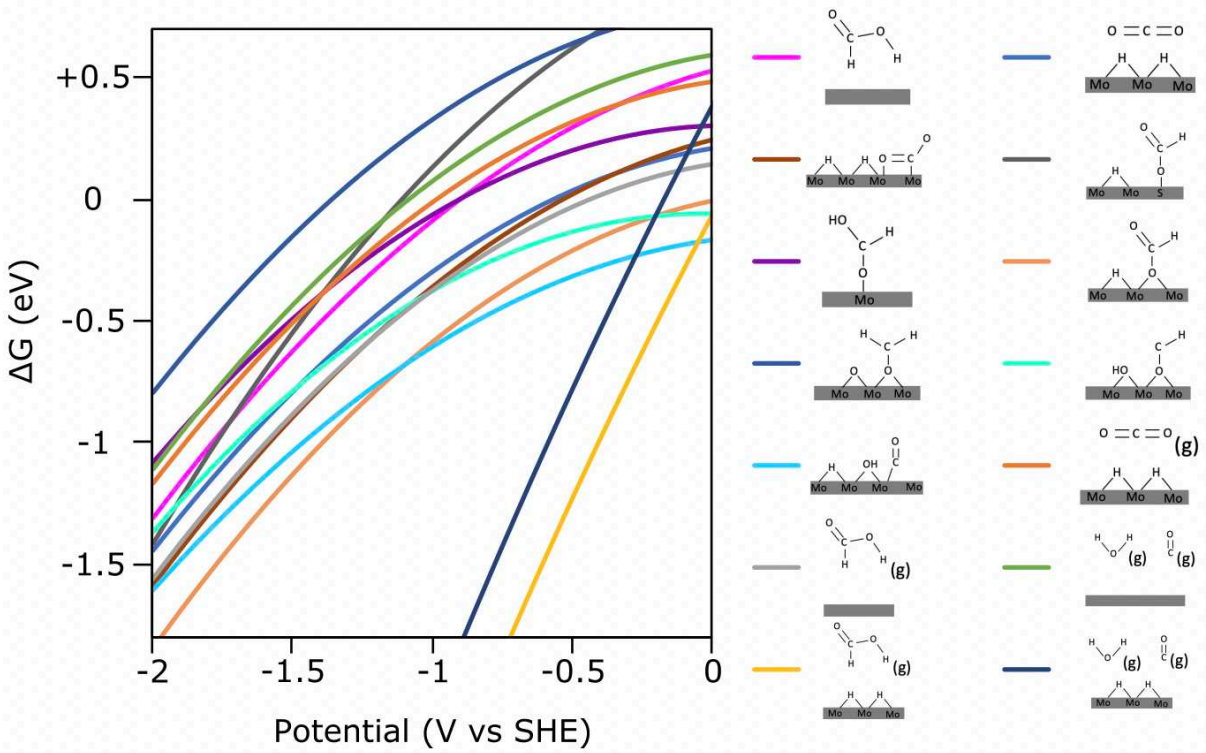

Figure A-8 : Extrapolation curves associated to all the intermediates considered in the mechanistic study on the S-edge 50%H.

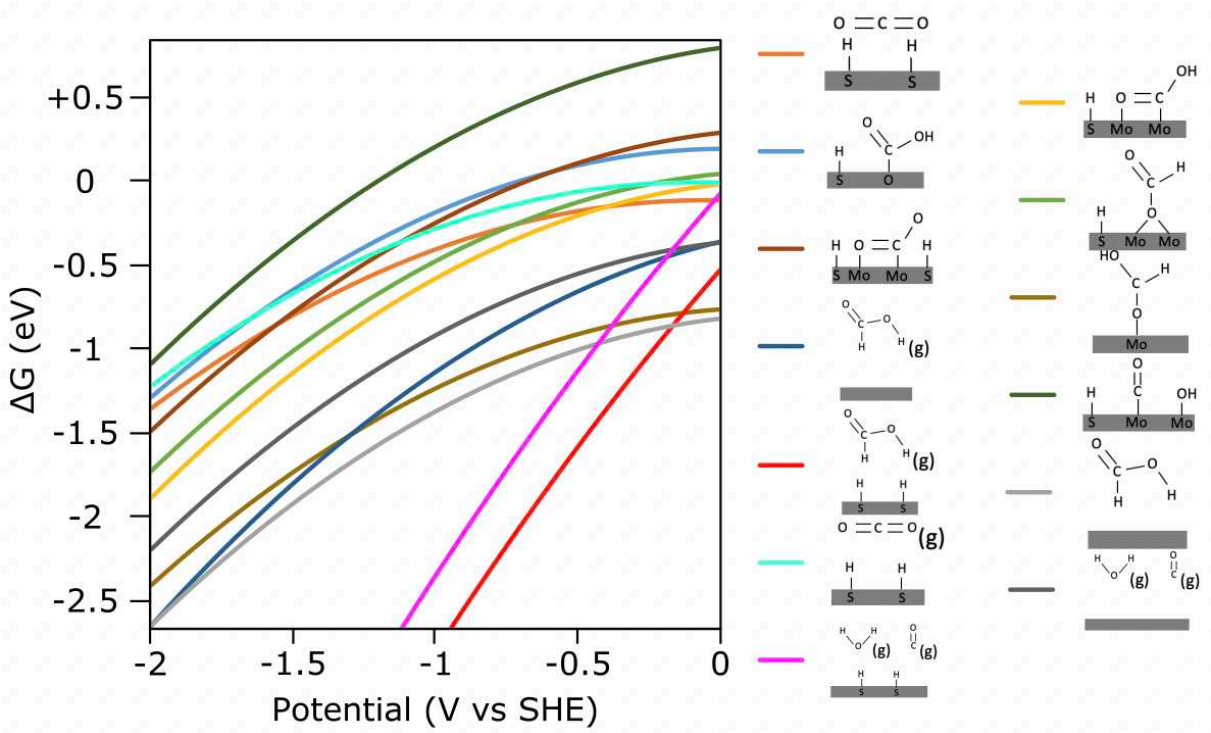

Figure A-9 : Extrapolation curves associated to all the intermediates considered in the mechanistic study on the Mo-edge 50%OH-50%SH.

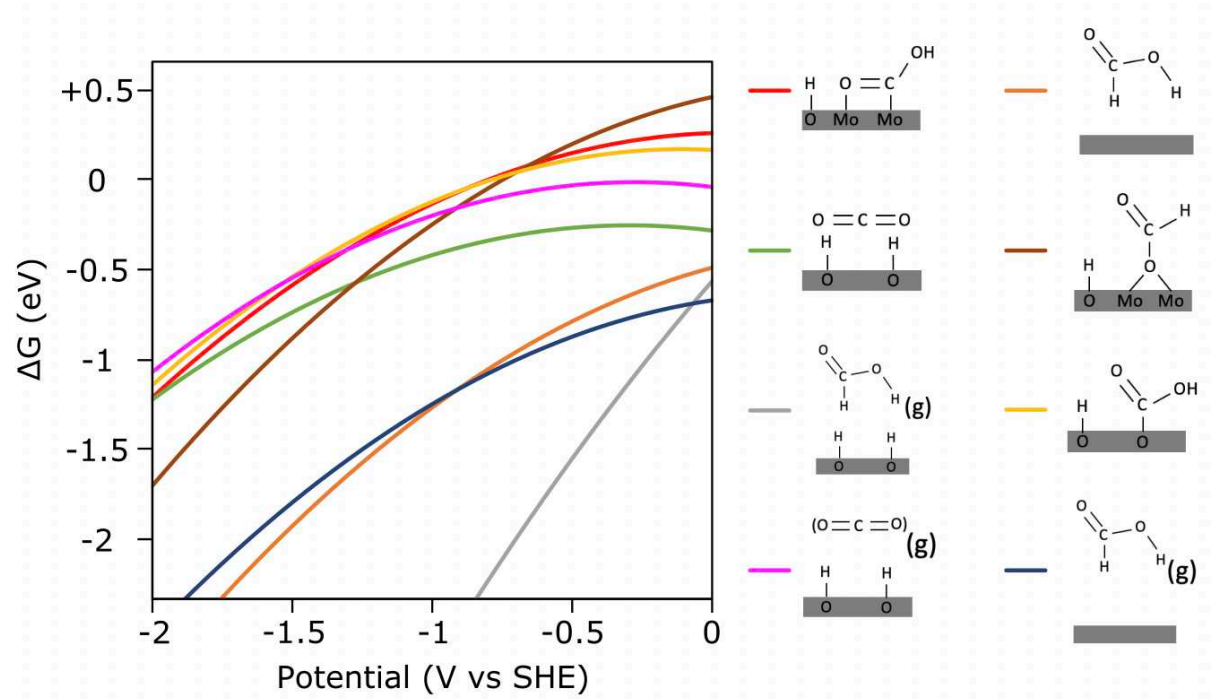

Figure A-10 : Extrapolation curves associated to all the intermediates considered in the mechanistic study on the Mo-edge 100%H.

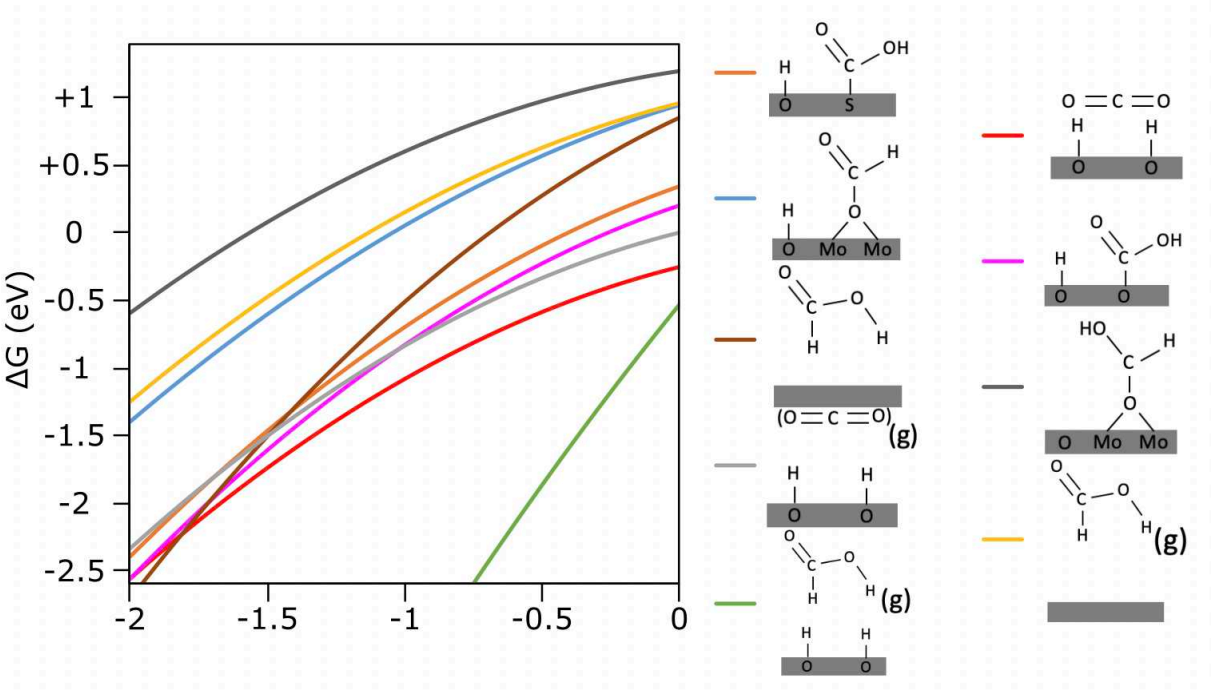

Figure A-11 : Extrapolation curves associated to all the intermediates considered in the mechanistic study on the S-edge hydroxylated.

Résumé :

Dans un contexte de transition énergétique, la communauté de la photocatalyse s'intéresse actuellement à la réduction de dioxyde de carbone (CO_2). Ces travaux de thèse visent à mieux comprendre les phénomènes complexes liés à cette réaction et aux matériaux photocatalytiques via l'utilisation de méthodes de chimie quantique. Les objectifs sont d'une part, de déterminer la faisabilité d'une hétérojonction impliquant MoS_2 (un matériau prometteur mais limité par son faible « bandgap ») et d'autre part, d'étudier les mécanismes de photoréduction du CO_2 sur ce matériau.
Dans un premier temps, nous explorons l'évolution de la position des bandes de conduction et valence pour différentes hétérostructures constituées d'un feuillet 2D-MoS_2 et d'une surface de TiO_2-anatase. En particulier, différentes surfaces de TiO_2, différents modes d'interaction (chimique ou physique), tailles de MoS_2 et compositions chimiques de l'interface sont étudiées. Les résultats identifient les paramètres de nano-structures ayant une influence sur la structure électronique de la jonction et ayant une influence sur le mécanisme de migration attendu (type I, type II ou schéma en Z).
Dans un second temps, les étapes du mécanisme de réduction du CO_2 en acide formique ou en monoxyde de carbone sur les sites de MoS_2 sous différentes conditions d'hydroxylation et d'hydrogénation sont étudiées. Cette étude est menée grâce à la méthode de la surface chargée, qui permet de simuler explicitement l'impact du potentiel électrochimique sur l'énergie des intermédiaires réactionnels.

Abstract:

In the actual context of energetic transition, the photocatalysis community is strongly interested in the reduction of carbon dioxide (CO_2). This thesis work aims at better understand the complex phenomenon associated to this reaction and the photocatalytic materials, by using quantum chemistry methods. The objectives can be divided in two axes. In a first time, the determination of the feasibility of a heterojunction involving MoS_2 (a promising material limiter by its small bandgap). In a second time, the investigations of the CO_2 photoreduction mechanisms on this material.
In a first part, we explore the evolution of the position of the conduction band and valence band for some heterostructures composed of 2D-MoS_2 and TiO_2 anatase surfaces. In particular, we study various TiO_2 surfaces, interaction modes (physical and chemical), MoS_2 sizes and chemical compositions of the interface. The results identify the nano-structuration parameters that have an influence on the electronic structure of the junction and that have an influence on the charge migration expected (type I, type II or Z-scheme).
In a second part, the steps of the CO_2 reduction mechanism are studied under different conditions of hydrogenation and hydroxylation of the MoS_2 edge. Mechanisms leading to the formation of formic acid or carbon monoxide are identified. This study is performed thanks to the surface charging approach, that manage to explicitly simulate the impact of the electrochemical potential on the energy of the reactional intermediates.